Rijkswaterstaat
Ministerie van Infrastructuur en Waterstaat

Deltares
Enabling Delta Life

TU Delft
Delft University of Technology

The Development of Creep in Peat over Time

A Validation of the Isotach Framework

T.R. van Straaten

The Development of Creep in Peat over Time

A validation of the Isotach Framework

by

T.R. van Straaten

Part of the requirements for obtaining the degree of

Master of Science
in Civil Engineering

at the Delft University of Technology,
to be defended publicly on Wednesday April 9, 2025 at 10:00 AM.

Thesis committee:

Dr. ir.	C. Zwanenburg	TU Delft / Deltares
Dr. ir.	F. Bisschop	Arcadis
Dr. ir.	F. J. van Leijen	TU Delft
Dr.	M. A. Cabrera	TU Delft
ir.	A. J. Grashuis	Rijkswaterstaat

Frontpage picture taken at the Zegveld polder by T.R. van Straaten.

Summary

Multiple long-term constant rate of strain (CRS) tests were performed on Zegveld peat from the Netherlands. The aim of performing these tests is to check the validity of the Isotach Framework. The Isotach Framework is built on the three fundamental concepts. 1.) There exists a unique relationship between strain rate ($\dot{\varepsilon}$), effective stress (σ'_v) and strain (ε). 2.) Lines of equal strain rate, called isotachs, run parallel when plotted on strain vs. the logarithm of effective stress. 3.) The mutual distance between these isotachs remains constant. The Isotach Framework forms the backbone of widely used settlement models. Postulated by Šuklje (1957) and later advanced by Bjerrum, Leroueil and Den Haan.

Different isotachs can be visualized by changing the applied displacement rate during CRS testing. The trajectories of these isotachs are determined to conclude on both the level of parallelism as well as the mutual distance between different isotachs. Five long-term CRS tests are performed on the same peat, taken form the same depth below surface level. The test configuration is kept the same for all of these five tests. The obtained results show a decent degree of parallelism for strain rates between $\dot{\varepsilon} = 10^{-7}\,s^{-1}$ and $\dot{\varepsilon} = 10^{-6}\,s^{-1}$. The mutual distance between the different isotachs remains largely unchanged within this strain rate regime.

However, the results show that the trajectory of the isotachs corresponding to the lowest strain rate of $\dot{\varepsilon} = 10^{-8}\,s^{-1}$ seem to diverge from those at higher strain rates. In practice, diverging isotachs result in stress-dependency of creep. Furthermore, it is concluded that the mutual distance between different isotachs increases with a decrease in strain rate. Additional CRS tests underline this observation. This increase in distance with lower strain rates in practice results in non-constant creep behaviour on logarithmic time scale, giving rise to tertiary creep. The observations made are important since field strain rates are shown to be a few orders of magnitude lower than those applied in conventional CRS tests.

To arrive at this conclusion, long-term subsidence data is studied of the Zegveld polder. A time series spanning over fifty consecutive years results in an estimated strain rate of $\dot{\varepsilon} = 10^{-12}\,s^{-1}$ - $10^{-11}\,s^{-1}$. Interferometric Synthetic Aperture Radar (InSAR) is used in the analysis of deformation behaviour of part of the Dutch A2 highway near Vinkeveen. The InSAR data shows a strong seasonal component in the estimated deformation pattern. A strain rate of approximately $\dot{\varepsilon} = 10^{-11}\,s^{-1}$ is subsequently calculated for this part of the A2. Analysis of settlement recorded using subsidence plates during construction of this part of the A2 shows an estimated strain rate around $\dot{\varepsilon} = 10^{-9}\,s^{-1}$ - $10^{-7}\,s^{-1}$.

From this it is concluded that strain of field projects are not comparable to the strain rates applied during conventional CRS testing. The validity of the classical isotach framework in describing the compression behaviour of peat is therefore questionable regarding field conditions. Current implementation of the classical isotach framework assumes parallel isotachs and thus a linear creep rate on logarithmic timescale. Existing settlement models such as the NEN-Bjerrum isotach model or the abc-isotach model are built on the assumed validity of the classical isotach framework. Consequently, not accounting for an increased divergence of isotachs with decreasing strain rate can result in the under-estimation of long-term settlement in peat.

The performed CRS tests showed transient behaviour around a change in strain rate. The time needed for the soil to fully adjust to the new strain rate increases with decreasing strain rate. This could give rise to invalid parameter determination since the soil's state has not yet moved to the isotach corresponding to the new strain rate. The obtained results of the step-changed CRS tests are simulated using the NEN-Bjerrum Isotach model, the abc-isotach model, the Soft Soil Creep model and the MIT Elasto-Viscoplastic model of Yuan and Whittle. Overall, a satisfactory fit is found between the models and the actual CRS test data. The MIT Y&W EVP model and the Soft Soil Creep model are capable of accurately simulating the observed transient behaviour around a change in strain rate.

Keywords: Isoatch, Strain Rate, Creep, Peat

Preface

The combination of following the master program of Geo-Engineering at the TU-Delft and simultaneously working at the Geotechnical cluster of Rijkswaterstaat gave me the opportunity to combine theory with practice. Over the last few years I truly enjoyed working on topics related to Geotechnical-Engineering. I therefore feel privileged to have gotten the opportunity to do a master thesis at Rijkswaterstaat and Deltares. The topic of creep development in peat proved to be intriguing. I am proud to report the findings of this study in this document.

Over the last months my understanding of the topic of this thesis increased significantly. Something which could not have been possible without the support of my thesis committee. I want to thank Cor Zwanenburg for giving me the opportunity to work on this subject and the guidance during the thesis period. Not only did I enjoy the weekly Wednesday morning progress meetings, I learned a lot from them as well. In addition I want to thank Rik Bisschop for his active support and valuable input, and Freek van Leijen and Miguel Cabrera for their insightful feedback over the last months. I want to thank Arjan Grashuis and Henkjan Beukema for providing the opportunity to work at the Geotechnical cluster at Rijkswaterstaat and giving me the possibility to complete my master thesis at Rijkswaterstaat. Without you I would not be where I am today.

Tom van Straaten
Utrecht, March 2025

Table of Contents

1. Introduction

1.1 Background

The Netherlands has a long history of transforming its landscape. Over millennia, major European rivers such as the Meuse (Maas) and Rhine (Rijn) shaped the Dutch landscape, forming deltaic areas and tidal estuaries. The shallow basins formed in this manner were shielded from strong tidal forces coming from the sea by natural sand dunes. Over time, sedimentation processes gradually isolated these tidal zones from the sea, allowing fresh water from precipitation and river inflows to replace the brackish water conditions. As a result of this, a hospitable environment formed over time allowing for the growth of aquatic vegetation. As time progressed, new vegetation continued to grow (Kasse, 2005). Simultaneously, layers of (partly decayed) organic matter accumulated below the groundwater level thereby preventing oxidation. Over time the peat layers formed in this manner continued to grow, resulting in the formation of large peat lands throughout much of the Netherlands.

Centuries ago nearly half of the Netherlands consisted of these impassable peat bogs, particularly in the western and northern regions (Van Veen, 1962). Since these peatlands were neither fully land nor water, they proved difficult to facilitate agricultural development. As a result of an increasing population, the need for hospitable land grew. Consequently, large-scale reclamation projects, excavation, and drainage of the peatlands began in the eleventh century (Van Veen, 1962). However, when peatlands are drained, the exposure to oxygen initiates oxidation, leading to land subsidence and the release of stored carbon dioxide into the atmosphere. This process has resulted in substantial ground-level lowering, with some areas now lying several meters below sea level (Van Veen, 1962).

Today, centuries after the first large scale land reclamation projects in the Netherlands started, the need for available space to facilitate the development of new infrastructure is no less. Building infrastructure on peat soils presents unique geotechnical challenges due to their high compressibility and high heterogeneity.

Rijkswaterstaat, part of the Ministry of Infrastructure and Water management, is responsible for design, construction and management of primary infrastructure in the Netherlands. Rijkswaterstaat faces significant challenges in managing infrastructure such as highways built on peatlands. As a result of strict standards to limit differential settlement, Rijkswaterstaat aims to maintain an exemplary infrastructural network which guarantees drivers safety and comfort. Consequently, accurate settlement prediction is essential for ensuring the safety, durability, and cost-efficiency of infrastructure projects built on soft soils such as peat.

1.2 Problem Statement

In the experience of Rijkswaterstaat, unforeseen premature repairs required on major highways such as the A4, A16, A20, A24, and A29, underscore the persistent challenges in accurate (long-term) settlement prediction of soft soils. Unforeseen settlement can compromise structural integrity, reduce ride comfort, and pose safety hazards for road users resulting in unexpected infrastructure deterioration and increased lifecycle costs. This process results in non-compliance with the settlement criteria set by Rijkswaterstaat. These recurring maintenance issues highlight a fundamental problem in current settlement prediction which could possibly be attributed to lacking theory on the development of long-term settlements in soft soils such as peat.

In practice, a multitude of phenomena could be responsible for the ongoing process of maintenance activities. Lacking quality of the realisation of a project or the self-weight of asphalt due to asphalt overlaying could both attribute to the settlement criteria of Rijkswaterstaat not being met. This thesis is however focussed on the deformation development of peat over time.

A key driver of long-term settlements in peat is creep, a time-dependent deformation that continues under constant load. In Geotechnical Engineering, the accurate determination of the creep rate and a comprehensive understanding of the theoretical models available for describing creep behaviour are crucial for making reliable settlement predictions. The settlement criteria of Rijkswaterstaat not being met suggests that commonly used settlement models may be insufficient for describing peat behaviour under real-world conditions.

One possible explanation for these deviations lies in the behaviour of creep over time and the theoretical frameworks used to describe this. The isotach framework is one of these theoretical frameworks and forms the backbone of common settlement prediction models used to describe the compression behaviour of soft soils. The classical isotach framework, as implemented in the Netherlands, is built on three fundamental concepts:

1. There exists a unique relationship between strain (ε), effective stress (σ'_v), and strain rate ($\dot{\varepsilon}$) called isotachs.
2. Lines of equal strain rate are parallel when plotted on strain vs. the logarithm of effective stress.
3. The mutual distance between different isotachs remains constant.

Deviations from the fundamental concept of parallel equidistant isotachs could have significant practical consequences. If the mutual distance between different isotachs changes over time, the creep rate would no longer be linear on logarithmic timescale, undermining the validity of current settlement prediction models. In addition, diverging isotachs imply that the creep parameter is stress-dependent, meaning that the creep rate would vary depending on the current stress level, rather than being an intrinsic property of the soil. Validation of the classical isotach framework in describing the compression behaviour of peat is therefore of great importance. Moreover, the validity of the classical isotach framework is studied on clay. It has however not been validated for peat. This Thesis therefore focusses on the main research question:

- ◊ Is the isotach framework valid for describing the compression behaviour of peat?

Additionally, changing loading conditions in practice result in different strain rates. Therefore, investigating the classical isotach frameworks ability to capture these strain rate changes is essential to ensure reliability in using the classical isotach framework in predicting real-world settlement behaviour. Validation of the isotach framework is therefore particularly crucial to Rijkswaterstaat and the Geotechnical-Engineering community.

1.3 Scope and Objectives

This thesis focuses on evaluating the validity of the classical isotach framework for describing the compression behaviour of peat. The study is confined to the evaluation of the compression behaviour of peat and does not extend to other soft soils. The applicability of the isotach framework in describing the compression behaviour of peat across different strain rates is of primary interest. Long-term Constant Rate of Strain (CRS) laboratory tests are performed to this end. The tests are limited to Zegveld peat only. Influence of changes in temperature on isotach behaviour of peat falls beyond the scope of this thesis.

The development of creep in peat, and the subsequent strain rates, are of great interest. The scope therefore includes analysing InSAR data and long-term subsidence records from the A2 highway near Vinkeveen to provide context to the expected difference in range of strain rates between field conditions and those in laboratory testing. Additionally, long-term deformation analysis of the Gaasp and Zegveld polder is performed to identify a lower limit of field strain rates.

The research further includes a comparison of the CRS test results with numerical simulations using four different constitutive models used for making settlement predictions of soft soils. The analysed models are limited to the MIT Elasto-Viscoplastic model of Yuan and Whittle, the Soft Soil Creep model, the abc-isotach model, and the NEN-Bjerrum isotach model.

In addition to answering the main research question this thesis therefore aims to:

1. Conclude on the validity of the classical isotach framework based on parallel equidistant isotachs in describing the compression behaviour of peat.
2. Analyse the isotach behaviour around a change in strain rate. By step-changed CRS testing, the time required for the soil to reach a new isotach is studied to give meaning to the classical isotach frameworks applicability in describing changing strain rates.
3. Quantify the difference in estimated peat strain rates of field projects and strain rates used in CRS laboratory testing on peat.
4. Conclude on the practical consequences of the observed isotach behaviour in step-changed CRS testing and the identified difference between strain rates used in laboratory testing and those estimated in field conditions.
5. Evaluate the performance of different constitutive models used to make settlement predictions of soft soils and capture the extent to which these models are able to accurately simulate changes in strain rate.

By integrating laboratory testing, field observations, and numerical modelling, this thesis strives to advance the theoretical understanding of peat compression behaviour under varying strain rates. The research connects theoretical insights with real-world observations from infrastructure projects constructed on peat. The outcomes of this research are intended to contribute to improving settlement prediction models, particularly for projects on soft soils such as peat.

1.4 Reader's Guide

Chapter 2 presents the state of the art in settlement theory on peat, with an emphasis on the Constant Rate of Strain (CRS) test and the classical isotach framework. Additionally, the chapter provides a formulation of the constitutive models used to simulate the step-changed CRS tests that are ultimately described in Chapter 6.

Chapter 3 investigates the difference in strain rates between CRS laboratory testing and projects built on peat, an area that has been studied extensively for clay, but not for peat. Using data from subsidence plates and InSAR measurements from project sites across the Netherlands, this chapter aims to quantify the difference in strain rates in peat. In addition, the field strain rates provide context to the strain rates applied during CRS testing described in Chapter 4 and Chapter 5.

Chapter 4 describes the methodology used in CRS laboratory testing to evaluate the validity of the classical isotach framework in describing the compression behaviour of peat. It details the CRS testing procedure including the method of visualizing isotachs through changes in applied rate of displacement, the test setup, and the geotechnical properties of the Zegveld peat samples.

Chapter 5 presents the results of the CRS tests on Zegveld peat, beginning with the findings from five step-changed long-term tests, followed by the results of two additional step-changed CRS tests. The chapter concludes with an analysis of tangent lines through different isotachs, which serves as a method for assessing the validity of the classical isotach framework. In addition, the chapter links the main findings of the CRS laboratory tests with practical implications. The chapter focuses on sketching the practical consequences of the results from the long-term CRS tests on Zegveld peat.

Chapter 6 describes the element-test simulation of step-changed CRS tests, focusing on evaluating the ability of common constitutive models to describe the compression behaviour of peat under varying strain rates. The simulations serve as a validation of existing constitutive models and as a means to contextualize the behaviour observed during strain rate changes in laboratory testing.

Chapter 7 presents the main conclusions derived from the CRS laboratory tests, simulations, and field observations, summarizing the findings on the validity of the classical isotach framework for peat compression behaviour and the subsequent implications for settlement prediction models.

Chapter 8 provides recommendations on improving settlement prediction models and enhancing constitutive models for peat compression behaviour. It also proposes additional tests aimed to further develop the understanding of creep in peat. Thereby proposing an extension of the findings described in this study.

2. State of the Art

This chapter first gives an overview and comparison of the existing one-dimensional oedometer tests available for determining settlement parameters. The emphasis will be on the Constant Rate of Strain (CRS) test. This apparatus allows for changes of applied strain rate during testing and is increasingly becoming more popular in the Netherlands as a means of determining settlement parameters. After highlighting the main differences between available oedometer tests, the different loading stages of a CRS test are described. The emphasis in here is on the creep phase. The theoretical framework currently used to describe the compression behaviour of soft soils is described in the next sections.

It is important to stress the fact that existing literature on the compression behaviour of soft soils is mainly focused on clay. Although the physical, mechanical and chemical properties of clay and peat are different, the deformation behaviour when subjected to loading is generally not. Both clay and peat behave like soft soils. Subsequently, developments within the field of oedometer testing on soft soils, and the theoretical frameworks used to describe the compression behaviour, are assumed to be valid for both clay and peat.

2.1 Oedometer Tests

This section describes the different available one-dimensional oedometer tests. The Incremental Loading test (IL) and the Constant Rate of Strain test (CRS) are the most common laboratory tests in soft soil engineering. The CRS test poses numerous advantages over the IL test. First and foremost is a continuous stress-strain plot. This allows for more accurate determination of required settlement parameters such as the pre-consolidation pressure, compression ratio, recompression ratio, creep parameter and over-consolidation ratio. Accurate prediction of these settlement parameters is pivotal in predicting settlement. In the laboratory two types of one-dimensional oedometer tests are mainly used to determine the necessary parameters.

2.1.1 Incremental Loading

Originally introduced by Karl von Terzaghi the Incremental Loading (IL) test is currently the most conventional laboratory test used for determining settlement parameters (Kumara et al, 2020). In an IL test, a soil sample is laterally confined by a metal ring, permitting only vertical deformation. In most cases the sample has a height of 20 mm and a diameter of 63.5 mm. Drainage is allowed at both the top and bottom of the sample. The test involves sequentially increasing the vertical load on the sample, hence the name "incremental loading." Typically the loading scheme consists of seven steps. Each step is maintained for at least 24 hours to allow for drainage of excess pore pressure and creep. It can be required to maintain a constant load for a period longer than 24 hours to better capture the creep phase. This however depends on the tested material. Usually the loading scheme consists of a minimum of 5 load increments followed by an unloading step. Followed by an unloading and reloading step. Elapsed time, the axial displacement and vertical stress are recorded during testing. These are ultimately used to determine the mechanical- and physical parameters of interest. Figure 2.1 sketches a typical IL test apparatus.

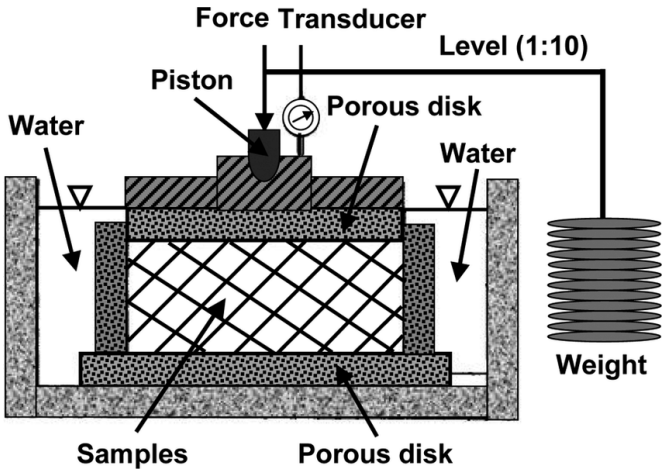

Figure 2.1: Schematic illustration of an Incremental Loading apparatus [After Wang et al, 2015].

Due to the time required for each loading step, the total number of steps in an Incremental-Loading test is often limited to nine. Consequently, the resulting stress-strain curve is not smooth but consists of a series of connected line segments, each corresponding to a load increment. This segmented curve can hamper accurate determination of the pre-consolidation pressure. This non-continuous stress-strain curve is a major limitation of the IL test.

2.1.2 Constant Rate of Strain

A constant rate of strain (CRS) test is displacement controlled. Introduced by Crawford in 1959, after the IL-test already existed, a CRS test deforms the sample axially (Adams et al., 2011). Figure 2.2 shows a schematic illustration of a CRS test. This displacement is applied at a constant rate over time. In a CRS test the soil sample is only allowed to undergo deformation in the vertical direction. A metal ring placed around the sample restricts lateral deformation of the sample. In most cases the soil sample has a height of 20 mm and a diameter of 63.5 mm, similar to the IL Test. Depending on the aim of the test the sample height can be increased to 30 mm. In a CRS test drainage is (only) allowed at the top of the sample and excess generated pore pressure during testing is recorded at the bottom of the sample. Because of this, the excess generated pore pressure in the sample follows a parabolic shape and is generally corrected for by multiplication with $\frac{2}{3}$. This is described in more detail in Section 2.5.1.

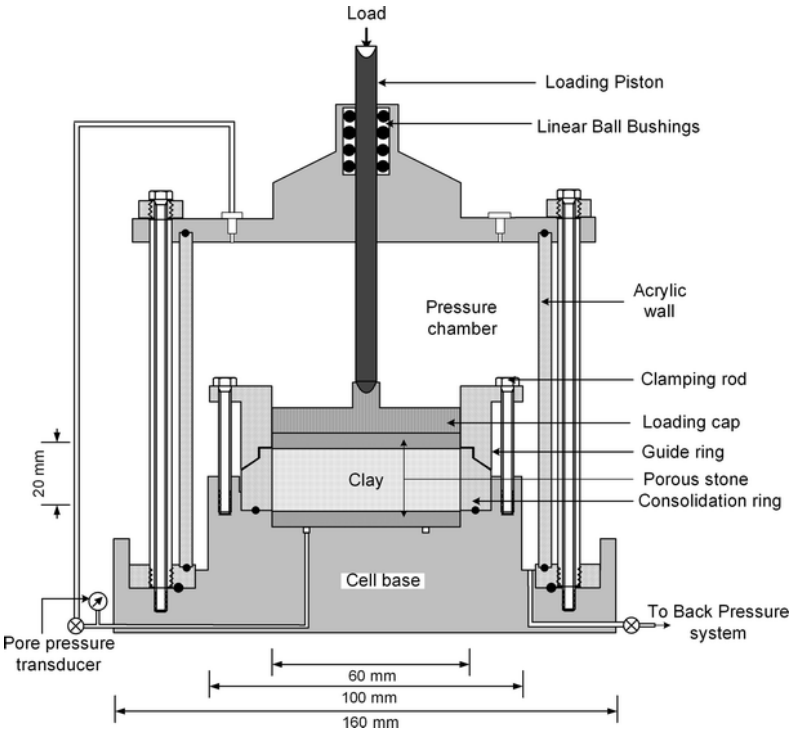

Figure 2.2: Schematic illustration of a Constant rate of Strain apparatus [After Robinson et al, 2018].

The major advantage of a CRS test over the IL-test is the continuous reading of datapoints. In an IL-test, the strain versus effective stress graph consists of multiple line segments corresponding to the number of applied load increments. In a CRS test the sample is deformed at a constant rate of displacement. The required vertical load to maintain this constant displacement rate is recorded throughout testing. Excess generated pore pressure is measured throughout testing. This allows for the continuous calculation of the effective stress resulting in a smooth graph. This ultimately helps in a more accurate prediction of parameters such as the pre-consolidation pressure. Leroueil et al. (1983) concluded that the pre-consolidation pressure is best determined using a CRS test, precisely because of this higher achievable accuracy.

Note that in a CRS test the sample is loaded with a constant displacement rate. When the initial sample height is known, the corresponding strain rate can easily be calculated. The different strain notations used in soft soil engineering are described further in Section 2.2.1.

Where an IL test often requires over seven days to complete, a CRS test can be finished within a few days, depending on the chosen displacement rate. This is a major advantage of the CRS test over the IL-test. Selecting an appropriate displacement rate however is critical, as a rate too high may prevent adequate dissipation of excess pore pressures. This in turn may lead to inaccurate calculated stresses in the sample due to a non-homogeneous stress distribution within the sample (NEN 8992:2024). To avoid this, the ratio of excess pore pressure to total stress is typically kept within a range of 3% to 15% (NEN 8992:2024) (Adams et al., 2011). A ratio lower than 3% may lead to inaccurate calculation of permeability but is of limited influence on other test results such as settlement parameters. In practise a ratio between 5% and 10% is often used. Because of this, the strain rate selection can be an iterative procedure. The NEN 8992:2024 standard suggests displacement rates based on the material type and its hydraulic conductivity. This is useful as a first reference for the displacement rate selection process. If this rate of displacement results in too much excess generated pore pressure it should be lowered in additional test to comply with NEN 8992:2024.

2.1.3 Rowe Cell

A third type of one dimensional oedometer test is the Rowe cell, developed by Professor Rowe at the University of Manchester in the 1960s. This type of test uses hydraulic pressure to load the soil sample. In a Rowe cell, back pressure can be applied allowing for simulating the in-situ conditions of the soil being tested (Premchitt et al., 1995). Even though a Rowe Cell test allows for different drainage conditions and test configurations, it is not used on a regular basis in the Netherlands. The most probable reason for this is cost related. A Rowe cell apparatus consists of more complex components, such as a flexible diaphragm, Figure 2.3. This makes the apparatus itself, and performing a laboratory test, more expensive compared to an incremental loading test or CRS test.

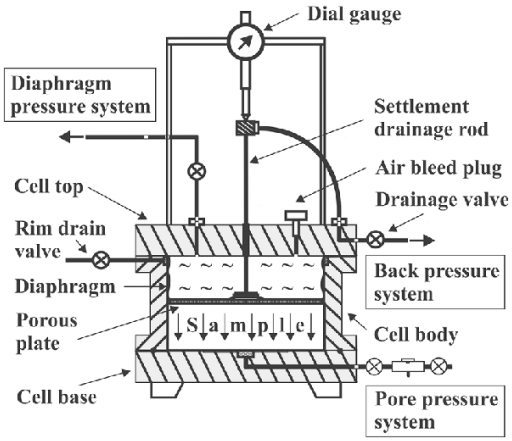

Figure 2.3: Schematic illustration of a Rowe cell. [After Olek et al, 2020].

2.2 Stress and Strain Development

This section describes the difference in strain notation used to quantify the compression behaviour of soft soils such as peat. It proves beneficial to use natural strain to account for the prevention of the sample height becoming zero. Three different loading stages can be identified. In addition to primary consolidation and secondary compression, studies of Den Haan (1994) and Edil (1979, 1980) show the development of tertiary compression in long-term laboratory testing on peat.

2.2.1 Strain Notations

The resulting strain-time plot from a laboratory test can be divided in different stages. The constitutive behaviour of the soil differs during each stage. The change in sample height due to loading is often described as an increase in strain. Relevant settlement parameters are commonly inferred form a strain *ε* vs. logarithm of effective stress *log(σ')* plot. In the scientific community it is generally more usual to express the change in sample height as a change in void ratio *e*. In the Netherlands however natural strain is often used to describe the compression behaviour of soft soils such as peat.

Settlement parameters such as the compression ratio (CR) and the recompression ratio (RR) are defined based on linear strain. Linear strain (Cauchy) relates the change in height of an element to the original height of the element as shown by Equation 2.1.

$$\varepsilon^c = \frac{\Delta H}{H_0} \quad [-] \qquad \text{Where;} \qquad (2.1)$$

ε^c = Linear strain [-]
ΔH = Change in sample height [mm]
H_0 = Original sample height [mm]

In case of soil volumes, both in-situ scale and laboratory scale, the soil volume thickness cannot reduce to zero, irrespective of the applied load (Zwanenburg, 2021). Linear strain does not account for this as is indicated in Figure 2.4. Consequently, at large strains the strain versus logarithm of effective stress plot will be non-linear. To capture this effect, natural strain (Hencky) can be used.

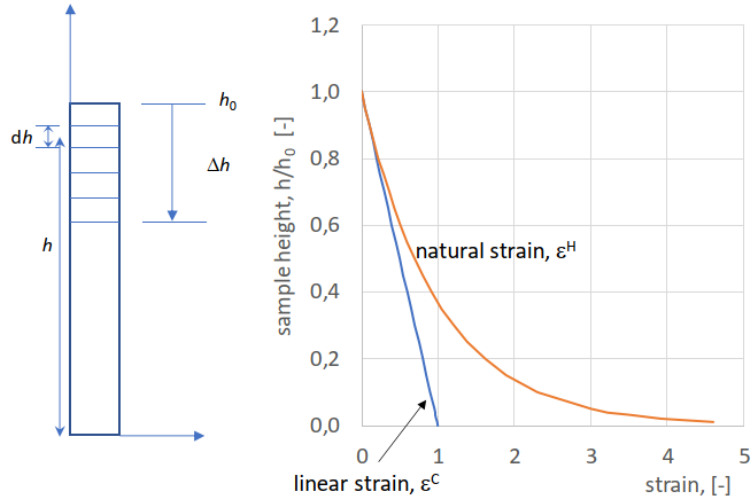

Figure 2.4: Difference between Linear and Natural strain. [After C. Zwanenburg, 2021].

Natural strain relates the increment in layer thickness to the actual height of an element is shown by Equation 2.2.

$$\varepsilon^H = -\ln\left(\frac{H_0 - \Delta H}{H_o}\right) = -\ln(1 - \varepsilon^c) \quad [-] \qquad \text{Where;} \qquad (2.2)$$

ε^H = Natural strain [-]
ε^c = Linear strain [-]
ΔH = Change in sample height [mm]
H_0 = Original sample height [mm]

This thesis is focused on peat. Natural strain will therefore be used to describe and analyse its constitutive behaviour. However, available (international) literature primarily uses linear strain or void ratio to describe the compression of soft soils. Note that the difference between linear strain and natural strain becomes significant above 50% strain (Den Haan et al., 2004).

2.2.2 Loading Stages

Three different loading phases can be identified in one-dimensional loading of a soil as shown in Figure 2.5. All three loading stages result in a volume decrease of the soil. Consequently this results in an increase in strain or a decrease in void ratio. In case of oedometer testing the vertical strain equals the volumetric strain.

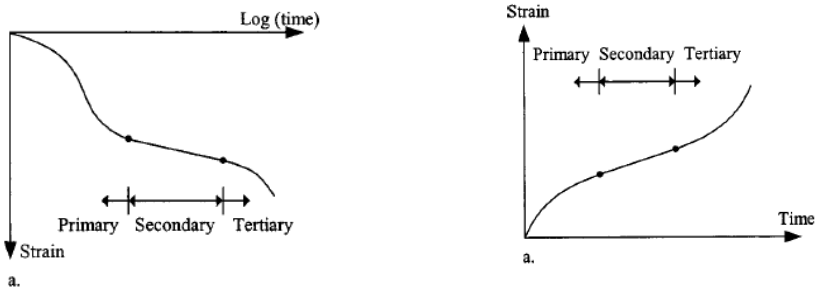

Figure 2.5: Three different loading stages in strain vs. log time plot. (Left) and three different creep stages in strain vs. time plot. (Right) [After Augusten et al., 2004].

Instantaneous compression is the immediate deformation observed when a load is applied to a soil body. The immediate deformation is dependent on the soil's Young's modulus.
Primary consolidation is defined as the phase in which excess pore pressure caused by the applied load dissipates. As a result, the load is shifted from the pore water to the soil skeleton. The duration of this phase varies significantly based on the soil's hydraulic conductivity.
Secondary compression refers to the continuation of volume change of the soil layer, often referred to as creep. In oedometer testing this phase relates to pure creep in which volume change of the soil element is attributed to changes in the soil skeleton due to the soils viscosity (Leroueil, 2006).
Finally, tertiary compression is marked by an accelerated rate of deformation on a logarithmic scale after secondary compression. This is known to occur in peat under loading conditions due to the high amount of organic matter that is being present in peat (Den Haan, 2007).

In addition to the different loading stages, different creep stages can be identified (Augusten et al., 2004). As shown in Figure 2.5, a primary, secondary and tertiary creep stage in strain versus time plot is visible corresponding to a decreasing, constant and increasing strain rate respectively.

2.3 Creep

This section describes the current knowledge gap on the origins of creep in soft soils. In addition, the physical and/or chemical processes responsible for creep are not completely understood. The results from studies performed by Buisman (1936) as well as Bishop et al. (1969) both indicate a constant creep rate on logarithmic time scale. Long term field studies indicate the same results. Both studies indicate stress-independent creep behaviour. The majority of these performed studies is on clay. Studies on peat performed by Edil et al. (1979) indicate a non-constant creep rate on logarithmic time scale. This marks a contradiction between observations made on long-term compression test on clay and long-term compression test of peat. Improving understanding on the rate at which creep takes place in peat is therefore of great importance.

2.3.1 Creep Origins

The consolidation period starts from the start of loading. And is finished when the excess generated pore pressure due to loading is dissipated. In practice this point of full dissipation will never be reached (Rajapakse, 2016). Creep is believed to be a continuous process as well. This is of great importance since the main driver of long-term settlement is creep. Difficulty arises when the starting point of creep needs to be determined. Two hypothesis exist which continue to spark debate within the geotechnical community till this day (Degago et al., 2011, 2013).

Hypothesis A, mainly supported by Ladd and Mesri assumes creep starts when the process of pore pressure expulsion is finished (Degago et al., 2013). Consequently, this theory distinguishes two sequential processes; primary consolidation and secondary compression (creep). Furthermore, this approach assumes there is no creep during the primary consolidation phase. As a result of this, the void ratio achieved after consolidation is finished would be independent from time and layer thickness. It would only depend on pore pressure dissipation. According to this theory, primary consolidation and creep are mutually exclusive.

Hypothesis B on the other hand assumes creep starts from the beginning of loading. This theory is supported by Den Haan, Bjerrum and Leroueil amongst others. In this theory creep takes place simultaneously with the consolidation phase of a (partly) saturated loaded soil element. As a result of this, the void ratio of the soil would be time and layer thickness dependent (Augusten et al., 2004).

Degagao et al. (2013) summarized the experiments performed to unravel this creep origin debate. They concluded that the results of some of these studies are convoluted. The subsequent results are simultaneously used to support hypothesis A as well as Hypothesis B (Degagao et al., 2013). The majority of scientific studies conducted around the world are in support of hypothesis B. In addition, Hypothesis A cannot be combined with the classical isotach framework since Hypothesis A assumed the final void ratio after a period of loading is time independent (Leroueil, 2006). This thesis therefore builds on the assumed validity of Hypothesis B.

The origins of creep are not fully understood. As of today, the reason for creep to take place in peat are mainly attributed to the following phenomena;

1. Flow of water from micro- to macro pores.
   Because of how peat layers are formed, a peat layer often has a dual porosity. This means a peat layer can be seen as a hybrid material containing micro and macro pores (Jommi et al., 2019). The outflow of water from these pores under constant loading leads to creep.
2. Gas expulsion.
   In general, peat has a large void ratio in which the pores in between the peat fibres can be (partly) filled with water. As a result of this biological and chemical processes take place in a peat layer. Degradation of material due to (an)aerobic processes or chemical processes such as oxidation are two examples of this. Due to these processes taking place, gas can become entrapped within the different peat fibres (Kaczmarek et al., 2017), (Tolunay et al., 2024). After time these gas bubbles can be expulsed from the peat layer due to loading. As a result of this a volume loss of the peat layer due to constant loading is achieved.
3. Decay of organic matter
   Peat is a highly organic material. Due to gas being trapped withing the peat fibres organic material can start to decay due to exposure to oxygen. This decay of organic matter results in volume loss of the organic matter resulting in volume loss of the peat layer (Edil et al., 1979).

It should be noted that the tendency for creep to occur is higher in materials that have a high percentage of organic matter and a high water content. This in general makes peat more susceptible to creep than clay (Malinowska et al., 2016).

2.3.2 Creep Definition

Creep is defined as the change of volume of a soil element over time under constant stress. In here there is a relationship between volume, stress and time as shown by Figure 2.6. Note that the volume change of a soil element can both be expressed as a change in void ration *e* or as a change in strain *ε*.

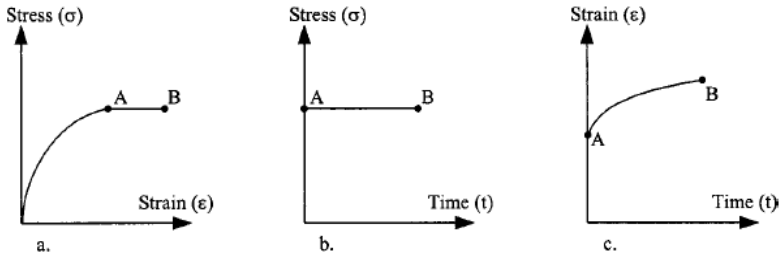

Figure 2.6: Visualization of creep in stress-strain plot (a), stress-time plot (b) and strain-time plot (c) [After Augusten et al., 2004].

After a load is exerted on a soil element the stress-strain state corresponds to point A in Figure 2.6a. From this point on the stress stays constant and a strain path from A-B is followed. Due to creep, the strain / volume of the soil element changes under constant stress (A-B). Over time, the stress remains constant whilst a change in strain is noted. This corresponds to (A-B) in Figure 2.6b and Figure 2.6c.

Buisman et al. (1936) showed how the settlement of a soil body can be described as the sum of the direct compression affect and a time dependent secular effect. Buisman therefore was the first to formulate a logarithmic creep law (Den Haan, 2007), as shown by Equation 2.3.

$$z_t = \alpha_p + \alpha_s \log_{10}(t) \qquad (2.3)$$

where; z_t = settlement per unit thickness [-]
α_p = direct compression coefficient [kg cm^{-2}]
α_p = secular compression coefficient [kg cm^{-2}]
t = time [minutes]

Distinction should be made between the two contributing factors in this equation. Buisman attributes α_p to the immediate effect of loading and α_s to a secular (temporal) effect. This distinction is not to be confused with the primary and secondary phase of consolidation as described in Section 2.2.2. According to Buismans hypothesis, an immediate effect and a temporal effect occur simultaneously, thereby abiding by Hypothesis B of the creep origin debate.

2.3.3 Tertiary Compression

During both the secondary and tertiary compression stages there are continuing changes in the soil fabric due to structural rearrangements within the peat fabric (Dhowian and Edil, 1980). As secondary creep progresses, there may be a transition phase where the rate of deformation starts to increase with the logarithm of time. This transition marks the beginning of the tertiary creep phase. In organic materials such as peat this is mainly attributed to structural breakdowns or internal shifts within the peat matrix, also called bifurcation points. Eventually this leads to a breakdown or failure of the matrix structure of the soil (Brandl, 2018).

Dhowian and Edil (1980) performed long-term incremental loading tests on different peat samples from Wisconsin. The performed consolidation tests took several months. The consolidation pressures were increased incrementally with a pressure increment ratio of 1. Starting with 25 kPa the load was increased until a final applied pressure of 400 kPa was reached. This last pressure increment was exerted on the peat sample for a duration of 300 days. After this time the compression rate became insignificant. Figure 2.7 shows the vertical strain, normalised outflow and excess pore pressure on logarithmic time scale for the first stress increment.

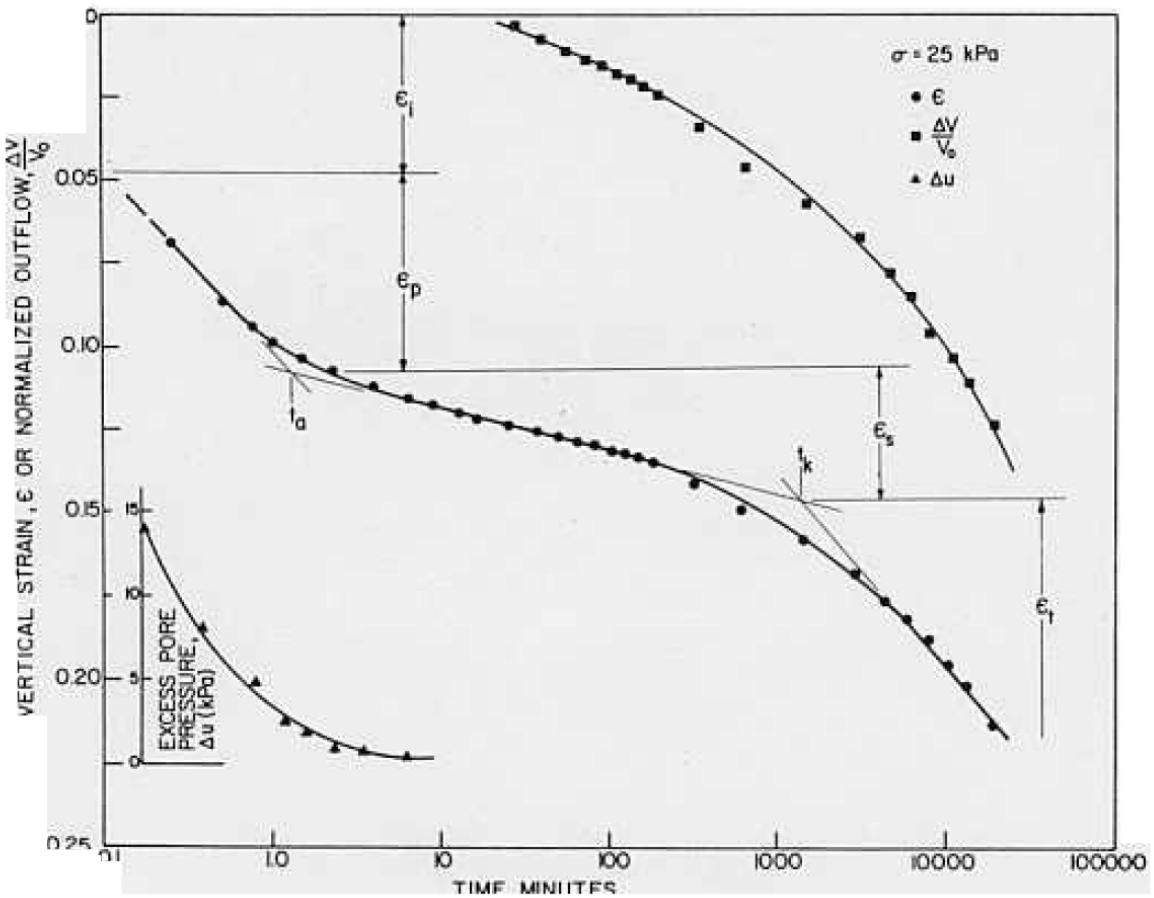

Figure 2.7: Tertiary creep observed in long-term consolidation tests on peat [After Dhowian and Edil, 1980].

Note the resemblance of Figure 2.5 to Figure 2.7. The different loading stages described in Section 2.2.2 can clearly be identified in Figure 2.7. An acceleration of the strain rate with the logarithm of time is clearly visible after 1000 minutes marked by t_k. Dhowian and Edil (1980) mark this point as the start of tertiary compression.

Dhowian & Edil (1980) attribute tertiary creep to the dual porosity of the peat. They hypothesize that gas is being generated during loading as a result of decomposition of the peat. Expulsion of this gas can give rise to an accelerated strain rate over time. In addition, Dhowian and Edil (1980) note that possible outflow of entrapped porewater from the micropore towards the macro pores of the peat can result in a non-constant deformation rate on logarithmic timescale.

Figure 2.8 shows the final load increment from 200 kPa to 400 kPa. An increase in vertical stain rate with the logarithm of time after 10000 minutes is clearly visible. After 300 days of maintaining this constant load the compression rate became insignificant and becomes constant.

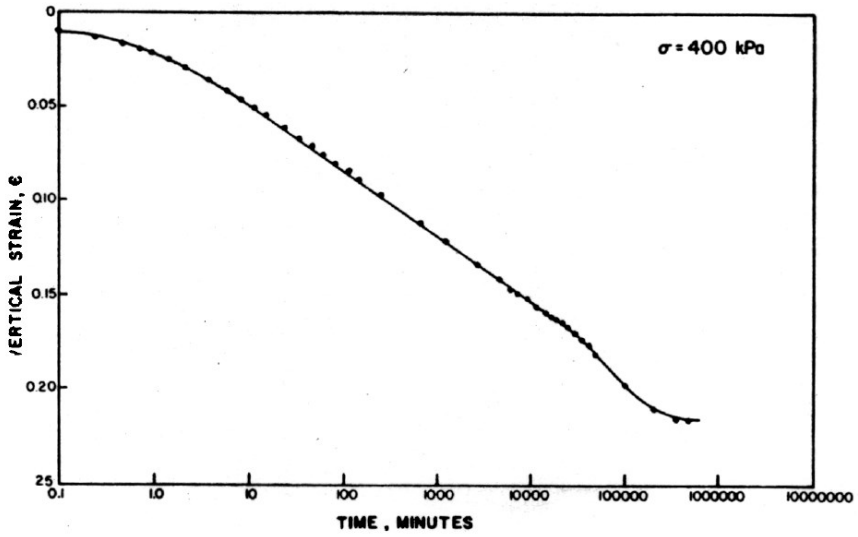

Figure 2.8: Tertiary creep is observed in the final loading stage after approximately 10000 minutes [After Dhowian and Edil, 1980].

The studies of Dhowian and Edil (1980) demonstrate the existence of tertiary compression phase in long-term consolidation test on peat. The existence of a tertiary compression phase can result in underestimating long-term deformation since the secondary compression phase is assumed to be linear on logarithmic time scale. The laboratory tests of Dhowian and Edil (1980) contradict this assumed continuous linear secondary compression stage. Furthermore, Dhowian and Edil (1980) note that serious errors may result from extending the linear portion of the secondary compression curve resulting in an underestimation of long-term settlement.

2.3.4 Studies on Creep

Throughout the years multiple researchers conducted experiments and studies on the long-term settlement behaviour of soft soils. The results of these studies are used to construct theoretical frameworks used to describe and quantify the compression behaviour of soft soils.

Buisman (1936) performed multiple long-term loading tests on peat and clay samples, one with a duration of over 500 days. From this study Buisman reported that it is observed that the values found of α_s (the slope of the load-time diagram representing the secular effect) are approximately proportional to the load applied. In other words, Buisman (1936) suggests that the slope of the load-time diagram increases as the load applied increases. From the tests of Buisman (1936) on clay and peat it can be concluded that the creep rate is linear on logarithmic time scale. Furthermore, Buisman (1936) compared the conducted tests to field studies where they again conclude that the long-term creep settlement appears to take place at a constant rate on logarithmic time scale.

A test section managed by Buisman in 1934 aimed to study the long-term settlement behaviour around Stolwijk, the Netherlands. Built on 9 meters of soft Holocene clay and peat layers, this 3.5 meter high embankment was monitored for multiple years until 1947. The load on these soft soil layers remained largely unchanged. Buisman concluded that the secular effects of the settlement behaviour of this test section were constant with the logarithm of time. This constant creep rate on logarithmic time scale underlines the observations made by Buisman by performing long term creep tests on clay (Heemstra, 2008, 2012).

Studies on the creep behaviour conducted by Bishop et al. (1969) revealed a linear relationship between strain rate and the logarithm of time. Bishop et al. performed tests taking up to 3.5 years on normally-consolidated Pancone clay from Italy. The results of these tests indicate a relatively constant creep rate on a logarithmic scale for this type of clay. They also found that, based on oedometer tests on London clay, the creep rate is influenced by the applied stress magnitude, suggesting a potential stress dependency in clay creep behaviour. Furthermore, Bishop et al. (1969) concluded from performed tests on undisturbed Osaka clay and Tilbury clay that a distinction can be made between the sample's behaviour below and above the pre-consolidation stress. In the over-consolidated state, the creep rate dropped to zero as the applied stress decreased, while in the normally consolidated state, the creep rate remained constant, irrespective of stress level.

Edil et al. (1979) performed compression tests on peat samples from four different sites in the United States of America. In these tests, as described in Section 2.3.3, each load step was maintained for 20 days. The initial applied stress of 25 kPa was increased by doubling the currently applied load up until a pressure of 400 kPa was reached. Furthermore, they conclude that the compression behaviour of all tested peat samples had the tendency to increase linearly with the logarithm of time. However, as time progresses, an increase in the compression rate with the logarithm of time is noted as described in Section 2.3.3. This sharp increase in compression rate it attributed to tertiary compression. Edil et al. (1979) ascribe this observation to structural changes in the peat as a result of time. The results of these long-term compression tests on peat thus indicate a non-constant secondary compression rate with the logarithm of time.

2.4 Rheological Model

This section shows that a unique relationship between effective stress σ'_v, strain ε and strain rate $\dot{\varepsilon}$ can be used to describe the compression behaviour of soft soils. The subsequent lines of equal strain rate are called isotachs. Different isotachs can be expressed in terms of strain rate or equivalent time. Each different applied displacement rate on a soil sample results in a different stress-strain response of the soil. The constitutive behaviour of soils can be described using the classical isotach framework. This theory builds on the assumption that these isotachs are parallel to each other in a ε vs. log σ'_v plot. The distance between each isotach in theory remains constant.

2.4.1 Rheology

Building on the widely accepted assumption that creep starts from the start of loading, numerous researchers have conducted additional laboratory investigations. These studies aim to deepen the understanding of soil behaviour under continued loading conditions (creep). In addition, these studies aimed to improve understanding of both the constitutive and rheological models used to describe soft soil behaviour. Such models are particularly relevant for predicting the performance of soft soils in geotechnical engineering applications.

Šuklje (1957) demonstrated that the consolidation rate depends on both the void ratio e and the effective stress σ'. To reach this conclusion, Šuklje performed oedometer tests using varying load increments and plotted the resulting stress-strain curves. In this analysis, Šuklje assumed that the primary consolidation rate is directly proportional to the porewater flow during the primary consolidation phase, therefore adhering to Darcy's law.

Leroueil et al. (1983, 1985) performed eighteen CRS tests on Batiscan clay. In these tests, Leroueil et al. (1983, 1985) varied the displacement rate of these eighteen tests ranging from $\dot{\varepsilon} = 1.7 \cdot 10^{-8}$ s^{-1} to $\dot{\varepsilon} = 4 \cdot 10^{-5}$ s^{-1}. During testing, the applied rate of displacement was kept unchanged. From these tests Leroueil et al. visualized the compression curves in a void ratio versus effective stress plot. From these results it was concluded that the compression curves are dependent on the selected strain rate. This conclusion is at odds with Hypothesis A since Hypothesis A postulates that the void ratio achieved after compression is independent of time or strain rate. Consequently, CRS tests build on the assumption that Hypothesis B is valid. Subsequently Hypothesis B assumes that creep starts from the moment of loading and therefore is a time dependent process (Leroueil et al., 1983).

2.4.2 Creep CRS Tests

In addition to conducting eighteen CRS tests, Leroueil et al. (1985, 1983) performed nine creep oedometer tests on the same Batiscan clay. During these tests the samples were loaded past the pre-consolidation stress after which the load was kept constant for 70 days. This allowed the sample to undergo a pure creep phase. The observed results of the effective stress versus strain curves were similar to the set of curves obtained from the eighteen conventional CRS tests in the sense that there exists a unique combination of strain, effective stress and strain rate. From this Leroueil et al. (1985, 1983) concluded that the change in effective stress over time; $\dot{\sigma} = \frac{\partial \sigma}{\partial t}$ does not influence the constitutive behaviour of the soil. As a result of this, the change in effective stress over time is not part of the rheological relationship used to describe the constitutive behaviour of soft soils.
This can be explained by realizing that by definition creep is defined as the change in volume of a soil element under constant effective stress. So, in a creep test ; $\dot{\sigma} = \frac{\partial \sigma}{\partial t} = 0$. This process is not to be confused with a relaxation phase in a CRS test. In a relaxation test deformation of the sample is prohibited whilst the reduction of effective stress is recorded. The different available loading/unloading stages in a CRS test are described in more detail in Section 2.5.3.

The results of the nine creep oedometer test resembled the results of the eighteen CRS tests in the sense that the constitutive behaviour of the tests could be described by a unique relationship between effective stress σ'_v, strain ε and strain rate $\dot{\varepsilon}$, $R(\sigma'_v, \varepsilon, \dot{\varepsilon})$, Leroueil et al. (1983, 1985, 2006).

2.4.3 Displacement Rates in CRS Testing

After the establishment of the rheological model able to describe the behaviour of soft soils it is important to underline the influence of different displacement rates on the soil sample in CRS testing. A CRS test is displacement controlled. This applied displacement rate can be converted to strain rate when the initial sample height is known. Note that the strain rate can be calculated both as linear strain rate as well as natural strain rate. During a CRS test the strain rate is not necessarily constant, even though the name might suggest this. This is described in Section 5.1.1.

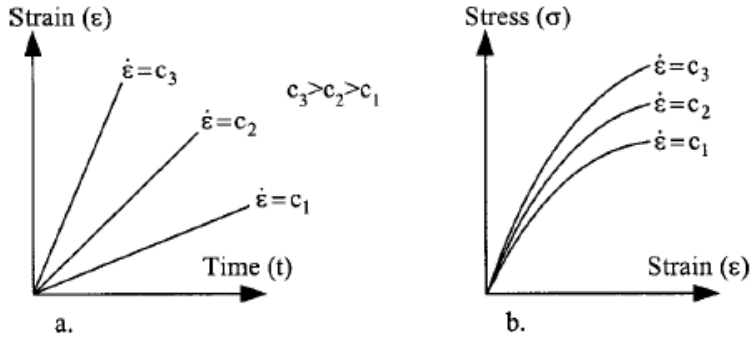

Figure 2.9: Comparison of different strain rates in strain vs. time plot (a) and the difference is stiffness response between three different strain rates in stress vs. strain plot (b) [After Augusten et al., 2004].

In a CRS test different displacement rates can be applied on a soil sample as indicated by Figure 2.9a. These displacement rates each have different effects on the soil sample. In general, in a CRS test, a higher applied displacement rate leads to a stiffer response of the soil. This is indicated by Figure 2.9b. In Figure 2.9b, this difference in behaviour is evident when comparing the Young's moduli across the three strain rates. The Young's modulus corresponding to the higher strain rate is noticeably larger than that of the lower strain rate. This highlights the material's increased stiffness at higher applied displacement rates.

During a CRS test, a soil sample undergoes deformation at a constant displacement rate. As deformation occurs, pore water pressure develops within the soil sample. Over time, this excess pressure dissipates, with the dissipation rate governed by the soil's hydraulic conductivity. During this process, the applied load is gradually transferred from the pore water to the soil skeleton.

At higher displacement rates, less time is available for pore water drainage, resulting in a stiffer soil response. This occurs because a portion of the applied load is temporarily carried by the pore water rather than the soil skeleton. Since water is nearly incompressible, the deformed soil exhibits reduced compressibility and increased stiffness, as illustrated in Figure 2.9b.

Figure 2.9a and Figure 2.9b show that the constitutive behaviour in a CRS test is strain rate dependent. Each strain rate results in a different stress-strain combination. One of the most used theoretical frameworks to describe the combination of strain, effective stress and strain rate is the isotach framework.

2.5 Classical Isotach Framework

This section describes the fundamental concepts of the classical isotach framework. The classical isotach framework builds on the assumption of the existence of a unique combination of strain, effective stress and strain rate called isotachs. In the classical implementation these isotachs are assumed to be equidistant and parallel. This classical framework is implemented in existing settlement prediction models used in the Netherlands.

2.5.1 Isotachs

Figure 2.9b showed how different displacement rates in a CRS test each result in a different, unique stress strain response of the soil. As a result, the behaviour of the soil can be described by a combination of effective stress σ'_v, strain ε and strain rate $\dot{\varepsilon}$. Šuklje et al. (1957) performed oedometer tests on Lacustrine chalk samples and drew the relationship between void ratio and effective stress. In here, Šuklje identified lines of equal strain rate and conveniently named them 'isotachs'. In greek 'iso' translates to 'equal' and 'tachy' to 'velocity'. These so-called 'lines of equal speed' are shown in figure 2.10.

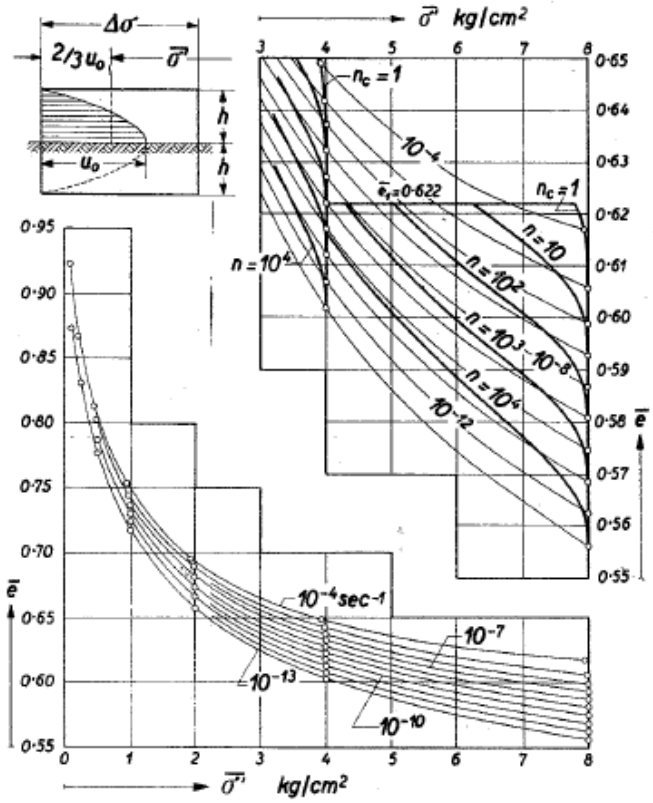

Figure 2.10: Initial Isotach Framework in e vs. σ'v space [After Šuklje, 1957].

In the lower left part of the graph it can be seen that each line corresponds to a different strain rate. The isotachs drawn continue to run parallel to each other. Towards the lower left corner of the graph, each isotach is 10 times lower compared to the isotach above. For convenience, the effective stress is often plotted on logarithmic scale. This renders linear parallel running isotachs. It is important to realize that Šuklje (only) drew ten isotachs, all with a difference in order of magnitude of 10. In theory however there are an infinite amount of isotachs all with a different strain rate which in theory all run parallel to each other on semi-logarithmic scale.

In here it is important to realize that the pore pressure distribution follows a parabolic shape. This parabolic shape is due to the fact that drainage is only allowed at the top of the sample. Build-up of excess generated pore pressure (u_b) is measured at the bottom of the sample. This results in an approximate pore pressure distribution as shown in the top left of Figure 2.10. The average pore pressure in the middle of the soil sample is found by multiplication of u_b with $\frac{2}{3}$. The effective stress in the middle of the soil sample is therefore calculated by Equation 2.4.

$$\sigma'_v = \sigma_v - \frac{2}{3} u_b \qquad (2.4)$$

Figure 2.10 showed the unique relationship of (σ'_v, ε, $\dot{\varepsilon}$) for each of the tests performed by Šuklje. By simplifying Figure 2.10 and only showing three different strain rates, Figure 2.11 is created. Plotting the effectives tress of the same graph of Figure 2.11 on semi-logarithmic scale results in Figure 2.12. As can be seen in Figure 2.12, parallel isotachs are obtained each with equal spacing between them.

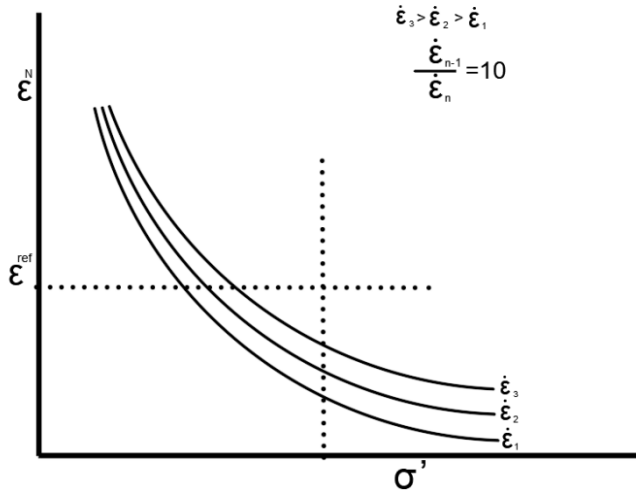

Figure 2.11: Three different isotachs corresponding to three different strain rates in strain vs σ' space.

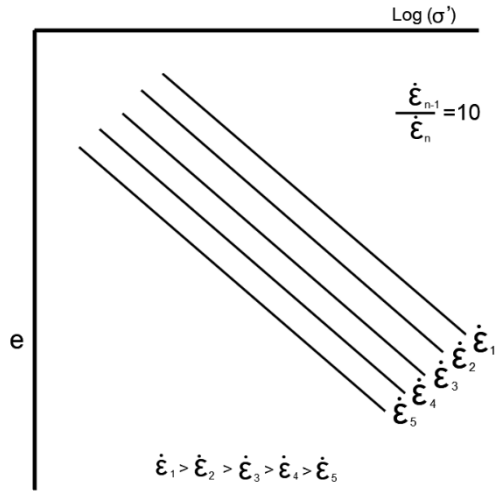

Figure 2.12: Three different isotachs corresponding to three different strain rates in strain vs log σ' space.

From Figure 2.11 and Figure 2.12 the following observation can be made;
Given that $\dot{\varepsilon}_3 > \dot{\varepsilon}_2 > \dot{\varepsilon}_1$, it is observed that for a certain reference strain ε^{ref}, $\sigma'_{\varepsilon 3} > \sigma'_{\varepsilon 2} > \sigma'_{\varepsilon 1}$. For a certain reference strain rate, a higher strain rate thus results in an higher effective stress level. This is explained by the stiffer response of the soil corresponding to a higher strain rate. From this observation it can be concluded that by convention, lines corresponding to lower strain rates are observed towards the lower left corner of a strain versus effective stress plot in the classical isotach framework. This is visualized in Figure 2.13.

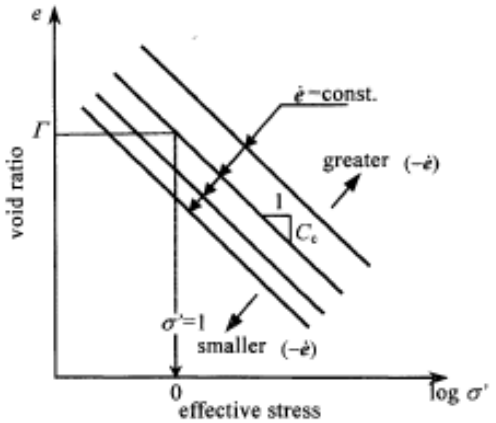

Figure 2.13: Visualization of different isotachs in e vs log σ' space with decreasing strain rate towards the origin. [After Imai et al, 2003].

Imai et al. (2003) define these isotachs as a single relationship between void ratio or strain and effective stress for a specific strain rate. By this definition, a straight line in a strain versus effective stress on semi logarithmic scale can be drawn for each possible strain rate. In doing so, a multitude of straight lines arise. Imai et al. (2003) continue by stating that these lines are parallel to each other, based on experimental data on clay samples.

2.5.2 Equivalent Time

A second way of presenting the isotach model is with isotachs corresponding to different equivalent times instead of strain rates. Taylor et al. (1942) was the first to draw the semi-logarithmic relationship showing time lines in an *e* vs log(*σ'*) plot (Den Haan, 2007). This is illustrated in Figure 2.14. In here it can be seen that isotachs towards the lower left corner of the graph correspond to an increase in equivalent time. As a result of this, lower strain rates relate to an increased equivalent time. This can logically be explained by realizing that a lower strain rate requires more time to accumulate the same amount of strain compared to a higher strain rate.

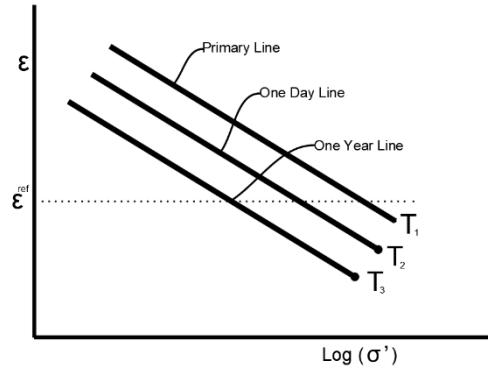

Figure 2.14: Three different isotachs corresponding to three equivalent times in strain vs σ' space.

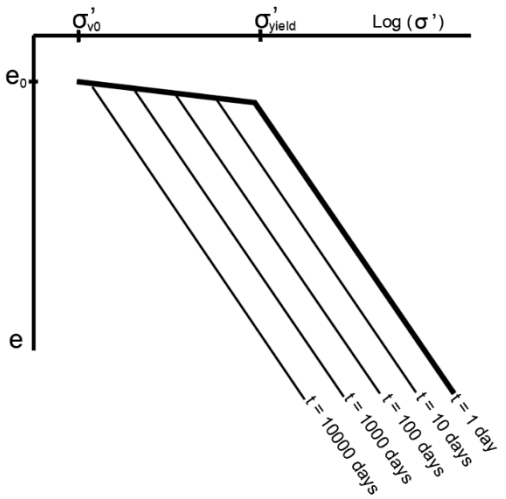

Figure 2.15: Three different isotachs corresponding to three equivalent times in strain vs log σ' space.

The compression behaviour of a normally consolidated soil sample is typically represented by a virgin consolidation line in the *e* versus log σ'_v plot (Yuan and Whittle, 2018). In Figure 2.14, this corresponds to the line indicating primary. Figure 2.15 illustrates this with the black line representing the 1-day reference isotach. Additionally, Figure 2.15 presents multiple isotachs, each reflecting a tenfold increase in equivalent time. It is important to note that an infinite number of isotachs can be constructed, each corresponding to a distinct equivalent time.

2.5.3 Isotach Framework in Practice

Different loading stages can be visualised in the isotach framework. Each isotach represents a specific strain rate, illustrating how soil stiffness and compressibility evolve over time. A CRS apparatus allows for different loading stages in soft soil laboratory testing. In general, five different loading phases can be identified. Namely;

1. Loading
2. Un-loading
3. Re-loading
4. Relaxation
5. Creep

Loading

In a loading phase the sample is axially loaded by applying a constant displacement rate on the top of the sample. Usually the applied displacement rate is kept unchanged during this step. The load applied by the load transducer on the sample, expressed in Newton, is recorded. In addition, the excess generated pore pressure at the bottom of the sample is logged. This allows for the calculation of the average effective stress in the sample. Depending on the amount of displacement applied during testing the sample is loaded past its yield stress. In the isotach framework this is visualized by the path A - B - C, Figure 2.16. Point B indicates the transition from over consolidated state to normally consolidated behaviour.

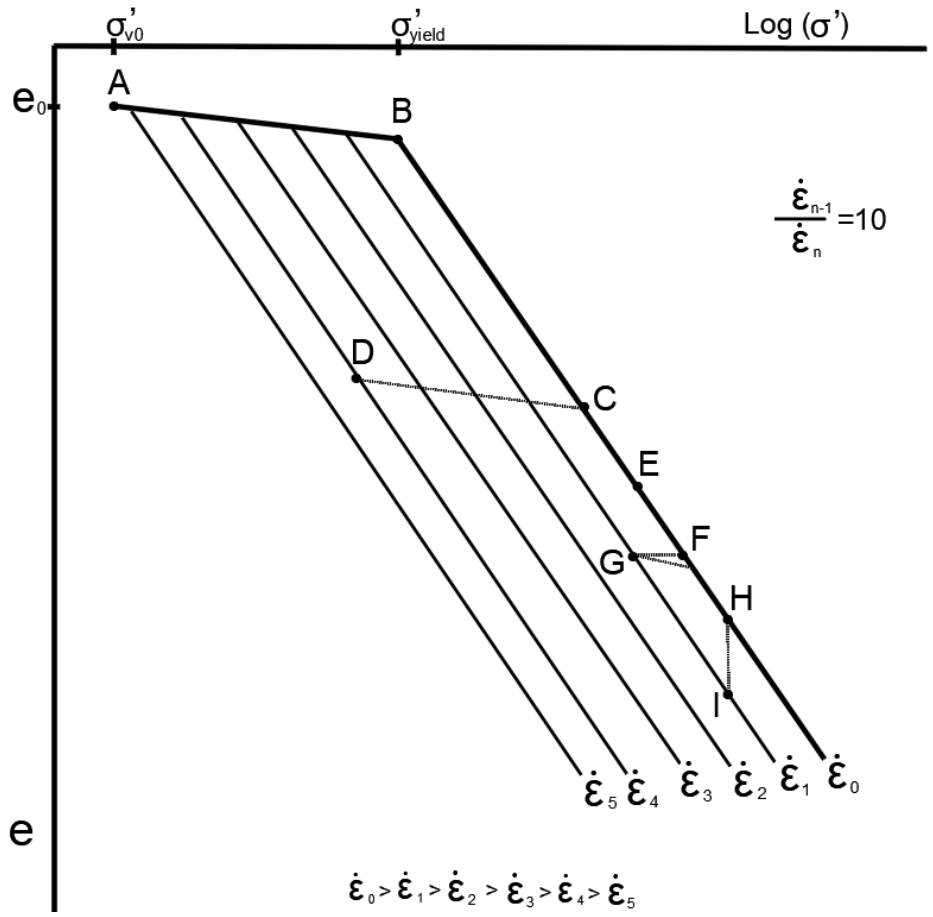

Figure 2.16: Illustration of different loading stages of CRS test in the classical isotach framework.

Un-loading
In the unloading phase, the axial displacement rate is reversed, consequently the loading platen or piston starts moving in the opposite direction compared to the loading phase. Instead of compressing, the soil sample is now allowed to expand at a controlled rate. The un-loading rate can be equal to the displacement rate applied in the loading phase. Depending on the material being tested, the strain rate might be reduced during unloading to allow for better control and more accurate measurement of the soil response. As the height of the soil sample increases due to swelling, the recorded stress reduces. During this step the pore pressures are monitored to observe how they develop as the soil decompresses. In the isotach framework this step can be visualized by path C – D in Figure 2.16. In here it can be seen that the effective stress reduces as a result of a decrease in applied strain.

Re-loading
During the reloading step the sample is loaded again with a constant displacement rate. The axial force applied on the top of the sample is again logged together with the development of pore pressures measured at the bottom of the sample. During reloading the path from D back to C is followed. After reaching point C in Figure 2.16 the soil is in normally consolidated state again and as loading progresses reaches point E.

Relaxation
In a relaxation step the height is kept constant over a certain period of time. This means that the applied displacement rate is set equal to 0. As time progresses the effective stress gradually decreases, it relaxes. In Figure 2.16 this step is visualized by path F - G . Inhere it can be seen that the strain remains constant whilst the effective stress gradually decreases. In theory a relaxation phase in the isotach framework is visualized by a horizontal stress path; maintaining a constant strain level. In practice however, a relaxation stress path can be slightly inclined due to mechanical limitations of the CRS apparatus (NEN 8992:2024), (Hoefsloot, 2022).

Creep
Once a target (effective)stress level is reached the displacement rate can be stopped. The CRS apparatus switches from displacement controlled to load controlled. As time progresses the change in strain due to creep is recorded. The displacement is recorded continuously over time, usually for a set duration, to capture the extent and rate of creep behaviour. In the isotach framework this theoretically pure creep step is visualized by stress path H - I in Figure 2.16. Note that this stress path is perpendicular to a relaxation phase. In practice, performing a pure creep step is difficult. Due to the physical limitations of the CRS apparatus it can be hard to maintain a constant stress level. Specialized testing equipment capable of fine-tuning and maintaining a specific stress level is necessary to perform this step. As a result of this, a pure creep phase is not a standard procedure in a CRS test.

2.5.4 Isotach Distortion

Šuklje (1957) describes how the isotach framework proves to be satisfactory in describing the rheological behaviour of the tests on Lacustrine chalk. However, one case of apparent disagreement with the isotach framework is found when describing the consolidation rates in the pre-consolidated phase. In light of this, Vergote et al. (2022) performed unloading and relaxation tests on reconstituted silty clay samples. The aim of these tests is to evaluate the consistency between the stress paths in both loading and unloading stages for different OCR's. They conclude that the process of swelling does not abide by the isotach framework but rather as a transient process. These findings are in line with Mesri et al. (1978) who postulated that unloading is not only associated with creep reappearance but also with viscous swelling (Vergote et al., 2022).

In line with findings by den Haan (1994), den Haan and Sellmeijer (2000), Tanaka et al. (2014), Nash and Brown (2015), it is hypothesized that unloading and corresponding swelling leads to soil destructurization. This destructurization results in breaking interparticle contacts and causing deviations from isotach behaviour. This divergence is particularly evident at high over-consolidation ratios (OCR > 1.25), which results in an underestimation of the creep rate, as shown by Vergote et al. (2022) in Figure 2.17.

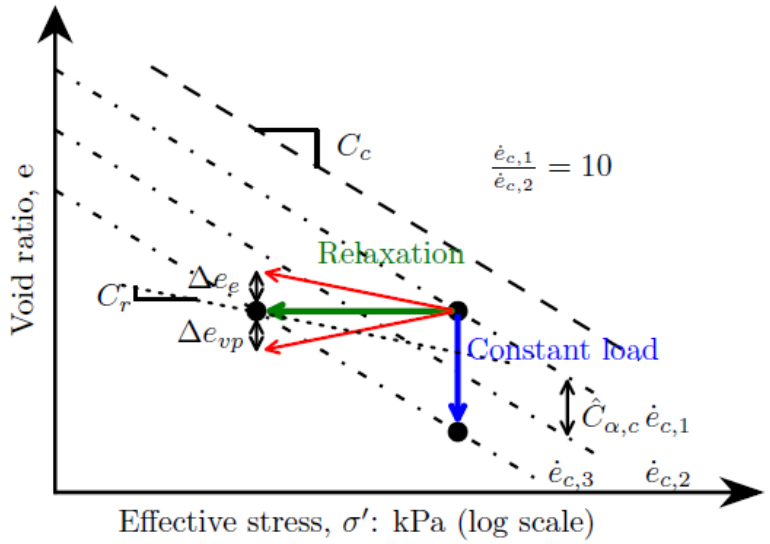

Figure 2.17: Pure creep path (Blue) and hypothesized mutual exclusivity of creep Δevp and swelling Δe (Green/Red) [After Vergote et al., 2020].

While traditional models treat creep and swelling as mutually exclusive processes, Vergote et al. (2022) observed that both effects can occur simultaneously, as illustrated in Figure 2.17. Due to the isotach distortion in the over-consolidated (OC) stage, this thesis focuses solely on the normally consolidated (NC) stage.

2.5.5 Strain rate influence on settlement parameters

Leroueil (1985) proposed an isotach model in terms of effective stress and total strain. Leroueil (1983) concludes that the yield stress is strain rate dependent. As can be seen from the graph in Figure 2.18, each strain rate produces a different yield stress. Furthermore, it can be concluded that an increase in strain relates to an increase in yield stress due to a stiffer response of the soil and subsequently an increased calculated pre-consolidation pressure. In order to achieve uniformity, Watabe and Leroueil (2013) proposes evaluation the pre-consolidation pressure with respect to a reference isotach.

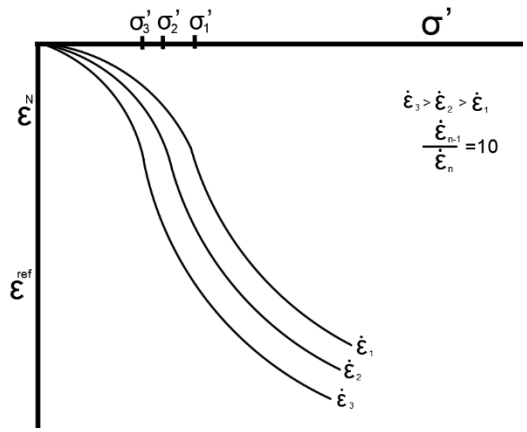

Figure 2.18: Yield stress dependency on strain rate selection.

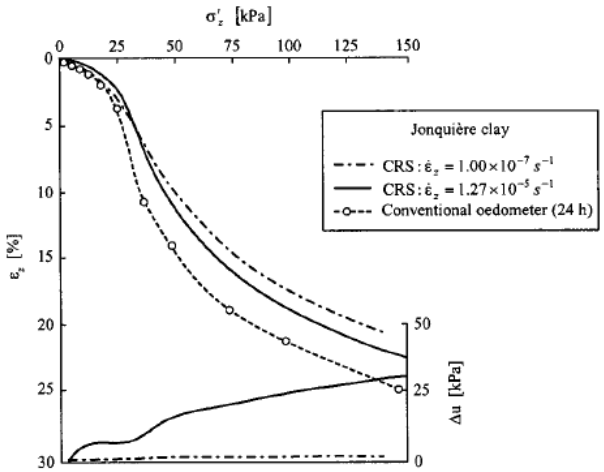

Figure 2.19: Fitting of conventional 24 hour oedometer test with different strain rate CRS tests. [After Jia et al., 2010].

The yield stress is often determined via Casagrandes method. Yuan and Whittle (2018) describe how the yield stress corresponds to the effective stress on the extension of the reference isotach. To avoid ambiguity the yield stress is commonly determined based on this reference isotach. Often the displacement rate corresponding to a 24 hour loading scheme of an incremental loading test ($\dot{\varepsilon} = 10^{-7}$ s^{-1}) is used as reference isotach (Yuan and Whittle, 2018). Jia et al. (2010) showed that a displacement rate of $\dot{\varepsilon} = 9.2 \cdot 10^{-8}$ s^{-1} resulted in the same load-displacement graph as obtained by an IL-test. This has bene verified by conducting oedometer tests on Japanese Ariake clay, as shown in Figure 2.19.

Jia et al. (2010) performed 114 CRS tests and 15 IL tests on undisturbed Ariake clay samples retrieved from boreholes on the southern island of Kyushu, Japan. From these tests it is concluded that for the soil tested, on average, the yield stress increases 15-16 percent for each tenfold increase of displacement rate.

As Figure 2.18 demonstrated a difference in strain rate results in a different yield stress. This is however of little influence to most settlement parameters such as the compression ratio (CR) and the secondary compression index (C_α) since the classical isotach framework assumes parallel equidistant isotachs. As a result of this, the slope of each isotach is independent of the corresponding strain rate resulting in a strain rate independent compression ratio. Moreover, since the classical isotach framework assumes equidistant isotachs, the value of the secondary compression index C_α is, in theory, strain rate independent.

2.6 Different Isotach Frameworks

This section shows different hypothesized isotach frameworks and their practical meaning of describing the compression behaviour of soft soils such as peat. The scientific community uses the ratio of the creep parameter divided by the compression index (C_α / C_c) to describe different isotach frameworks. The classical isotach framework builds on the assumption of parallel equidistant isotachs. As a result, the ratio of (C_α / C_c) is assumed to be constant. Consequently, the rate at which creep develops over time is linear on logarithmic timescale. Different researchers hypothesize an isotach framework in which the mutual distance between different isotachs decrease with a decrease in strain rate. As a result of this, the creep rate would decrease as time progresses. At infinite time creep would eventually come to an end.

2.6.1 Diverging Isotachs

The volume change of a soil sample under constant load over time is commonly quantified by the creep parameter C_α. In the isotach framework C_α is used to quantify the mutual distance between different isotachs with one log 10 cycle in difference. This is indicated in Figure 2.20. The compression index C_c is used to quantify the slope of different isotachs as demonstrated in Figure 2.20.

Figure 2.20 shows the classical isotach framework consisting of five isotachs of different strain rates. In Figure 2.20 it is assumed that the five different isotachs are parallel to one another and have a continuous spacing. As a consequence of this, the accumulated viscoplastic strains are stress independent. This is illustrated by stress path A - B which corresponds to a lower effective stress point than stress path C – D; $\sigma'_1 < \sigma'_2$. The net creep strain accumulated by stress path A – B is equal to the net creep strain accumulated by stress path C – D. This renders the creep process in the classical isotach framework stress independent.

Conversely, Figure 2.21 depicts a hypothetical isotach framework with unparallel isotachs. As a result of the isotachs not remaining parallel, their mutual distance changes depending on the effective stress level. As a consequence of this, the accumulated viscoplastic strain is stress dependent. In practice this would mean that the net amount of creep strain accumulated over a certain period of time is dependent on the current stress level. This is against the current understanding of creep development. Validating the trajectories of different isotachs is therefore of importance to accurately predict deformations in peat.

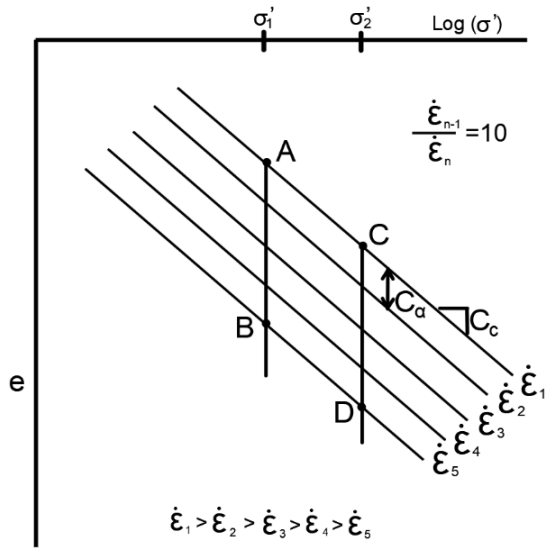

Figure 2.20: Illustration of classical isotach framework. Stress paths A-B and C-D result in the same net reduction of void ratio.

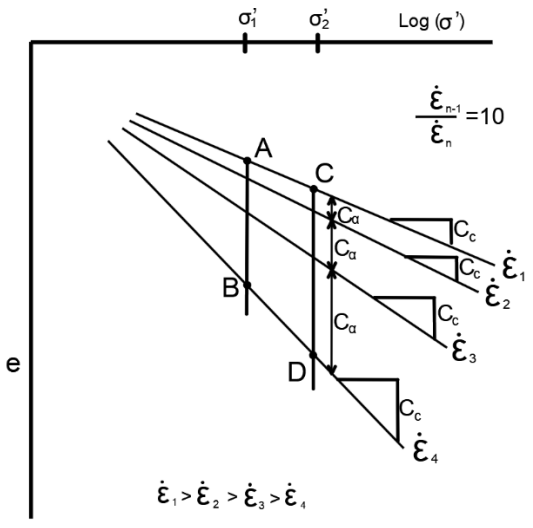

Figure 2.21: Illustration of different isotach framework with diverging isotachs. Stress path A-B and C-D result in a different change in void ratio.

2.6.2 Non-equidistant Isotachs

The second fundamental concept of the isotach framework is that of equidistant isotachs. Consequently, the mutual distance between different isotachs should in case of the classical isotach framework theory remain constant. Note that parallel isotachs not automatically result in equidistant isotachs, as is illustrated in Figure 2.22 and Figure 2.23.

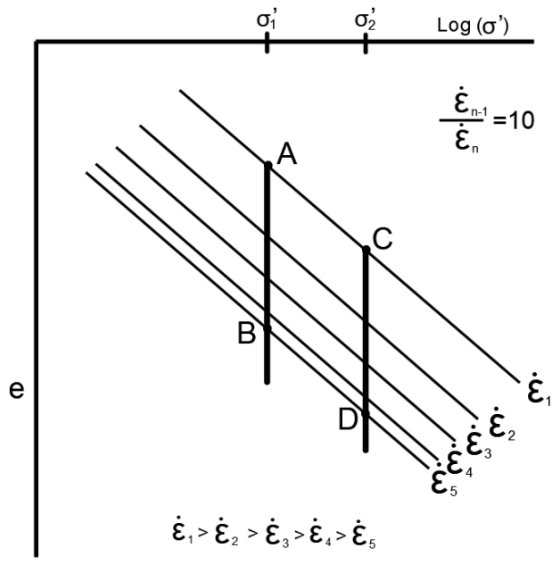

Figure 2.22: Illustration of different isotach framework with non-equidistant isotachs. Stress path A-B and C-D result in the same change in void ratio. The creep rate is however non-linear on logarithmic time scale. In this case creep would eventually come to an end.

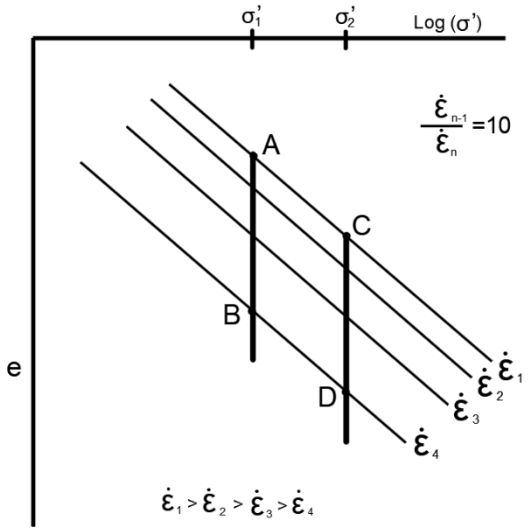

Figure 2.23: Illustration of different isotach framework with non-equidistant isotachs. Stress path A-B and C-D result in the same change in void ratio. The creep rate is however non-linear on logarithmic time scale due to changing mutual distance between different isotachs.

Figure 2.22 and Figure 2.23 show isotachs corresponding to different strain rates for which it is assumed that the difference in strain rate is equal to one log-cycle. The amount of pore volume reduction accumulated over stress path A – B is equal to that of stress path C – D. Afterall, the isotachs remain parallel. However, the mutual distance between different isotachs changes. In a practical sense this means that, as time progresses, the rate at which creep occurs changes. Note that in case of the classical isotach framework creep is assumed to take place at a constant rate on logarithmic time scale. As a result of this the mutual distance between different isotachs is assumed to remain constant. A constant creep rate on linear time scale results in Figure 2.20. If the mutual distance between different isotachs starts to increase over time, the creep rate would change over time as indicated in Figure 2.23. Note that in this case the creep rate continues to slow down on logarithmic time scale, al be it with a different rate.

2.6.3 Limit Timeline

Section 2.5.1 described how isotachs corresponding to smaller strain rates are found towards the lower left corner in a conventional *e* versus log(*σ'*) plot. Hypothetically this decrease in strain rate would eventually result in a (close to) zero strain rate. The existence of this infinitesimal strain rate would mean that, at some point in time, creep would come to an end. First proposed by (Graham et al., 1983) and later described in (Watabe and Leroueil, 2013), an infinitesimal strain rate called 'end of creep isotach' is hypothesized as shown in Figure 2.24.

To reach this end of creep isotach the mutual distance between different isotachs reduces with a decrease in strain rate. At some hypothetical point isotachs would start to overlap. Their mutual distance in this case would be close to zero. As a result of this, as time progresses, the creep rate eventually diminishes. This goes against current implementation of the classical isotach framework which assumes parallel equidistant isotachs. The proposed limit timeline concept therefore requires a different isotachs framework where the mutual distance between different isotachs can change over time as illustrated in Figure 2.24.

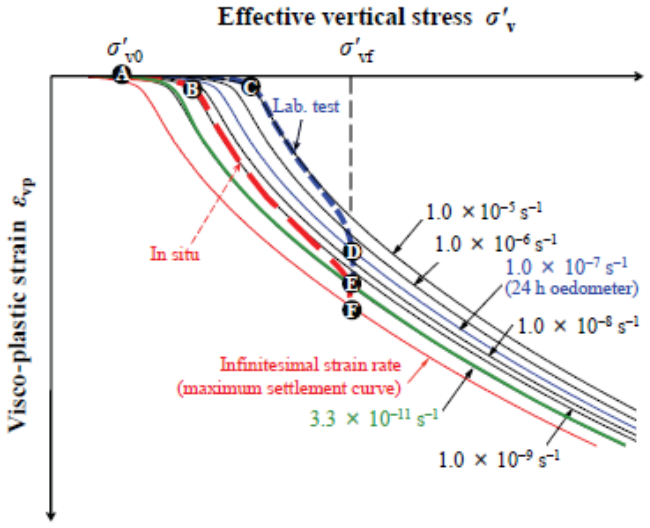

Figure 2.24: Schematic illustration of different strain rates in laboratory testing and in situ behaviour with indicated hypothetical infinitesimal strain rate [After Watabe et al., 2013].

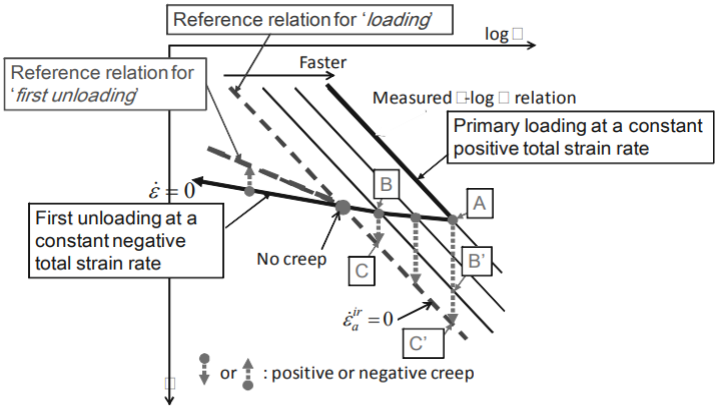

Figure 2.25: Hypothesis of Kawabe et al. to identify low strain rates including infinitesimal strain rate by applying (un)loading cycles [After Kawabe et al., 2013].

Imai et al. (2003) and Watabe & Leroueil (2015) hypothesized a possible limit isotach corresponding to an infinitesimal strain rate, i.e. $\dot{\varepsilon} = 10^{-\infty}$. The range of applied strain rates during CRS testing is generally in the range of $\dot{\varepsilon} = 10^{-9}$ s^{-1} – 10^{-5} s^{-1}, whereas the strain rates encountered at Osaka bay, Japan are believed to be $\dot{\varepsilon} = 3.3 \cdot 10^{-11}$ s^{-1}. Due to the assumption that the time needed to reach this limit isotach is infinite, Imai et al. (2003) state that this zero creep isotach will in practice never be reached.

In light of this, Kawabe et al (2013) hypothesized that it would be possible to evaluate very low strain rates like those encountered in the field i.e. $\dot{\varepsilon} < 10^{-9}$ s^{-1}, by performing unloading cycles on soil samples by means of CRS testing (Kawabe et al., 2013). To prove this Kawabe et al. (2013) performed unloading/reloading tests on reconstituted Fujinomori clay and on reconstituted Kaolin clay by changing the strain rate from positive (compression) to negative (decompression). Figure 2.25 illustrates these proposed unloading steps.

The main advantage of performing tests like these is the assumed possibility to achieve strain rates similar to those typically encountered in the field. This would be achieved within a relatively short timeframe by incorporating unloading cycles in the soil test as shown in Figure 2.25. The obtained results by this method are however perilous since Vergote (2020) showed that isotachs can be distorted due to unloading of a soil sample.

2.6.4 Ratio of C_α / C_c

The isotach framework can be described using the ratio of C_α / C_c. Under the hypothesis of parallel equidistant isotachs the ratio of C_α / C_c remains constant. The ratio of C_α / C_c therefore is assumed to remain constant in case of the classical isotach framework. After all, parallel isotachs result in identical inclinations of different isotachs and thus identical values of C_c. Additionally, in case of equidistant isotachs the mutual distance between different isotachs remains constant, resulting in identical values of C_α.

Mesri et al. (1995) show that for two eastern Canada clays the ratio of C_α / C_c falls within a certain range for each soil type, Figure 2.26. Moreover, the ratio of C_α / C_c is believed to be around 0.04 for inorganic clays. For organic soils such as peat Mesri et al. (1995) provide a ratio of C_α / C_c around 0.06. This observed linearity within the studied strain rate regime is used to demonstrate the validity of the classical isotach framework consisting of parallel equidistant isotachs.

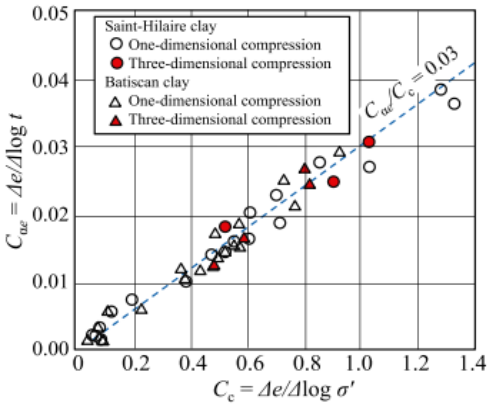

Figure 2.26: Assumed linearity between Cα and Cc [After Watabe and Leroueil, 2015].

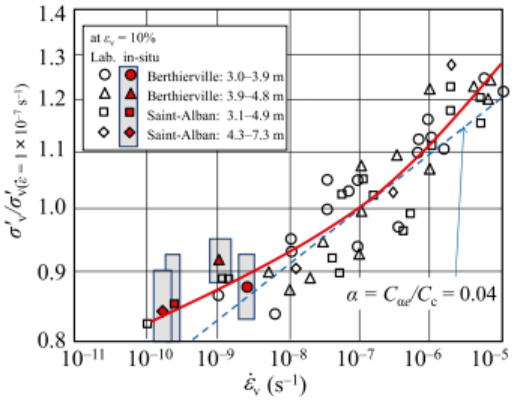

Figure 2.27: Asymptotically decrease of ratio of Cα and Cc [After Watabe and Leroueil, 2015].

Watabe and Leroueil (2015) observed that the ratio of the creep parameter C_α to the compression index C_c generally falls within a narrow range for various tested materials. However, they also found that for tested clay materials, this ratio is not constant and decreases with a decrease in strain rate as shown in Figure 2.27. Watabe & Leroueil (2015) hypothesize the validity of this observation by stating that the tendency of C_α / C_c to asymptotically decrease towards zero is reasonable under the assumption that secondary compression eventually stops at infinite time.

Looking at Figure 2.27, it should be realized that due to the physical limitations of CRS tests apparatuses, it is (only) possible to achieve strain rates in the region of $\dot{\varepsilon} = 10^{-9}$ s^{-1} and upwards. The conclusion of Mesri et al. (1995) where it is hypothesized that the ratio of C_α / C_c is constant is not surprising when realizing that the studied strain domain is relatively small. Studies by Watabe et al. (2012, 2013, 2015) show the contribution of fields data from Osaka bay clay which is characterized by low strain rates i.e. $\dot{\varepsilon} < 10^{-9}$ s^{-1}. As a result of this, the tendency for the ratio of C_α / C_c to decrease with decreasing strain rate is clearly noticeable.

Under the hypothesis that the ratio of C_α / C_c asymptotically decrease towards zero the mutual distance between different isotachs would decrease with a decrease in strain rate. This hypothesis is inconsistent with the classical isotach framework. A decreasing ratio of C_α / C_c results in a decrease in creep rate on logarithmic time scale. As a result creep would eventually come to an end. Watabe and Leroueil (2015) describe this by hypothesizing a different isotach framework where the mutual distance between different isotachs becoming infinitesimal at infinite time.

Note that C_α can be used to quantify the mutual distance between different isotachs, Figure 2.20. The value of C_c is defined by the slope of an isotach, Figure 2.21. The ratio of C_α / C_c is assumed to be linear (constant ratio of C_α / C_c) in case of the classical isotach Framework. In case of diverging isotachs however, C_α would change. Figure 2.28 demonstrates different ratios of C_α / C_c. Mesri et al. (1995) provide a value of the ratio of C_α / C_c for peat of 0.06. In case of the Zegveld peat analysed in this study the calculated value of C_α / C_c equals 0.0634. This is based on the parameters as derived in Annex 4.

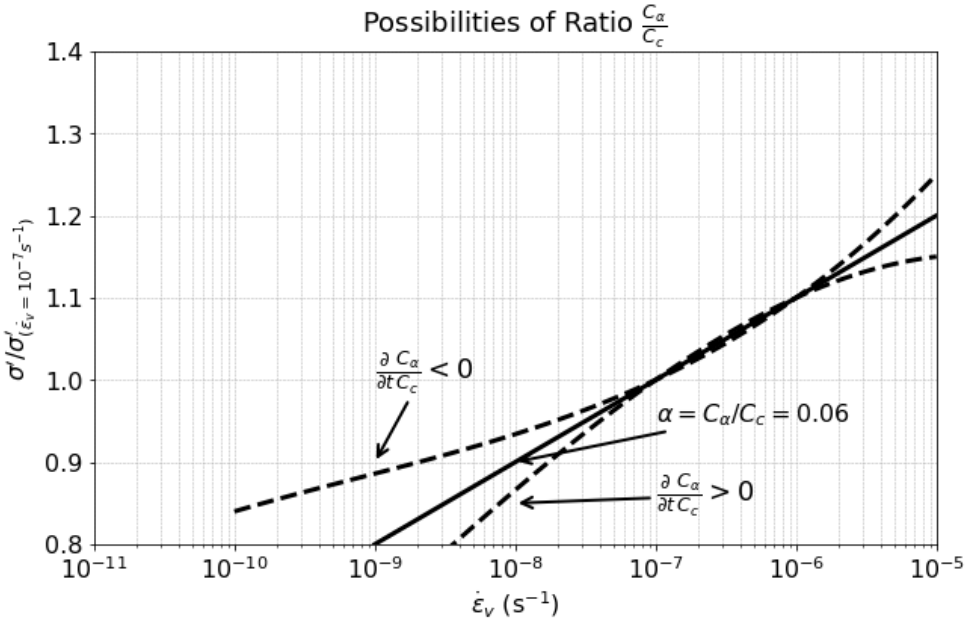

Figure 2.28: Development of Cα / Cc in case of different isotach frameworks [Based on Watabe and Leroueil, 2015].

The following cases are possible;

A. Parallel equidistant isotachs.
This case follows the fundamental concepts of the classical isotach framework. Since in this case neither C_α nor C_c changes, the ratio of C_α / C_c remains constant. This is in accordance with the results of Mesri et al. (1995) as shown in Figure 2.26. As time progresses, and the soils state moves to a different isotach, the ratio of C_α / C_c is constant. As a result; $\alpha = \frac{\partial}{\partial t}\frac{C\alpha}{Cc} = 0$ in Figure 2.28.

B. Parallel isotachs with reducing mutual distance.
This case results in a constant C_c but a changing C_α. When the mutual distance between isotachs reduces, C_α reduces, and creep would eventually come to an end. In this case isotachs remain parallel, the ratio of C_α / C_c reduces asymptotically to zero as shown in Figure 2.22, in accordance with the hypothesis of Watabe & Leroueil (2012). In Figure 2.28 parallel non-equidistant isotachs with reducing C_α result in; $\frac{\partial}{\partial t}\frac{C\alpha}{Cc} < 0$.

C. Parallel isotachs with increasing mutual distance.
This case can be described by a constant C_c but an increasing value of C_α. When the mutual distance between isotachs increases, C_α increases as shown in Figure 2.23. Isotachs remain parallel over time, the ratio of C_α / C_c therefore increases asymptotically as shown in Figure 2.28. This case results in parallel non-equidistant isotachs with $\frac{\partial}{\partial t}\frac{C\alpha}{Cc} > 0$.

D. Non-parallel non-equidistant isotachs.
Since in this case both C_α as well as C_c changes, the ratio of C_α / C_c remains constant. In case of diverging isotachs with an increase in mutual distance the ratio of C_α / C_c is dependent on the rate of change of both parameters but can remain constant. This is in shown in Figure 2.21.

2.7 Constitutive Models

This section describes four constitutive models used to model the compression behaviour of soft soils. The NEN-Bjerrum isotach model and the abc-isotach model clearly built on the assumed validity of parallel equidistant isotachs. This is less evident in case of the soft soil creep model or the MIT Y&W EVP model. The four models described in this section are ultimately used in Chapter 6 to simulate the step-changed CRS tests.

2.7.1 NEN-Bjerrum isotach model

The NEN-Bjerrum model is a common used settlement model able to describe the time-dependent behaviour of soft soils. The NEN-Bjerrum isotach model is, as the name suggests, based on the classical isotach framework as described in Section 2.5.1. As a result of this the model is able to simulate rate dependent effects. Because of the models ability to capture time dependent effects such as creep the model is often used to model and predict long-term settlement. The NEN-Bjerrum model defines the compression behaviour in terms of linear strain (Hoefsloot, 2022). The effective stress is conventionally plotted on logarithmic scale with 10 as base of the logarithm.

The NEN-Bjerrum Isotach model distinguishes the following main settlement parameters;

Recompression Ratio according to Equation 2.5.

$$RR = \frac{\Delta\varepsilon_C^d}{\Delta\log(\sigma_v')} \tag{2.5}$$

where;
ε_C^d = direct elastic linear (Cauchy) strain [-]
σ_v' = effective stress [kPa]

Compression Ratio according to Equation 2.6.

$$CR = = \frac{\Delta\varepsilon_C}{\Delta\log(\sigma_v')} \tag{2.6}$$

where;
ε_C = elastic natural (Cauchy) strain [-]
σ_v' = effective stress [kPa]

Secular strain rate coefficient according to Equation 2.7.

$$C_\alpha = \frac{\Delta\varepsilon_C}{\Delta\log(t)} \tag{2.7}$$

where;
ε_C = elastic natural (Cauchy) strain [-]
t = time [s]

The total linear strain is then calculated as the sum of the direct strain component plus the visco-plastic strain component as shown in Equation 2.8.

$$\varepsilon^C = \varepsilon^d + \varepsilon^{vp} \quad = RR \cdot \log\left(\frac{\sigma'_i}{\sigma_{ri-1}}\right) + C_\alpha \cdot \log\left(\frac{\tau_i + \Delta t}{\tau_i}\right) \quad \text{where;} \tag{2.8}$$

$$\tau_i = \tau_{i-1} \cdot \left(\frac{\sigma'_{yield}}{\sigma_{rv0}}\right)^{\frac{CR-RR}{C_\alpha}} \tag{2.9}$$

In which $\tau_0 = 24$ hours to comply with the defined reference isotach.

2.7.2 abc-isotach model

The abc-isotach model is a widely used settlement model in the Netherlands. The model defines the total strain as the sum of direct strain and viscous strains (Den Haan et al., 2004). The natural logarithm of effective stress is plotted against the change in pore volume. Conventionally, the change in pore volume is expressed in natural strain. This makes the abc-isotach model suited for describing the compression behaviour of soft soils such as peat. Furthermore, the abc-isotach model is based on the classical isotach framework as described in Section 2.5.1. Regarding the theoretical background of the abc-isotach model the reader is referred to (Den Haan, 1994). The abc-isotach model distinguishes the main settlement parameters as shown by Equation 2.10, Equation 2.11 and Equation 2.12.

Direct compression coefficient a according to Equation 2.10.

$$a = \frac{\Delta\varepsilon_H^d}{\Delta \ln(\sigma_v')} \tag{2.10}$$

where;
ε_H^d = direct elastic natural (Hencky) strain [-]
σ_v' = effective stress [kPa]

Secular compression coefficient b according to Equation 11.

$$b = = \frac{\Delta\varepsilon_H}{\Delta \ln(\sigma_v')} \tag{2.11}$$

where;
ε_H = elastic natural (Hencky) strain [-]
σ_v' = effective stress [kPa]

Secular strain rate coefficient c according to Equation 12.

$$c = \frac{\Delta\varepsilon_H}{\Delta \ln(t)} \tag{2.12}$$

where;
ε_H = elastic natural (Hencky) strain [-]
t = time [s]

The effective stress is plotted on natural logarithmic scale. The natural (total) strain is the sum of the direct viscoplastic strain component as shown in Equation 13.

$$\varepsilon^H = \varepsilon^d + \varepsilon^{vp} \quad = a \cdot \ln\left(\frac{\sigma'_i}{\sigma_{i-1}}\right) + c \cdot \ln\left(\frac{\tau_i + \Delta t}{\tau_i}\right) \tag{2.13}$$

where;

$$\tau_i = \tau_{i-1} \cdot \left(\frac{\sigma'_{yield}}{\sigma_{i v0}}\right)^{\frac{b-a}{c}} \tag{2.14}$$

In which $\tau_0 = 24$ hours to comply with the defined reference isotach.

The main difference between the NEN-Bjerrum model and the abc-isotach model is the presentation of the reduction of pore volume. The abc-isotach model is based on natural strain. The NEN-Bjerrum model on the other hand defines the reduction of pore volume as linear strain. Figure 2.29 shows the comparison between natural strain and linear strain of a CRS test on peat. In case of large strains i.e. ε > 50% it is recommended to use the abc-settlement parameters (Den Haan et al., 2004). One reason for this is the linearized virgin compression curve in case of natural strain. This facilitates accurate determination of the secular compression coefficient b. In addition, natural strain accounts for the sample height not becoming 0 as is described in Section 2.2.1.

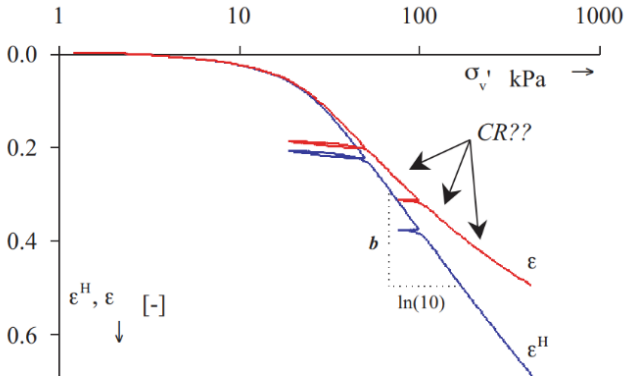

Figure 2.29: Difference between natural- and linear strain starts to become noticeable around 50% strain [After Den Haan et al., 2004].

2.7.3 Soft Soil Creep

The SSC model provides a mathematical framework used to describe the constitutive behaviour of normally consolidated soils such as clay an peat (Brinkgreve, 2021). The model is able to capture time-dependent deformation such as creep. Elastic strains are instantaneous and viscoplastic strains accumulate over time. Failure is modelled in the SSC model in accordance with the Mohr-Coulomb failure criterion. The evolution of the pre-consolidation stress and the accumulation of creep strains are both modelled to be time dependent processes. Regarding the theoretical background of the SSC model, the reader is referred to (Vermeer and Neher, 1999). The main model parameters of the SSC model show a close resemblance to the settlement parameters of the abc model as well as the Y&W EVP model.

Moreover, the compression parameters of the SSC model are defined according to Equation 2.15, Equation 2.16 and Equation 2.17.

Modified swelling index (κ^*) according to Equation 2.15.

$$\kappa^* = \frac{C_r}{2.3(1+e)} \tag{2.15}$$

Modified compression index (λ^*) according to Equation 2.16 .

$$\lambda^* = \frac{C_c}{(1+e)} \tag{2.16}$$

Modified creep index (μ^*) according to Equation 2.17 .

$$\mu^* = \frac{C_\alpha}{2.3(1+e)} \tag{2.17}$$

Regarding the formal definition of the parameters of the SSC-model the reader is referred to (Vermeer and Neher, 1999). In addition to the compression parameters described above, additional parameters are required to simulate the CRS test data using the soil test environment of Plaxis 2D. All required parameters are shown in Table 2.1.

Parameter	*Symbol*	*Unit*
Modified swelling index	κ^*	[-]
Modified compression index	λ^*	[-]
Modified creep index	μ^*	[-]
Poisson ratio	υ	[-]
Cohesion	c	kPa
Effective friction angle	φ'	°
Dilatancy angle	ψ	°

Table 2.1: SSC-Model parameters in Plaxis 2D soil test environment.

2.7.4 The MIT EVP Model

Yuan and Whittle proposed a new EVP model able to describe the compression behaviour of clay. The model incorporates an auto-decay mechanism that is dependent on the internal strain rate of the soil skeleton. As a result of this, the model is able to describe time dependent effects in different loading conditions in CRS testing. The Y&W EVP strongly focusses on the compression behaviour of clay. Evaluating the models ability of describing the compression behaviour of peat therefore serves as validation of this model. This is important since the amount of strain and expected creep is higher in a test on peat compared to a CRS tests on clay. For more detail on the coefficients used in the EVP model of Yuan and Whittle the reader is referred to (Yuan and Whittle, 2018).

Model Formulation

As is shown in Figure 2.30, Yuan and Whittle illustrate the typical compression behaviour of clay in a log (*e)* – log (σ'_v) plot. The total strain rate during loading of the soil sample in over-consolidated state is dominated by the elastic strain rate. The slope of this linearised elastic loading/unloading part of the graph is defined by the parameter ρ_r.

During loading in normally consolidated range the total strain rate is dominated by the viscoplastic strain rate. The slope of this linearised virgin compression curve is defined by the parameter ρ_c. In the Y&W EVP model this is called the limiting compression curve (LCC).

In addition to ρ_r and ρ_c, Yuan and Whittle introduce a material constant characterising creep behaviour ρ_α. Significant similarity is noted between the parameters ρ_r, ρ_c, ρ_α and the a, b, c parameters of Den Haan's abc-model. Mind that the ρ_r, ρ_c, ρ_α parameters are defined by evaluating the change in the logarithm of void ratio. This differs from the definition of the a, b, c parameters which are defined by evaluating the change in pore volume expressed as a change in natural strain.

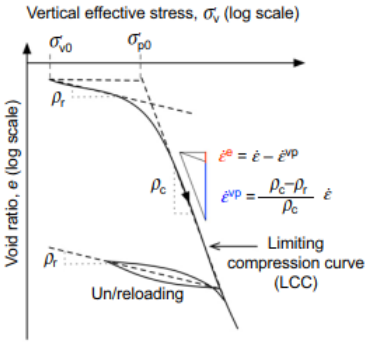

Figure 2.30: Compression behaviour in log σ'v vs log e plot. [After Yuan & Whittle, 2018].

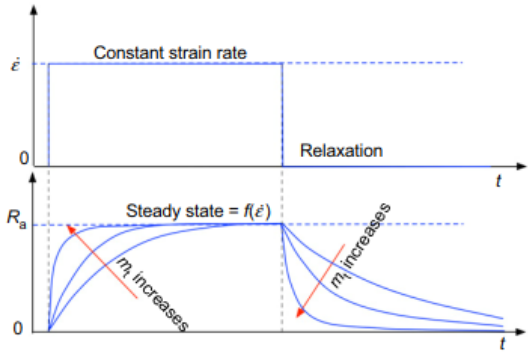

Figure 2.31: Working principle of transient coefficient mt. Larger values of mt result in faster adaptation to a new strain rate.

The EVP model uses the following parameters as input:

1. Slope of linearised elastic unloading/reloading curve (ρ_r) of log *e* vs log σ'_v .
2. Slope of linearised virgin compression curve (ρ_c) of log *e* vs log σ'_v .
3. Material constant characterising creep behaviour (ρ_α).
4. Reference strain rate ($\dot{\varepsilon}_{ref}$).
5. Current total strain rate ($\dot{\varepsilon}$) as applied by the CRS apparatus.
6. Initial void ratio (e_0).
7. Initial effective stress (σ'_{v0}).
8. Yield stress (σ'_{p0})

Regarding the derivation of these parameters the reader is referred to Annex 7. For more detail on the coefficients used in the EVP model of Yuan and Whittle the reader is referred to (Yuan and Whittle, 2018).

The following section describes the mathematical relationships used to quantify the amount of accumulated elasto- and visciplastic strains. This primarily serves to show the dependency of elastic- and viscoplastic strain rates on the parameters as listed above. Regarding derivation of these functions the reader is again referred to (Yuan and Whittle, 2018).

The proposed model distinguishes an elastic strain rate component ($\dot{\varepsilon}^e$) and a viscoplastic strain rate component ($\dot{\varepsilon}^{vp}$). These two components define the total strain rate($\dot{\varepsilon}$) as shown in Equation 2.18.

$$\dot{\varepsilon} = \dot{\varepsilon}^e + \dot{\varepsilon}^{vp} \tag{2.18}$$

In CRS testing the applied displacement rate by the CRS apparatus on the soil sample is equal to the total strain rate. Formula 2.18 can be rewritten to form Equation 2.19.

$$\dot{\varepsilon}^e = \dot{\varepsilon} - \dot{\varepsilon}^{vp} \tag{2.19}$$

In the EVP formulation of Yuan and Whittle the viscoplastic strain rate ($\dot{\varepsilon}^{vp}$) is defined by the product of the state variable R_a and the ratio of vertical effective stress (σ_v') divided by the pre-consolidation pressure (σ_p') as shown in Equation 2.20.

$$\dot{\varepsilon}^{vp} = R_a \cdot \left(\frac{\sigma_v'}{\sigma_p'}\right) \tag{2.20}$$

During compression past the pre-consolidation pressure of the soil the sample undergoes hardening. In the Y&W EVP model this density hardening is defined as per Equation 2.21.

$$\frac{\dot{\sigma_p'}}{\sigma_p'} = \frac{\dot{\varepsilon}}{\rho_c \cdot n} = \frac{\dot{\varepsilon}^{vp}}{(\rho_c - \rho_r) \cdot n} \tag{2.21}$$

From Equation 2.21 it becomes clear that the density hardening predominantly occurs when the sample is loaded past the pre-consolidation pressure where the total strain rate is dominated by the viscoplastic strain rate.

The state variable represents the internal strain rate corresponding to the perturbation of the clay particles. The internal strain rate is attributed to motion of particles within a granular assembly. It is therefore assumed that this state variable plays an important role in the development of plastic strain rates in peat as well. The change of this internal state variable over time is defined as Equation 2.22.

$$\dot{R_a} = [f(\dot{\varepsilon}) - R_a] \cdot m_t \tag{2.22}$$

Yuan and Whittle relate the changing internal state variable to an activation- and decay mechanism, Figure 2.31. They conclude that the soil particles adjust to a new equilibrium state after a change in strain rate. This phenomena is controlled by an auto-decay process governed by the internal strain rate. The change in internal strain rate is scaled by a transient coefficient m_t [1/time]. Note that the transient coefficient is non-constant throughout a step changed CRS test. By definition, the transient coefficient is directly proportional to the applied (total) strain rate. Stated differently, larger values of m_t are found corresponding to larger strain rates. The transient coefficient is defined as shown in Equation 2.23

$$m_t = \left(\frac{\rho_c}{\rho_\alpha} - 1\right) \cdot \left(\frac{\dot{\varepsilon}^{vp}}{\rho_r \cdot n}\right) + O(\dot{\varepsilon}) \tag{2.23}$$

The rate dependent activation function $f(\dot{\varepsilon})$ is formulated using a rate sensitivity parameter β as per Equation 2.24.

$$f(\dot{\varepsilon}) = \left(\frac{\rho_c - \rho_r}{\rho_c}\dot{\varepsilon}\right) \cdot \left(\frac{\dot{\varepsilon}}{\dot{\varepsilon}_{ref}}\right)^{-\beta}, \text{ where } 0 \leq \beta \leq \frac{\rho_\alpha}{\rho_c}. \tag{2.24}$$

Variation of the rate sensitivity parameter allows the Y&W EVP model to describe different CRS phenomena. The effects of changing this rate sensitivity β are described in more detail in Section 6.4.4.
As time progresses and the effect of the internal state variable reaches equilibrium Equation 2.24 can be rewritten to Equation 2.25.

$$\dot{\varepsilon}^{vp} = \left(\frac{\rho_c - \rho_r}{\rho_c}\dot{\varepsilon}\right) \cdot \left(\frac{\dot{\varepsilon}}{\dot{\varepsilon}_{ref}}\right)^{-\beta} \cdot \left(\frac{\sigma_v'}{\sigma_p'}\right) \tag{2.25}$$

The Y&W EVP model is able to describe relaxation phases in CRS testing as well. In this case $f(\dot{\varepsilon}) = 0$ and the evolution of the internal state variable over time becomes equal to $-m_t$. The change in effective stress can then be described as shown in Equation 2.26.

$$\frac{\dot{\sigma_v'}}{\sigma_v'} = -\frac{\dot{\varepsilon}^{vp}}{\rho_r \cdot n} \approx \left(\frac{1}{\frac{\rho_c}{\rho_\alpha} - 1}\right) \cdot \left(\frac{\dot{R_a}}{R_a}\right) \tag{2.26}$$

2.8 Recapitulation of reviewed literature

The literature review gave an overview of the different oedometer apparatus commonly used in soft soil engineering. The constant rate of strain (CRS) apparatus poses numerous advantages over the incremental loading (IL) test. The continuous generation of data points is of particular importance since this allows for more accurate parameter determination. These settlement parameters are ultimately used in theoretical frameworks to make settlement predictions. The isotach framework is one of these models.

Šuklje's (1957) isotach framework establishes a unique relationship between effective stress, strain, and strain rate. Lines of equal strain rate are called isotachs. The classical isotach model as implemented in the Netherlands builds on three main assumptions;

- There exists a unique relationship between strain (ε), effective stress (σ'v), and strain rate ($\dot{\varepsilon}$).
- Different isotachs are parallel in a strain (ε), vs. logarithm of effective stress log (σ'_v) plot.
- The mutual distance between two different isotachs remains constant in a strain (ε), vs. logarithm of effective stress log (σ'_v) plot.

The classical isotach framework therefore assumes that neither the trajectories of the isotachs, nor their mutual distance, changes over time. Different studies, including those of Leroueil et al. (1983, 1985), validate the isotach framework for describing the compression behaviour of clay through step-changed CRS testing. These studies demonstrate that strain rates significantly influence soil behaviour. This relationship therefore underlines the classical isotach framework's validity for describing the deformation behaviour of clay.

It does however not prove the validity of the classical isotach framework for describing the deformation behaviour of peat. This is a major knowledge gap since peat can often be described as a heterogeneous anisotropic material which makes describing its constitutive behaviour arguably more difficult than clay. It is therefore important to improve the understanding of the constitutive behaviour of peat under different applied displacement rates during CRS testing.

In addition, the literature review showed challenges in applying the classical isotach framework to field conditions. Different researchers hypothesize varying isotach frameworks based on laboratory tests and field data on clay. The gap between displacement rates applied in laboratory testing on clay and those observed in the field remain a substantial difficulty. Establishing the order of magnitude in difference between laboratory testing on peat and field data is not covered by existing literature.

The following chapters therefore focus on evaluating the validity of the classical isotach framework for describing the constitutive compression behaviour of peat.

3 Strain Rates in Clay and Peat

It is well established that the difference in strain rates between project sites on clay and laboratory testing on clay can differ by a factor of 10^4 - 10^6 (Leroueil, 2006), (Yuan and Whittle, 2018). It has however not been evaluated if this degree of difference in strain rate is encountered in peat as well. This proves to be important since it has been shown how determination of settlement parameters such as the pre-consolidation pressure are strain rate dependent (Leroueil, 2013). This chapter describes the difference in strain rate in peat between applied displacement rates in CRS laboratory testing and those encountered in the field. Subsidence plates and Interferometric Synthetic Aperture Radar (InSAR) data of project sites throughout the Netherlands is used to quantify this gap in strain rate in peat.

3.1 Strain Rates in Clay

This section demonstrates the well-known difference in strain rates between project sites located in a clay area and those applied during oedometer testing on clay. Regarding more information on the projects used to arrive at this conclusion the reader is referred to (Leroueil, 2006).

3.1.1 Strain Rates in Laboratory Testing

The typical range of strain rates in laboratory testing on clay and peat is generally in the range of $\dot{\varepsilon} = 10^{-7}\ s^{-1} - 10^{-5}\ s^{-1}$ (Leroueil, 2013). This range of strain rates is economically viable since CRS tests on clay and peat can often be finished within 1-2 days. In addition, this range of strange rates generally does not result in too much excess pore pressure being generated. Thereby resulting in valid determination of both permeability parameters and settlement parameters (NEN 8992:2024).

3.1.2 Field Strain Rates in Clay

Yuan&Wittle (2018) describe how a limitation of the isotach framework is the tendency to overestimate the initial viscoplastic (creep) rate. This limitation has practical implications, as it can lead to overestimating initial creep. The discrepancy arises because laboratory-tested soil samples are of limited size compared to soil layers at field scale. Additionally, the strain rates applied in laboratory tests to deduce parameters for settlement calculations are often significantly higher than the strain rates observed in the field. Figure 3.1 clearly shows the range of strain rates conventionally applied in laboratory testing on clay. The observed strain rates of projects built on clay are a few orders in magnitude lower than those applied in the laboratory. Consequently, the actual position of the field-scale soil layer within the isotach framework should be shifted in an e vs. log σ'_v plot corresponding to a lower strain rate (Yuan and Whittle, 2018). Note that Figure 3.1 shows a difference in strain rate between laboratory testing and field observations in clay of 10^4 - 10^6. The following section provides strain rate estimates of projects and locations situated in a peat area in the Netherlands.

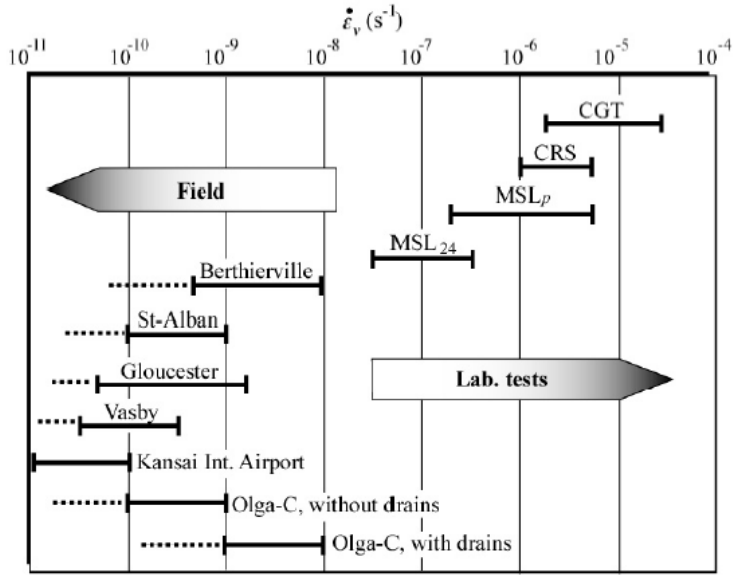

Figure 3.1: Discrepancy between strain rates in clay in conventional CRS testing and strain rates observed in practice [After Kawabe et al., 2013].

3.2 Strain Rate Zegveld

This section describes estimation of the strain rate of the Zegveld peat meadow in the Netherlands using long-term subsidence plates. The Zegveld meadow in not affected by any form of construction. It therefore serves as a lower limit of strain rates primarily caused by creep. The estimated strain rates of the Zegveld meadow are in the range of $\dot{\varepsilon} = 10^{-12}\ s^{-1}$ - $10^{-11}\ s^{-1}$. This is substantially lower than the range of strain rates applied during conventional laboratory testing.

3.2.1 Zegveld

It is well-established that peat oxidation is one of the primary contributors to land subsidence in the Netherlands (Hessel et al., 2024), (Massop et al., 2024). This is particularly significant in the western part of the Netherlands, where understanding the processes driving land subsidence is crucial in keeping this part of the country liveable (NWA-LOSS, 2024). Quantifying land subsidence is challenging because annual fluctuations in soil surface levels in drained peat areas often exceed the yearly subsidence rate (Hessel et al., 2024). To improve understanding of subsidence rates, long-term deformation time series are essential. In this context, subsidence plates were installed at various depths between 1970 and 1973 on a peat meadow farm in the Zegveld polder, Netherlands. Figure 3.2 shows the location of Zegveld. A continuous measuring series of deformation in a peat meadow of this duration is rare. These subsidence plates therefore provide a unique subsidence time series spanning over 50 consecutive years.

Figure 3.2: Location of the Zegveld peat meadow within the Netherlands.

Due to the geological characteristics of the Netherlands, soil surface subsidence has been an ongoing process. However, subsidence rates of peat meadows increased significantly around 1965 due to the modernization of farming practices (Hessel et al., 2024). As a result of this, farmers lowered groundwater tables to enhance the bearing capacity of agricultural lands. While lowering groundwater tables inherently accelerates peat oxidation, it does not necessarily result in increased creep settlement (Hessel et al., 2024). Beuving and Van den Akker (1996) reported that creep, and to a lesser extent consolidation (as their study focused on a peat meadow), accounted for approximately 38% of total subsidence over a 25-year period. This highlights the relevance of the 50-year-long Zegveld data set for evaluating creep rates in peat. Note that the Zegveld meadow in which the subsidence plates are installed is not loaded due to, for example, adding sand layers or construction. The only change in loading conditions is due to the change in water level. Measured deformations below groundwater level are therefore assumed to primarily be caused by creep. Since the initial peat layer thickness is known, the strain rate below ground water level can be estimated. This makes the Zegveld peat meadow suited for evaluating the lower limit of strain rates encountered in practice.

3.2.2 Measuring Technique

Subsidence plates as indicated by Figure 3.3 were placed at different depths ranging from 0.2 meters below ground level to 1.4 meters below ground level. A set of subsidence plates was placed in a plot of land in which the ditchwater level was lowered in 1969 (called field 16). Another set of plates were installed in a plot of land in which the ditchwater level was not lowered (called field 13). Figure 3.4 shows the location of both field 13 and field 16 within the Zegveld polder.

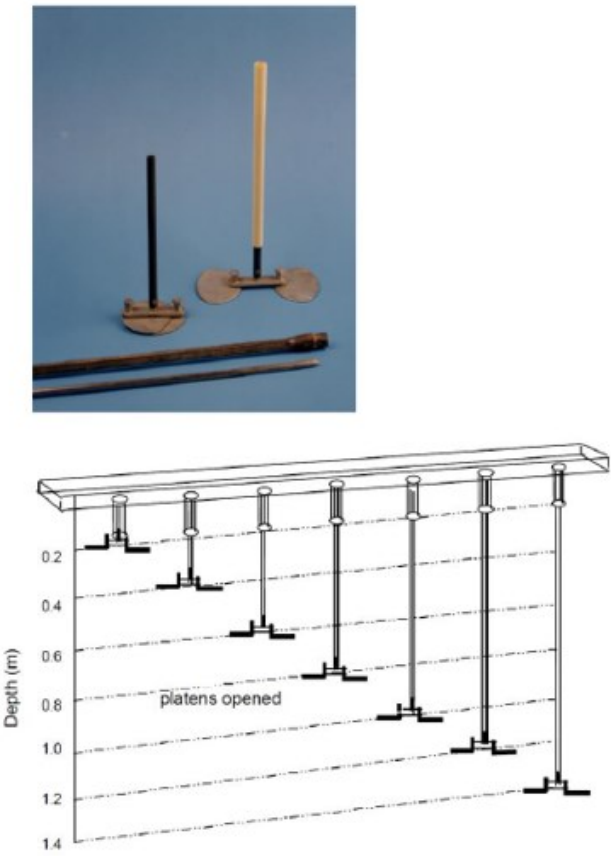

Figure 3.3: Used settlement plates (top) and their theoretical placement depth (bottom) [After, Hessel et al., 2024].

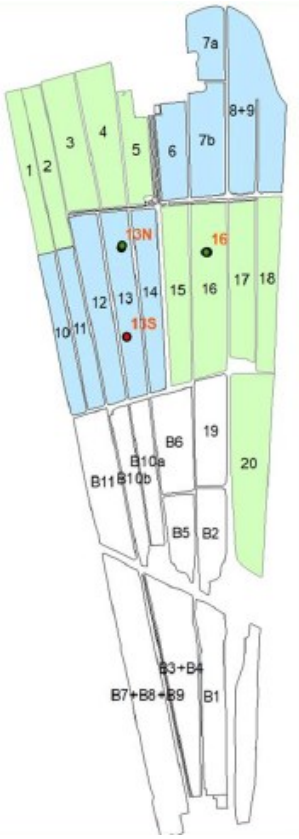

Figure 3.4: Division between field 13 in which the groundwater table was not lowered (blue) and field 16 (green) where the ground water table was lowered [After, Hessel et al., 2024].

In order to provide a consistent timeseries, the elevation of the subsidence plates was measured using surveyor levelling each year in March. This is important since the elevation of the soil surface can change substantially due to swelling and shrinkage depending on the time of year. By measuring in March each year the effects of monthly fluctuations are minimized. Groundwater tables were measured on the same day as the subsidence plates. A reference point founded in the Pleistocene sand layer is used as reference point. The position of this reference point is measured with respect to the Dutch Ordnance Datum (NAP) benchmark on a nearby farm and bridge. Data from the Dutch Department of Waterways and Public Works showed that the benchmark is close to stable. In the period between 1989 and 2017 this benchmark subsided around 3 mm (Hessel et al., 2024). A stable benchmark is important since the expected deformation rate of the subsidence plates is low.

Figure 3.3 shows a schematic illustration of the theoretical placement depths of the subsidence plates. Hessel et al. (2024) discuss how some of the plates are lost in the period between 1973 and 2023. An example of this is the subsidence plate installed at 20 cm below surface level in field 16 which was lost in 1988. The majority of the subsidence plates are however measured every year and therefore provide a continuous deformation series.

3.2.3 Groundwater Levels

To evaluate the creep rate over a 50-year period, it is essential to focus exclusively on the subsidence plates installed below the lowest recorded groundwater table. Analysing long-term subsidence data from plates positioned above this the groundwater table would reflect both creep-induced subsidence and peat oxidation, making it nearly impossible to distinguish between the two processes. The major driver of subsidence below the groundwater table will however be creep (Hessel et al., 2024). Figure 3.5 shows the groundwater table measured near the subsidence plates. From this it is assumed that subsidence of plates placed 1.2 and 1.4 meters below ground level is primarily caused by creep. However, oxidation processes can still occur below the groundwater table due to the entrapment of gas within the peat layers (Jommi et al., 2019).

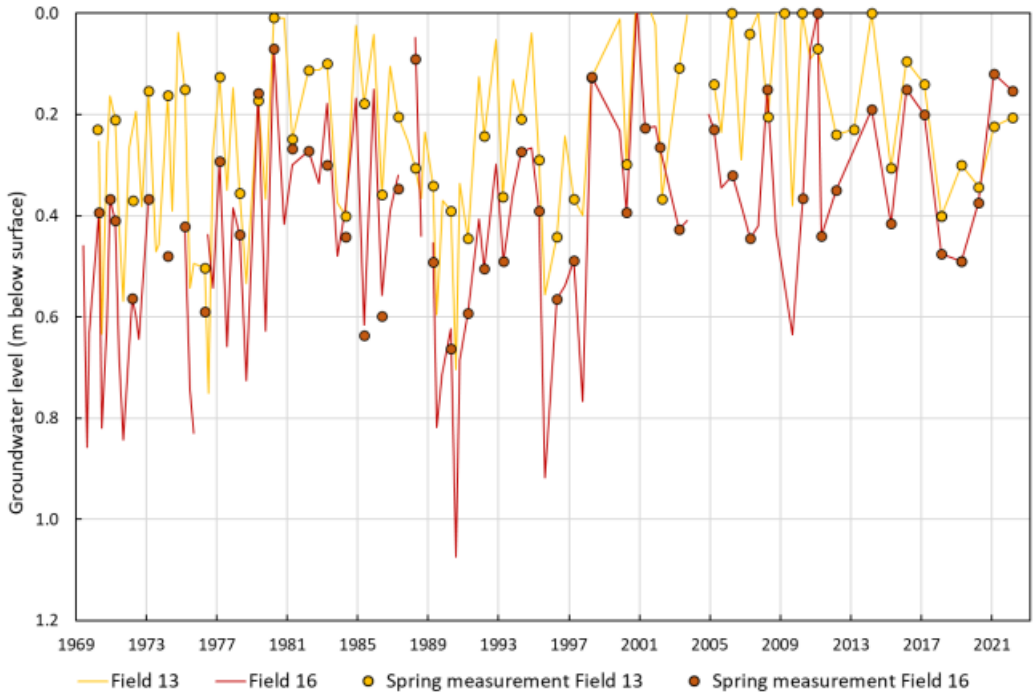

Figure 3.5: Groundwater levels below surface level in the Zegveld polder of field 13 and field 16.

The subsidence plates are placed on two meadows, field 13 and field 16 as shown in Figure 3.4. Note that the ditchwater level near Zegveld has not been constant in the period 1965 – 2023. Table 3.1 shows the water levels below surface level throughout the years. This is important since lowering of the ditchwater level increases the effective stress of the soil layer thereby creating subsidence due to consolidation. Since the subsidence rate due to creep is of interest, it is important to distinguish these two processes.

Year	*Waterlevel Field 13 [m NAP]*	*Waterlevel Field 16 [c NAP]*
1969	-2.90	-2.90
1970 – 1996	-2.55	-2.80
1995 - 2012	-2.55	-2.55
2012-2023	-2.45	-2.75

Table 3.1: Groundwater development with respect to surface level throughout the years.

Note that for field 13 the groundwater level is raised only during the measuring period. As a result of these actions, it can be concluded that the effective stress below the groundwater table has not increased due to lowering of the water levels. Increasing the water levels could however induces swelling of the peat layer above the water level. However, the effects of swelling are considered negligible at depths below the lowest recorded groundwater level. The water level in field 16 was lowered around 2012 resulting in an increased effective stress level, and thus a period of consolidation. The primary focus of the subsidence analysis will therefore be on the subsidence plates below groundwater level in field 13.

3.2.4 Estimated Deformation Rate Zegveld

Figure 3.6 shows the recorded subsidence development of field 13. Figure 3.6 only shows the subsidence development of the plates with a theoretical placement depth of 1.0m, 1.2m and 1.4m below surface level. The other installed subsidence plates are near or above the lowest recorded ground water level, and are therefore omitted. A linear trendline is fitted through the data. The slope of this linear trendline gives a first estimate of the average annual subsidence rate in mm per year. This estimated annual deformation is used to find an approximate strain rate. Other trendlines, such as logarithmic, have been fitted through the data as well. These did however not fit the data better than a linear trendline. This was evaluated by comparing the coefficients of determination (R^2) between data and fitted trendline.

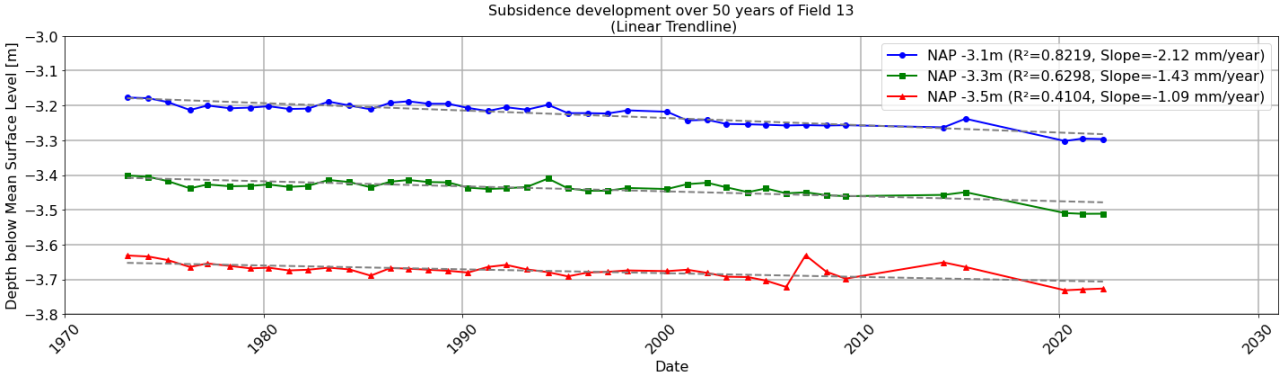

Figure 3.6: Recorded subsidence over time over the period 1973 until 2023 of field 13. The subsidence plate placed 1.0 m below surface level (blue) shows a higher estimated subsidence rate than the subsidence plate placed 1.2 m below surface level (green) or the subsidence plate placed 1.4 m below surface level (red).The estimated annual deformation rate is best described using a linear trend line.

Note that the subsidence development is roughly the same for all three subsidence plates. All three subsidence plates show similar deformation behaviour over time. An unexpected increase of depth of subsidence plate MSL -1.4 around 2008 is visible in Figure 3.6. The other two subsidence plates do not show this increase. No plausible explanation is found for this observed datapoint other than a possible measuring error.

Furthermore the average subsidence rate over time decreases with depth. This is to be expected since the influence of peat oxidation is larger closer towards the ground water level. As a result of gas entrapment, peat oxidation can be initiated resulting in compaction of the peat layer (Jommi et al., 2019). The influence of gas entrapment is less noticeable at greater depth. This is due to the reducing influence of groundwater fluctuations with increasing depth below surface level (Hessel et al., 2024).

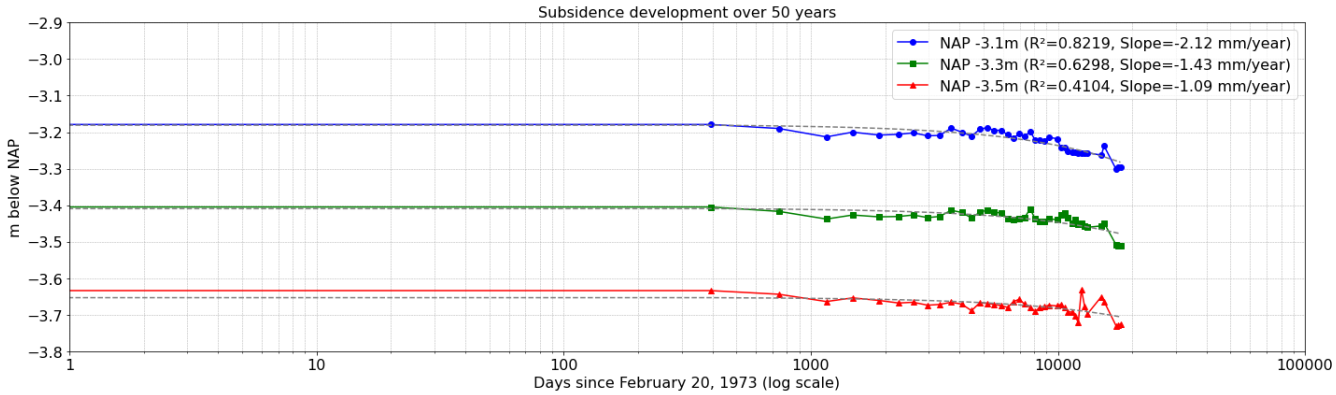

Figure 3.7: Recorded subsidence on logarithmic timescale of three evaluated subsidence plates.

The estimated annual subsidence rate does not seem to accelerate or slow down during the measuring period. This is to be expected since the changes in water level as described in Table 3.2 are of little influence on the analysed subsidence plates. In addition, no clear increase in effective stress is recorded throughout the years. Figure 3.7 shows the elapsed number of days starting on February 20th 1973. No clear trend is visible when the subsidence rate is plotted on logarithmic time scale. It is noted that after 10000 days the estimated deformation rate sows more volatile behaviour. During the last 2000 days of the time series the estimated deformation rate seems to increase over time. This is observed in the estimated deformation time series of all three evaluated subsidence plates. A possible explanation is the increase in average temperature during the last 30 years. It is of future interest to further investigate this phenomena and the effects of an increased average temperature on the development of peatlands and groundwater.

3.2.5 Estimated Strain Rate Zegveld

The estimated average annual displacement can be converted to a corresponding strain rate. This serves as a lower bound of observed strain rates since the meadow of field 13 is not subjected to loading during the measuring period. The calculated strain rates of field 13 can then be compared to the range of strain rates applied in laboratory CRS testing. This helps in quantifying the difference between applied strain rates in CRS testing and those encountered in the field.

The strain rate is defined as the amount of strain divided by the amount of time needed to accumulate this strain as shown in Equation 3.1.

$$\dot{\varepsilon} = \frac{\Delta\varepsilon}{\Delta t} = \frac{\Delta H}{H_0 \cdot \Delta t} . \qquad [s^{-1}] \tag{3.1}$$

In order to determine the strain rate, information about the original layer thickness is required. By looking at Annex 18 it becomes clear that multiple soil investigation datapoints are available near the location of the subsidence platens. A peat layer with a thickness of 5.75 meter is present at the location of the subsidence plates. The Pleistocene sand layer is situated directly below this peat layer.

Using Equation 3.1 the strain rate of each of the three evaluated subsidence plates of field 13 is estimated. The subsidence rate in millimetres per year and the resulting strain rate is shown in Table 3.2. The surface level in the Zegveld polder is at Dutch Ordnance Datum (NAP) -2.1m.

Depth [m NAP]	*Subsidence rate [mm/year]*	*Strain rate [s^{-1}]*
-3.1	-2.1	$1.3 \cdot 10^{-11}$
-3.3	-1.4	$9.0 \cdot 10^{-12}$
-3.5	-1.1	$7.0 \cdot 10^{-12}$

Table 3.2: Estimated subsidence rates and strain rates of subsidence plates below groundwater table of field 13 with respect to Dutch Ordnance Datum (NAP).

The estimated strain rates of the meadow in field 13 are in the range of $\dot{\varepsilon} = 10^{-12}$ s^{-1} - 10^{-11} s^{-1}. The Zegveld meadow is not subjected to any loading resulting in an increase of effective stress. The performed analysis on Zegveld described in this section therefore primarily serves as a lower limit of strain rates encountered in the field. It is interesting to note that the recorded subsidence over the last 50 years appears to take place at a constant rate. This observed linearity goes against current understanding of the creep rate in peat since creep is assumed to occur linearly on logarithmic time scale. The Zegveld meadow thus shows a higher than expected creep rate over time.

3.3 A2 Vinkeveen 2003 - 2006

This section analyses the estimated strain rates of part of the A2 highway near Vinkeveen. The estimated strain rates during construction are in the range of $\dot{\varepsilon} = 10^{-9}\ s^{-1} - 10^{-7}\ s^{-1}$. The estimation of these strain rates gives practical meaning of strain rates of a project situated in a predominantly peat area during construction. The estimated strain rates during construction are already lower than the range of strain rates used in conventional CRS testing.

3.3.1 A2, Vinkeveen

The A2 highway is a crucial part of the Dutch infrastructure connecting Amsterdam to Maastricht. Rijkswaterstaat was tasked with increasing the number of lanes. On the highway section between Amsterdam and Utrecht, the number of lanes increased from three to five in both directions. The increase in number of available lanes is completed in 2012 (Rijkswaterstaat), This section is focussed on the embankment connecting Vinkeveen to the A2, Figure 3.8.

A substantial part of the A2 between Amsterdam and Utrecht is situated in an area that predominantly consists of soft Holocene layers. These peat and clay layers are at some locations well over 6 metres deep making expansion of the existing highway challenging (Rijkswaterstaat, 2007). The peat layers are compressed by gradually adding layers of sand as shown in Figure 3.9. As the peat layers compact, excess pore water in the peat layer flows out due to the increase in effective stress. This process takes time. Rijkswaterstaat, together with contractors, therefore made use of new consolidation methods such as Beaudrain and IFCO (Rijkswaterstaat, 2007). This new connection is made directly adjacent to the then existing A2, as illustrated in Figure 3.8.

Figure 3.8: Widening of the A2. The embankment construction connecting Vinkeveen to the A2 is under construction on the right side of the image [Rijkswaterstaat].

Figure 3.9: Widening of the A2 near Vinkeveen. Sand layers are gradually added to create the new embankment structure connecting Vinkeveen to the A2 [Rijkswaterstaat].

3.3.2 Strain Rate A2 2003-2006

During the process of gradually adding sand layers to construct the new embankment both the pore water response as well as the settlement of the embankment was monitored thoroughly using settlement plates (Rijkswaterstaat, 2007). Annex 16 shows this recorded settlement both during and after construction. Techniques such as vacuum consolidation where employed to reduce the consolidation period. Annex 16 shows the settlement graphs of the northern embankment connecting Vinkeveen to the A2. From these graphs it is concluded that the primary consolidation period is finished after approximately 2 years. Consequently, due to the adding of sand layers the existing Holocene layers are not only compacted but also pushed below the ground water level. Resulting subsidence after 2006 is therefore assumed to be primarily caused by creep.

Figure 3.10 shows the estimated deformation rate of the embankment connecting Vinkeveen to the A2. This subsidence rate was measured using subsidence plates (Rijkswaterstaat, 2007). Annex 16 shows an enlarged view of this graph. Figure 3.11 shows the data of Figure 3.10 with a logarithmic function fitted through the data. Note that the measured deformation rate, expressed in millimetres per week, follows a near logarithmic shape during the period of measuring. This is to be expected since the settlement during this stage is primarily caused by primary consolidation.

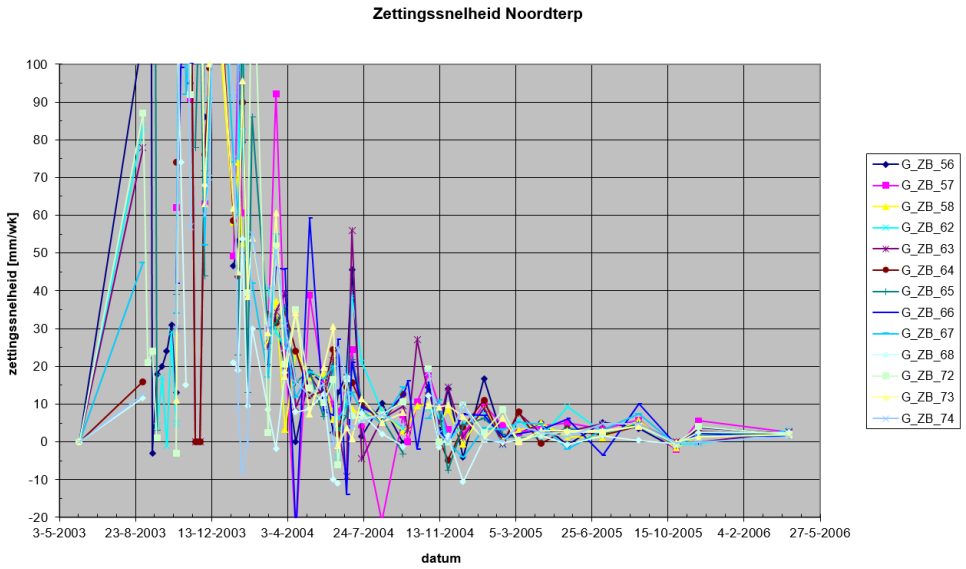

Figure 3.10: Recorded deformation rate of A2 exit Vinkeveen between 2003 and 2006 using subsidence plates. Observe how the deformation rate reduces as time progresses due to the primary consolidation phase coming to an end.

Approximately 800 days after the construction phase is started this measured deformation rate becomes relatively constant. As a result, since the thickness of the peat layer is approximately known, the corresponding strain rate can be approximated for different moments within the first 800 days after construction of the embankment.

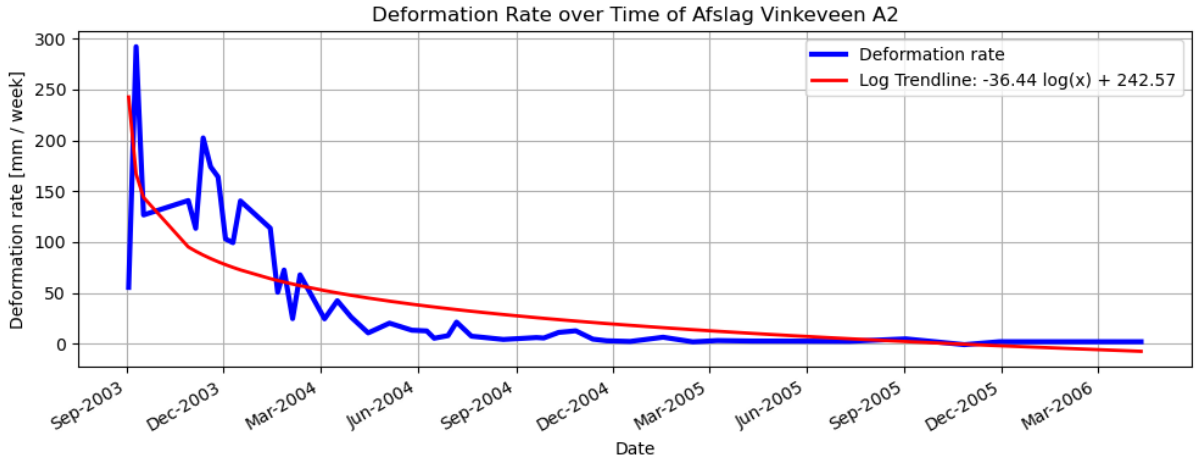

Figure 3.11: Fitted logarithmic trendline through recorded deformation rate. This deformation rate follows from Figure 3.10 where subsidence plates were placed in the embankment construction connecting Vinkeveen to the A2. Note that the fitted logarithmic function (only) serves to show that the recorded deformation rate follows a logarithmic shape.

Annex 18 shows the soil profile before widening of the A2. The initial peat layer thickness was approximately 5.55 meters. Due to gradual adding of sand layers to construct the embankment this peat layer compresses over time. The resulting settlement directly after the addition of these sand layers is recorded as well. This means that the layer thickness of the peat layer can be estimated throughout the measuring period.

Figure 3.12 shows the recorded settlement over time of the embankment connecting Vinkeveen to the A2 during construction. Annex 16 provides an enlarged view of this measuring series. Figure 3.13 shows how the recorded settlement is logarithmic shape. Note that the recorded settlement remains approximately constant around the start of 2006.

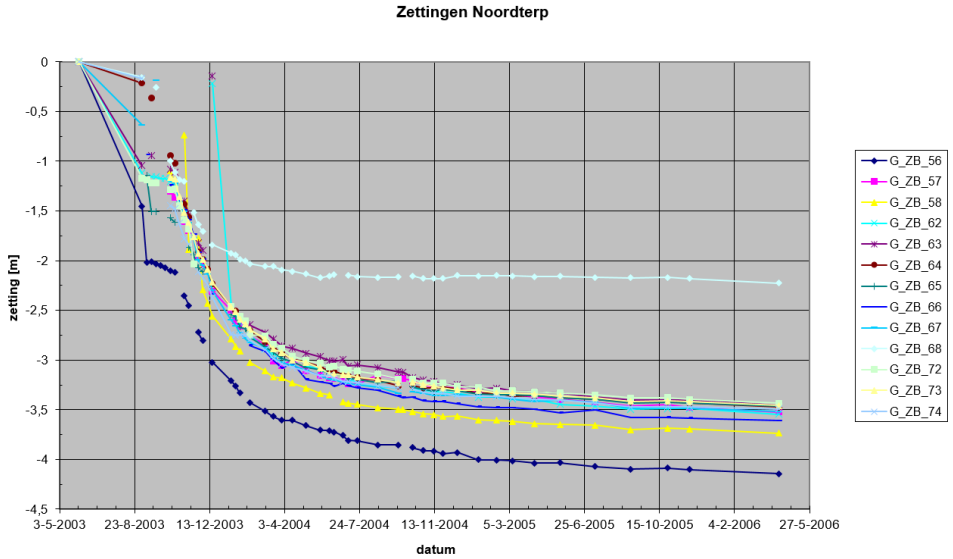

Figure 3.12: Recorded settlement of A2 exit Vinkeveen between 2003 and 2006.

The settlement at each moment of the timeseries can be estimated via the fitted logarithmic function of Figure 3.13. Combined with the initial layer thickness of the peat this results in an approximated peat layer thickness throughout the measuring period. This approximated peat layer thickness is required to estimate the strain rate at each moment of the timeseries.

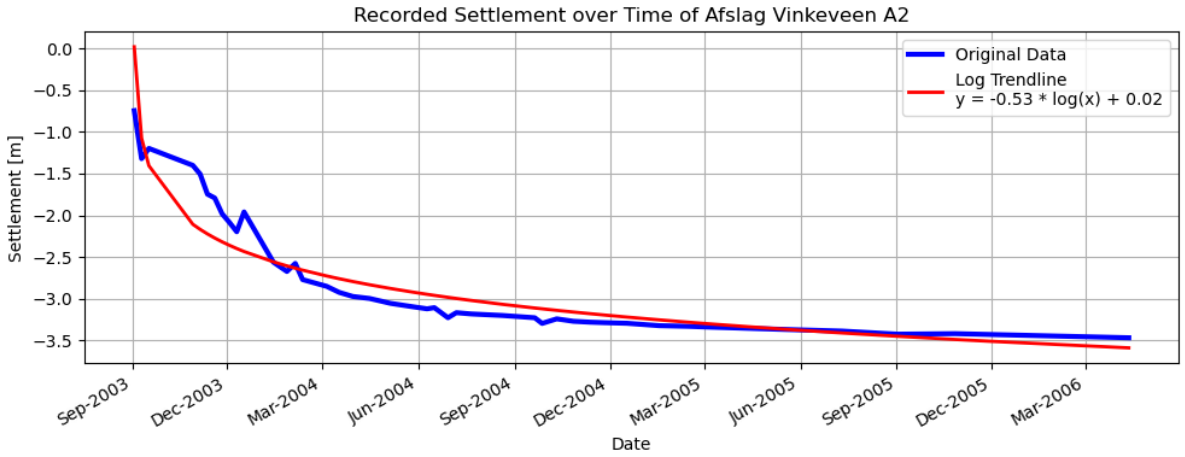

Figure 3.13: Fitted logarithmic trendline through recorded settlement.

An estimated strain rate in the peat later is calculated by combining the recorded weekly deformation rate with the approximated peat layer thickness. The deformation rate is recorded in millimetres per week. The strain rate is calculated at each moment by Equation 3.2.

$$\dot{\varepsilon}_{A2\_2006} = \frac{\dot{D}/604800}{(H_0 - S)} \quad [s^{-1}] \qquad \text{where;} \qquad (3.2)$$

$\dot{D}$ = deformation rate [mm / s].
H_0 = Initial peat layer thickness [mm].
S = recorded settlement [mm].

This estimation results in the strain rates over time as shown in Figure 3.14. Note that this estimated strain rate over this measuring period is primarily caused by primary consolidation pf the peat layer as a result of the embankment construction built on top of this layer.

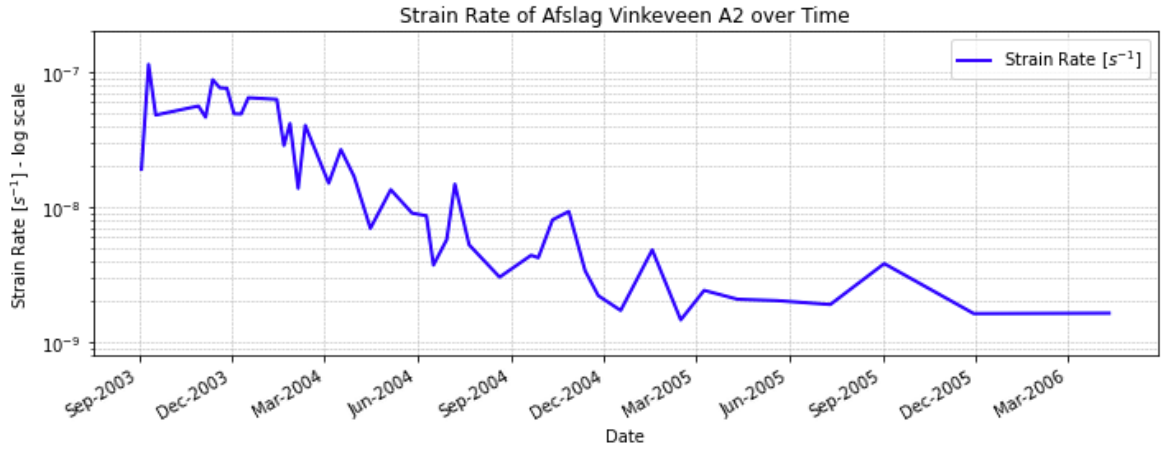

Figure 3.14: Approximated strain rate of A2 exit Vinkeveen between 2003 and 2006.

Figure 3.14 shows how an estimated strain rate at the start of construction of $\dot{\varepsilon} = 10^{-7}$ s^{-1}. Observe how the approximated strain reduces as time progresses. The measuring period of Figure 3.14 looks to show a logarithmic decrease of strain rate over time. At the end of the measuring period the estimated strain rate has reduced to approximately $\dot{\varepsilon} = 2 \cdot 10^{-9}$ s^{-1}. Note that the order of magnitude of approximated strain rates during the construction phase is comparable to the lower limit of applied strain rates in conventional CRS testing. From this it is concluded that (only) during the first month of construction the strain rates in the field are comparable to the lowest possible strain rates in conventional CRS testing. Note that the field strain rates during this phase are largely the result of the primary consolidation phase.

As time progresses, and the primary consolidation phase comes to an end, the strain rate continues to reduce and can be orders of magnitude lower than during the initial months of construction. This results in an even larger difference between strain rates in the field and those applied during conventional CRS laboratory testing. This is demonstrated in the following section.

3.4 A2 Vinkeveen 2018 - 2022

This section shows how Interferometric Synthetic Aperture Radar (InSAR) can be used to acquire an estimated deformation timeseries of part of the A2 highway near Vinkeveen. Regarding the methodology of using InSAR to estimate an annual deformation rate the reader is referred to Annex 17. The seasonal patterns observed in the estimated InSAR deformation time series are primarily attributed to changes in temperature. An average annual deformation rate is estimated from this time series, approximately 20 years after construction of this part of the A2 is finished. The subsequent strain rates estimated from this deformation time series are in the range of $\dot{\varepsilon} = 10^{-11}$ s^{-1}.

3.4.1 EGMS InSAR Data

The European Ground Motion Service (EGMS) provides three different InSAR products derived from the Sentinel-1 satellite (Copernicus, 2024). Since the EGMS program is financed by European funds, the data is freely accessible by European users (Netherlands Space Office, 2023). The EGMS data used in this section spans four years; 2018-2022. Depending on the goal of the deformation analysis this time series can be extended. Extending the timeseries is an economic decision. Extension of the time series does not alter the code used in this section, nor the procedures followed; it simply requires acquiring additional InSAR data. The main goal of this section is strain rate estimation primarily caused by creep, 20 years after construction work on this part of the A2 is finished. The time series spanning four years is therefore deemed sufficiently long.

Three types of annually updated EGMS data are publicly available namely;

1. Basic
2. Calibrated
3. Ortho

The satellite radar emits a radar beam towards the area of interest under an angle. Depending on this angle and surface roughness, the radar beam is scattered back toward the satellite. The direction in which the radar pulse is emitted is defined as the line of sight (LOS) of the satellite. This LOS direction is dependent on the viewing geometry towards the satellite (Brouwer et al., 2023).

The *basic* data is estimated for both ascending and descending orbits and provides displacement data in the LOS direction.
The *calibrated* data provides data in the LOS-direction which is referenced to an auxiliary set of data obtained by the Global Navigation Satellite Systems (GNSS).
The *ortho* data is often used to detect deformation patterns since the measured surface deformation is decomposed in horizontal and vertical components. Regarding more information on the available EGMS products the reader is referred to (Copernicus, 2024). Regarding more information on the working principle of InSAR used in this section the reader is referred to Annex 17.

The calibrated data is used to analyse the estimated strain rate of a predominantly peat area over a multi-year period. Since the calibration process employs a collection of points with position timeseries in a well-defined reference system, in this case the GNSS network, this data is more reliable in estimating vertical displacements than for example the basic uncalibrated data (Copernicus, 2024).

As described in Annex 17, data of at least 3 independent SAR satellite orbits is required to solve for the full 3-dimensional displacement field. To improve the stability of the estimated displacement vector, four different data sets are used to study the deformation area of the A2-Vinkeveen area, two ascending orbits and two descending orbits. The track angles of the four flightpaths are shown in Table 3.3. The colour used in Figure 3.15 per data set is indicated as well.

Dataset	*Track number*	*Path*	*Incidence angle*	*Track angle*	*Date*		*Colour*
1	37	Ascending	42°	189°	02-01-2018	25-12-2022	green
2	88	Ascending	36°	349°	05-01-2018	28-12-2022	red
3	110	Descending	34°	191°	01-01-2018	30-12-2022	purple
4	161	Descending	44°	351°	04-01-2018	21-12-2022	yellow

Table 3.3: Used Sentinel-1 satellite tracks in the InSAR analysis.

3.4.2 Data Visualization

The height of the datapoints from the four independent flight tracks is calibrated using the AHN-network (Natijne, 2023) and visualized with QGIS. As shown in Figure 3.15, the A2 near Vinkeveen is covered by a substantial number of data points. This is expected, as features such as roadside barriers, Matrix-sign constructions, and the road surface provide sufficient backscatter of the emitted radar pulses. Note that the different coloured datapoints in Figure 3.15 correspond to the four available different flight orbits as described in Table 3.3.

Figure 3.15: A2 Highway near exit Vinkeveen showing data of four satellite orbits.

Figure 3.15 highlights that the width of the road or revetment plays a crucial role in the eventual number of usable data points. Narrow roads, such as bicycle paths and access roads (erftoegangswegen in Dutch), generally fail to generate sufficient data points for effective deformation analysis. The few scattered data points along these narrower roads typically result from objects that provide adequate backscatter, such as light poles and road side barriers.

The first consideration to make when evaluating the InSAR data points is the temporal coherence threshold. As described in Annex 17, the temporal coherence measures the consistency of a data point over time. Temporal coherence is represented by a value between 0 and 1, where 0 indicates no coherence over time. In this study, the threshold is set at 0.60, a value that ensures a sufficient number of data points useable for deformation analysis while maintaining consistency and reliability over time.

In addition to ensuring that the data points are consistent during the measuring period, it is crucial to verify the estimated height of the datapoints. In a two-dimensional view like Figure 3.15 it is nearly impossible to distinguish the physical attribute responsible for the backscatter of the radar pulse. For example, the estimated height of a datapoint can be used to differentiate a Matrix sign from a road side barrier. This is important since both objects do not necessarily share the same expected deformation pattern.

3.4.3 Vertical Projection Deformation Estimate

Depending on the deformation pattern to be expected two different approaches can be followed to estimate the deformation time series. As described in Annex 17, displacement data is acquired in the LOS direction of the satellite. In some situations it proves possible to (only) focus on the vertical displacement field, thereby omitting terrain deformations in the horizontal directions. In this approach the LOS displacement is projected on the Cartesian vertical direction by dividing the LOS displacement value by the cosine of the incidence angle (Brouwer et al., 2023). In case of the A2 embankment it can be assumed that the displacement field is dominated by the vertical component. In case of, for example, land-sliding studies this assumption generally does not hold true (Casu et al., 2004). Figure 3.16 shows the estimated vertical deformation time series in the LOS-direction. Observe how an annual deformation rate of 4.47 mm / year is estimated. In addition, a seasonal component is clearly visible through the estimated deformation time series. Annex 15 shows how the result of Figure 3.16 is reproduceable for different available datapoints.

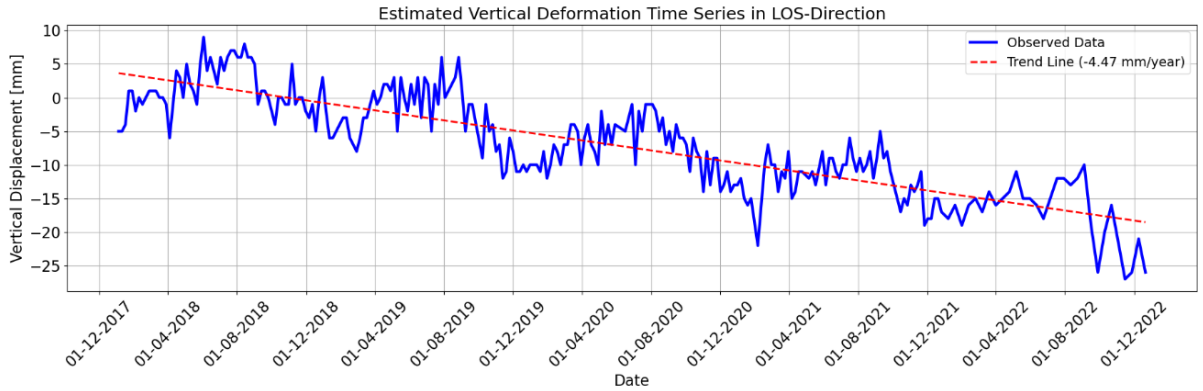

Figure 3.16: Estimated vertical displacement of single datapoint over time shows a clear seasonal pattern. In this estimated deformation timeseries the LOS-deformation is projected on the vertical displacement vector.

Figure 3.16 shows the estimated deformation pattern over time in blue. In addition, a linear trendline is fitted through the data shown in red. This trend line shows the annual estimated deformation rate in millimetres per year. The values found in this procedure are in line of what is to be expected for this part of the Netherlands (Rijksoverheid, 2024).

To verify the obtained results, a supposed stable reference points is analysed. In this case one of the foundation pillars of the bridge abutment over the Oukoop waterway is analysed. This point provides a stable reference point since the bridge pillars of the foundation are placed in the Pleistocene sand layer. This results in limited settlement throughout the years. Annex 15 shows the bridge abutment used as supposed stable reference point. The InSAR calculated deformation rate of this bridge pillar is -0.3 mm/year which is considered plausible.

3.4.4 Full Displacement Field Deformation Estimate

If LOS data is available of multiple independent satellite orbits, an estimate of the full displacement field can be realized. By combining the LOS displacement vectors of both ascending and descending satellite orbits it becomes possible to estimate the deformation patterns in the East-West, North-South and Up-Down (ENU) directions (Brouwer et al., 2023). By definition, to get an estimation of the full 3D-displacement vector in ENU direction, the information of at least three independent viewing directions, obtained by at least three satellite orbits, are required. This allows for a full-rank matrix with three unknowns. Under the assumption that the three ENU directions are independent, the constructed matrix containing the 3D displacement decomposition generally has a rank of 3 leading to three independent displacement directions estimates. The three unknown displacement values can be solved by solving this inverse problem using for example a least squares approach. This procedure is described in more detail in Annex 17.

Estimating the full 3D- displacement vector thus requires LOS-data of at least three datapoints. It is crucial to include only those datapoints for which the assumption holds that they belong to a Region of Uniform Motion (RUM) (Brouwer et al., 2023). This assumption implies that the deformation behaviour of the selected datapoints is governed by the same underlying physical phenomena. Consequently, these datapoints can be grouped to form a set used for decomposing the full displacement vector. Multiple datapoints form different independent satellite orbits within a RUM improve the accuracy and stability of the decomposed deformation vector. The size of each set may vary, as the number of available coherent scatterers within a RUM differs. Therefore, an optimal balance must be achieved. A RUM containing a large number of datapoints risks incorporating points that do not necessarily follow the same deformation behaviour, leading to inaccuracies. A RUM too small risks there not being enough available datapoints from different viewing directions.

After defining the RUM and verifying that the data points meet the set requirements, a system of equations is assembled using the LOS displacement values of each data point. As described in Annex 17, the system of equations can easily become over-determined when more than three data points are used. In such cases, the matrix is checked for ill-conditioning before solving the inverse problem for each moment. This process generates the full estimated Cartesian 3-dimensional displacement field for each moment. This can then be used to construct a time series showing the estimated deformation behaviour of the RUM. Figure 3.17 shows the estimated vertical component of the full displacement vector of part of the A2. Similar results are found over the whole available area of this part of the A2. Annex 15 shows this results as well as the exact locations of the datapoints used.

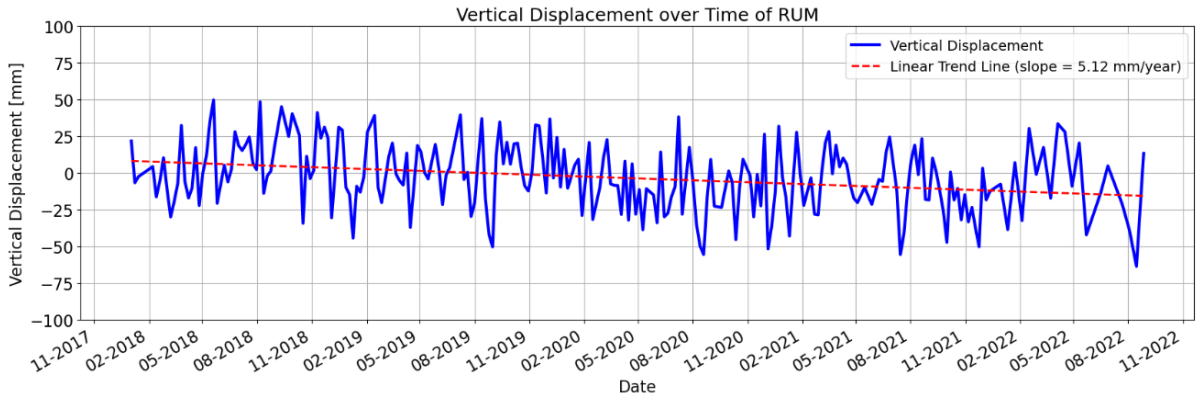

Figure 3.17: Timeseries of RUM using LOS data of four different satellite orbits.

It is again emphasized that the main goal of this section is to estimate an order of magnitude of strain rate. Note that the estimated deformation time series yields a similar average annual deformation rate as estimated using the vertical projection of a single datapoint. This value will thus be used to estimate a strain rate of this part of the A2, approximately 20 years after construction on the embankment is finished.

3.4.5 Strain Rate A2 2018-2022

The initial peat layer, before the expansion of the A2 highway, had a layer thickness of 5.55 meters as shown in Annex 18. Annex 18 shows the soil profile taken near the connection of Vinkeveen with the A2. As is described in Section 3.3.1, sand was gradually added which resulted in compression of the peat layer. After approximately 800 days the primary consolidation phase is close to finished. After this point it is assumed that the majority of settlement is caused by creep in the peat layer. After 800 days the recorded settlement is 3.5 meters. Subsequently, the Holocene peat layer will have an approximate layer thickness at this point of approximately 5.55 – 3.5 = 2.05 meters.

The deformation rate $\dot{D}$ is defined as $\dot{D} = \frac{\Delta H}{\Delta t}$ [mm / year] which follows from the performed InSAR analysis. In case of Figure 3.16 the estimated annual deformation rate equals 4.47 mm / year. The strain rate is defined as the amount of strain divided by the amount of time needed to accumulate this strain. In this case the calculated deformation rate can be converted to strain rate via Equation 3.3.

$$\dot{\varepsilon}_{A2} = \frac{\Delta H}{H_0 \cdot \Delta t} = \frac{\dot{D}}{H_0} = \frac{4.47 \cdot 10^{-3}\ \text{m}}{2.05\ \text{m}} = 2.2 \cdot 10^{-3}\ \text{year}^{-1} = 6.9 \cdot 10^{-11}\ \text{s}^{-1}. \quad (3.3)$$

This calculated strain rate provides an estimation of a strain rate corresponding to an existing infrastructural project built on peat, approximately 20 years after the primary consolidation phase is finished. Observe how this estimated strain rate is approximately three orders of magnitude lower than those estimated during the construction phase. In addition, the order of magnitude is substantially lower than the strain rates applied during conventional CRS testing. In fact the difference between this observed strain rate and a conventional CRS test strain rate is as much as 10^6.

By looking at the estimated deformation patterns in Figure 3.16 and Figure 3.17, a seasonal trend can be recognized. The seasonality observed in Figure 3.16 is less evident in Figure 3.17. This is due to the limited amount of datapoints used to solve the inverse matrix problem resulting in increased erratic behaviour between different moments. Given the available dataset it proved difficult to find more than six datapoints within a RUM which meet the threshold of temporal coherence and have the same height. A seasonal pattern can however still be observed. Moreover, this seasonality shows similar behaviour as observed in in Figure 3.16. The next section aims to determine the main cause of the observed seasonality as shown in Figure 3.16 and Figure 3.17. The results of Figure 3.16 are used to this end since the observed seasonality is more clear in Figure 3.16 than Figure 3.17. It is again noted that both approaches yield a similar annual estimated deformation rate and show a comparable seasonal trend.

Two hypothesis on the main cause of the observed seasonality are evaluated. Namely;

1. Shrinkage and swelling cycles of the peat layer due to the precipitation balance.
2. Thermal extension of roadside infrastructure due to changes in temperature.

In reality, a combination of multiple phenomena are most likely responsible for the observed seasonality in the time series estimate. Changes in the precipitation balance and temperature are however of main interest since these phenomena are known to play a crucial role in the development of peatlands (NWA-LOSS, 2024). Moreover, the two evaluated hypothesis are opposite. During winter, peat is expected to swell due to a surplus in the precipitation balance. However, due to lower temperatures and limited amount of sun in winter, the effects of thermal expansion of infrastructure are assumed to be lower compared to warmer summer months.

3.4.6 Shrinkage and Swelling Seasonality

A shortage or surplus in precipitation leads to shrinkage and swelling respectively of peatlands (Conroy et al., 2024). The underlying assumption is that the peatlands on either side of the A2 highway are hydraulically connected through the peat and sand layers beneath the highway embankment. Consequently, changes in the groundwater table on one side of the embankment could influence groundwater levels both beneath the A2 highway and the adjacent peat meadows.

To test this hypothesis, an understanding of the deformation patterns of peatlands is essential. In this context, the analysis of deformation motion using corner reflectors proves highly valuable. The estimated deformation behaviour can be used to verify whether the seasonal component as shown in Figure 3.16 and Figure 3.17 is caused by a deficit in the precipitation balance.

Rijkswaterstaat has installed several corner reflectors across the Netherlands, including one near Gaasp along the A9 highway, Figure 3.18. As shown in Figure 3.19, this particular corner reflector is positioned in a meadow. The corner reflectors are installed in such a way, for example using light-weight materials, that vertical deformation measured by InSAR techniques can mainly be attributed to the swelling and shrinkage of the peatlands.

Figure 3.18: Location of Gaasp, the Netherlands.

Figure 3.19: Satellite view of the peat meadow near Gaasp with the locations of the corner reflectors marked in red.

InSAR analysis of a peat meadow remains challenging (Conroy et al., 2024). New techniques incorporate a wider range of data such as soil data and meteorological data with the aim of gaining a deformation time series of vegetated areas such as meadows. This proves beneficial in evaluating long-term subsidence rates which can be used to calculate a corresponding strain rate. Corner reflectors can therefore be deployed in areas where strong radar backscatter is not naturally guaranteed, such as meadows and agricultural fields (Garthwaite et al., 2015). These devices consist of metallic surfaces arranged at precise angles to form corner-like structures. Their primary function is to redirect incoming radar pulses back toward the satellite's radar sensor, thereby enhancing the accuracy of the deformation time series analysis.

To evaluate the deformation of the corner reflector over time the publicly available data of EGMS is again used. The timeseries estimate of the corner reflector near Gaasp shows a clear seasonal trend due to shrinkage and swelling of the peat land, Figure 3.20. It is assumed that shrinkage and swelling cycles are the main contributors to the vertical deformation of the corner reflector. Note that analysis of the deformation pattern of this corner reflector only serves to detect if the seasonal pattern observed Figure 3.16 and Figure 3.17 is primarily caused by shrinkage and swelling of the peat. In reality the observed deformation pattern is caused by numerous phenomena. The exact deformation of the corner reflector for each day is therefore of limited interest since it only serves to detect the main origin of an observed seasonal pattern.

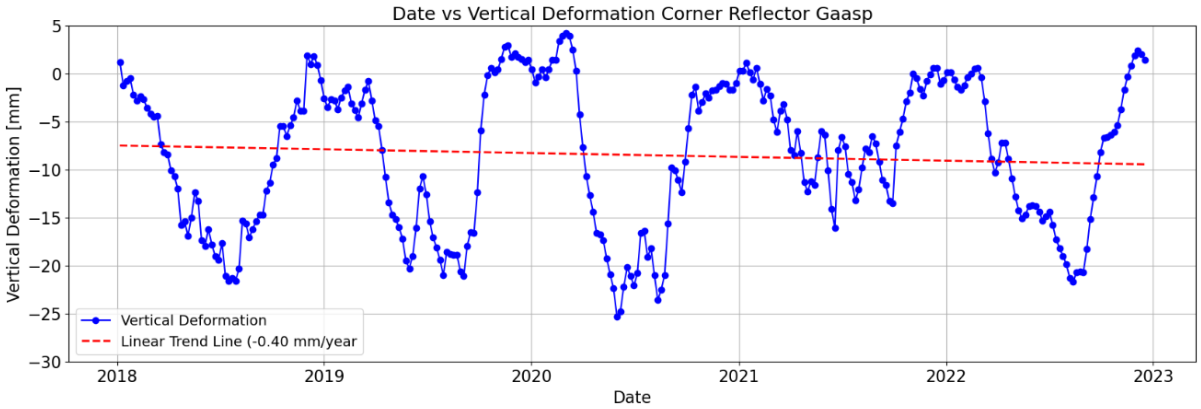

Figure 3.20: EGMS vertical deformation of corner reflector near Gaasp.

The corner reflector near Gaasp shows an average estimated annual deformation rate of 0.40 mm per year. This annual deformation rate can be converted to a strain rate since the peat layer thickness is known. The peat layer thickness of 6.0 meters near the Gaasp corner reflector is estimated using Dinoloket as shown in Annex 18.

The deformation rate $\dot{D}$ is defined as $\dot{D} = \frac{\Delta H}{\Delta t}$ [mm / year] which follows from the estimated vertical deformation as shown in Figure 3.20. The strain rate is defined as the amount of strain divided by the amount of time needed to accumulate this strain. In this case the calculated deformation rate can be converted to strain rate via Equation 3.4.

$$\dot{\varepsilon}_{Gaasp} = \frac{\Delta H}{H_0 \cdot \Delta t} = \frac{\dot{D}}{H_0} = \frac{0.4 \cdot 10^{-3}\, m}{6.0\, m} = 6.7 \cdot 10^{-5}\ \text{year}^{-1} = 2.1 \cdot 10^{-12}\ \text{s}^{-1}. \quad (3.4)$$

The estimated strain rate using the corner reflector near Gaasp is similar to the estimated strain rate of Zegveld described in Section 3.2. Both the Zegveld peat meadow and the Gaasp corner reflector are unaffected by construction. These estimated strain rate therefore serve as a lower bound of strain rates encountered in the field in predominantly peat areas.

It is important to emphasize that the analysis of the vertical deformation of the corner reflector serves solely to identify the origin of the observed seasonality. It is unrealistic to assume that the soil lithology at the corner reflector near Gaasp is exactly identical to that of the A2 highway near the Vinkeveen exit. The corner reflector near Gaasp is however the closest Rijkswaterstaat corner reflector. A comparison of the soil profiles at both locations reveals that their soil layering is comparable. In example, 6 meters of Holocene peat layers above a Pleistocene sand layer. This similarity validates the assumption that the deformation pattern observed at the corner reflector can be used to analyse the seasonal pattern detected in the InSAR time series.

Figure 3.21 shows a comparison of the obtained corner reflector data to the estimated deformation time series of part of the A2 highway. A fitted sinusoidal is plotted to ease comparison of the two phenomena. Note that the aim of Figure 3.21 is to compare trends. Fitting of the sinusoidal as shown in Figure 3.21 is therefore deemed acceptable. It can be concluded that the seasonality's do not match. In fact it is noted that the observed patterns are opposite. From this it is concluded that swelling or oxidation of the peat layer beneath the A2 is not the main cause of the seasonality observed in Figure 3.16 and Figure 3.17.

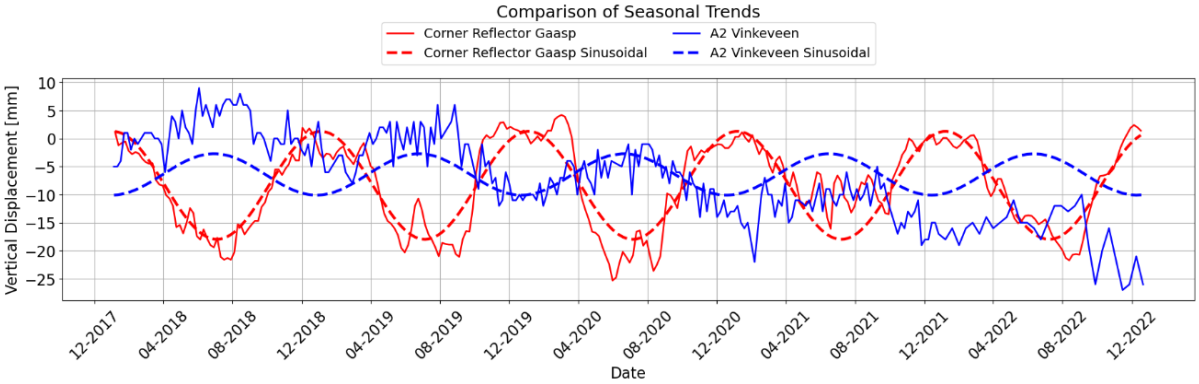

Figure 3.21: Comparison of seasonal trends. Estimated vertical displacement of A2 near Vinkeveen (blue) and estimated vertical displacement of corner reflector Gaasp (red).

3.4.7 Yearly average Temperature

The second hypothesis of the cause of the observed seasonality in Figure 3.16 and Figure 3.17 is the influence of temperature on infrastructure at the surface level. The influence of changes in temperature below surface level is limited and diminishes with increasing depth (Van Straaten et al., 2022). The emitted radar pulse is scattered back by structures such as roadside barriers. It is plausible that these structures undergo volume change due to an increase in temperature resulting in a seasonal component in the deformation time series. The effects of changes in temperature reduce with increased depth below surface level. As a result of this it is assumed that strongest effect of changes in temperature is noticeable in expansion of road side infrastructure such as road side barriers and matrix-sign constructions.

To check this hypothesis, the 30-day moving average of the daily averaged temperature of Schiphol is analysed. This data is freely accessible via the Royal Dutch Meteorological Institute (KNMI). The data is visualized in Figure 3.22. Note that this procedure only serves to detect if the observed seasonality is caused by a change in temperature. In reality multiple phenomena are responsible for the observed seasonality in the deformation time series of Figure 3.16 and Figure 3.17.

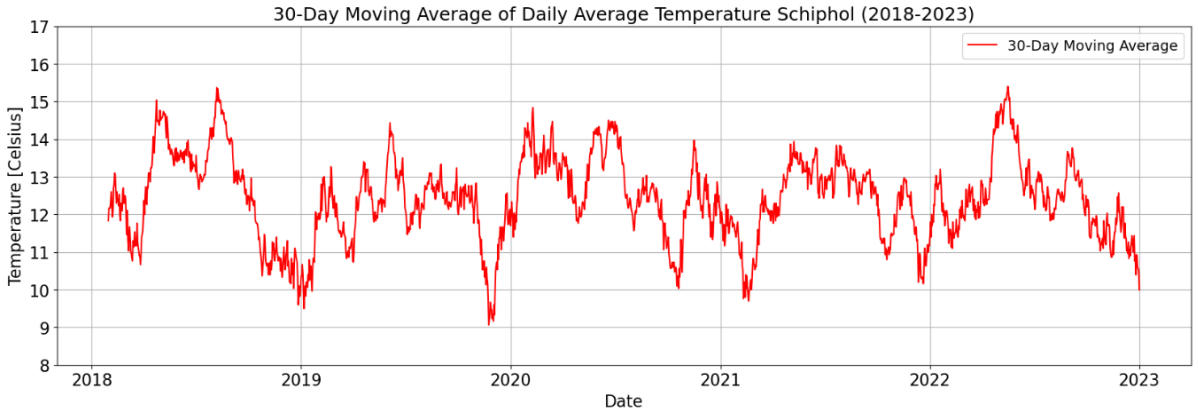

Figure 3.22: 30-day moving average of temperature recorded at Schiphol, the Netherlands. The difference in average temperature between winter and summer is clearly visible.

Visualising the observed daily temperature of Schiphol and super imposing this on estimated deformation time series of the A2 results in Figure 3.23.

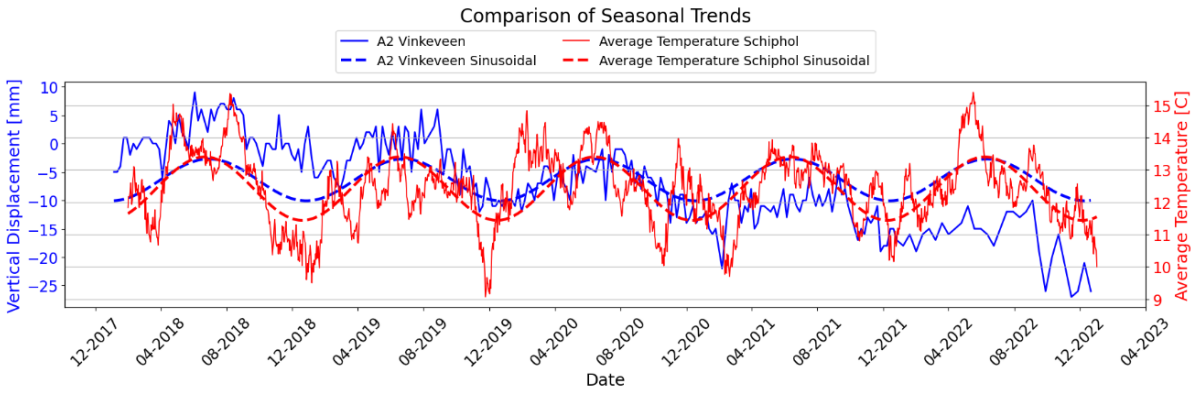

Figure 3.23: Comparison of seasonal trends. Estimated vertical displacement of A2 near Vinkeveen (blue) and average temperature of Schiphol (red).

From Figure 3.23 it can be concluded that the vertical displacement of the A2 and the 30-day average temperature of Schiphol show approximately the same behaviour. Fitting a sinusoidal trend line through both the estimated deformation timeseries and the average Schiphol temperature allows for an improved comparison between the two trends. From this it can be concluded that the temperature data matches the deformation data well throughout the whole time series.

Because the 30-day averaged temperature matches the calculated deformation, it is assumed that the observed seasonality in the vertical projection of the LOS displacement is primarily caused by expansion of line infrastructure at the surface level due to temperature. It is difficult to estimate the infrastructure responsible for this observed thermal expansion. Note that the thermal expansion index is different for each material. As a result of this, due to an increase in temperature, a road shoulder can expand more than for example asphalt. Further optimization can be achieved by further analysis of this seasonal component.

3.5 Strain Rates Range in Peat

The estimated strain rates in projects situated in peat areas are a few orders of magnitude lower than those applied during conventional CRS laboratory testing. In this aspect the findings are in line with the observed gap in strain rates between laboratory testing on clay and projects built on clay. Only during the first months of construction are the observed strain rates comparable to the lower limit applied in conventional CRS testing.

3.5.1 Estimated strain rates in peat

Table 3.4 displays the estimated strain rates as determined in Sections 3.2, Section 3.3 and Section 3.4.

Project	Estimated strain rate [s^{-1}]
Zegveld	$7.0 \cdot 10^{-12}$ - $1.3 \cdot 10^{-11}$
Gaasp	$2.1 \cdot 10^{-12}$
A2, 2003 – 2006	$2 \cdot 10^{-9}$ - 10^{-7}
A2, 2018 - 2022	10^{-11} - 10^{-10}
Conventional CRS Testing	10^{-4} – 10^{-8}

Table 3.4: Estimated strain rates in projects in peat areas.

The estimated strain rates in peat can be visualised on a logarithmic scale as shown in Figure 3.24. The conventional strain rates used in CRS laboratory testing are visualised as well. Note that the difference in strain rate between laboratory testing and field conditions can differ a few orders in magnitude, similar to the observations made by Leroueil (2006) in Figure 3.1. The practical consequences of this difference in strain rate are described in Chapter 5.

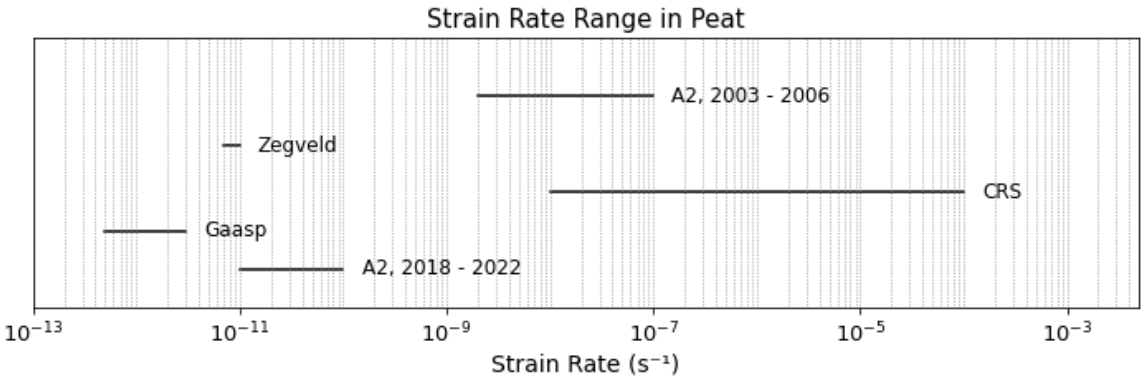

Figure 3.24: Estimated strain rate ranges in peat.

3.5.2 Comparison strain rate range clay and peat

The strain rates in projects built on clay range from $\dot{\varepsilon} = 10^{-11}\ s^{-1}$ - $10^{-8}\ s^{-1}$ (Leroueil, 2006). The estimated strain rates in peat show even lower strain rates. Zegveld and Gaasp are examples of this with estimated strain rates ranging from $\dot{\varepsilon} = 10^{-12}\ s^{-1} – 10^{-11}\ s^{-1}$. This is to be expected since these strain rates relate to a peat meadow wich is unaffected by construction. Nevertheless, the estimated strain rates of the A2, 20 years after construction was finished, have a comparable order of magnitude to the Zegveld and Gaasp meadows. The estimated strain rate during construction of the A2 is comparable to the projects on clay evaluated by Leroueil et al. (2006). From this it is concluded that the strain rates of field projects and conventional laboratory tesing only have a similar order of magnitude during the first months of construction.

3.6 Strain Rates in Peat Conclusions

This chapter described the difference in strain rate in peat between conventional laboratory testing and field conditions. The following conclusions can be drawn:

- The difference in strain rates applied during conventional laboratory testing on clay and estimated strain rates of projects built on clay can be as much as 10^6. Regarding differences in strain rates in peat this difference is shown to be even larger.
- Analysis of peat meadows in Zegveld and Gaasp result in an estimated strain rate ranging from $\dot{\varepsilon} = 10^{-12}\ s^{-1} - 10^{-11}\ s^{-1}$. This serves as a lower limit since both sites are unaffected by construction.
- During construction of the A2 near Vinkeveen the estimated strain rate ranges from $\dot{\varepsilon} = 10^{-9}\ s^{-1} - 10^{-7}\ s^{-1}$. During this stage the strain rate is primarily caused by primary consolidation of the peat layer. The estimated strain rate during this period is different compared to the applied range of strain rates in conventional constant rate of strain (CRS) laboratory testing of $\dot{\varepsilon} = 10^{-4}\ s^{-1} - 10^{-8}\ s^{-1}$. Only during the first months of construction is the strain rate comparable to the lower limit applied during conventional CRS testing. From this it is concluded that the (long-term) strain rate in field conditions in peat cannot be simulated during conventional CRS testing.
- During construction of the embankment connecting Vinkeveen to the A2 the strain rate is in the range of $\dot{\varepsilon} = 10^{-9}\ s^{-1} - 10^{-7}\ s^{-1}$. As time progresses the estimated strain rate of the Vinkeveen embankment gradually reduces to $\dot{\varepsilon} = 10^{-11}\ s^{-1} - 10^{-10}\ s^{-1}$, eventually reaching a similar order of magnitude as the estimated strain rate in the peat meadows of Gaasp and Zegveld of $\dot{\varepsilon} = 10^{-12}\ s^{-1} - 10^{-11}\ s^{-1}$.
- Interferometric Synthetic Aperture Radar (InSAR) is a powerful method of estimating deformation patterns. InSAR analysis is a delicate process prone to user errors and invalid assumptions. Care should therefore be taken into understanding the physical phenomena responsible for the estimated deformation.
- InSAR (only) provides an estimation of a deformation timeseries. It is therefore suited for visualising patterns or as a first estimate of deformation. Care should be taken in deducing definitive conclusions of the estimated deformation values and observed patterns.
- InSAR can be used to estimate the annual deformation of a location of interest and subsequently approximate a strain rate when the initial layer thickness is known.
- In case of the A2 Vinkeveen embankment projection of the vertical component in the line of sight (LOS) direction results in a similar estimated deformation time series as decomposition of the LOS-data into the full Cartesian three-dimensional displacement vector.
- A strong seasonal component is visible in the estimated deformation time series. The main driver of this seasonality is attributed to thermal expansion of infrastructure due to changes in temperature.
- Analysis of a corner reflector in a peat meadow shows a strong seasonality attributed to swelling and shrinkage of the peat land due to the precipitation balance. The estimated annual deformation rate is close to zero.
- The estimated deformation rate of subsidence plates placed below the groundwater table in Zegveld show, after 50 consecutive years, an ongoing linear deformation rate on linear timescale. This phenomena is observed at three different depths. This goes against current understanding of creep since creep is assumed to develop linearly on logarithmic scale. The Zegveld subsidence plates thus show a higher than expected creep rate. No clear explanation is found for this observation. One possibility is the increase of average yearly temperature. This is however of future interest to investigate further.

The range in strain rates in peat is shown to be similar to the known range in strain rates in clay. The next chapter describes the process of performed CRS tests on Zegveld peat. The aim of these tests is to evaluate the validity of the classical isotach framework. Improving the understanding of the constitutive behaviour of peat at low strain rates is of particular interest since this chapter demonstrated that these best approach field conditions.

4. Methodology

This chapter outlines the methodology used to assess the validity of the classical isotach framework based on parallel equidistant isotachs. To evaluate the model's effectiveness in describing peat compression behaviour, a series of CRS tests were conducted at the Deltares geotechnical laboratory in Delft. The first section details the characteristics of the Zegveld peat used in the CRS tests, followed by an explanation of how changing the applied rate of displacement allows for the visualization of different isotachs. The third section describes the test setup of the different performed CSR tests.

4.1 Zegveld Peat

This section provides a description of the Zegveld peat used for laboratory testing. Wooden branches, sedge and reed can clearly be identified from visual inspection of the peat. CT-scans of the Zegveld peat underline this observation. From this it is concluded that CT-scans provide a useful way of ensuring testing of a pristine peat sample.

4.1.1 Visual Inspection

The peat used for constant rate of strain (CRS) tests is extracted from the Zegveld polder in the Netherlands. Figure 4.1 presents a map of the Netherlands, highlighting estimated Holocene peat layer thicknesses. Notably, the Zegveld region features some of the thickest peat deposits in the Netherlands. The Zegveld area is considered representative of much of the western Netherlands, characterized by small creeks, willows, and meadows, as shown on the front page of this Thesis.

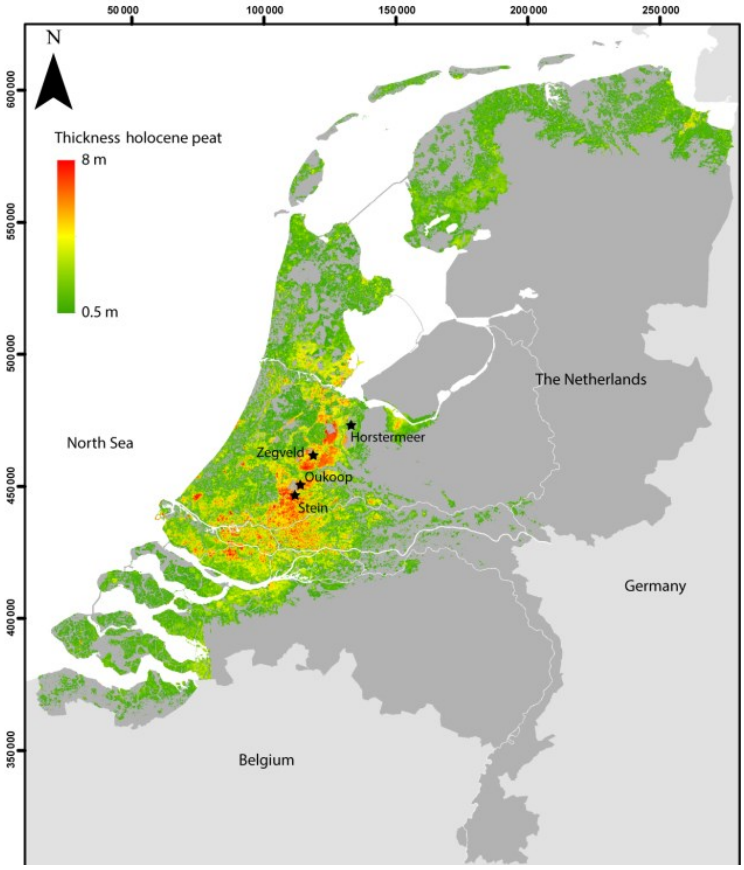

Figure 4.1: Estimated Holocene peat layer thickness in the Netherlands [After Koster et al., 2020].

Because the main constituent of peat is organic matter, which in practice is not all of the same size, peat typically has large pores that are irregular in size. This allows for flow and drainage of water within a peat layer. Additionally, peat often has close-ended pores in which water or gas is trapped. Peat therefore can best be described as a dual porosity medium (Jommi et al., 2019). As a result of the way in which organic material, that ultimately form peat layers, is stratified, peat can generally be classified as a highly heterogenic and isotropic material. This further complicates the mechanical and hydrological properties of peat and hence the results of the tests.

4.1.2 Zegveld Peat Specifications

Zegveld got its name after the plant Zegge. Zegge, Carex in Latin, is a type of gras that is found in wetlands across the globe (GroenRijk, 2024). The Zegveld peat used for testing proves to be highly heterogenic. Even within the same tube of extracted material a range of constituents making up the peat layer such as wooden branches, reed, leaves and sedge can be identified as shown in Figure 4.2. Regarding the procedure followed to extract and prepare the peat samples, the reader is referred to Annex 1.

Figure 4.2: Wood can clearly be identified in the Zegveld peat used for CRS testing.

Each sample used for testing is taken from the same material and from the same dept below surface level. Despite the visually observed heterogeneity of the peat the values of different parameters show a high degree of uniformity as shown in Table 4.1. Consequently, comparison of different test results is deemed valid. The configurations of the different tests are described in Section 4.3.

Test	*Depth [m – MSL]*	*Initial watercontent [%]*	*Specific gravity [g cm^{-3}]*	*Initial void ratio [-]*	*Depth [m – MSL]*	*Initial unit weight [kN m^{-3}]*	*Sample height [mm]*
CRS 1	1.65 - 1.80	515.62	1.606	8.3	1.65 - 1.80	10.43	30.0
CRS 1.2	1.65 - 1.80	515.73	1.587	8.2	1.65 - 1.80	10.42	30.0
CRS 2	1.65 - 1.80	515.00	1.600	8.2	1.65 - 1.80	10.49	30.0
CRS 3	1.65 - 1.80	519.07	1.603	8.3	1.65 - 1.80	10.46	30.0
CRS 4	1.65 - 1.80	524.93	1.593	8.3	1.65 - 1.80	10.50	30.0
CRS 5	1.65 - 1.80	512.16	1.603	8.2	1.65 - 1.80	10.46	30.0
CRS 6	1.65 - 1.80	515.09	1.604	8.3	1.65 - 1.80	10.41	30.0
CRS 7	1.65 - 1.80	516.82	1.603	8.3	1.65 - 1.80	10.43	30.0
CRS Creep	1.65 - 1.80	501.65	1.622	8.1	1.65 - 1.80	10.52	30.0
CRS RT	1.65 - 1.80	505.92	1.629	8.2	1.65 - 1.80	10.53	30.0

Table 4. 1: Zegveld peat characteristics.

4.1.3 Computerized Tomography Inspection

In addition to this visible inspection, medical CT-scans of the used peat are made at the Geotechnical Laboratory at the TU-Delft. The aim of performing CT-scans on peat is to evaluate the possibility of identifying organic matter much larger than the peat fibres such as wooden branches. The presence of wood within the sample can result in invalid test results and should be prevented when preparing the sample. Early detection of wood presence in the sample can therefore help in preventing invalid test results. This ultimately improves soft soil laboratory testing by eliminating the need to redo a laboratory test in case of wood being present in the sample. Figure 4.3 shows a 3-dimensional render of a 20 cm in diameter Zegveld peat cylinder. From this figure the presence of wood is clearly visible. Wooden branches can easily be identified at the top of the peat cylinder. Annex 2 describes the followed procedure of CT-scanning on peat and shows an enlarged view of the different CT-scans as well as the non-annotated scans.

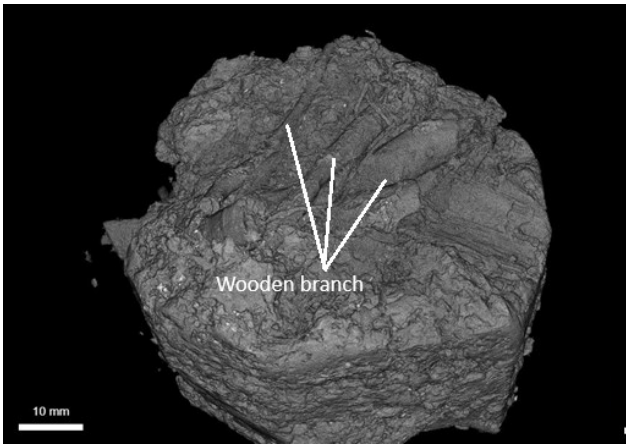

Figure 4.3: 3-Dimensional scan of Zegveld peat.

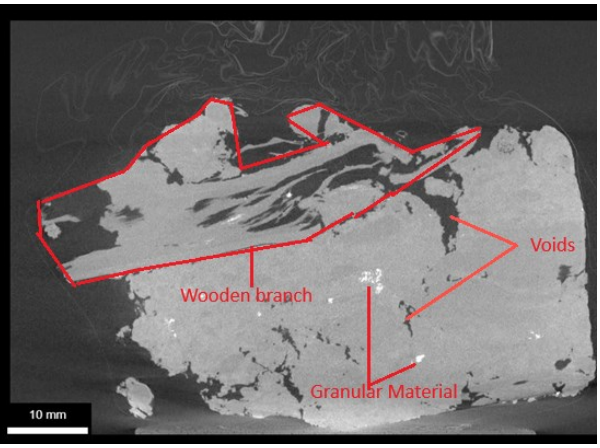

Figure 4.4: Cross-sectional view of Zegveld peat.

Figure 4.4 shows a cross-section of the same peat cylinder. The cross-section confirms the heterogeneous nature of the Zegveld peat. Black spots in Figure 4.4 indicate (partly) saturated pores. The branches visible at the top in Figure 4.3 are again clearly visible in Figure 4.4 as well. White spots in Figure 4.4 indicate granular material such as sand. Different cross-sections are made of the same peat cylinder as well as on other smaller peat samples. All CT-scans yielded similar results. Pore volumes and undecomposed sedge are abundantly distributed throughout the peat layer. Wood much larger than the peat fibres can clearly be identified in a CT-scan. The process of performing a CT-scan takes less time than dismantling and rebuilding a CRS test in case of a failed test due to the presence of wood. It is therefore advisable, if possible, to perform early CT-scans to ensure the testing of a pristine peat sample without the presence of wooden branches. This is underlined by one of the performed CRS tests which had to be stopped prematurely due to abnormal test result. Evaluating the used peat sample reviewed a wooden branch in the sample. An early CT-scan could possibly have prevented this test from failing. The failed, test including pictures of the wooden branch, is shown in Annex 12.

4.1.4 Sample Preparation

Preparation of the peat samples used for CRS testing is performed by the same laboratory technician of Deltares in accordance with the set safety guidelines and regulations as stipulated by Deltares. The samples are prepared in accordance with NEN-EN 8992:2024. In order to use a pristine peat sample in CRS testing the laboratory technician visually ensures that no large pieces of organic matter such as wood or reeds are present in the sample. However, even though the sample looks pristine on the outside, wood can still be present within the sample. Using a metal ring, a sample with the exact dimensions is taken from the previously extracted peat blocks, Figure 4.5. A porous stone is placed on one side of the peat sample to allow for drainage of excess pore pressure during CRS testing. The temperature is kept constant at 10 degrees Celsius. Regarding the procedure followed to extract and prepare the peat samples, the reader is referred to Annex 1.

Figure 4.5: Sample preparation for CRS testing.
Upper left: part of the quartered peat disk is cut roughly matching the desired dimensions.
Upper centre: excess material is carefully trimmed-off to shape the sample.
Upper right: peat sample confined by the material ring with all excess material trimmed of.
Lower left: eventual peat sample with a height of 30.0 mm and a diameter of 62.5mm.
Lower centre: the porous stone used to allow drainage of the sample.
Lower right: peat sample placed in the CRS apparatus.

All used samples are 30.0 mm in height and 62.5 mm in diameter. The aim of the CRS tests is to visualize part of different isotachs. A sample height of 30 mm is deemed sufficient to allow for sufficiently long parts of isotachs being generated. A lower, perhaps more conventional, sample height of 20mm would under the same amount of strain applied generate shorter lengths of isotachs. Shorter isotachs makes analysis of the trajectory more difficult and is therefore unwanted. The process of isotach visualisation is described in Section 4.2.1. In addition , a sample size of 20 mm would risk the sample getting compacted to such an extent that too much excess generated pore pressure is generated in the final phases of the test. This would violate the set threshold of excess generated pore pressure over total applied stress (NEN-EN 8992:2024). Figure 4.5 shows the Zegveld peat sample used for testing as shown in detail in Annex 1.

4.2 Different Isotachs in CRS Testing

This section illustrates how changing the displacement rate during CRS testing enables the visualization of different isotachs. The trajectories of tangent lines through parts of these isotachs provide insights into the level of parallelism and mutual spacing. Isotachs may become distorted due to swelling (Vergote, 2022). As a result of this, the trajectories are analysed within the normally consolidated range.

4.2.1 Isotach Changes

The classical isotach framework in theory consists of parallel equidistant running lines of equal strain rate (Šuklje, 1957), (Imai et al., 2003). In principal, this means that the classic isotach framework is composed of an infinite number of parallel equal isotachs corresponding to different strain rates. Conventionally, different isotachs are visualized with a spacing of one log 10 cycle.

Yuan & Whittle (2018), Leroueil et al. (1985, 1986, 2006) and Imai et al. (2003) describe how by changing the applied displacement rate during a CRS tests a jump in effective stress is initiated. This means that by changing the displacement rate, it becomes possible to follow parts of different isotachs corresponding to different strain rates. In doing so it is possible to visualize parts of different isotachs. This principle is illustrated in Figure 4.6. Note that the length of the followed isotach depends on the amount of displacement applied in that particular step. Note that the effective stress in Figure 4.6 is not plotted on logarithmic scale. Visualizing the effective stress on logarithmic scale renders, in theory, straight parallel isotachs as shown in Figure 2.20.

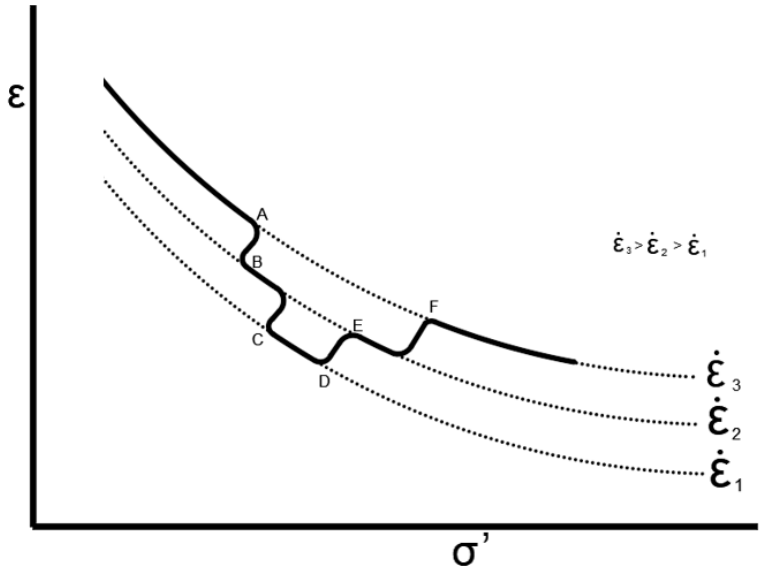

Figure 4.6: Illustration of applying changes in strain rate in a CRS test.

4.2.2 Extrapolation of Tangent Lines

The trajectories of (parts of) different isotachs can be evaluated by drawing tangent lines through each visualised isotach. The tangent lines through each isotach can then be used to conclude on the mutual distance between different isotach. The slopes of the tangent lines are evaluated to conclude on the degree of parallelism of the different isotachs. In doing so the fundamental concept of parallel equidistant isotachs of the classical isotach framework is analysed.

Vergote (2022) showed that for the tested material isotachs tend to be distorted when the sample is unloaded. Changes in rate of displacement are therefore (only) applied in normally consolidated range. A test is performed to determine the yield stress of the Zegveld peat as shown in Annex 3. The strain rate configuration used for testing is based on this test to ensure changes in displacement are only applied after the sample is loaded past the yield stress.

4.3 Test Set-up

This section describes the strain rate configuration table used in CRS testing. Five identical tests are performed in which the applied rate of displacement is changed during testing. An extra CRS test with a creep phase included is carried out. Furthermore, a CRS test is performed in which the applied displacement rate is rapidly changed. All tests are performed on the same peat with identical sample dimensions.

4.3.1 Long-term CRS Tests

The lower bound of strain rate is fixed and is a direct result of the physical limitations of the CRS apparatus. In case of the Deltares CRS apparatus a strain rate of $\dot{\varepsilon} = 10^{-8}$ s^{-1} serves as the lower bound. Table 4.2 depicts the strain rate selection table of the five long-term step changed CRS tests.

Step	*Type*	*Strain rate [s^{-1}]*	*Displacement [mm]*	*Linear Strain [-]*	*Displacement rate [mm h^{-1}]*	*Time [h]*	*Time [days]*
1	Loading	10^{-6}	4.0	0.133	0.108	37.0	1.54
2	Loading	$5 \cdot 10^{-7}$	2.0	0.1	0.054	37.0	1.54
3	Loading	10^{-7}	1.5	0.067	0.0108	138.9	5.79
4	Loading	10^{-8}	1.0	0.05	0.00108	925.9	38.58
5	Loading	10^{-7}	1.5	0.05	0.0108	138.9	5.79
6	Loading	$5 \cdot 10^{-7}$	2.0	0.067	0.054	37.0	1.54
7	Loading	10^{-6}	2.0	0.067	0.108	18.5	0.77
Total			14	0.467		1333	55.56

Table 4.2: Strain rate configuration table of long-term CRS tests.

Iterative Process

Initially step 1 consisted of a strain rate of to $\dot{\varepsilon}_1 = 10^{-5}$ s^{-1} which led to too much excess generated pore pressure being generated. This step is therefore changed to a strain rate 10 times higher to $\dot{\varepsilon}_1 = 10^{-6}$ s^{-1}. This displacement rate is sufficiently low to allow for the dissipation of excess generated pore pressure. The results of this initially too high rate of displacement resulted in the CRS test stopped prematurely. The results of this stopped test are shown in Annex 1.

As shown in Table 4.2, the rate of displacement is decreased three consecutive times until the lowest possible strain rate of $\dot{\varepsilon}_4 = 10^{-8}$ s^{-1} in step 4 achieved. After completion of this step the displacement rate is increased again in the three next consecutive steps until a final strain rate of $\dot{\varepsilon}_7 = 10^{-6}$ s^{-1}.

Symmetry

The strain rate selection of Table 4.2 is symmetrical around the slowest strain rate of $\dot{\varepsilon}_4 = 10^{-8}$ s^{-1}. This allows for comparison of different parts of isotachs which theoretically should have the same trajectory, Figure 4.6 illustrates this. In Figure 4.6 path C – D corresponds to the lowest strain rate. Point B and E correspond to a higher strain rate. Since the paths are symmetrical around path C – D, the paths corresponding to higher strain rates can easily be extended. This is important since, in theory, B and E should lay on the same isotach corresponding to strain rate $\dot{\varepsilon}_2$.

To allow for a fair comparison of the different visualised isotachs it would be preferable to have an equal displacement in every step. This would result in equal length of the parts of visualized isotachs. However, the time required for the sample to deform is substantially higher at lower strain rates. As a result, the decision is made to reduce the applied displacement in the stages of lower strain rate. This still allows for a sufficient part of each isotach to be visualised whilst not compromising too much on the overall test duration.

Five CRS tests in total are performed according to the test set-up as shown in Table 4.2. Performing multiple tests with the same set-up improves the validity of subsequent test results. This is especially important given the visually established heterogenic nature of the Zegveld peat. In addition to the five long-term CRS tests as shown in Table 4.2, two more CRS tests are performed. The aim of these two tests is to contextualize the results of the long-term CRS tests.

4.3.2 Creep Test

The aim of the creep test is to conclude on the isotach behaviour after a period of constant effective stress. First, the sample is loaded past the yield stress, indicated by the stress path A-B-C in Figure 2.16. When the sample is in normally consolidated state, the CRS apparatus is switched from displacement controlled to load controlled. At this point the effective stress level is remained constant for 16 days. During these 16 days the sample is allowed to creep. The void ratio will decrease due to this creep phase. The vertical displacement is recorded. The reduction in void ratio, or increase in strain, is subsequentially calculated from this recorded displacement. During this creep phase the state of the soil moves vertically downwards to point D in Figure 2.16. In doing so it crosses multiple isotachs corresponding to strain rates lower than to $\dot{\varepsilon}_1 = 10^{-6}$ s^{-1}. After 16 days, the CRS apparatus is switched again from load controlled to displacement controlled. The sample will now be loaded with the same displacement rate as before the creep phase. Table 4.3 shows this test configuration. As a result, the state of the soil should in theory move to the isotach corresponding to this initial rate of displacement.

Step	*Type*	*Strain rate [s^{-1}]*	*Displacement [mm]*	*Linear Strain [-]*	*Displacement rate [mm h^{-1}]*	*Time [h]*	*Time [days]*
1	Loading	10^{-6}	7.0	0.233	0.108	64.8	2.7
2	Constant Load	-	2.9	0.1	-	384.0	16
3	Loading	10^{-6}	5.0	0.167	0.108	46.3	1.9
Total			14.9	0.5		495.1	20.6

Table 4. 3: Strain rate configuration table of Creep CRS test.

4.3.3 Rapid Transition Test

The Rapid Transition Test is aimed to evaluate the influence on the compression behaviour of intermediate steps of applied displacement rate. The five performed long-term CRS tests consist of three decelerating steps followed by three acceleration phases. As a result of this, the time between the initial strain rate of $\dot{\varepsilon}_1 = 10^{-6}$ s^{-1} and the slowest possible strain rate of $\dot{\varepsilon}_4 = 10^{-8}$ s^{-1} is 213 hours, as is shown in Table 4.2. In the rapid transition test the initial strain rate of $\dot{\varepsilon}_1 = 10^{-6}$ s^{-1} is applied for a duration of almost 65 hours, as shown in Table 4.4. This ensures that the sample is loaded past the yield stress. After these 65, the strain rate is immediately changed, without any intermediate steps, to $\dot{\varepsilon}_2 = 10^{-8}$ s^{-1}. After 926 hours, when the sample is compressed another millimetre, the strain rate is increased again to $\dot{\varepsilon}_3 = 10^{-6}$ s^{-1}. In theory the tangent line corresponding to $\dot{\varepsilon}_1 = \dot{\varepsilon}_3 = 10^{-6}$ s^{-1} should have the same trajectory.

Step	*Type*	*Strain rate [s^{-1}]*	*Displacement [mm]*	*Linear Strain [-]*	*Displacement rate [mm h^{-1}]*	*Time [h]*	*Time [days]*
1	Loading	10^{-6}	7.0	0.233	0.108	64.8	2.7
2	Loading	10^{-8}	1.0	0.033	0.00108	925.9	38.6
3	Loading	10^{-6}	4.0	0.133	0.108	37.0	1.5
Total			12.0	0.4		1027.7	42.8

Table 4.4: Strain rate configuration table of Rapid Transition CRS test.

4.3.4 Overview of performed CRS Tests

The initial strain rate of CRS test 1 resulted in too much excess generated pore pressure being generated. This test was therefore stopped prematurely. CRS test 1.2 is used to determine the yield stress as shown in Annex 3. CRS test 2 failed due to technical difficulties during testing. CRS test 3, 4, 5, 6 and 7 are used to validate the classical isotach framework. The tests program of these tests is identical, as shown in Table 4.2. The test configuration of the CRS creep test is shown in Table 4.3. The additional rapid transition test is performed according to Table 4.4. The results of the different tests are summarised in Table 4.5.

Test	*Type of Test*	*Aim of Test*	*Result*
CRS 1	Step-changed	Validation of classical isotach framework	Failed
CRS 1.2	Constant	Determination of yield stress	Succes
CRS 2	Step-changed	Validation of classical isotach framework	Failed
CRS 3	Step-changed	Validation of classical isotach framework	Succes
CRS 4	Step-changed	Validation of classical isotach framework	Succes
CRS 5	Step-changed	Validation of classical isotach framework	Succes
CRS 6	Step-changed	Validation of classical isotach framework	Succes
CRS 7	Step-changed	Validation of classical isotach framework	Succes
CRS Creep	Loading type changed	Analysis of transient behaviour	Succes
CRS RT	Step-changed	Analysis of transient behaviour	Succes

Table 4.5: Performed CRS tests.

4.4 Methodology Conclusions

This chapter described the material used in CRS testing and the procedures followed in sample preparation. The following conclusions are drawn:

- Visual inspection of the Zegveld peat results in clearly identifiable organic matter such as roots, branches, reed and sedge. Large fragments of these products should be prevented from ending up in the prepared peat samples used in laboratory testing.
- Computerized Tomography (CT) inspection can help in identifying different peat constituents before sample preparation. Large wooden branches are clearly identifiable in a CT-scan. This can help the laboratory technician in improving the quality of the sample used in testing. Performing a CT-scan takes less time than preparing and placing a new sample in the CRS apparatus. Early CT-scanning can therefore optimize the efficiency of laboratory testing on peat.
- The computerized tomography scans reveal substantial pore volumes distributed throughout the peat layer. The calculated initial void ratio's underline this observation. CT-scans can therefore be used to contextualize calculated peat properties such as void ratio.
- The calculated peat characteristics of the samples used for testing show a high degree of uniformity, making comparison of the CRS test results valid.
- Changing the applied rate of displacement during CRS testing allows for the visualisation of parts of different isotachs. These can ultimately be used to conclude on the level of parallelism and mutual distance between different isotachs. This method is used to conclude on the validity of the classical isotach framework.
- The strain rate configuration of the five step-changed CRS tests is identical and symmetrical around the lowest possible strain rate of $\dot{\varepsilon}_4 = 10^{-8}\,s^{-1}$. This facilitates comparison of the trajectories of isotachs before and after an applied change in strain rate since parts of different isotachs corresponding to the same strain rate should in theory have the same trajectory. Two additional CRS tests aim to contextualize the results of the five step-changed CRS tests. A creep CRS test and a CRS test in which the applied displacement rate is rapidly changed are used to this end.

The next chapter describes the results of the CRS tests which are ultimately used to conclude on the validity of the classical isotach framework.

5. CRS Test Results

This chapter describes the results of the CRS tests on Zegveld peat. The results of the five long-term CRS tests are shown first. After that the results of two extra CRS tests are described. In addition, the minor differences between natural strain rate, linear strain rate and displacement rate are described in relation to the performed CRS tests. This chapter concludes by analysing the tangent lines through part of different isotachs which are used to conclude on the validity of the classical isotach framework.

5.1 Rate of Displacement

The strain rate configuration as shown in Table 4.2 does not violate the set threshold of excess pore pressure over total stress. Moreover, the changes in applied rate of displacement are clearly visible and occur within 1-2 minutes. The differences between calculated linear strain rate and natural strain rate during each loading step are shown to be minimal.

5.1.1 Displacement

Figure 5.1 shows the displacement over time of one of the five long-term CRS tests. In this case the recorded displacement over time of CRS 6 is shown. The results of each of the step-changed CRS tests shows similar results. The strain rate configuration of Table 4.2 is clearly identifiable in Figure 5.1. It is clearly visible how the strain rate is decreased in the first three steps. After the completion of these steps the strain rate is increased again. In Figure 5.1 this corresponds to an increased displacement over time. Note the target strain rate of each step as indicated in blue. As mentioned before, the strain rate configuration is symmetrical around the lowest strain rate of $\dot{\varepsilon}_4 = 10^{-8}\ s^{-1}$.

The true displacement rate varies between different moments due to mechanical limitations of the CRS apparatus. Because of this it is important to verify the alignment of recorded displacement rate over multiple moments with the target strain rates. To do this the following steps are followed.

1. Fit a straight line through each line segment of the displacement over time plot corresponding to each loading stage of Table 4.2.
2. The first derivative of each line segment provides the recorded rate of displacement in mm per hour of that loading stage.
3. Knowing the initial sample height of 30.0 mm, convert the recorded displacement rate, expressed in mm per hour, to a strain rate expressed in s^{-1}.

This ultimately yields the calculated strain rate as shown in red in Figure 5.1. It can be concluded that the target strain rate and the recorded strain rate differ slightly. The difference between target strain rate and recorded strain rate are considered negligible. The difference is attributed to;

- Mechanical accuracy of the CRS apparatus.
- Displacement rates in mm/hour are implemented with an accuracy of three digits. This becomes relevant for loading stages 3, 4 and 5 of Table 4.2. A strain rate of $\dot{\varepsilon}_4 = 10^{-8}\ s^{-1}$ converts to a displacement rate of 0.00108 mm per hour which is implemented as 0.001 mm $hour^{-1}$.

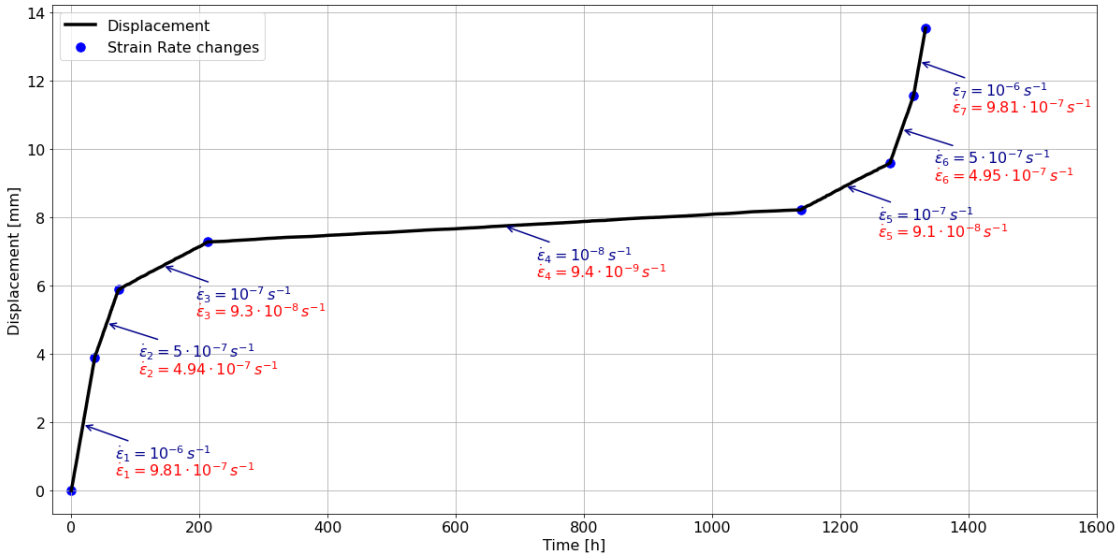

Figure 5.1: Comparison of theoretical strain rate (blue) and recorded strain rate (red) for each loading stage of CRS Test 6. All five step-changed CRS tests show similar results since the strain rate configuration is identical.

5.1.2 Pore Pressure

Figure 5.2 shows how the selected displacement rates of Table 4.2 do not lead to too much excess generated pore pressure. NEN-EN-8992:2024 provides an upper limit of excess pore pressure over total stress of 15%. The measured pore pressure response throughout the performed CRS tests falls well below this upper limit.

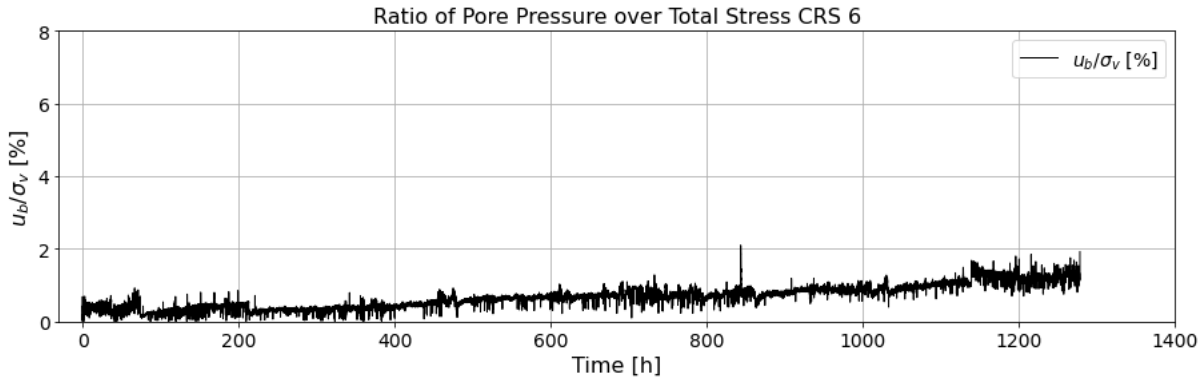

Figure 5.2: Ratio of excess generated pore pressure over total applied stress.

The graph of Figure 5.2 shows spikes throughout the test. This can be explained by measurement accuracy of the pore pressure transducer causing volatile measurements. Another explanation for this erratic behaviour is the fact that peat (often) has a dual porosity (Jommi et al., 2019). Due to loading excess generated pore pressure needs to be dissipated from both micro pores and macro pores. As the loading progresses, and the sample compresses, the void ratio reduces. This reduction of void ratio results in an increase of excess generated pore pressure since the permeability of the sample decreases. Afterall, the permeability of the soil is dependent on the strain rate as well as the reducing porosity of the sample due to loading sample as described by Equation 5.1 (NEN-EN 8992:2024).

$$k = \frac{H \cdot H_0 \cdot \gamma_w}{2 \cdot u_b} \cdot \dot{\varepsilon} \qquad (5.1)$$

This non continuous permeability throughout CRS testing therefore leads to a change in the amount of excess generated pore pressure throughout testing. Especially at the end of testing after approximately 1100 hours, when the soil sample is compressed approximately 40%, an increase in excess generated pore pressure can be noticed due to the decreased permeability in this stage of the test.

5.1.3 Strain Rate Differences

The rate of displacement, and thus the strain rate, is assumed to be constant during a loading stage in a CRS test. However, due to mechanical limitations the applied displacement rate is non-constant and varies between different moments. This is illustrated in Figure 5.3 where part of the displacement over time plot is enlarged around the decrease in strain rate from $\dot{\varepsilon}_2 = 5 \cdot 10^{-7}\ s^{-1}$ to $\dot{\varepsilon}_3 = 10^{-7}\ s^{-1}$. Note that the CRS apparatus of Deltares has a measuring frequency of 0.033 Hertz.

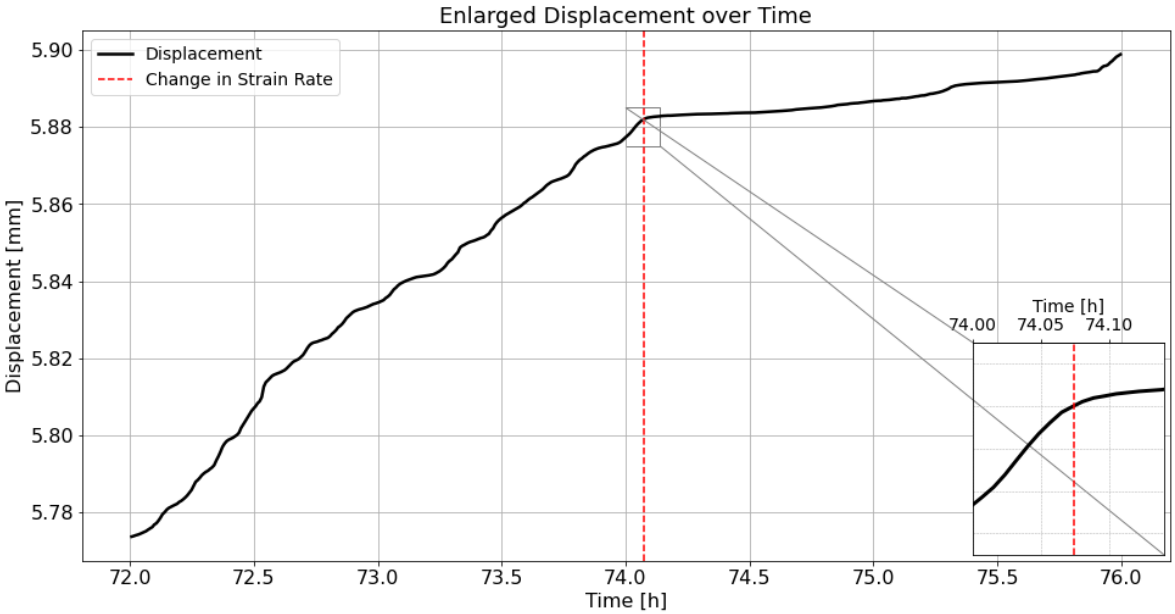

Figure 5.3: Enlarged view of displacement over time. A change in strain rate happens almost instantaneous and on average takes 1-2 minutes.

As can be seen in Figure 5.3, the applied displacement rate is changed after 74.07 hours. In Table 4.2 this corresponds to the change from step 2 to step 3. The acceleration/deceleration happens within 1-2 minutes as shown by the enlarged view in Figure 5.3. Both for steps with decreasing strain rate as well as increased strain rate. Furthermore it can be concluded that the stability of the displacement rate increases with decreasing strain rate. As a result of this the displacement over time shows less volatile behaviour between different moments during steps 3, 4, 5 from Table 4.2.

Section 2.2.1 described the difference in strain notation. At large strains i.e. $\varepsilon > 50\%$, natural strain and linear strain start to diverge (Den Haan et al., 2004). Figure 5.4 shows the comparison between calculated linear strain rate and natural strain rate throughout the performed CRS tests. From this it can be concluded that the difference between the two strain rate notations is minimal. This is to be expected since the applied strains per step are relatively low, as indicated in Table 4.2.

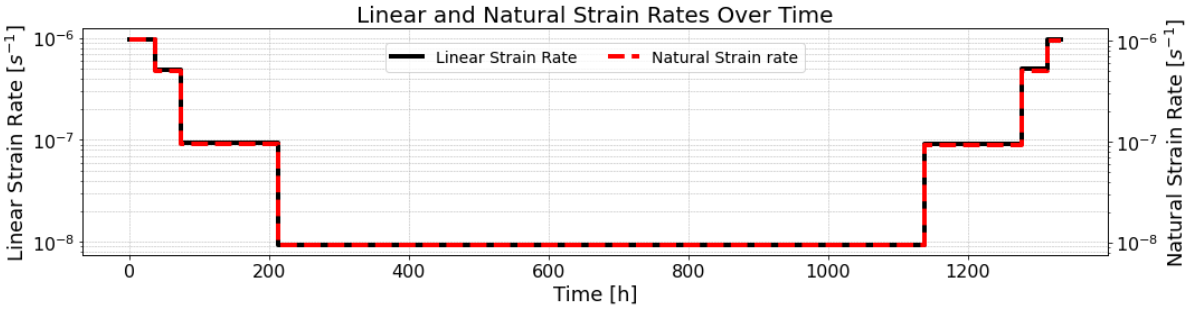

Figure 5.4: Comparison of natural strain rate and linear strain rate throughout the performed CRS tests.

Note that the applied changes in displacement rate are clearly visible in Figure 5.4. Both the linear strain rate over time as well as the natural strain rate over time show resemblance to a step function. This underlines the observation made earlier that a change in applied displacement rate happens within 1-2 minutes.

5.2 Constitutive Behaviour

This section shows how changes in applied displacement rate are clearly visible in the stress development of the CRS tests. Transient behaviour is observed around a change in strain rate. The time needed for the sample to adjust to this new strain rate increases with a decrease in strain rate. This phenomena is observed both in steps of decreasing strain rates as well as increasing strain rates and is noticed in the results of all five step-changed CRS tests.

5.2.1 Stress Development

The strain rate configuration of Table 4.2 leads to a stress development as shown in Figure 5.5. In here the recorded excess generated pore pressure is shown in blue. The selected strain rates are relatively low. As a result of this, there is ample time for excess generated pore pressure to dissipate throughout the test. After 1300 hours of testing a small increase in excess generated pore pressure is noticeable. This is explained since during this stage of the test the strain rate is increased again from $\dot{\varepsilon}_6 = 5 \cdot 10^{-7}\ s^{-1}$ to $\dot{\varepsilon}_7 = 10^{-6}\ s^{-1}$. In addition, around 40% strain is reached in this part of the test meaning the porosity of the soil sample has decreased substantially due to the reduced sample height. As a result of this, the permeability of the sample decreases. The sample is now being compressed with an increased displacement rate whilst the permeability is reduced. This results in a noticeable higher amount of excess generated pore pressure compared to the rest of the test.

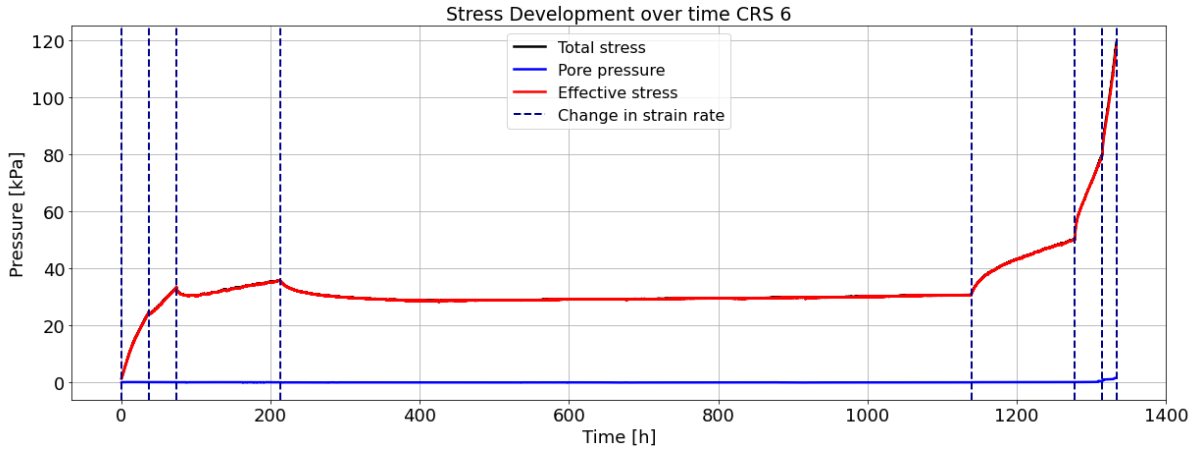

Figure 5.5: Stress development over time in which changes in strain rate are marked by the purple vertical lines.

The recorded total stress (σ_T) is almost equal to the effective stress (σ'_v) throughout the whole test, Figure 5.5. This is the result of the excess generated pore pressure (u_{exces}) being close to zero. The effective stress is calculated in accordance with Terzaghi's law and accounting for the parabolic pore water distribution in the soil sample as shown in Equation 5.2.

$$\sigma'_v = \sigma_T - \frac{2}{3} u_{exces} \tag{5.2}$$

Looking at Figure 5.5 the strain rate is decreased three consecutive times after which it is increased three times. The moments at which the strain rate is changed are indicated by the vertical dashed lines. The applied changes in displacement rate can be identified in Figure 5.5 by visual inspection as well. A (sudden) bending point in effective stress is noted at these moments. Here two cases, both resulting in different behaviour of the soil, can already be distinguished namely;

1. Decreasing strain rate
2. Increasing strain rate

The constitutive behaviour of the soil sample when subjected to these changes in strain rate is covered in the next section.

5.2.2 Strain Rate Sensitivity

The calculated effective stress directly reduces after the strain rate is decreased. As time progresses the effective stress starts to increase again. After all, the sample is still being compressed, all be it with a lower rate of displacement. The continuing compression of the sample therefore inherently leads to an increase in effective stress since the sample is still allowed to drain. This behaviour is clearly visible in Figure 5.6 where part of the graph of Figure 5.5 is enlarged around the applied change in strain rate from $\dot{\varepsilon}_2 = 5 \cdot 10^{-7}\ s^{-1}$ to $\dot{\varepsilon}_3 = 10^{-7}\ s^{-1}$.

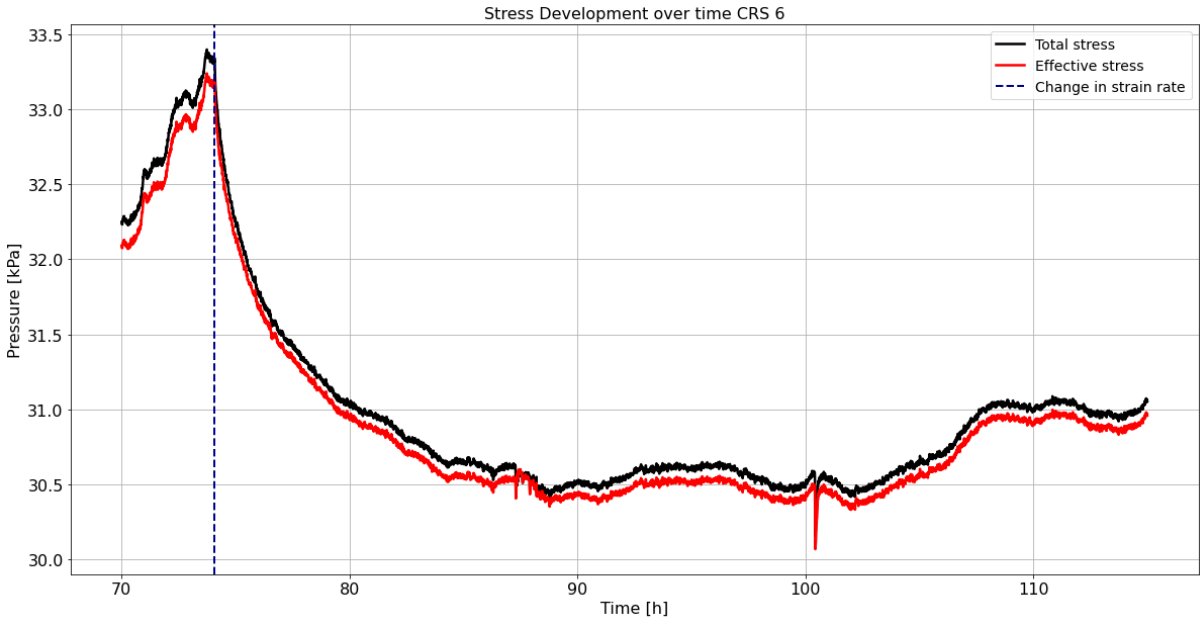

Figure 5.6: Enlarged view of total- and effective stress development over time after a change in strain rate.

The observed behaviour can be explained by looking at Figure 5.5 and Figure 5.6. After 74.07 hours the strain rate is decreased from $\dot{\varepsilon}_2 = 5 \cdot 10^{-7}\ s^{-1}$ to $\dot{\varepsilon}_3 = 10^{-7}\ s^{-1}$. As a result of this the sample is being compressed at a lower rate of displacement. This allows the sample to relax slightly and adapt to this new strain rate. Adaptation to this new applied strain rate takes time and is therefore a transient process. The effective stress depends on both the current strain and the current strain rate. When the strain rate is suddenly reduced, the material needs time to adjust to the new loading conditions. This is done by redistributing internal stresses in the soil skeleton, leading to a temporal drop in effective stress. One hypothesis for this observation is that when the strain rate suddenly changes it takes time for the internal fibre structure of the peat to adapt to this new strain rate, resulting in a decrease in effective stress. This delayed response is observed in each of the performed CRS tests. It is of future interest to investigate if this behaviour is observed in clay as well.

As time progresses the immediate effect of this change in strain rate diminishes. This can be seen in Figure 5.6 by the levelling out of the drop in effective stress between hour 74 and 84. This trend is visible in Figure 5.5 as well. This can, for example, be seen between hour 100 and 200 where the increase in effective stress occurs at almost constant rate. From this it is concluded that during this phase the effects of the change in strain rate are no longer noticeable. The sample has completely adapted to the new strain rate. This means that the change in strain rate effects are (only) temporal.

Figure 5.6 illustrates an example where the strain rate is suddenly decreased. If on the other hand the strain rate increases the opposite behaviour is noticed. The effective stress increases rapidly after an increase in strain rate. The rate of change of effective stress again reduces as time progresses. The observed rate sensitivity is again explained by the time needed for the soil skeleton to adjust to this new strain rate.

5.2.3 Stress-Strain Behaviour

The ultimate goal of performing strain rate controlled CRS tests is to conclude on the trajectories and spacing of different isotachs. As is described in Section 2.2.1, given the large strain level it proves beneficial to express the deformation of the soil sample as natural strain. The effective stress is plotted on logarithmic scale since this, in theory, renders parallel straight isotachs. Note that the effective stress is plotted on logarithmic scale with 10 as base of the logarithm. Figure 5.7 shows the results of CRS test 6 on Zegveld peat, plotted on natural strain vs. logarithm of effective stress scale. Similar results are found for each of the performed CRS tests. Annex 8 shows the results of the other strain rate controlled CRS tests.

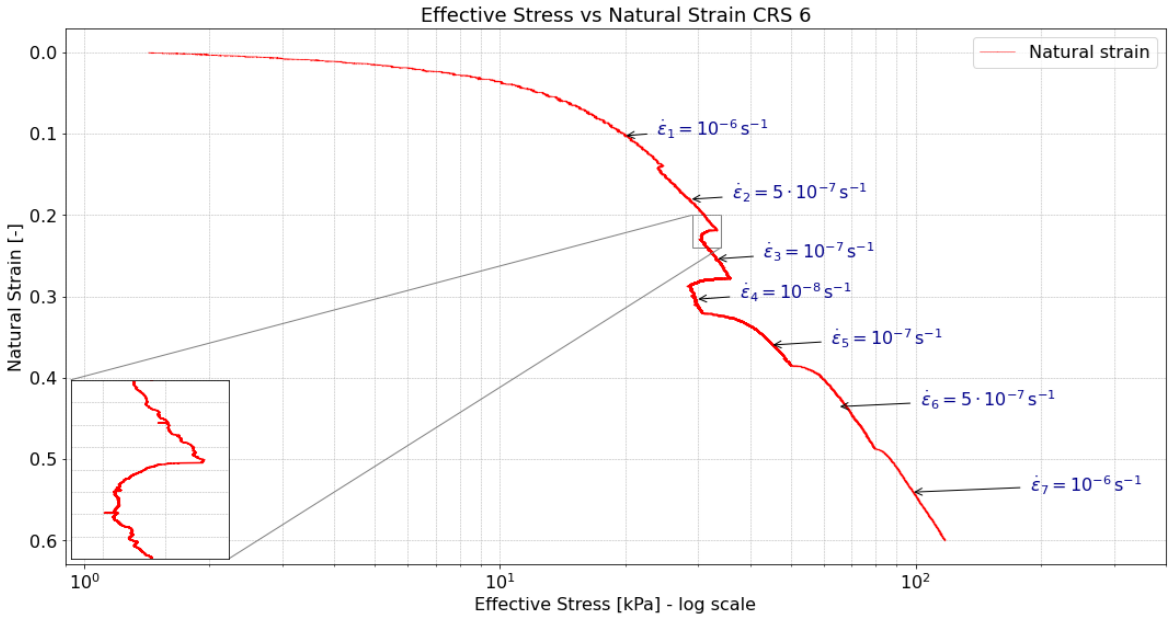

Figure 5.7: Effective stress versus natural strain. Parts of each different visualised isotachs and the corresponding target strain rate are annotated in blue.

The applied changes in strain rate, as shown in Table 4.2, can easily be identified in Figure 5.7. By definition, at the start of testing, the sample is uncompressed resulting in zero natural strain. The calculated effective stress starts slightly above zero due to the self-weight of the load transducer and the soil sample.

Change in Strain Rate

During the first stage of the CRS test the sample is loaded past its pre-consolidation stress with a strain rate of $\dot{\varepsilon}_1 = 10^{-6}\ s^{-1}$. After approximately 37 hours the strain rate is decreased to $\dot{\varepsilon}_2 = 5 \cdot 10^{-7}\ s^{-1}$. Additional decelerating and accelerating steps according to Table 4.2 can clearly be identified in Figure 5.7.

As is to be expected, due to the rapid change in strain rate, a reduction in effective stress is noticed. During this reduction in effective stress the change in natural strain level remains negligible; 0 – 1%. Figure 5.7 provides an enlarged plot around the change in strain rate from $\dot{\varepsilon}_3 = 10^{-7}\ s^{-1}$ to $\dot{\varepsilon}_4 = 10^{-8}\ s^{-1}$. The sample relaxes as a result of decreasing strain rate or tenses up due to an increasing strain rate. Note the similarity between this observed phenomena and a relaxation phase during a conventional CRS test. A decrease in applied strain rate thus results in the same temporary observed constitutive behaviour as a relaxation phase of a CRS test. Once the sample is adjusted to this new strain rate, and consequently shows behaviour corresponding to the new isotach, the effective stress starts to increase again as the sample is continued to be compressed. During the last three stages of the tests the strain rate is increased again. This can be seen in Figure 5.7 by the increase of the effective stress.

Practical Consequences
Note that the time needed for the CRS apparatus to accelerate/decelerate to an new strain rate is 1-2 minutes as shown in Section 5.1.3. The time needed for the sample to adjust to a new strain rate is however a few orders of magnitude larger than the time needed for the apparatus to undergo this change in strain rate. When the displacement rate changes, the time needed for the sample to fully move to a different isotach is inversely proportional to the new strain rate. More time is needed for the soil to adapt to a lower strain rate than is needed to adapt to a faster strain rate. Transition to/from a lower strain rate requires more time for the sample to adjust than the transitions around higher strain rates. This phenomena is clearly visible in Figure 5.5 where the time needed for a constant increase of effective stress is the largest around the lowest strain rate of $\dot{\varepsilon}_4 = 10^{-8}\,s^{-1}$. Section 6.4.4 mathematically explains this observed transient behaviour around a change in strain rate.

Section 3.5 showed how strain rates in field conditions can be substantially lower than those applied during conventional laboratory testing. The observed inverse proportionality in transient behaviour around a change in strain rate is of practical importance as well. Figure 5.5 clearly shows how changes around the lowest strain rate of $\dot{\varepsilon}_4 = 10^{-8}\,s^{-1}$ require more time for the sample to fully adjust than changes at higher strain rates. Consequently, time is needed for the soil to fully move to a different isotach. Figure 5.8 shows how in case of a decrease in strain rate from $\dot{\varepsilon}_3 = 10^{-7}\,s^{-1}$ to $\dot{\varepsilon}_4 = 10^{-8}\,s^{-1}$ approximately 200 hours are needed for the soil to fully behave corresponding to the new isotach. During this 'interim' period difficulty arises with determining settlement parameters. Afterall, what is the inclination of the virgin compression curve (*b*) during this period, or the mutual distance between different isotachs (*c*)?

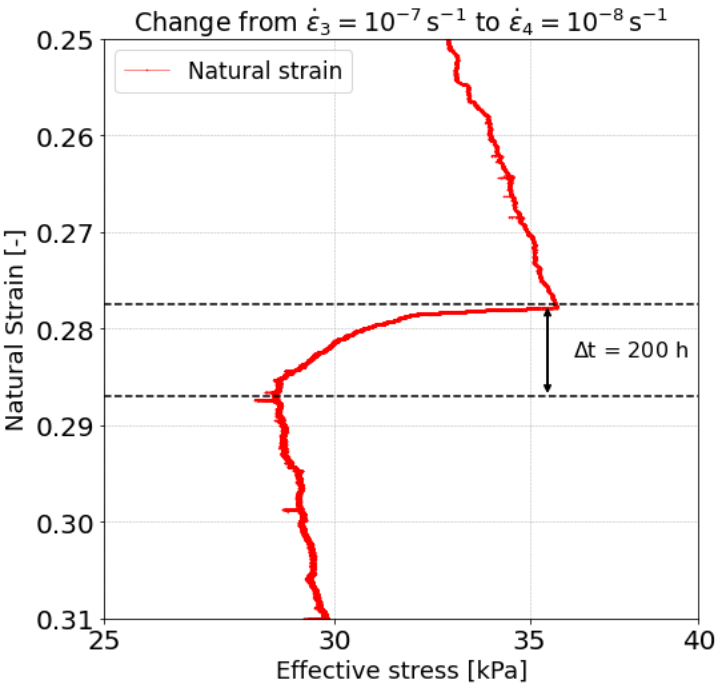

Figure 5.8: Enlarged view of an acceleration in strain rate in CRS 6.

Figure 5.5 showed how the time needed for the sample to fully adjust to a new strain rate increases with a decrease in strain rate. At a strain rate of $\dot{\varepsilon}_4 = 10^{-8}\,s^{-1}$ this already adds up to approximately 200 hours as shown in Figure 5.8. Consequently, in case of field conditions, the time needed for the soil to move to the new isotach can be substantially higher due to the inverse proportionality of time needed for the sample to fully move to new isotach. This gives rise to problems with determining settlement parameters as shown in Figure 5.8.

In practice, a change in loading conditions causes a change in strain rate. It is therefore possible that in field conditions, when the loading conditions change, the isotachs only become 'valid' after a number of days due to the increased time for the soil to fully move to a new isotach.

5.3 Combined Test Results

This section shows the combined results of the five long-term CRS tests. The observed stress-strain response is similar in each of the five tests. Visualization of the test results on void ratio scale underlines this. Minor differences in constitutive behaviour exist between the five tests. These differences are primarily attributed to the heterogenic nature of the peat.

5.3.1 Combined Results in Natural Strain

The five long-term CRS tests are performed according to Table 4.2. As shown in Figure 5.9, the performed tests show similar results. This is to be expected since the test set up is identical for all of these five tests.

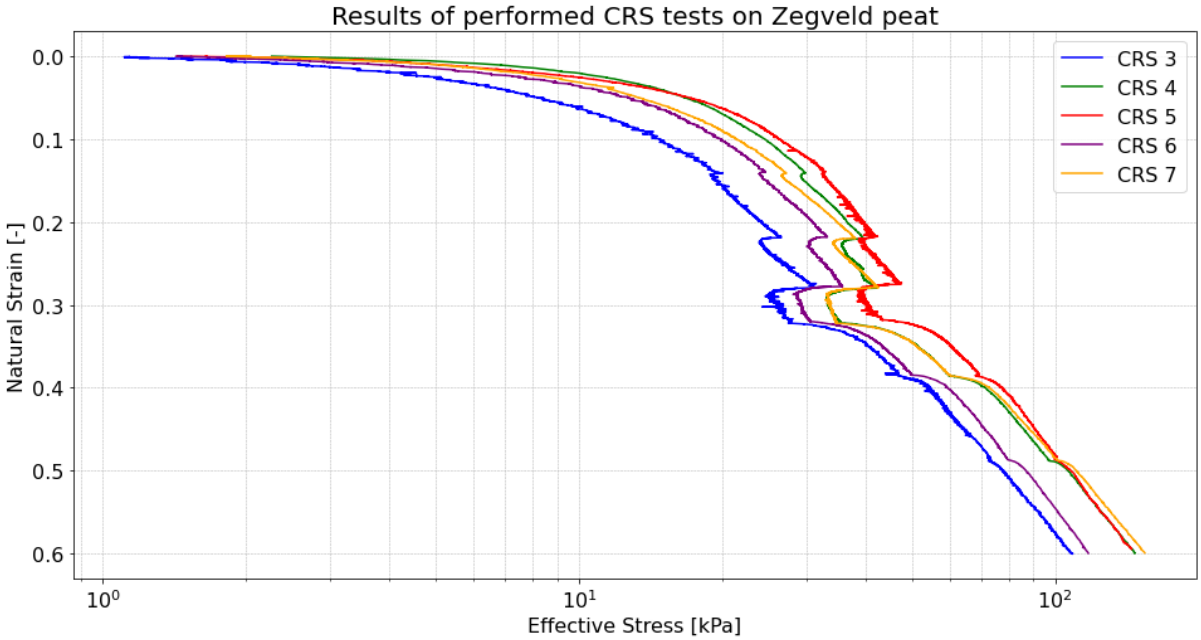

Figure 5.9: Results of all five long-term CRS tests plotted on natural strain vs. logarithm of effective stress show similar results.

By definition, all five tests start at zero natural strain. The difference in horizontal spacing of the five tests can mainly be attributed to the heterogenic nature of the peat. Even though the soil samples are all taken from the same depth, there is a substantial degree of visible heterogeneity in the peat layer. Different fibres present in the peat layer can clearly be identified. This heterogeneity, combined with the anisotropic nature of the peat means not all five samples are exactly the same. This results in slightly different constitutive behaviour as is evident in Figure 5.9.

5.3.2 Combined Results in Void Ratio

To account for the difference in initial condition, the five tests are plotted on void ratio vs effective stress scale. As is shown in Figure 5.10. Table 4.1 shows the initial water content of each sample as well as the specific gravity of the samples used.

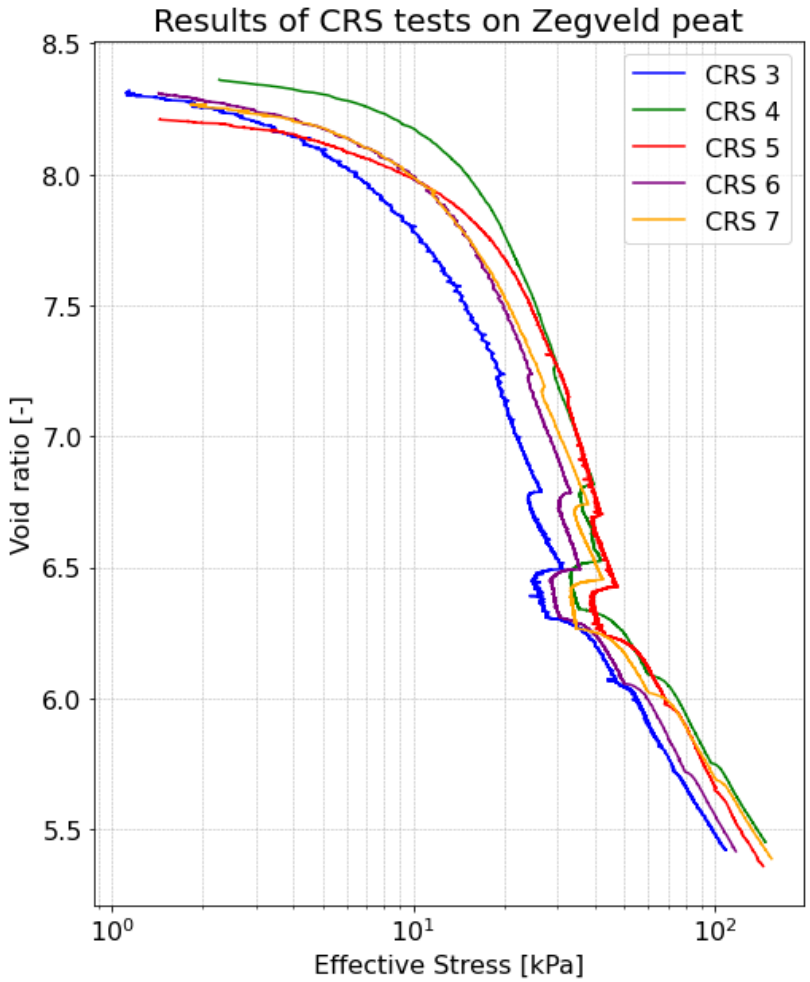

Figure 5.10: Results of performed CRS tests shown on void ratio vs. logarithm of effective stress.

CRS test number 6 is considered representative for the five CRS tests. Figure 5.9 and Figure 5.10 show that the results of CRS 6 falls within the bounds of the other performed CRS tests. As a results of this, the data of CRS test number 6 is used to visualize the methods used to conclude on the trajectories of the different isotachs in the following sections. In addition, the data of CRS test 6 is used to conclude on the comparison between different constitutive models and actual laboratory, as described in Chapter 6. The results of each CRS test is shown in Annex 8. Simulations of each strain rate controlled CRS test is shown in Annex 14.

5.4 Isotach Visualisation

This section describes the method used to draw tangent lines through part of each visualised isotach. The procedure followed results in a uniform approach used in each CRS test. It is observed how the trajectory of the isotach through the lowest strain rate of $\dot{\varepsilon}_4 = 10^{-8}\ s^{-1}$ diverges compared to those of higher strain rates. This phenomena is observed in all five step-changed CRS tests.

5.4.1 Polynomial Fitting

A minimum of two points is needed to draw a tangent line through each part of the different isotachs. A clear, consistent approach is required to determine these points. This becomes clear by looking at Figure 5.5. In Figure 5.5 it is noted that some time is needed for the soil sample to fully adjust to a new strain rate. The time needed for the soils state to fully behave on a different isotach varies with strain rate. Consequently, when a change in strain rate is initiated, the first datapoints of this new applied strain rate are unsuited to conclude on the overall trajectory of this isotach since the soil sample is not yet fully adjusted to this new strain rate. As a result, (only) the part of the isotach where the sample is fully adjusted to the new strain rate should be used in the trajectory analysis.

The following procedure is used to determine the points used to conclude on the isotach trajectories:

- Distinguish the different isotachs visible on a natural strain vs. logarithm of effective stress plot. These can easily be identified, as is demonstrated in Figure 5.7.
- Fit a third order polynomial through the isotach. The goodness of fit is determined by evaluating the coefficient of determination R^2 between the fitted polynomial and the underlying natural strain vs. logarithm of effective stress data. Figure 5.11 and Figure 5.12 demonstrate this step.
- Evaluate the second derivative of the fitted polynomial. The datapoint on the isotach where the second derivative equals zero marks the transition (inflection) from convex to concave or vice versa. This point is used as the first point of the tangent line through the isotach.
- The second point is chosen as the last datapoint on each isotach before a step change is initiated to a different strain rate.
- With these two points known it becomes possible to draw a tangent line through part of each isotach.

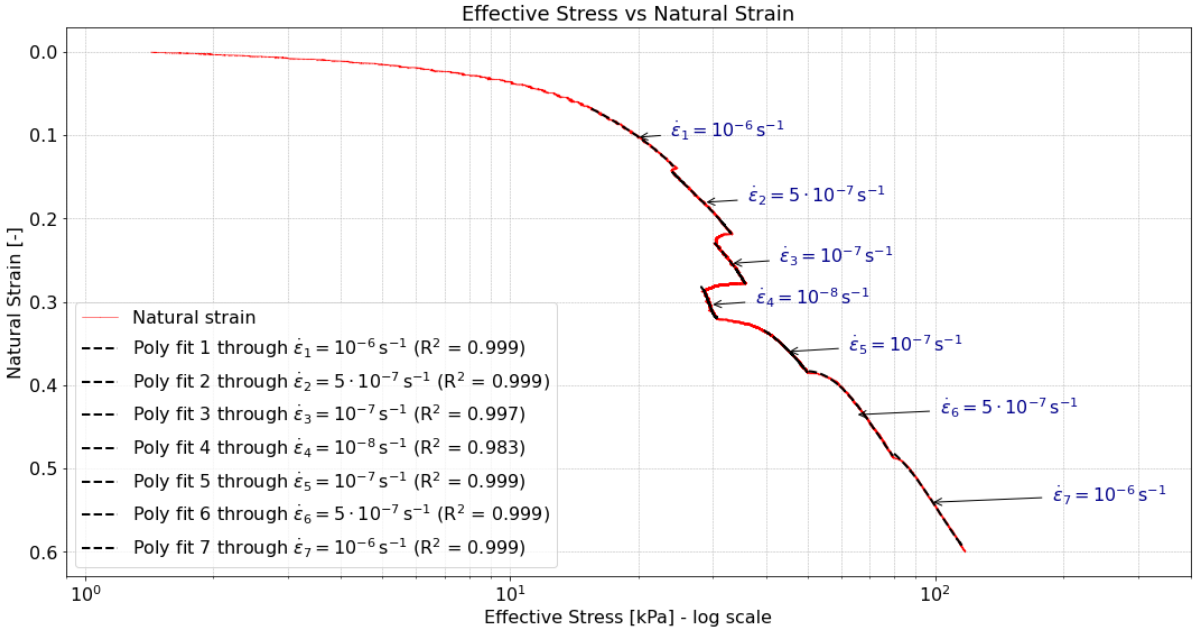

Figure 5.11: Third order polynomial fit through part of each isotach.

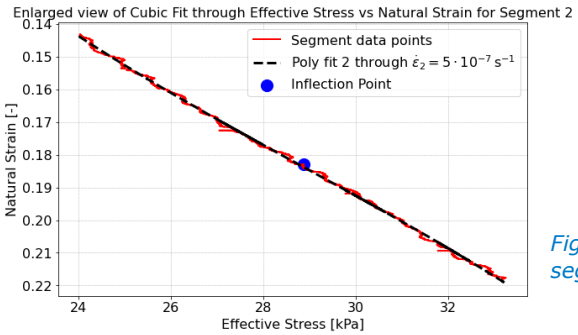

Figure 5.11 shows that a third order polynomial is generally able to fit the data segment well. Given the high coefficient of determination, higher order polynomials were not deemed necessary. Especially since the usage of higher order polynomials risks overfitting of the data.

Figure 5.12: Enlarged view of fitted polynomial through segment corresponding to $\dot{\varepsilon}_2 = 5 \cdot 10^{-7}\ s^{-1}$.

5.4.2 Tangent Lines

By following this procedure, tangent lines can be drawn through the different visualized isotachs. The evaluation of these tangent lines is in turn used to conclude on the overall trajectories of the isotachs. This approach ensures that each tangent line is based on the same underlying phenomena where some level of adjustment is needed for the sample to adjust to a new strain rate. Analysis of the inflection point of the fitted polynomial ensures that the tangent lines are drawn through the part of the isotach where the sample is fully adjusted to this new strain rate.

Following this procedure ultimately results in tangent lines as shown in Figure 5.13. Note that Figure 5.13 illustrates the tangent lines for CRS test 6. The results of the other performed tests are analysed in the same manner. The subsequent results are shown in Annex 8.

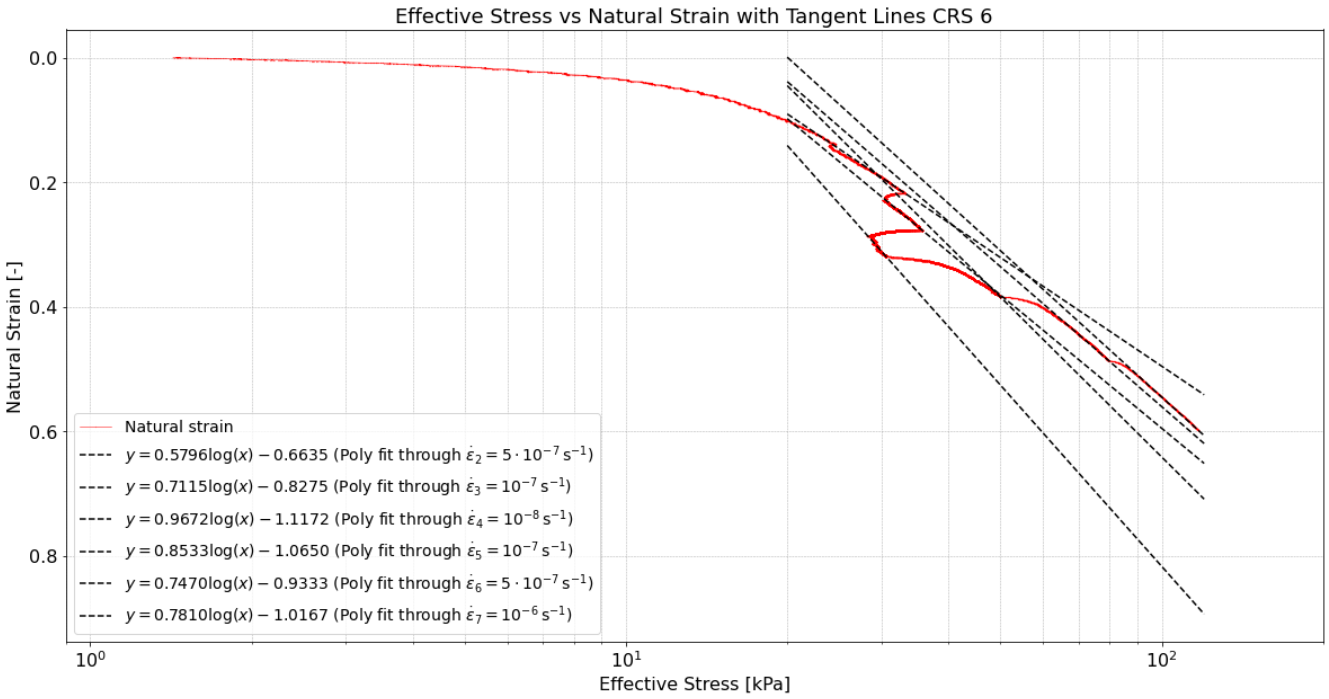

Figure 5.13: Tangent lines through each visualised isotach.

By looking at Figure 5.13 it can already be concluded that;

- The change from the first applied strain rate of $\dot{\varepsilon}_1 = 10^{-6}\,s^{-1}$ to $\dot{\varepsilon}_2 = 5{\cdot}10^{-7}\,s^{-1}$ happens in the transition phase from over-consolidated state to normally consolidated state. Not enough strain has accumulated to fully load the sample past its yield stress. As a result of this, the trajectory of this isotach is substantially different compared to the other tangent lines. This thesis (only) focusses on the isotach behaviour in normally consolidated range. The tangent line through part of the isotach corresponding to $\dot{\varepsilon}_1 = 10^{-6}\,s^{-1}$ is therefore neglected.
- The tangent line through the isotach corresponding to $\dot{\varepsilon}_4 = 10^{-8}\,s^{-1}$ diverges compared to those of higher strain rates.
- It appears that isotachs with the same strain rate show variability in their trajectories. For example, there is a difference in trajectory between $\dot{\varepsilon}_3 = 10^{-7}\,s^{-1}$ and $\dot{\varepsilon}_5 = 10^{-7}\,s^{-1}$.

Based on Figure 5.13 it is concluded that the tangent lines, and thus the isotachs, show a decent degree of parallelism for strain rates larger than $\dot{\varepsilon} = 10^{-7}\,s^{-1}$. The tangent line through the lowest visualised isotach of $\dot{\varepsilon}_4 = 10^{-8}\,s^{-1}$ diverges compared to the other visualised isotachs.

5.5 Trajectory Analysis

This section demonstrates how the coefficient of variability is used to conclude on the uniformity of the slopes of the tangent lines through different isotachs. These slopes are evaluated in three different ways. It is shown how each evaluation method yields similar results for all five tests. A maximum coefficient of variability of 0.21 is found. From this it is concluded that the visualised isotachs overall show a decent degree of parallelism for strain rates larger than $\dot{\varepsilon} = 10^{-7}\,s^{-1}$. The trajectories of the isotachs start to diverge with decreasing strain rate.

5.5.1 Slope Evaluation Methods

The same procedure to determine the slope of the tangent lines, as described in Section 5.4.1, is used for all five CRS tests. Each of these five tests renders six tangent lines. Per performed test, this yields tangent lines corresponding to the following strain rates, as is evident from Figure 5.13;

- One tangent line through $\dot{\varepsilon} = 10^{-6}\,s^{-1}$.
- Two tangent lines through $\dot{\varepsilon} = 5{\cdot}10^{-7}\,s^{-1}$.
- Two tangent lines through $\dot{\varepsilon} = 10^{-7}\,s^{-1}$.
- One tangent line through $\dot{\varepsilon} = 10^{-8}\,s^{-1}$.

The trajectories of these tangent lines are evaluated in the following manner;

1. Evaluation of the slopes per CRS test.
   Because of the heterogenic nature of peat, the constitutive behaviour can differ from sample to sample. The slopes of the tangent lines are therefore evaluated per performed test.
2. Evaluation of the slopes per test, per different strain rate.
   Per performed CRS test a total of four different strain rates are analysed. As described in Section 4.3.1, the strain rate configuration is symmetrical around the lowest strain rate of $\dot{\varepsilon}_4 = 10^{-8}\,s^{-1}$. The hypothesis of the classical isotach framework is the validity of parallel equidistant isotachs of unique strain rate. Subsequently, the tangent lines through the isotachs corresponding to $\dot{\varepsilon}_2 = \dot{\varepsilon}_6 = 5{\cdot}10^{-7}\,s^{-1}$ and $\dot{\varepsilon}_3 = \dot{\varepsilon}_5 = 10^{-7}\,s^{-1}$ should in theory have the same slope.
3. Evaluation of the slopes of all available tangent lines.
   Based on the hypothesis that the classical isotach framework is valid for the tested material, all applied changes in strain rate should, in theory, render parallel isotachs. It is of interest to evaluate the combined slopes of all available tests since all five tests are from the same material, taken from the same depth.

Histograms of the slopes of the tangent lines are made for each evaluation method as listed above. Per histogram the mean (μ) and standard deviation (σ) of the slopes are determined. The coefficient of Variation (CV) is then evaluated to conclude on the level of parallelism of the tangent lines through the isotachs. In here the coefficient of variation is defined as $\frac{\sigma}{\mu}$.

Note that the slopes of the tangent lines through different isotachs are evaluated in terms of the logarithm of effective stress with 10 as base of the logarithm. This results in different slope values than for example the classical abc-implementation where the effectives stress is evaluated in terms of the natural logarithm. The calculated slopes of CRS test 6 are shown in Table 5.1. Regarding the slopes of the other performed CRS tests the reader is referred to Annex 8.

CRS 6

Step	Slope
$\dot{\varepsilon}_2 = 5 \cdot 10^{-7}$	0.5796
$\dot{\varepsilon}_3 = 10^{-7}$	0.7115
$\dot{\varepsilon}_4 = 10^{-8}$	0.9672
$\dot{\varepsilon}_5 = 10^{-7}$	0.8533
$\dot{\varepsilon}_6 = 5 \cdot 10^{-7}$	0.7470
$\dot{\varepsilon}_7 = 10^{-6}$	0.7810

Table 5. 1: Slopes of CRS test 6.

5.5.2 Slope Distribution per Test

Figure 5.14 shows the distribution of the slopes per performed CRS test. Evaluation of the slopes of the tangent lines per CRS test underlines the inherent heterogeneity of the tested material. The mean slope values is different for each of the five tests. In addition, the coefficient of variation of these five tests ranges from 0.08 (CRS 4) to 0.20 (CRS 3). CRS 7 showed an increase in pore pressure during testing which is described in more detail in Annex 10. The tangent line through this one particular isotach of CRS 7 is therefore corrected and not considered in the slope distribution analysis.

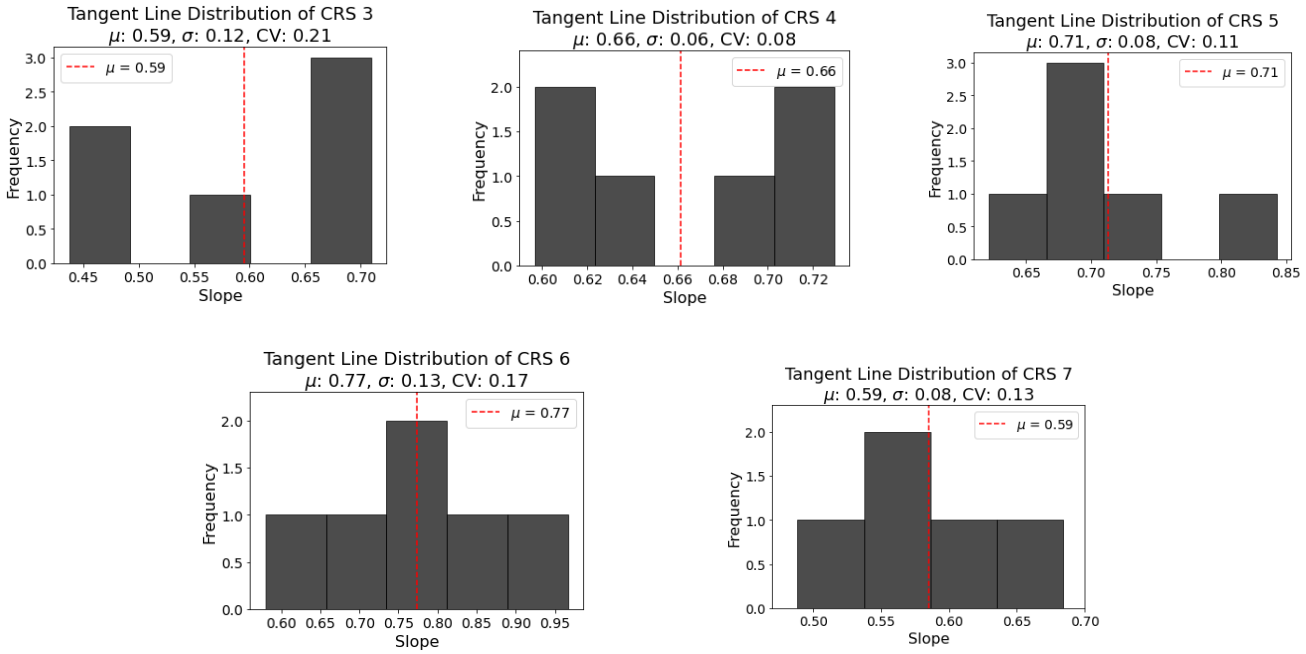

Figure 5.14: Slope distribution of each performed CRS test individually.

5.5.3 Slope Distribution per Strain Rate

Figure 5.15 shows the slope distribution per test, per strain rate. Note that this evaluation procedure results in a lower coefficient of variation compared to the results in Figure 5.14. This indicates that the trajectory of each unique strain rate shows a higher level of parallelism compared to the evaluation of each isotach as shown in Figure 5.14. It is noted however that the number of slope values, in this case four, is limited. The slope analysis primarily serves to show that the degree of variability between different isotachs is low.

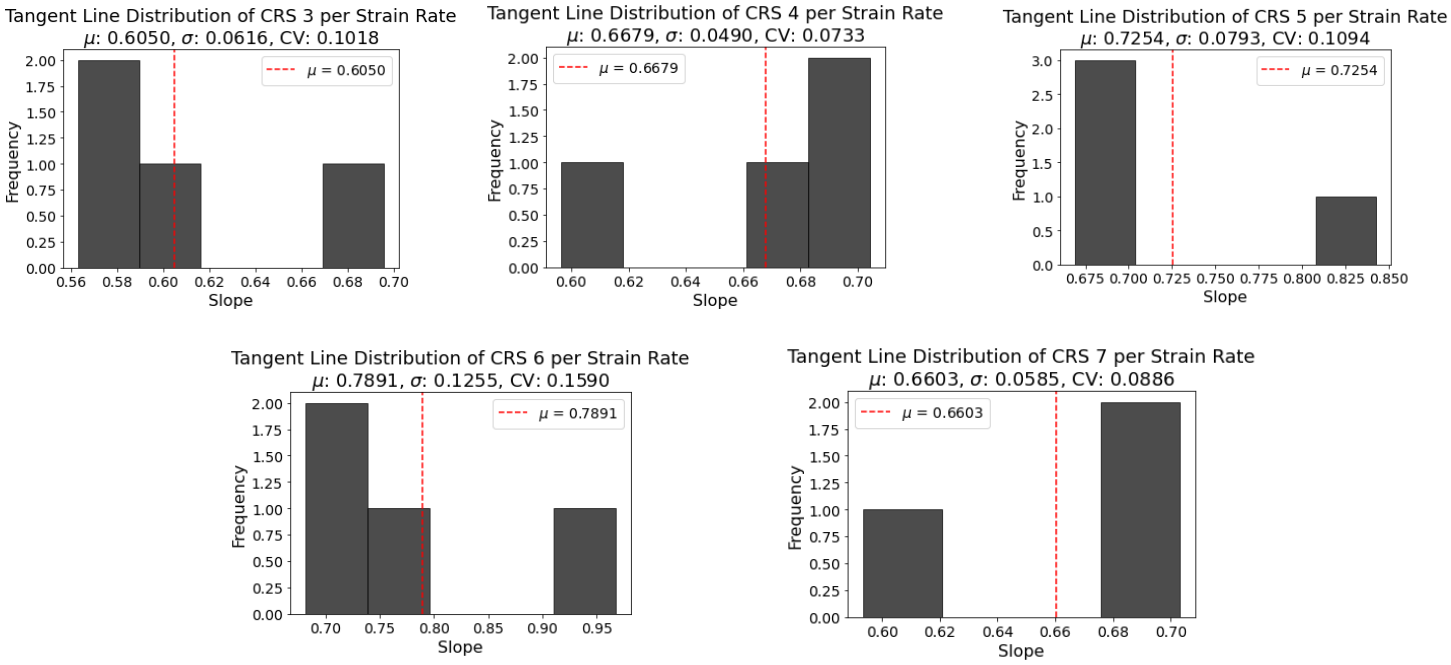

Figure 5.15: Tangent line distribution of each unique strain rate per test.

5.5.4 Slope Distribution Combined

The results of the five performed step-changed CRS tests, with each six tangent lines, result in 30 slopes total. Combining all available isotach trajectories results in a coefficient of variation of 0.17. Figure 5.16 illustrates how the slope values seem to be normally distributed around a mean value of 0.67. The slopes of each test are shown in Annex 8.

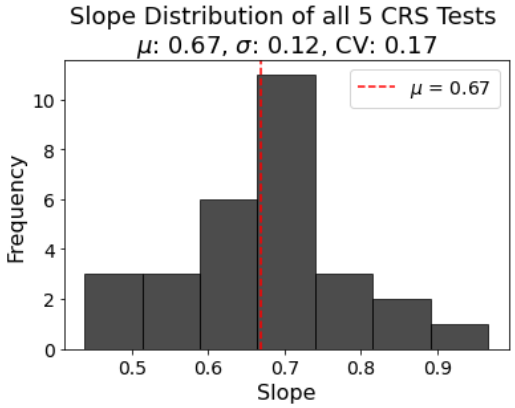

Figure 5.16: Slope distribution of all five CRS tests.

The trajectories of the tangent lines through the lowest strain rate of $\dot{\varepsilon}_4 = 10^{-8}\ s^{-1}$ diverge from those corresponding to higher strain rates. This becomes clear by evaluating the different slopes per CRS test as shown in Annex 8. Moreover, comparison of the slopes of all tangent lines of all CRS test, without the tangent line through $\dot{\varepsilon}_4 = 10^{-8}\ s^{-1}$ result in a lower coefficient of variation as shown in Figure 5.17. From this it concluded that the visualised isotachs start to diverge with decreasing strain rate. In practice diverging isotachs result in stress dependency of the creep parameter as described in Section 2.6. Furthermore, diverging isotachs result in non-equidistant isotachs and thus a changing creep rate over time. The next section evaluates the mutual distance between the different visualised isotachs.

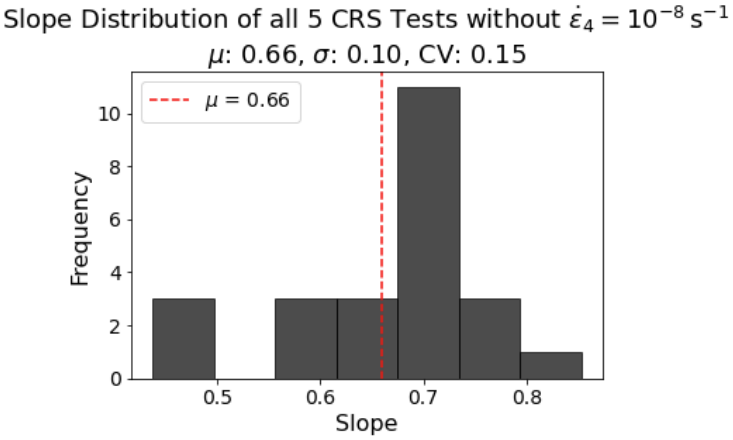

Figure 5.17: Slope distribution of all five CRS tests excluding the tangent line through $\dot{\varepsilon}_4 = 10^{-8}\ s^{-1}$.

5.6 Spacing of Isotachs

This section describes the procedure followed to conclude on the mutual distance between different isotachs. It is observed how the spacing of different isotachs increases with a decrease of strain rate. This increase in mutual distance with lower strain rate is observed in all five CRS tests.

5.6.1 Mutual Distance Procedure

The classical isotach framework is built on the concept of parallel isotachs of equal strain rate. The previous section showed that a high degree of parallelism is found when evaluating the trajectories of different isotachs. Isotachs corresponding to lower strain rates seemed to diverge from those corresponding to higher strain rates. The second fundamental concept of the isotach framework is that of equidistant isotachs. Consequently, the mutual distance between different isotachs with a spacing of one log cycle should in case of the classical isotach theory remain constant. Note that parallel isotachs not automatically result in equidistant isotachs, as is described in Section 2.6.2.

In order to test the concept of equidistant isotachs, the following procedure is followed;

1. Plot a vertical line within the stress regime of visualised isotachs.
2. Determine the intercept of each tangent line with this vertical line.
3. Evaluate the y-coordinate (in this case natural strain level) of each intersection point.
4. Analyse the difference in natural strain between different intersection points.

The difference obtained by following this procedure corresponds to the vertical distance between different isotachs. Note that the vertical axis displays natural strain on linear scale. By evaluating the vertical distance between different isotachs it is possible to conclude on the mutual distance between them. The mutual vertical distance of different isotachs is evaluated at three different positions in order to achieve consistent results. Figure 5.18 shows this. The mutual distance between each part of a visualised isotach is evaluated at a stress level of; σ_1 = 30 kPa, σ_2 = 35 kPa, σ_3 = 40 kPa.

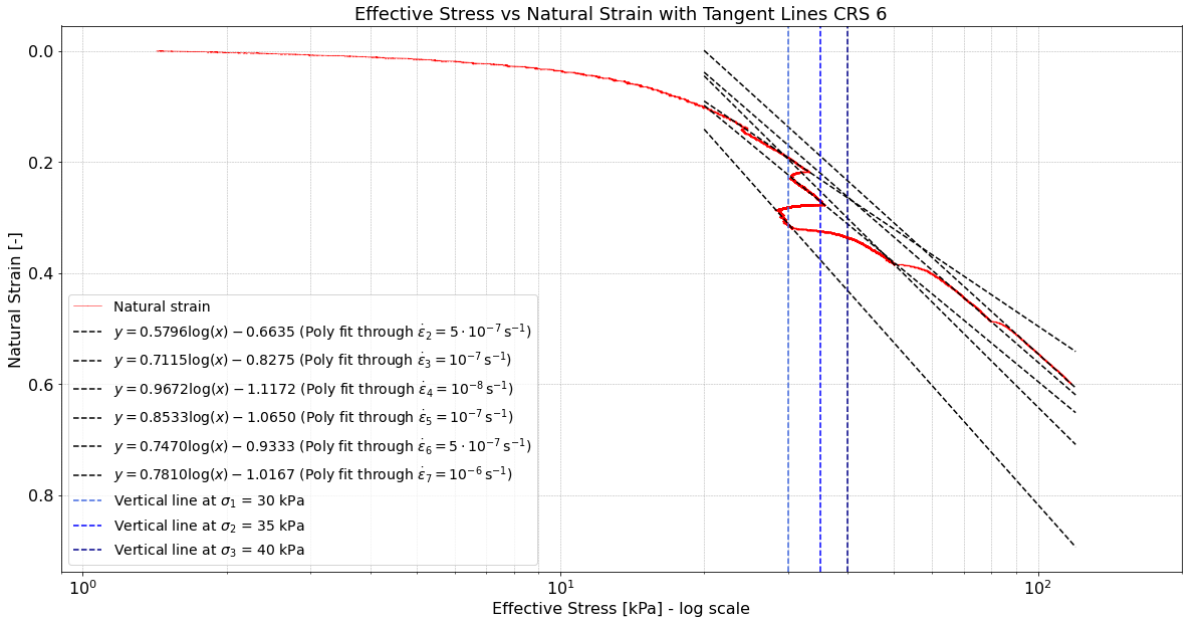

Figure 5.18: Evaluation of mutual distance between isotachs.

The strain rate controlled long-term CRS tests are performed according to the strain rate configuration as shown in Table 4.2. As a result of this, intermediate steps such as $\dot{\varepsilon}_6$ = 5·10^{-7} s^{-1} are present in the test results.

5.6.2 Calculated Isotach Spacing

Table 5.2 shows the calculated distances between different isotachs for CRS test 6. Note that no isotach is drawn through part of the effective stress vs. natural strain graph corresponding to a strain rate of $\dot{\varepsilon}_1 = 10^{-6}\ s^{-1}$. As is described in Section 5.4.2, this isotach has been omitted since the soil does not yet fully behave normally consolidated.

Step	*Strain rate [s^{-1}]*	*Distance at σ_1 = 30 kPa*	*Distance at σ_2 = 35 kPa*	*Distance at σ_3 = 40 kPa*
2	$5 \cdot 10^{-7}$	0.031	0.039	0.047
3	10^{-7}			
3	10^{-7}	0.088	0.105	0.120
4	10^{-8}			
4	10^{-8}	0.116	0.124	0.130
5	10^{-7}			
5	10^{-7}	0.025	0.032	0.039
6	$5 \cdot 10^{-7}$			
6	$5 \cdot 10^{-7}$	0.033	0.031	0.029
7	10^{-6}			

Table 5.2: Calculated mutual distances between isotachs of CRS Test 6.

The values given in Table 5.2 primarily serve to validate the concept of equidistant isotachs. The numerical value changes at different positions of the vertical line. This is to be expected since it was noted in Section 5.5 that the slope of the tangent lines through different isotachs is different for each drawn tangent line.

Table 5.2 underlines the observations made earlier in Section 5.4.2 where it was concluded that the trajectory of the tangent line through the lowest strain rate of $\dot{\varepsilon}_4 = 10^{-8}\ s^{-1}$ seems to be diverging compared to those corresponding to higher strain rates. From Figure 5.18 and Table 5.2 it is concluded that regarding CRS test 6, the mutual distance between different isotachs increases with decreasing strain rates. Similar results are found in the analysis of the other performed CRS tests. These results are shown in Annex 9.

5.7 Additional CRS Test Results

This section shows the results of the extra CRS tests. Analysis of the results generates reproduceable results compared to the five long-term CRS tests. A creep test in which the sample is allowed to creep for 16 days shows a decent degree of classical isotach behaviour. The slope of the tangent line through the isotach prior and after this creep phase differs thereby not fully complying with the hypothesized classical isotach behaviour. An extra CRS test is performed in which the applied displacement rate is rapidly changed. The results show a converging isotach corresponding to the lowest strain rate of $\dot{\varepsilon}_4 = 10^{-8}$ s^{-1}. This is at odds with the observed phenomena of the five long-term CRS tests.

5.7.1 Creep Test

The prime goal of the creep test is to investigate the isotach behaviour of the tested soil when the sample is allowed to creep. The strain rate before and after this creep phase is set equal. As a result of this, the soil behaviour before and after the creep phase should, in theory, behave on the same isotach. Namely the one corresponding to $\dot{\varepsilon}_1 = \dot{\varepsilon}_3 = 10^{-6}$ s^{-1}. To test this hypothesis, the sample is first loaded past its yield stress. After the sample is in normally consolidated state, the CRS apparatus is switched from displacement controlled to load controlled. The sample is then allowed to creep for a total of 16 days. Figure 5.19 illustrates this. After 16 days the loading mechanism is again switched from load controlled to displacement controlled as indicated by the dashed orange line in Figure 5.19.

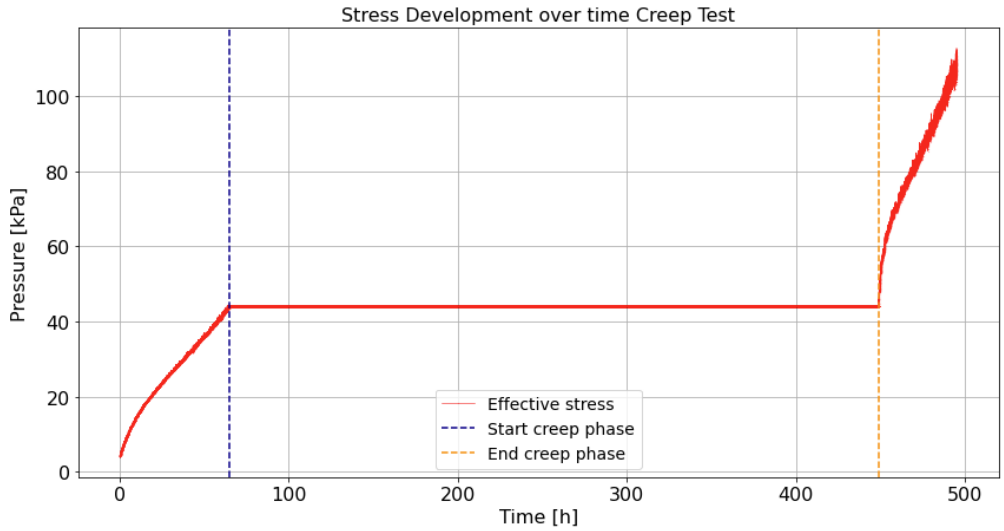

Figure 5.19: Effective tress development over time of creep test.

Isotach slopes

Figure 5.20 shows the effective stress vs. natural strain of the performed CRS creep test. Note that the creep phase is clearly visible. After completion of the creep phase, the sample is loaded again. The soil shows similar behaviour as in over-consolidated state until the sample is fully adjusted to the strain rate of $\dot{\varepsilon}_3 = 10^{-6}$ s^{-1} marked by a smooth transition to a new isotach. Moreover, the shape of the curvature after the creep phase is finished is similar as the transition from over-consolidated state to normally consolidated state. This is noticeable in Figure 5.20 by the smooth curvature after the creep phase. Note that the procedure followed to draw tangent lines is the same as described in Section 5.4.1.

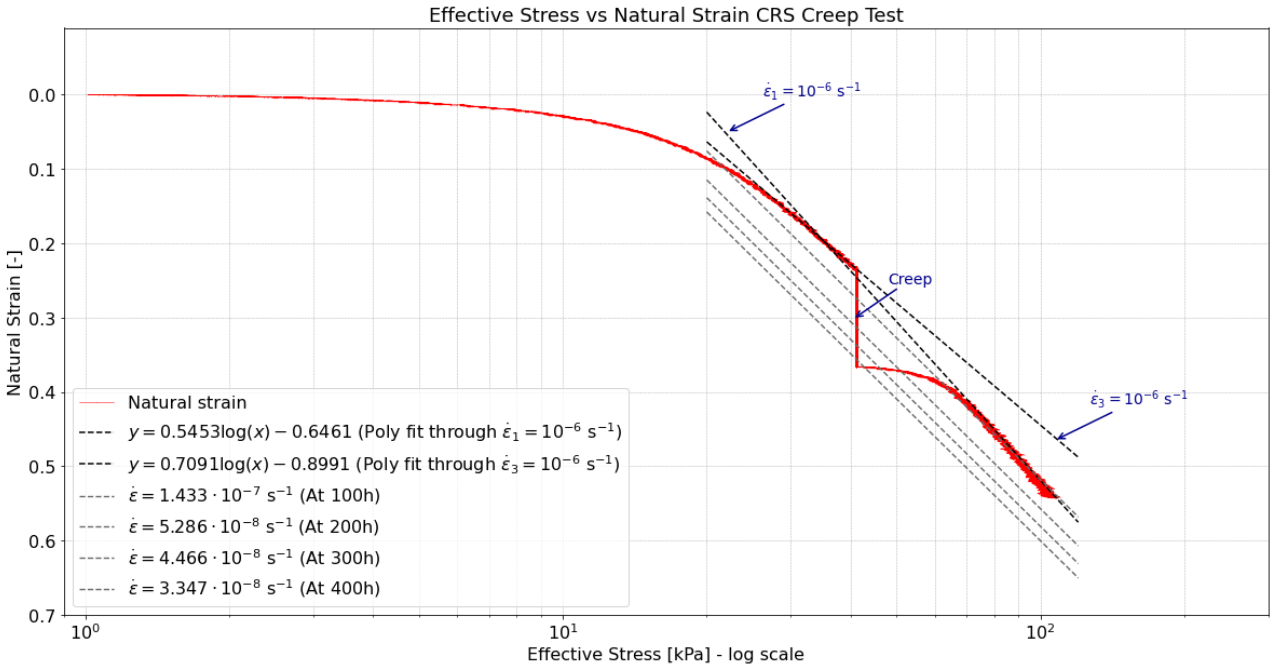

Figure 5.20: Effective stress vs. natural strain of CRS creep test. The grey dotted lines indicate the crossed isotachs during this creep phase.

Furthermore, it is observed how after the creep phase the sample does not completely get on the isotach prior to initiation of the creep phase. This is underlined by the difference in slope of the two drawn tangent lines. These tangent lines should, in theory, have the same slope in order to describe classical isotach behaviour.

In addition, note that the shape of the curvature after the creep phase is finished in similar to the over-consolidated part of the compression curve. This observation is in line with those of the five performed long-term CRS tests, described in Section 5.4.1. When the strain rate is increased, part of the compression curve is similar in shape until the sample is fully adjusted to this new strain rate. When the sample is completely adjusted to this new strain rate, the soil's state is on a new isotach. From this point on the curvature transforms into a straight line corresponding to the new strain rate. This observation is made by evaluating the five long-term CRS tests and is clearly visible in Figure 5.20 as well.

The results of the performed creep test are thus in line with the obtained results from the five long-term CRS tests. Both the shape of the compression curve, as well as the trajectory of the isotachs show similar results. It is of future interest to further investigate the influence of the duration of the creep phase on the isotach behaviour. A creep phase of 16 days resulted in - to some extend – classical isotach behaviour. The influence of longer and shorter creep stages on this isotach behaviour can be investigated in more detail in additional tests.

Mutual distance of isotachs
Figure 5.20 shows four of the isotachs that are crossed during the creep phase. Annex 11 described the procedure followed to estimate these different isotachs. From this it can clearly be observed how, as time progresses, the (creep)strain rate decreases. At the start of the creep phase the soil sample behaves on the isotach corresponding to $\dot{\varepsilon}_1 = 10^{-6}$ s^{-1}. When 100 hours have passed since the start of the test the strain rate has reduced to $\dot{\varepsilon} = 1.433 \cdot 10^{-7}$ s^{-1}.

Note how the mutual distance between different isotachs increases with a decrease in strain rate. This underlines the observation of increasing mutual distance with a decrease in strain rate of Section 5.6. The increasing mutual distance with decreasing strain rate is evaluate in more detail in Figure 5.21.

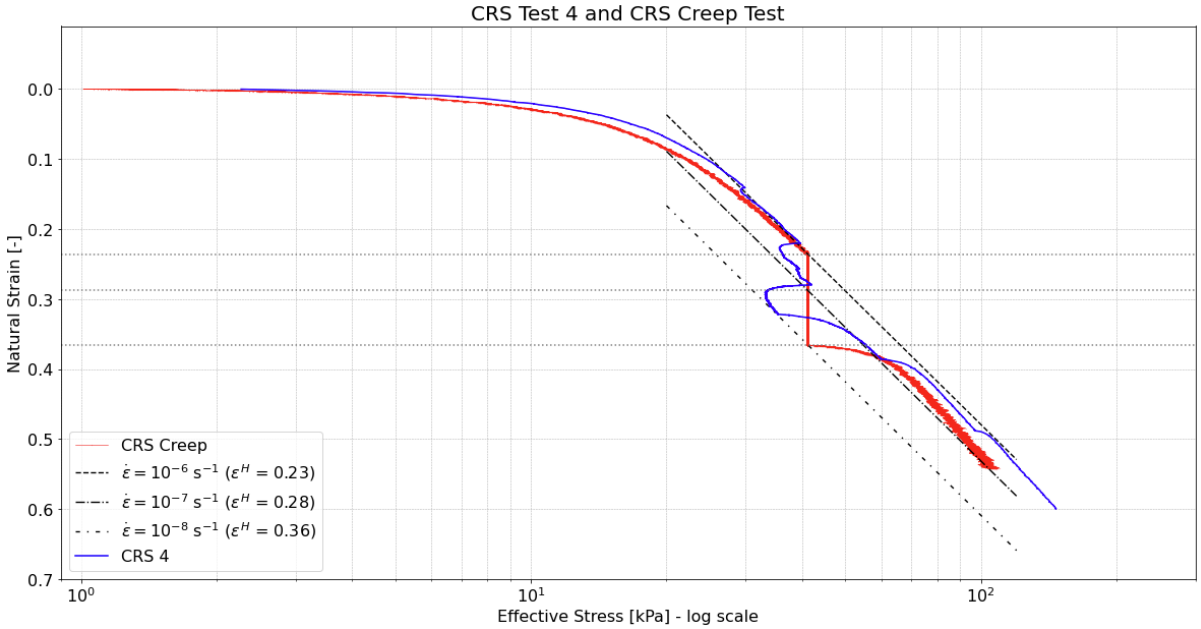

Figure 5.21: Effective stress vs. natural strain of CRS creep test. The grey dotted lines indicate the crossed isotachs during this creep phase.

The mutual distance between different isotachs is evaluated with one log 10 cycle different isotachs. Figure 5.21 shows the CRS creep test in red. The CRS creep test is comparable to step-changed CRS test 4. Both tests show a comparable pre-consolidation pressure and subsequently a similar transition from over-consolidated state to normally consolidated state. At the start of the creep phase the sample behaves corresponding to a strain rate of $\dot{\varepsilon}_1 = 10^{-6}$ s^{-1}. This point corresponds to a natural strain level of 0.23 as indicated in Figure 5.21. At this point the loading mechanism switches from displacement controlled to load controlled. As time progresses, and creep strains accumulate, the isotach corresponding to a strain rate of $\dot{\varepsilon} = 10^{-7}$ s^{-1} is crossed. This point corresponds to a natural strain level of 0.28. From this it is concluded that the difference in natural strain between $\dot{\varepsilon}_1 = 10^{-6}$ s^{-1} and $\dot{\varepsilon} = 10^{-7}$ s^{-1} is 0.05.

CRS 4 is used to evaluate the position of the isotach corresponding to a strain rate of $\dot{\varepsilon} = 10^{-8}$ s^{-1}. Observe how the $\dot{\varepsilon} = 10^{-8}$ s^{-1} isotach coincides with the CRS creep test approximately at the end of the creep phase. This point corresponds to a natural strain level of 0.36. As a result, the difference in natural strain between $\dot{\varepsilon}_1 = 10^{-7}$ s^{-1} and $\dot{\varepsilon} = 10^{-8}$ s^{-1} is 0.08. The mutual distance between different isotachs thus increases with decreasing strain rate. From this it is concluded that the results of the CRS Creep Test are similar to the results of the five step-changed CRS tests. In both cases does the mutual distance between different isotachs increase with decreasing strain rate.

5.7.2 Rapid Transition Test

The Rapid Transition Test is aimed at investigating the influence on isotach behaviour of intermediate steps when changing the strain rate is a CRS test. Five long-term CRS tests are performed where the strain rate is reduced from $\dot{\varepsilon}_1 = 10^{-6}$ s^{-1} to $\dot{\varepsilon}_4 = 10^{-8}$ s^{-1} with two intermediate steps. These intermediate steps are omitted in the rapid transition test. As a result of this, the strain rate reduces by a factor of 100 within minutes. After this lowest possible strain rate of $\dot{\varepsilon}_2 = 10^{-8}$ s^{-1} is applied for a total duration of 926 hours the strain rate is increased again by a factor 100 to $\dot{\varepsilon}_3 = 10^{-6}$ s^{-1}. Figure 5.22 shows the displacement over time. In here it is clearly visible how the strain rate is first (drastically) decreased and later increased again.

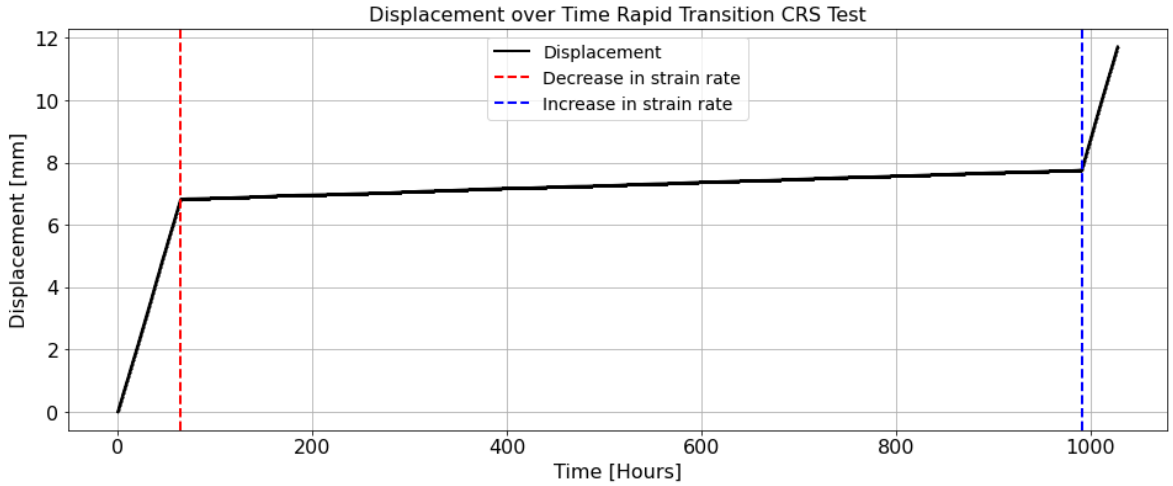

Figure 5.22: Displacement over time of Rapid Transition CRS test. Note the deceleration in strain rate (red) and the acceleration in strain rate (blue).

As can be seen in Figure 5.23, the strain rate is decreased after 64 hours. This reduction in strain rate results in a sharp decrease of effective stress. As time progresses, and the sample is compressed with a lower displacement rate, the effective stress gradually starts to increase again. These results are similar to those observed in the five long-term CRS test described in Section 5.5. During the final stage of testing, the excess generated pore pressure starts to increase again due to the reduced permeability as the sample is continued to be compressed.

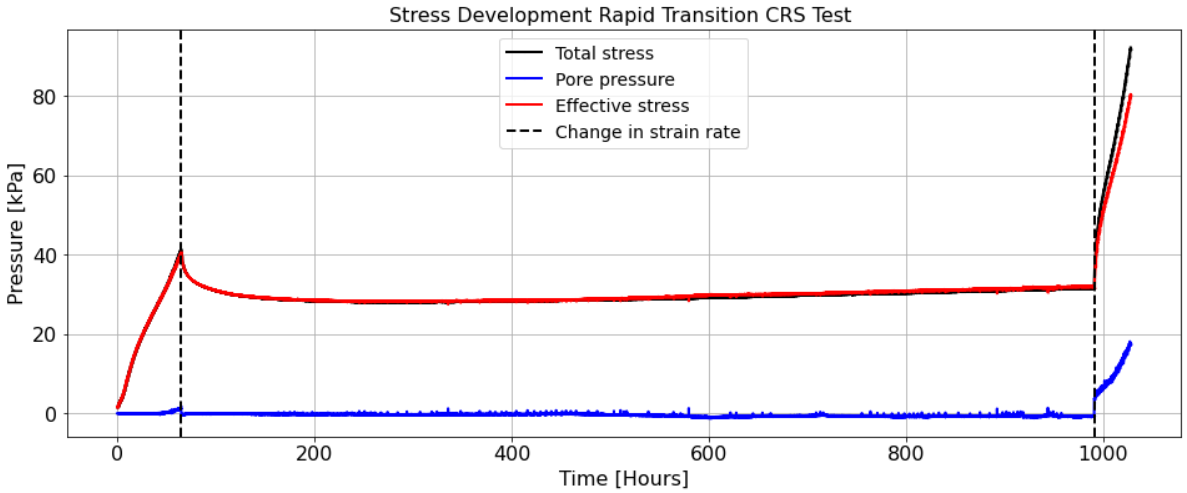

Figure 5.23: Stress development over time of CRS Rapid Transition Test.

Figure 5.24 shows the tangent lines through part of each isotach. Note that in order to construct these tangent lines the same procedure as described in Section 5.4.1 is followed. Observe how the slopes of the tangent lines through the isotach corresponding to a strain rate of $\dot{\varepsilon}_1 = \dot{\varepsilon}_3 = 10^{-6}$ s^{-1} is almost identical. From this it is concluded that after the strain rate is increased again from $\dot{\varepsilon}_2 = 10^{-8}$ s^{-1} to $\dot{\varepsilon}_3 = 10^{-6}$ s^{-1} the soil's state behaves corresponding to the same isotach. In this aspect the observation is in line with the concepts of the classical isotach framework.

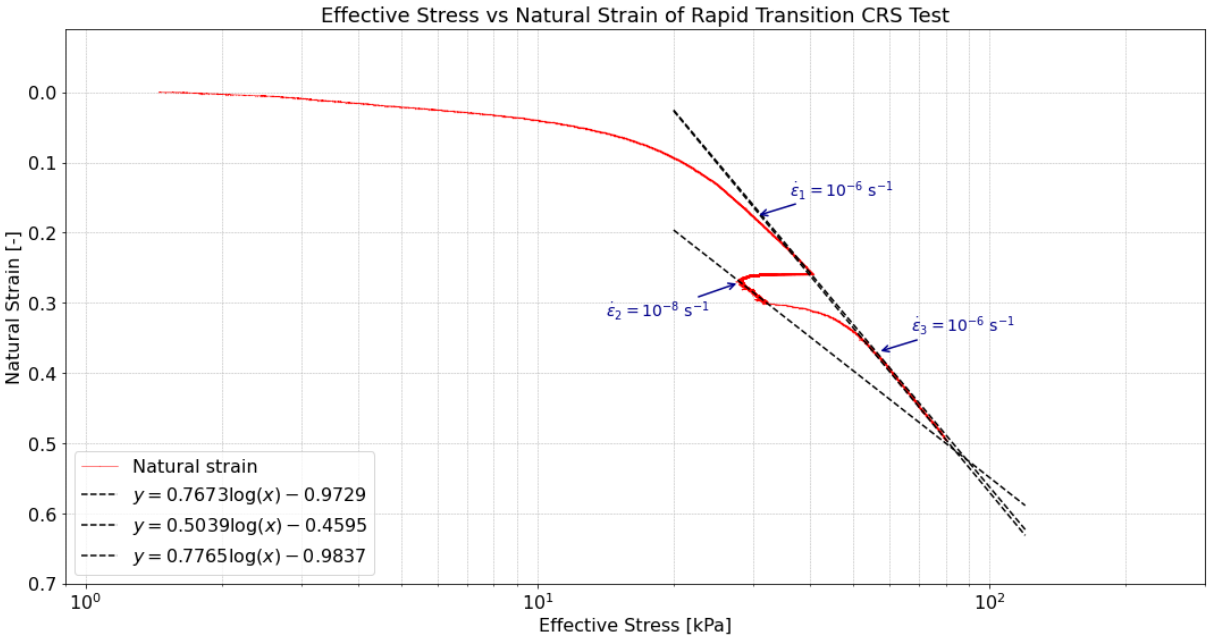

Figure 5.24: Effective stress vs. natural strain of CRS Rapid Transition Test.

However, the slope of the line through the isotach corresponding to a strain rate of $\dot{\varepsilon}_2 = 10^{-8}$ s^{-1} is substantially different compared to those of $\dot{\varepsilon}_1 = \dot{\varepsilon}_3 = 10^{-6}$ s^{-1}. This observation is similar to those made in Section 5.4. In here it was concluded that the slope of the tangent lines through the isotach of the lowest strain rate of $\dot{\varepsilon} = 10^{-8}$ s^{-1} diverges compared to those of higher strain rates. The results of the rapid transition test however show a converging tangent line. No physical explanation is found for this observed behaviour. It therefore is of future interest to repeat this test in order to increase the total number of test results and verify if similar results are found.

In addition, performing extra tests with an even larger change in strain rate might prove beneficial in evaluating the influence of a rapid decrease/increase in strain rate. This is important from a practical point of view since changes in loading conditions can cause a large change in strain rate as described in Section 5.2.3.

The transient behaviour around a change in strain rate is especially noticeable in the results of the rapid transition test. After decreasing the strain rate from $\dot{\varepsilon}_1 = 10^{-6}$ s^{-1} to $\dot{\varepsilon}_2 = 10^{-8}$ s^{-1}, approximately 200 hours are needed for the sample to adjust to this new strain rate. These observations are, again, in line with those made by evaluating the results of the five long-term CRS tests. In here it is observed how the time needed for the sample to adjust to a new strain rate is higher around lower strain rates.

5.8 Practical Consequences

This section describes the practical consequence of the results of the CRS tests. Diverging isotachs with decreasing strain rate can give rise to an accelerated creep rate with the logarithm of time. Tertiary compression can help explain this observation. Not accounting for this accelerated creep rate on logarithmic time can in practice lead to the underestimation of long-term expected settlement.

5.8.1 Creep Rate

Section 2.5.3 described how during a period of constant effective stress the soils state moves vertically down in the isotach framework. During this creep path as shown in for example Figure 2.16 different isotachs are crossed. As time progresses, when different isotachs are crossed, the corresponding stain rates decrease logarithmically. The CRS creep test described in Section 5.7 showed this processes of crossing different isotachs as well. As described in Section 2.5, the classical isotach framework assumes parallel equidistant isotachs. Consequently, the compression rate is assumed to be linear on logarithmic time scale. In case of the propositions of the classical isotach framework creep would continue indefinitely. On logarithmic timescale this results in a linear secondary compression rate over time. This is visualised by the continuous black line in Figure 5.25.

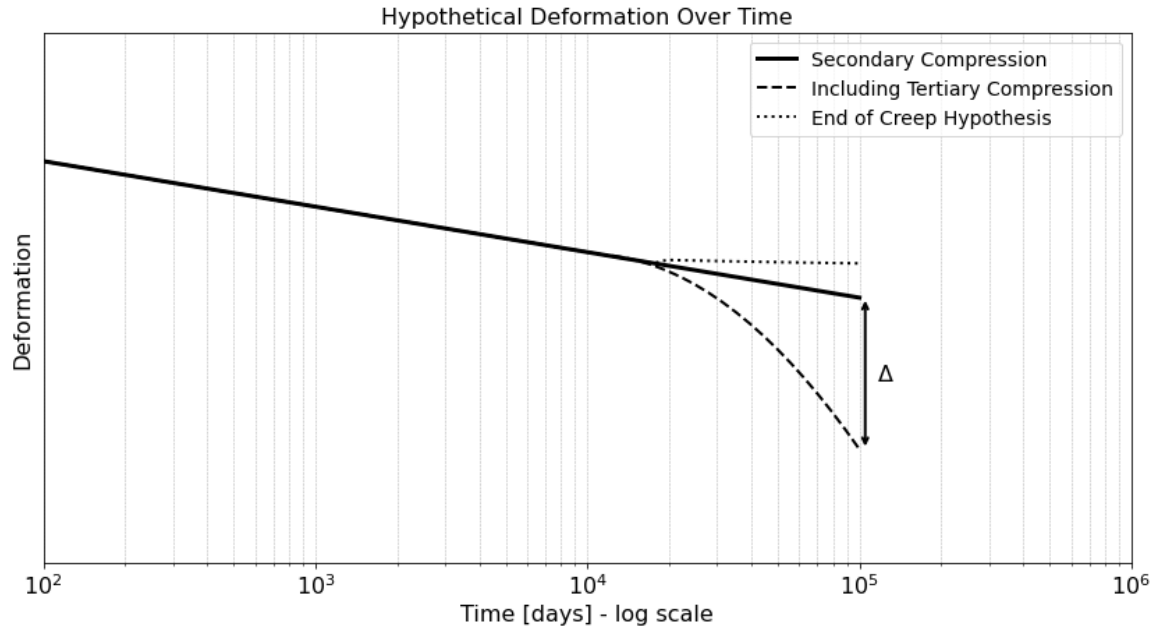

Figure 5.25: Hypothetical development of creep over time.

Different researchers (Imai et al., 2003), (Watabe and Leroueil, 2015) hypothesized the existence of an infinitesimal strain rate resulting in creep eventually coming to an end. As a result of this the compression curve would eventually become horizontal as shown by the black dotted line in Figure 5.25. In this case, as time progresses, no additional (creep) strains would be accumulated. This would violate the fundamental concepts of the classical isotach framework because an and of creep isotach would mean a reduced mutual distance between different isotachs with a decrease in strain rate. This is hypothesized based on studies performed on clay (Watabe and Leroueil, 2015).

5.8.2 Tertiary Compression

The results of the five long-term CRS tests on peat showed opposite results. The test results showed increased divergence of isotachs with a decrease in strain rate. Moreover, isotachs corresponding to higher strain rates showed a higher degree of parallelism and equal mutual distance compared to isotachs corresponding to lower strain rates. Under a constant load as time progresses, and isotachs corresponding to lower strain rates are crossed, the mutual distance between these isotachs could hypothetically continue to increase. This increased mutual distance between different isotachs results in non-linear compression over time on logarithmic scale. This inherently would give rise to a changing compression rate over time. This is illustrated by the black dotted line in Figure 5.25. The existence of this non-linear compression curve would result in tertiary compression. Note that the existence of tertiary compression in peat is noted by different researchers (Edil, 1979), (Dhowian and Edil, 1980), (Den Haan and Edil, 1994).

Tertiary compression therefore provides a possible explanation of the observed divergent isotachs with a decreasing strain rate noted in the five long-term CRS tests and the CRS creep test. This makes implementation of the classical isotach framework only valid for describing the compression behaviour of peat corresponding to strain rates larger than 10^{-7} s^{-1}. Chapter 3 showed however that field strain rates are generally lower than 10^{-7} s^{-1} thereby questioning the validity of the classical isotach framework in describing the compression behaviour of field projects built in peat. It is of interest to analyse the capability of different constitutive models in simulating this increased divergence of isotachs with decreasing strain rate. The next chapter evaluates the simulation process of the performed strain rate controlled CRS tests.

5.9 Conclusions on CRS Tests

This chapter aimed to validate the classical isotach framework used to describe the compression behaviour of Zegveld peat. The classical isotach framework of parallel equidistant isotachs, as implemented in the Netherlands, is built on three fundamental concepts as described in Section 2.6.

Based on the performed strain rate controlled CRS tests it is concluded that:

- The difference between target strain rate and recorded strain rate in the performed CRS tests is negligible. The recorded ratio of excess pore pressure over total stress of 2% does not exceed the threshold of 15% described in NEN-8992:2024. From this it is concluded that the evaluated strain rates, and subsequent results of the CRS tests, can be used to conclude on the validity of the classical isotach framework.
- Different isotachs can clearly be identified in each of the five tests. Moreover, all five tests show similar results. Minor differences are attributed to the heterogeneity of the peat.
- Changes in applied rate of displacement result in movement to a new isotach and thus visualisation of unique compression curves. Parts of different isotachs can clearly be identified when the results are plotted on natural strain versus the logarithm of effective stress. Subsequently, the constitutive behaviour of the tested soil samples is strain rate dependent. The first concept of the classical isotach framework is thus met.
- Only in the strain rate regime of $\dot{\varepsilon} = 10^{-6}$ s^{-1} - 10^{-7} s^{-1} do the trajectories of parts of different isotachs show a high degree of parallelism. A calculated coefficient of variability of the slopes of different isotachs of 0.17 underlines this.
- The degree of parallelism is shown to decrease with a decrease in strain rate. The second fundamental concept of the classical isotach framework is therefore not met below a strain rate of $\dot{\varepsilon} < 10^{-7}$ s^{-1}. This observation is made in all five long-term CRS tests. In practice this divergent behaviour would result in stress-dependency of the creep parameter in case of strain rates lower than 10^{-7} s^{-1}.
- The mutual distance between different isotachs is shown to increase with decreasing strain rate. The CRS creep test underlined this observation. The third concept of the classical isotach is therefore not met below a strain rate of $\dot{\varepsilon} < 10^{-7}$ s^{-1}. This observation is made in all five long-term tests. In practice this increased spacing results in a changing creep rate with the logarithm of time.
- The observed increase in mutual distance between different isotachs with decreasing strain rates result in an increased creep rate with the logarithm of time. This can be explained by tertiary compression which is known to occur in peat.
- Transient behaviour is observed around a change in strain rate. Time is needed for the soil to fully adjust to the new strain rate. The time needed for the sample to fully move to the isotach corresponding to the new strain rate increases with a decrease in strain rate. No physical explanation is found for this observed inverse proportionality.
- CRS laboratory test are generally performed with a constant rate of displacement. The results of the observed transient behaviour around a change in strain rate are therefore assumed to be minimal for conventional CRS laboratory testing. This is however not the case in changing loading conditions in field projects.
- The time needed for the soil to fully move to a new isotach increases with decreasing strain rate. Field strain rates are shown to be lower than those applied during laboratory testing. Consequently, due to changing loading conditions in practice, the time needed for the soils state to fully move to the isotach corresponding to the new strain rate can be substantial. Not accounting for this interim period between different isotachs can result in invalid parameter determination in field conditions since the soil does not yet fully behave corresponding to a new isotach.

The concepts of the classical isotach framework proved to be valid for strain rates in the range $\dot{\varepsilon} = 10^{-7}$ s^{-1} – 10^{-6} s^{-1}. This strain rate regime is however not comparable to field conditions. The validity of the classical isotach framework in describing the compression behaviour of Zegveld peat is therefore questioned regarding field conditions.

6. Simulation of CRS data

This chapter describes the simulation process of the step-changed CRS tests. The aim of these simulations is multifaceted. The simulations partly serve as validation of the capability of common constitutive models of describing step-changed CRS tests. This is important since diverging isotachs result in different constitutive behaviour with a change in strain rate. It proves beneficial to captivate how this is incorporated in existing constitutive models. In addition, simulating the performed CRS tests helps in mathematically contextualizing the temporal behaviour observed around a change in strain rate. The constitutive models used for simulation are described in Section 2.7.

6.1 NEN-Bjerrum Isotach Model

The NEN-Bjerrum isotach model is built on the concepts of the classical isotach framework. As a result, the model is unable to simulate diverging isotachs. The model is however well equipped in capturing changes in different strain rates.

6.1.1 NEN-Bjerrum Isotach Model Simulation

The NEN-Bjerrum isotach model serves as an important internationally recognized settlement model. The model expresses reduction of pore volume in terms of linear strain, as described in Section 2.7.1. CRS test number 6 is simulated using the initial parameters of the NEN-Bjerrum-isotach model as shown in Table 6.1. The parameter set of Table 6.1 is optimised in Section 6.1.2 to evaluate a possible better fit between the NEN-Bjerrum simulation and the CRS data of test 6. The coefficient of determination (R^2) is used to evaluate the goodness of fit between the actual CRS data and the simulation.

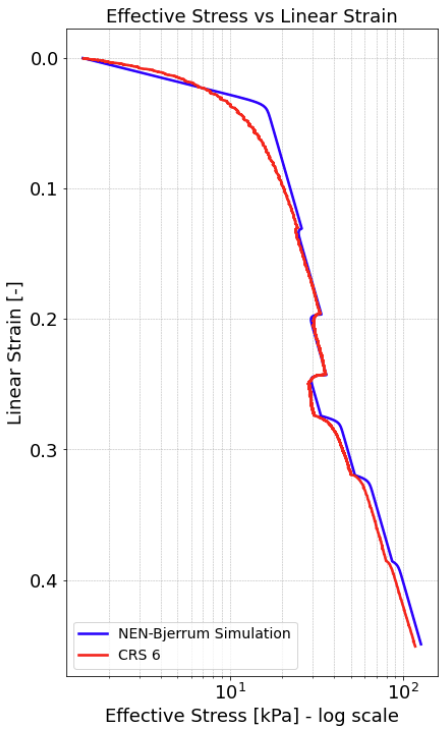

Figure 6.1: NEN-Bjerrum Isotach simulation of CRS Tets 6.

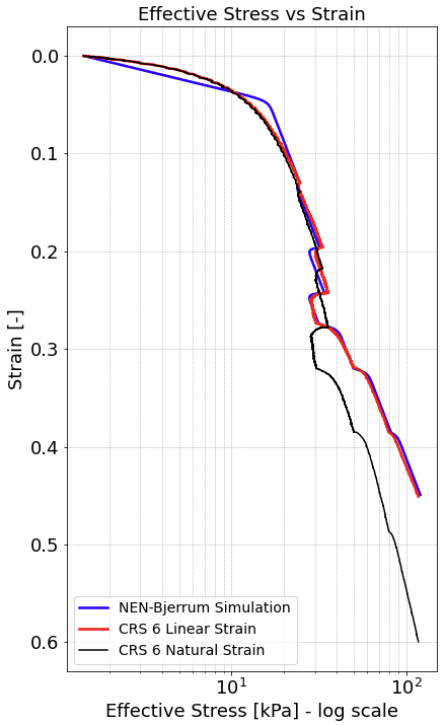

Figure 6.2: Strain comparison with NEN-Bjerrum Isotach model.

As can be seen in Figure 6.1, the NEN-Bjerrum isotach model is able to describe the compression behaviour of CRS test number 6 with a decent degree of accuracy. In this simulation, the coefficient of determination is calculated to be $R^2 = 0.74$. Note that the actual laboratory data of CRS test number 6 is plotted in terms of linear strain instead of natural strain. Evidently, the test results can be simulated quite well using the NEN-Bjerrum model.

Parameter	*Symbol*	*Value*
Recompression Ratio	RR	0.033
Compression Ratio	CR	0.463
Secular strain rate coefficient	C_α	0.046
Reference time	τ_0	24 h

Table 6.1: Initial parameters used in NEN-Bjerrum isotach simulation of CRS 6.

Den Haan et al., (2004) describe how above a strain level of 40-50% using natural strain instead of linear strain becomes preferable. Given the results of Figure 6.1 this would require changing the strain notation used. As can be seen in Figure 6.2, the difference between natural- and linear strain becomes noticeable in the last stages of the test. Given the large strain this would make the NEN-Bjerrum less suited for describing the compression behaviour of this part of the test.

6.1.2 Optimisation of NEN-Bjerrum Parameters

To find the optimal parameter set, the Limited-memory Broyden–Fletcher–Goldfarb–Shanno with Box constraints (L-BFGS-B) method is used (Nayak, 2020). This method limits the required memory required to find the optimal fit between the simulation and the actual laboratory data. In addition, the method allows implementation of constraints on certain variables. This is important since the optimal parameters still need to be physically possible. Table 6.2 shows the bounds used in the optimisation process. Annex 14 shows the simulation of the other step-changed CRS tests.

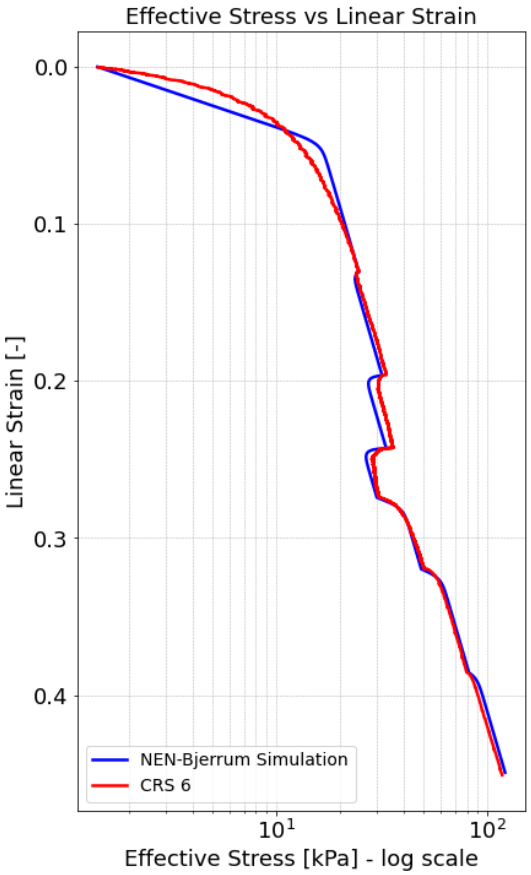

Figure 6.3: NEN-Bjerrum isotach simulation of CRS 6 using optimised parameter set.

Parameter	*Lowerbound*	*Upperbound*
RR	0.01	0.1
CR	0.1	0.7
C_α	0.001	0.1

Table 6.2: Constraints used to find the optimal parameter set of CRS 6.

CRS test number 6 is optimised using the parameter set of Table 6.3. Figure 6.3 shows that the NEN-Bjerrum model is able to accurately simulate the laboratory data of CRS 6. A coefficient of determination of R^2 = 0.85 underlines this observation.

Parameter	*Symbol*	*Value*
Recompression Ratio	RR	0.045
Compression Ratio	CR	0.463
Secular strain rate coefficient	C_α	0.052
Reference time	τ_0	24 h

Table 6.3: Optimised parameters used in NEN-Bjerrum isotach simulation of CRS 6.

6.2 abc-Isotach Model

This section shows simulation of CRS laboratory data using the abc-isotach model. The model is able to capture changes in applied displacement rate. Transient behaviour around a change in strain rate is captured to a lesser extent. In this aspect findings are similar to those made by simulation using the NEN-Bjerrum isotach model. The model is unable to simulate diverging isotachs observed in the step-changed CRS tests described in Section 5.5.

6.2.1 abc-Isotach Model Simulation

Figure 6.4 shows the result of the abc-isotach-model simulation compared to the original CRS 6 data. In this simulation the abc-parameters as derived in Annex 4 are used. Note that the abc-isotach-model is unable to capture the smooth transition from over-consolidated state to normally consolidated state. This is however inherent to using the abc-isotach-model. From Figure 6.4 it can be concluded that the model is decently able to simulate the applied changes in strain rate as indicated by the enlarged view. By definition, the abc-isotach-model shows parallel isotachs with equal mutual distance between them.

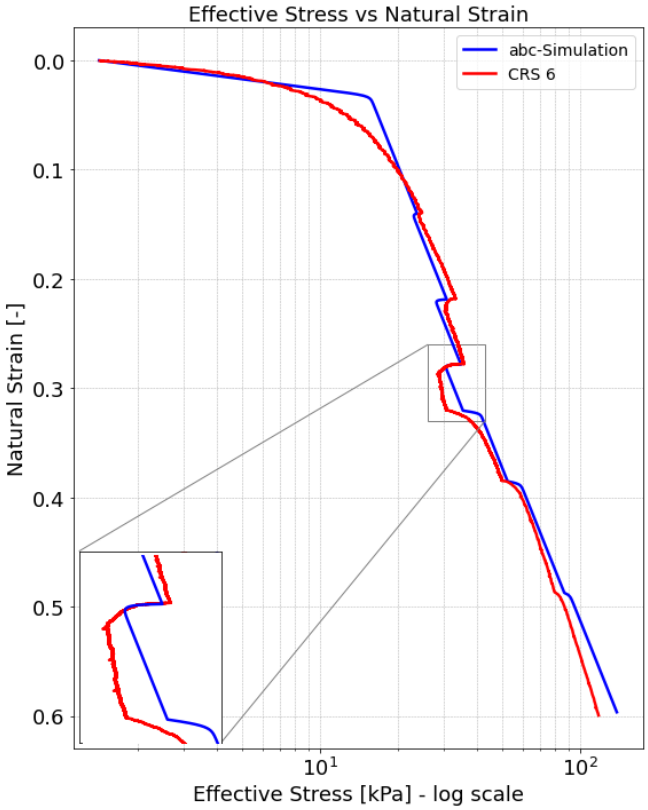

Figure 6.4: abc-simulation of CRS Test 6.

CRS test number 6 is simulated using the parameters of the abc-isotach-model of Table 6.4. Using this parameter set, the abc-isotach simulation under-estimates the effective stress level during the first three loading steps. The model then continues to over-estimate the effective stress level of the last three loading steps. The calculated coefficient of determination between the actual laboratory data and the abc-simulation in this case in $R^2 = 0.72$.

Parameter	*Symbol*	*Value*
Direct compression coefficient	a	0.014
Secular compression coefficient	b	0.263
Secular strain rate coefficient	c	0.0167
Reference time	τ_0	24 h

Table 6.4: Initial parameters of abc-simulation of CRS Test 6.

By looking at the results in Figure 6.4 it is clear that the abc-model is based on the classical isotach framework. Each loading step in the simulation results in parallel isotachs with equal mutual distance. Changes in strain rate lead to jump to a new isotach until the strain rate is changed again.

6.2.2 Optimization

Using the parameters set as derived in Annex 4, the abc-isotach model is able to provide a decent simulation of the performed CRS test 6. A better fit is achievable using a different parameter set. The method described in Section 6.1.2 is used to find the optimal parameter set. In order to determine the quality of the simulation, the coefficient of determination (R^2) between the actual CRS 6 data and the simulation is used. The constraints of Table 6.5 are used to find the optimal parameter set;

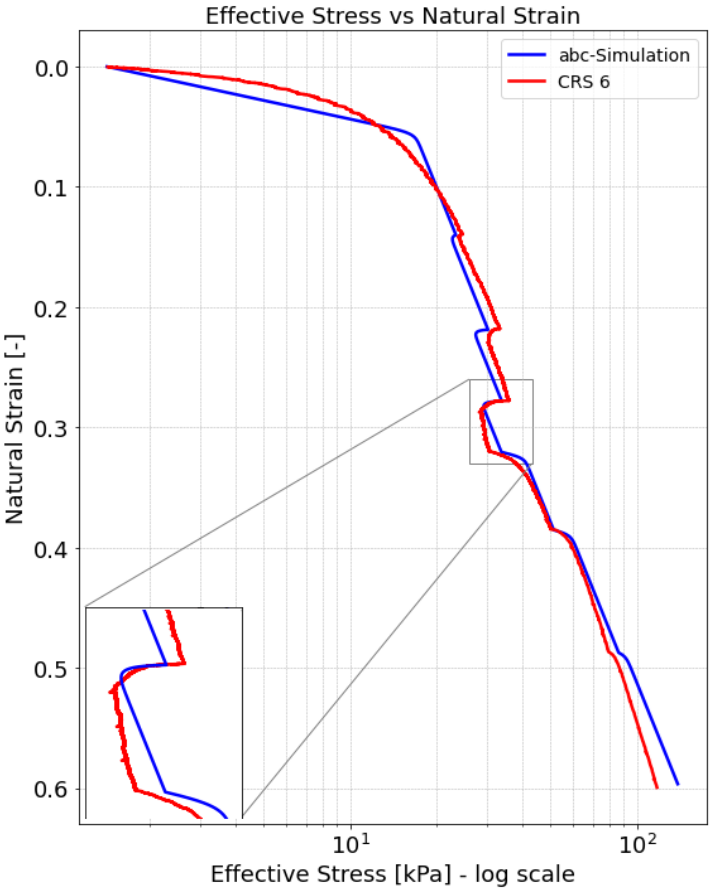

Figure 6.5: Optimised abc simulation of CRS Test 6.

Parameter	*Lowerbound*	*Upperbound*
a	0.01	0.1
b	0.1	0.4
c	0.001	0.1

Table 6.5: Constraints used to find the optimal parameter set of CRS 6.

As can be seen in Figure 6.5, a better fit resulting in a coefficient of determination of R^2 = 0.74 can be obtained using the optimized parameters as shown in Table 6.6.

Parameter	*Symbol*	*Value*
Direct compression coefficient	a	0.023
Secular compression coefficient	b	0.261
Secular strain rate coefficient	c	0.019
Reference time	τ_0	24 h

Table 6.6: Optimised parameters used in NEN-Bjerrum isotach simulation of CRS 6.

Note that the optimized parameters are very close to the parameter derived in Annex 4. Using this optimized parameter set, the abc-model simulation is less able to capture the over-consolidated state of the soil. However, the transient effects around a change in strain rate is captured with more accuracy compared to the initial parameter set as shown in Section 6.2.1. This is achieved by a higher value of the creep parameter and an increased direct compression coefficient as shown in Table 6.6.

6.3 Soft Soil Creep Model

This section demonstrates how the soft soil creep model is able to simulate the step changed CRS tests accurately. The model is able to simulate transient behaviour around a change in strain rate well. In addition, the SSC-model is able to simulate diverging isotachs with a decrease in strain rate. This makes the SSC-model better in describing the CRS laboratory test results than the NEN-Bjerrum isotach model and the abc-isotach model, especially at low strain rates.

6.3.1 SSC Simulation

Simulation of the performed CRS tests using the soil test environment of Plaxis 2D requires the input of strain and duration. The steps as shown in Table 4.2 are used as input for the simulation, as shown in Table 6.7. Figure 6.6 shows the result of the SSC-model simulation compared to the original CRS 6 data.

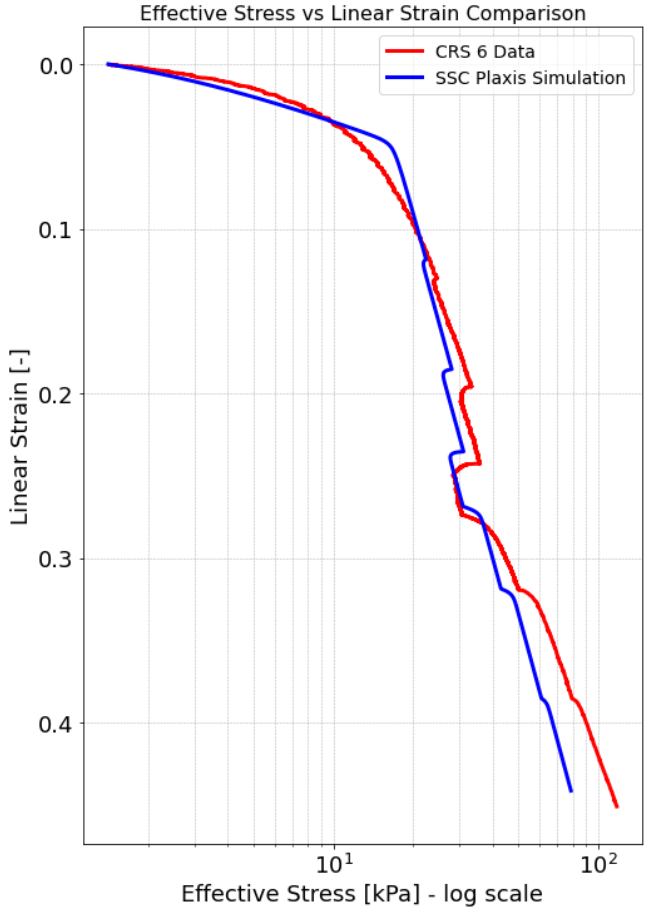

Figure 6.6: SSC-Model simulation of CRS Test 6 using the initial parameter set.

	Duration [day]	Strain inc. [%]	Steps
1	1.543	-13.33	100
2	1.543	-6.667	100
3	5.787	-5.000	100
4	38.59	-3.333	100
5	5.787	-5.000	100
6	1.543	-6.667	100
7	0.7717	-6.667	100

Table 6.7: Input strain rate configuration.

CRS test number 6 is initially simulated using the parameters of the SSC model as shown in Table 6.8.

Parameter	*Symbol*	*Value*
Modified swelling index	κ^*	0.028
Modified compression index	λ^*	0.263
Modified creep index	μ^*	0.0167
Poisson ratio	υ	0.15
Cohesion	c	0 kPa
Effective friction angle	φ'	40°
Dilatancy angle	ψ	5°

Table 6.8: Initial parameter set of SSC-Model simulation.

As can be seen, the SSC-model is able to describe the applied changes in strain rate. A shift in effective stress after the strain rate is changed is clearly visible. Using this parameter set, calculation of the coefficient of determination between the actual CRS laboratory data and the SSC-simulation yields R^2=0.70. Furthermore, by looking at the results in Figure 6.6 it is evident that the SSC-model is based on the concepts of the isotach framework. This is concluded by observing that a unique combination of strain, effective stress and strain rate exists for each loading step in the simulation. Changes in strain rate lead to jump to a new isotach until the strain rate is changed again.

The SSC-simulation under-estimates the effective stress level during the first three loading steps. The simulation is able to accurately model the lowest strain rate of $\dot{\varepsilon}_4 = 10^{-8}\,s^{-1}$. The model then continues to under-estimate the effective stress level of the last three loading steps. From this it is concluded that the initial value of the modified compression index (λ^*) as shown in Table 6.8 is too high.

6.3.2 Optimized parameters

Figure 6.7 shows that a lower value of the modified compression index leads to a more accurate simulation of the CRS test results. In this case the parameters are iteratively optimized in order to fit the actual CRS data as good as possible. Using this optimized parameter set, calculation of the coefficient of determination between the actual CRS laboratory data and the SSC-simulation yields R^2=0.95. This high coefficient of determination underlines the excellent fit obtained using this optimized parameter set. The simulation is thus able to accurately model the CRS test data. The simulation over-estimates the pre-consolidation pressure. Using this parameter set the model is able to accurately simulate the applied changes in strain rate. Furthermore it can be conclude that the SSC-model in this case shows parallel isotachs, with equal distance between them.

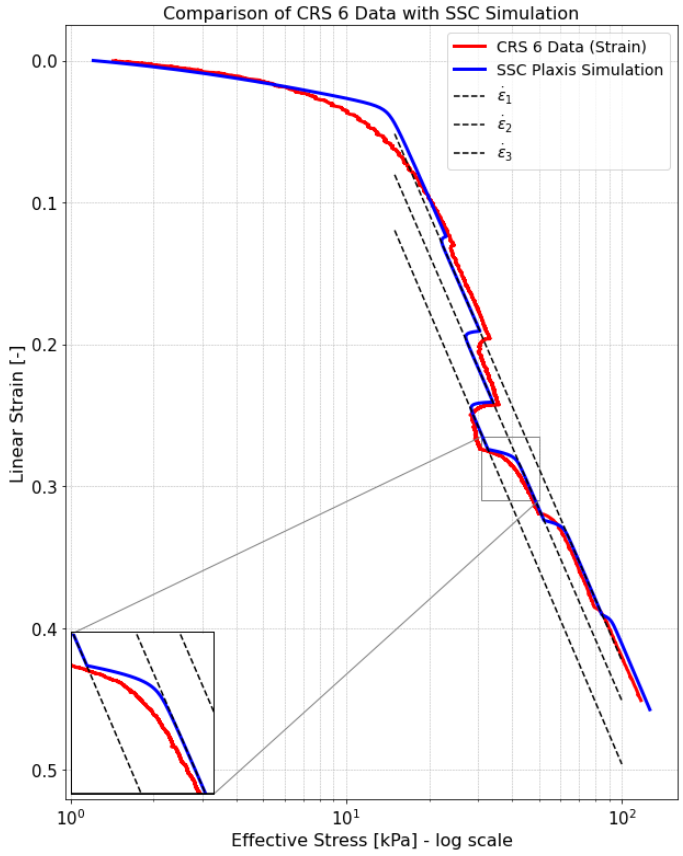

Figure 6.7: Optimised SSC-Model simulation of CRS test 6.

	Duration [day]	Strain inc. [%]	Steps
1	1.543	-13.33	100
2	1.543	-6.667	100
3	5.787	-5.000	100
4	38.59	-3.333	100
5	5.787	-5.000	100
6	1.543	-6.667	100
7	0.7717	-6.667	100

Table 6.9: Input strain rate configuration.

CRS test number 6 is simulated using the optimized parameters of the SSC-model as shown in Table 6.10. Note that the derived SSC-model parameters are already close to the optimal parameters. Furthermore, it is concluded that the SSC-model is able to accurately model the transient effects due to a change in strain rate. The next section evaluates the influence of the compression parameters of the SSC-model on this transient behaviour and the subsequent trajectories of different isotachs.

Parameter	*Symbol*	*Value*
Modified swelling index	κ^*	0.020
Modified compression index	λ^*	0.200
Modified creep index	μ^*	0.018
Poisson ratio	υ	0.150
Cohesion	c	0 kPa
Effective friction angle	φ'	40°
Dilatancy angle	ψ	5°

Table 6.10: Optimised parameter set of SSC-Model simulation of CRS 6.

6.3.3 Parameter Influence

modified compression index

The modified compression index (λ^*) and the modified swelling index (κ^*) are of influence on the slope of the virgin compression curve and the unloading/reloading curve respectively. As demonstrated in Figure 6.8, an increase of the compression index results in a more inclined stress-strain response. In this example, all the model parameters as shown in Section 6.3.1 are kept unchanged. The modified compression index (λ^*) is however increased as shown in Table 6.11.

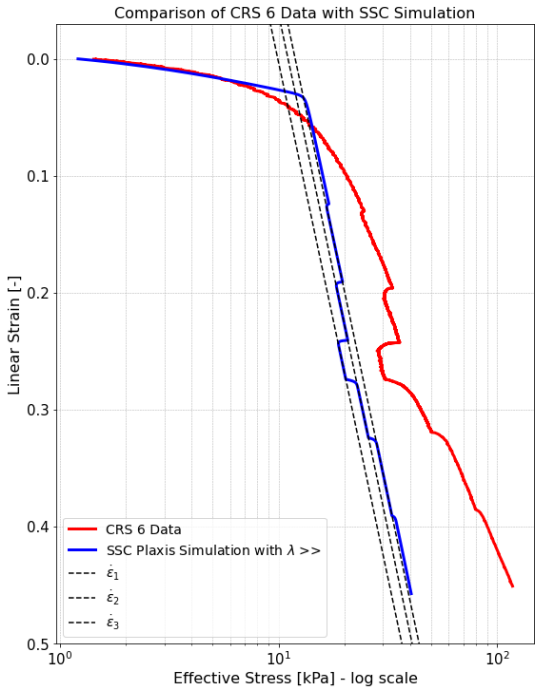

Figure 6.8: SSC simulation with increased modified compression coefficient, λ.*

Parameter	*Symbol*	*Value*
Modified swelling index	κ^*	0.020
Modified compression index	λ^*	0.400
Modified creep index	μ^*	0.018
Poisson ratio	υ	0.150
Cohesion	c	0 kPa
Effective friction angle	φ'	40°
Dilatancy angle	ψ	5°

Table 6.11: Parameter set used with increased λ.*

The doubling of(λ^*) results in a softer response of the soil. This becomes clear by observing that for a given strain level the effective stress response of the soil is lower compared to the actual CRS 6 data. In addition, it can be concluded that by changing the modified compression index the model still describes a unique relationship between strain, effective stress and strain rate. This is indicated in Figure 6.8 by the parallel dotted black lines, each corresponding to a different isotach. The modified compression index seems of little influence on the transient behaviour around a change of strain rate. In this case the change in strain level needed for the sample to adjust to a new strain rate is independent of the strain rate.

Table 6.12 shows the functions of the tangent lines through different isotachs as visualised in Figure 6.8. Note that the slope of the different tangent lines in this case are identical resulting in parallel isotachs.

Isotach	*Tangent line*
$\dot{\varepsilon}_1=5\cdot10^{-7}s^{-1}$	$y = 0.881 \cdot \log_{10}(x) - 0.949$
$\dot{\varepsilon}_2=10^{-7}s^{-1}$	$y = 0.881 \cdot \log_{10}(x) - 0.919$
$\dot{\varepsilon}_3=10^{-8}s^{-1}$	$y = 0.881 \cdot \log_{10}(x) - 0.878$

Table 6.12: Tangent line functions of Figure 91 indicate parallel isotachs.

Modified swelling index

An increase of the modified swelling (κ^*) index results in a softer response of the soil as well. This is demonstrated in Figure 6.9. In this example, all the model parameters as shown in Section 6.3.1 are kept unchanged. The modified swelling index (κ^*) is however increased as shown in Table 6.13.

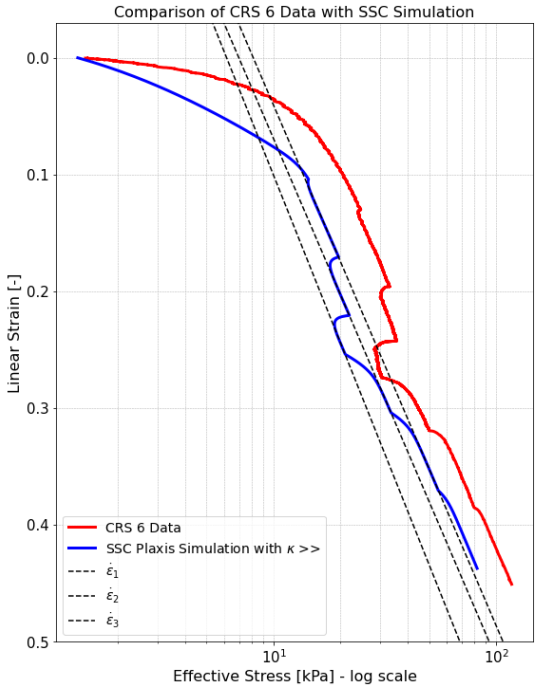

Figure 6.9: SSC simulation with increased modified compression coefficient, κ.*

Parameter	*Symbol*	*Value*
Modified swelling index	κ^*	0.06
Modified compression index	λ^*	0.2
Modified creep index	μ^*	0.018
Poisson ratio	υ	0.15
Cohesion	c	0 kPa
Effective friction angle	φ'	40°
Dilatancy angle	ψ	5°

Table 6.13: Parameters with increased κ.*

In this example, the model is still able to describe classical isotach behaviour. This is concluded by observing close to parallel lines corresponding to different strain rates as shown by the slopes in Table 6.14. In addition, the model is better able to capture the smooth transition to a higher strain rate. This is to be expected since the modified swelling index governs the slope of the unloading/reloading curve. An increase in strain rate effectively shows similar constitutive behaviour as a pure reloading of a soil sample. Note that in these examples the SSC-model simulates close to parallel isotachs. In case of an increased swelling index the isotach through the lowest strain rate of $\dot{\varepsilon}_4 = 10^{-8}\,s^{-1}$ diverges by a small margin compared to those through higher strain rates as show in Table 6.14.

Isotach	*Tangent line*
$\dot{\varepsilon}_1 = 5 \cdot 10^{-7} s^{-1}$	$y = 0.445 \cdot \log_{10}(x) - 0.404$
$\dot{\varepsilon}_2 = 10^{-7} s^{-1}$	$y = 0.444 \cdot \log_{10}(x) - 0.375$
$\dot{\varepsilon}_3 = 10^{-8} s^{-1}$	$y = 0.477 \cdot \log_{10}(x) - 0.376$

Table 6.14: Tangent line functions of Figure 6.9 indicate close to parallel isotachs.

Modified swelling index
Figure 6.10 shows an increase of the modified creep index (μ^*). In this example, all the model parameters as shown in Section 6.3.1 are kept unchanged. The modified swelling index (μ^*) is however increased as shown in Table 6.15.

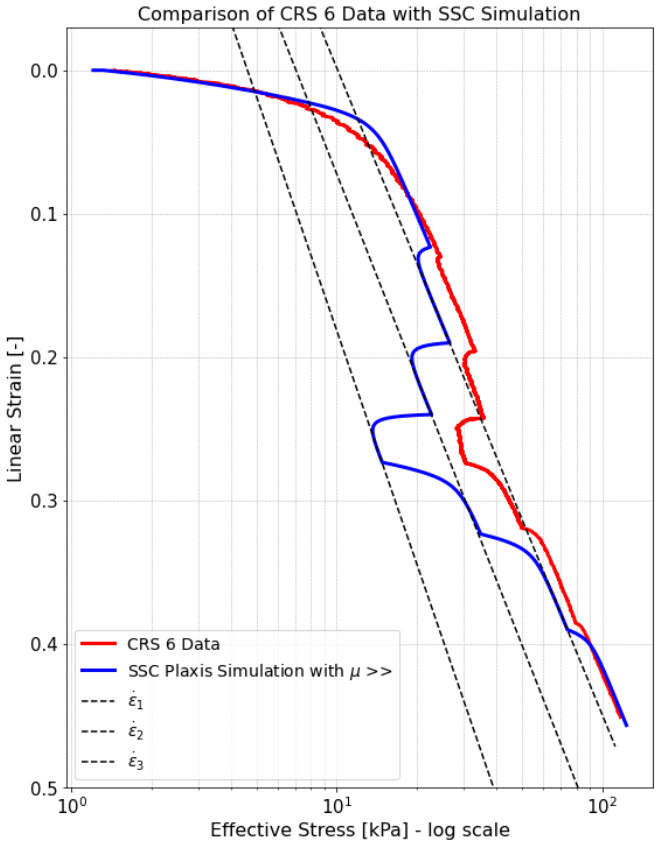

Figure 6.10: SSC simulation with increased modified creep index.

Parameter	*Symbol*	*Value*
Modified swelling index	κ^*	0.02
Modified compression index	λ^*	0.2
Modified creep index	μ^*	0.05
Poisson ratio	υ	0.15
Cohesion	c	0 kPa
Effective friction angle	φ'	40°
Dilatancy angle	ψ	5°

Table 6.15: Parameter set used with increased μ.*

In this example the model is (still) able to accurately capture the over-consolidated part of the compression curve and the slope of the virgin compression curve since the compression index (λ^*) and the swelling index (κ^*) are unchanged. The simulation does however exaggerate the shift in effective stress due to a change in strain rate. The simulation shows increased transient effects due to a change in strain rate. In addition, Figure 6.10 shows that an increase of the modified creep index results in non-parallel diverging isotachs. Especially the trajectory of the isotach through the lowest strain rate of $\dot{\varepsilon}_4 = 10^{-8}\,s^{-1}$ diverges from the other two isotachs as shown in Table 6.16. Note that this behaviour is similar to the observed trajectories of the isotachs of the performed CRS tests described in Section 5.5. In addition, the distance between different isotachs increases with a decrease in strain rate.

Isotach	*Tangent line*
$\dot{\varepsilon}_1=5\cdot10^{-7}s^{-1}$	$y = 0.450 \cdot \log_{10}(x) - 0.452$
$\dot{\varepsilon}_2=10^{-7}s^{-1}$	$y = 0.470 \cdot \log_{10}(x) - 0.398$
$\dot{\varepsilon}_3=10^{-8}s^{-1}$	$y = 0.539 \cdot \log_{10}(x) - 0.358$

Table 6.16: Tangent line functions of Figure 6.10 indicate close to parallel isotachs.

6.3.4 Conclusions on Soft Soil Creep Model
The step-changed CRS test can be accurately simulated using the SSC-model. The transition from over-consolidated range to normally consolidated is captured well. In addition, transient behaviour around a change in strain rate can be simulated. Increasing the modified creep index allows for the simulation of diverging isotachs with a decreasing strain rate. As a result of this the SSC-model is able to simulate the CRS 6 data well. An optimised fit between the CRS 6 data and the simulation can be achieved by increasing the modified creep index.

6.4 MIT Yuan and Whittle EVP Model

This section demonstrates the MIT Y&W EVP model's capability of accurately simulating the step-changed CRS laboratory tests. The model is able to simulate the smooth transition from over-consolidated state to normally consolidated state. In addition, the model simulates the transient behaviour around a change in strain rate well. The model is able to simulate diverging isotachs corresponding to lower strain rates. Moreover, the MIT Y&W EVP provides a mathematical quantification of the observed transient behaviour around a change in strain rate.

6.4.1 Simulation

By definition, the constitutive behaviour of the CRS tests simulated by the EVP model of Yuan and Whittle, is visualized by plotting the logarithm of change in void ratio vs. the logarithm of effective stress (log e vs log σ'_v). Using the MIT Y&W EVP model formulation as described in Section 2.7.4, the results of CRS test number 6 can be simulated. When simulating the CRS results the (total) strain rate is calculated by evaluating the applied displacement rate per phase. The elastic strain rate is then evaluated by subtracting the calculated visco-plastic strain rate from this total strain rate. The effective stress is subsequently evaluated at each moment. Note that the long-term CRS 6 test is simulated with steps of 30 seconds in order to match the measuring frequency of the Deltares CRS apparatus. This step size results in a smooth simulation graph whilst not compromising too much on the time needed to perform the simulation. In this case the rate sensitivity parameter β is bounded between 0 and $\frac{\rho_\alpha}{\rho_c}$.

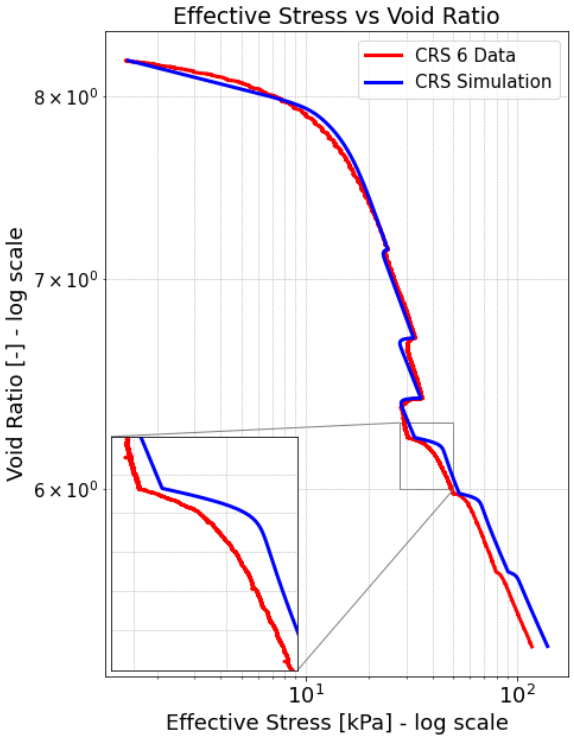

Figure 6.11: MIT-EVP simulation of CRS Test 6 using the initial parameter set.

The simulation as shown in Figure 6.11 is performed with the parameter set as shown in Table 6.17. This simulation results in a coefficient of determination of R^2 = 0.83, indicating a good fit. Regarding the derivation of the parameters as listed above the reader is referred to Annex 7.

Parameter	*Symbol*	*Value*
Slope of linearised elastic unloading/reloading curve	ρ_r	0.017
Slope of linearised virgin compression curve	ρ_c	0.215
Material constant characterising creep behaviour	ρ_α	0.022
Total strain rate as applied by the CRS apparatus	$\dot{\varepsilon}_t$	~
Reference strain rate	$\dot{\varepsilon}_{ref}$	$1.93 \cdot 10^{-7}$ s^{-1}
Initial void ratio	e_0	8.21
Initial effective stress	σ'_{v0}	1.46 kPa.
Rate sensitivity	β	0.1023

Table 6.17: Initial parameter set used in MIT-EVP simulation of CRS 6.

The viscoplastic strain rate in the MIT-EVP model is strongly dependent on the reference strain rate ($\dot{\varepsilon}_{ref}$). As a result, the parameters used to simulate the CRS 6 data are derived with respect to this reference strain rate. Regarding the derivation of these parameters the reader is referred to Annex 4.

The model is able to simulate the step changed CRS data well. The smooth transition from over-consolidated state to normally consolidated state is captured with a high degree of accuracy. The simulation over-estimates the effective stress level during the last phases of the test. With the parameter set as shown in Table 6.17 the Y&W EVP model is not able to fully capture this transient effect. This is visible in Figure 6.11 by a rather abrupt jump to a new isotach when the strain rate is changed instead of a smooth curvature as is visible in the CRS 6 data. The enlarged view of Figure 6.11 shows this.

6.4.2 Optimization

Using the parameters as derived in Annex 7, the Y&W EVP model is able to provide a decent simulation of the performed CRS test number 6. This section shows that a better simulation is achievable using a different parameter set, Figure 6.12. In this case resulting in R^2 = 0.85. The constraints used in the optimization are shown in Table 6.18.

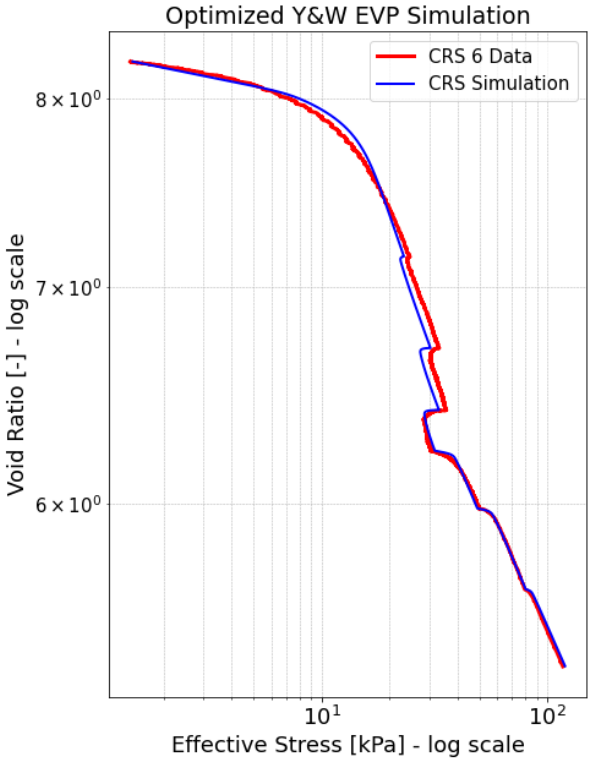

Figure 6.12: Optimised SSC-Model simulation of CRS test 6.

Parameter	*Lowerbound*	*Upperbound*
ρ_r	0.01	0.02
ρ_c	0.1	0.4
ρ_α	0.005	0.06
β	0	0.6

Table 6.18: Constraints used in optimisation process.

Note that the rate sensitivity parameter β is not bounded between zero and $\frac{\rho_\alpha}{\rho_c}$ anymore. This allows for an increased rate sensitivity of the simulation. The physical interpretation of this increased rate sensitivity is described in Section 6.4.3. As can be seen in Figure 6.12, a close fit is achieved using the optimized parameters as shown in Table 6.19.

Parameter	*Symbol*	*Value*
Slope of linearised elastic unloading/reloading curve	ρ_r	0.014
Slope of linearised virgin compression curve	ρ_c	0.227
Material constant characterising creep behaviour	ρ_α	0.015
Total strain rate as applied by the CRS apparatus	$\dot{\varepsilon}_t$	~
Reference strain rate	$\dot{\varepsilon}_{ref}$	$1.93 \cdot 10^{-7}\ s^{-1}$
Initial void ratio	e_0	8.21
Initial effective stress	σ'_{v0}	1.46 kPa.
Rate sensitivity	β	0.09 ($> \frac{\rho_\alpha}{\rho_c} = \frac{0.015}{0.227} = 0.066$)

Table 6.19: Optimised parameter set of SSC-Model simulation of CRS 6.

6.4.3 Parameter Influence

The optimised parameter set of Table 6.19 is already close to the initial parameter set of Table 6.17. This indicates that the used parameters, derived based on the obtained CRS 6 result, are able to simulate the data well. The one parameter that is notably different compared to the initial simulation parameters is the rate sensitivity parameter β. The EVP model of Yuan and Whittle describe how β is bounded between 0 and $\frac{\rho_\alpha}{\rho_c}$.

To achieve the best fit between the actual CRS 6 data and the EVP model, β needs to be larger than the bounds defined by Yuan and Whittle. Figure 6.12 demonstrates this. When the value of β is increased, the model is able to accurately simulate the smooth transition to a new strain rate. The soil behaviour gradually moves to a new isotach, closely matching the observations made in the actual CRS laboratory data. The following section describes the influence on the constitutive behaviour when the rate sensitivity parameter β is changed.

In principle, the behaviour of the simulation around a change in strain rate is governed by the rate sensitivity parameter β. The effects of changing the rate sensitivity parameter are demonstrated using three examples. Note that the other parameters used to simulate this test, as described in Table 6.17 are kept unchanged. Except for the rate sensitivity parameter β. In the Y&W EVP model $0 \leq \beta \leq \frac{\rho_\alpha}{\rho_c}$.

Strain Rate Independence

When β equals zero, the virgin compression line is independent of the applied strain rate changes during CRS testing, Figure 6.13. As a result of this there exists a unique compression curve, irrespective of the applied displacement rate. In this case the EVP model is still able to describe changes in effective stress due to a change in strain rate. These effects are however (only) temporary, they dissipate over time as loading of the sample continues. In this case the change of strain rate has no lasting effect on the compression behaviour of the soil. As time progresses the soil behaviour moves back to the unique compression curve. Irrespective of the new applied strain rate. This strain rate independence practically means that variations in strain rate due to, for example loading, have no lasting effect on the overall compression behaviour of the soil. The CRS tests described in Section 5.5 contradict this behaviour however.

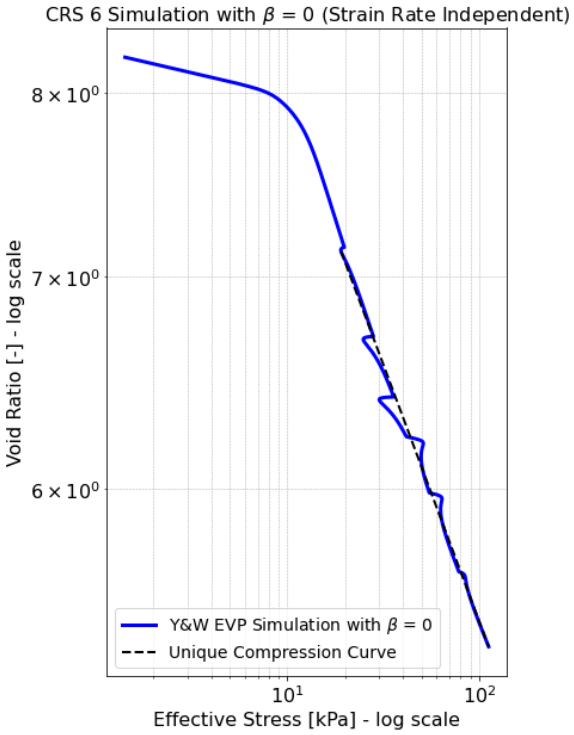

Figure 6.13: Y&W EVP Simulation with strain rate independence.

Strain Rate Dependence

The other extreme of the rate sensitivity parameter Beta is when $\beta = \frac{\rho_\alpha}{\rho_c}$. In this case the rate sensitivity is governed by both the slope of the virgin compression curve in log e vs. log σ'_v as well as the creep parameter ρ_α. A rate sensitivity of $\frac{\rho_\alpha}{\rho_c}$ results in parallel isotachs as demonstrated in Figure 6.14. Figure 6.14 shows the simulation of CRS test number 6 with $\beta = \frac{\rho_\alpha}{\rho_c}$. In this case parallel isotachs are visible, each conforming to a different strain rate. The distance between different isotachs remains constant. In this case one log cycle. Note that in this case the model confirms to the concepts of the classical isotach framework as implemented in the Netherlands. In this example the parameters as described in Section 6.4.1 are kept unchanged, except for the rate sensitivity parameter β.

As evident from Figure 6.14, a change in strain rate results in a (horizontal) shift in effective stress until the sample is adjusted to this new strain rate. In this case there exists a unique relationship between strain, effective stress and strain rate; $R(\varepsilon, \sigma'_v, \dot{\varepsilon})$. In other words, after a change in strain rate a jump to a new isotach is initiated corresponding to this new strain rate. The model describing the soil behaviour is therefore strain rate dependent in case of $\beta = \frac{\rho_\alpha}{\rho_c}$. Physically a rate sensitivity of $\beta = \frac{\rho_\alpha}{\rho_c}$ results in isotach behaviour where an increase in strain rate leads to a an increase in effective stress level. Table 6.20 shows the functions of the tangent lines of the visualised tangent lines of Figure 6.14. From this it is concluded that the model simulates parallel isotachs when $\beta = \frac{\rho_\alpha}{\rho_c}$. This conforms to the concepts of the classical isotach framework.

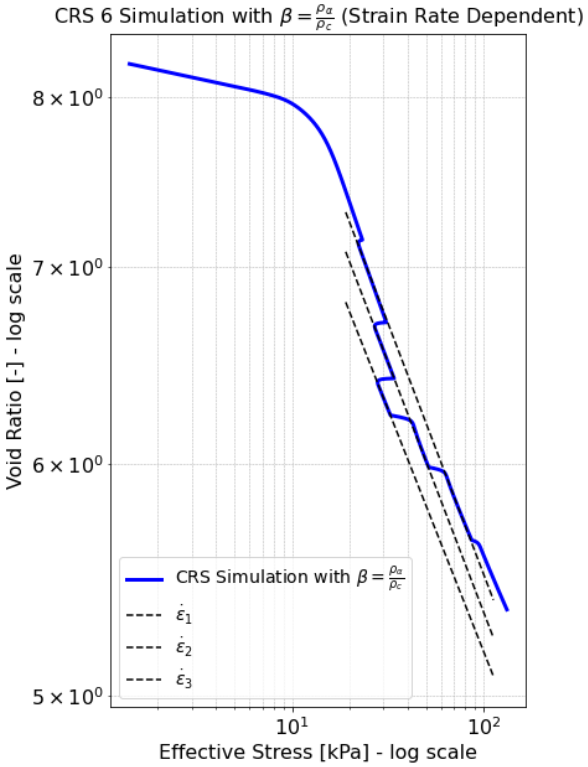

Figure 6.14: Y&W EVP model simulation with strain rate dependence.

Isotach	*Tangent line*
$\dot{\varepsilon}_1 = 5 \cdot 10^{-7} s^{-1}$	$y = -0.171 \cdot \log_{10}(x) + 2.49$
$\dot{\varepsilon}_2 = 10^{-7} s^{-1}$	$y = -0.171 \cdot \log_{10}(x) + 2.46$
$\dot{\varepsilon}_3 = 10^{-8} s^{-1}$	$y = -0.171 \cdot \log_{10}(x) + 2.40$

Table 6.20: Tangent line functions of Figure 97 indicate parallel isotachs.

High Strain Rate Dependence

An interesting question would be what the effect of a rate sensitivity larger than $\frac{\rho_\alpha}{\rho_c}$ physically means. When this is the case, the soil shows an extreme rate sensitivity. A change in strain rate therefore results in abnormally high shifts in effective stress. This is demonstrated in Figure 6.15. The parameters as described in Section 6.4.1 are kept unchanged, except for the rate sensitivity parameter β. The constitutive behaviour of the soil can no longer be described according to classic isotach theory since the stress-strain relationship for different strain rates are no longer parallel. In Figure 6.15, $\beta = 2 \cdot \frac{\rho_\alpha}{\rho_c}$ which results in diverging, non-parallel strain-effective stress-strain rate relationships $R(\varepsilon, \sigma'_v, \dot{\varepsilon})$. From Figure 6.15 it can be concluded that the isotachs diverge more with lower strain rates. Table 6.21 underlines this observation. As a result of this, the distance between different isotachs increases with a decrease in void ratio. This would be the case when the creep parameter ρ_α is high compared to ρ_c. Another possibility is decoupling of the rate sensitivity parameter from ρ_α and ρ_c and treating it as a separate (unbounded) parameter. In this case the soil would show (very)high viscous properties.

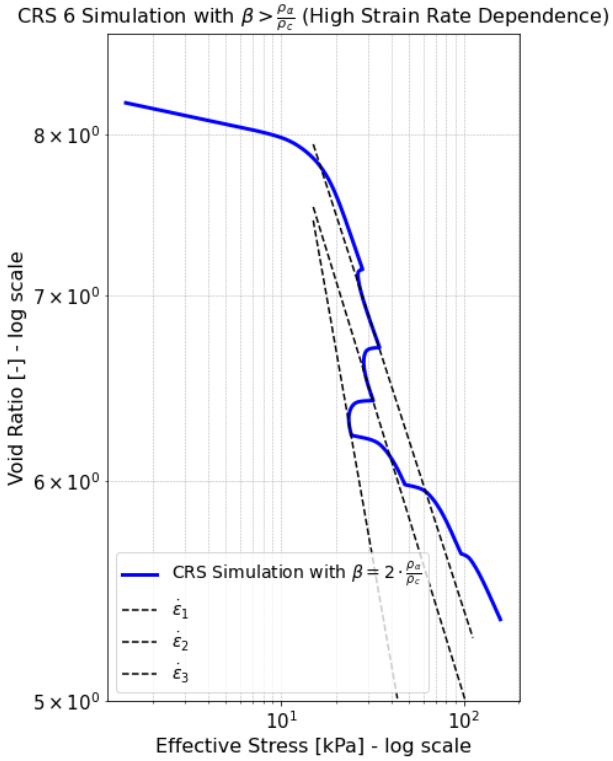

Figure 6.15: Y&W EVP model simulation with high strain rate dependence.

Isotach	*Tangent line*
$\dot{\varepsilon}_1 = 5 \cdot 10^{-7} s^{-1}$	$y = -0.203 \cdot \log_{10}(x) + 2.62$
$\dot{\varepsilon}_2 = 10^{-7} s^{-1}$	$y = -0.214 \cdot \log_{10}(x) + 2.59$
$\dot{\varepsilon}_3 = 10^{-8} s^{-1}$	$y = -0.374 \cdot \log_{10}(x) + 3.02$

Table 6.21: Tangent line functions of Figure 97 indicate parallel isotachs.

As is evident from Section 5.2.2, the performed CRS tests show a high degree of rate sensitivity. The tangent lines through (part of) different isotachs show that the isotachs corresponding to strain rates $\dot{\varepsilon} \geq 5 \cdot 10^{-7}\ s^{-1}$ are reasonably parallel to each other. As a result of this, the constitutive behaviour of this part of the tests be described with a rate sensitivity of $\beta = \frac{\rho_\alpha}{\rho_c}$.

However, especially for the low strain rate of $\dot{\varepsilon}_4 = 10^{-8}\ s^{-1}$ the trajectory of this particular isotach is different compared to the rest of the isotachs and shows a divergence. This behaviour is observed in all performed tests and shown in Annex 8. It therefore seems that an increased value of the rate sensitivity parameter β is needed to accurately simulate this phase of the CRS test.

The MIT EVP model of Yuan and Whittle is designed to describe the compression behaviour of clay. In general, the degree of organic matter in clay is lower compared to peat. Peat generally shows more creep due to this high degree of organic matter compared to clay (Malinowska et al., 2016). The high creep parameter needed to best fit the EVP model to the observed CRS test data might therefore be reasonable. An increase of the rate sensitivity parameter β results in diverging isotachs which better describe the observed results of the performed CRS tests.

6.4.4 Temporal Behaviour

As is described in Section 5.2.2, when the strain rate changes, the sample needs time to adjust to this new strain rate. The time needed for the sample to adjust to a new strain rate is shown to be inversely proportional with strain rate, Figure 5.5.

In the Y&W EVP model formulation the transient coefficient m_t is used to quantify the evolution of the internal strain rate variable $\dot{R}_a$, see Section 2.7.4. A high value of m_t results in faster adaptation of the soil to a new strain rate. This becomes evident by looking at Equation (6.1). Figure 6.16 shows the development of the transient coefficient over time when the Y&W EVM model is used to simulate the data of CRS test 6. The corresponding natural strain rate as per Table 4.2 is shown as reference in the same figure too.

By looking at Figure 6.16 it can be observed that the transient coefficient of case around $\dot{\varepsilon}_3 = 10^{-7}\ s^{-1}$ is higher than during the change in strain rate around $\dot{\varepsilon}_4 = 10^{-8}\ s^{-1}$. As a result of this higher transient coefficient, the time needed for the soil sample to adjust to the new (lower) strain rate of $\dot{\varepsilon}_3 = 10^{-7}\ s^{-1}$ is shorter compared to the time needed for the soil to adjust $\dot{\varepsilon}_4 = 10^{-8}\ s^{-1}$. This makes sense since the auto-decay process occurs at a faster rate due to this higher value of m_t.
Vice versa, the transient coefficient around $\dot{\varepsilon}_4 = 10^{-8}\ s^{-1}$ is lower than around $\dot{\varepsilon}_3 = 10^{-7}\ s^{-1}$, as can be seen in Figure 6.16. As a result of this, the time needed for the soil sample to adjust to this new (lower) strain rate of $\dot{\varepsilon}_4 = 10^{-8}\ s^{-1}$ is high. This behaviour is, again, clearly visible when the effective stress is plotted against time, as shown in Figure 5.5.

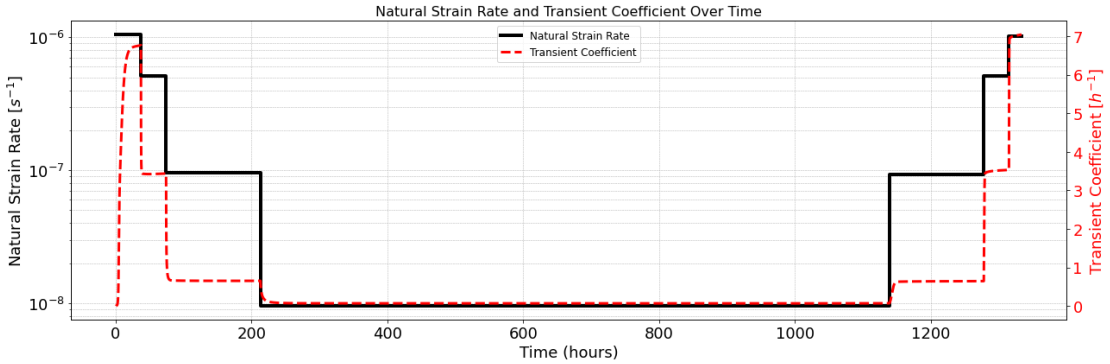

Figure 6.16: Development of transient coefficient over time in Y&W EVP simulation of CRS test 6.

From this observation it becomes clear that larger values of the transient coefficient m_t are found corresponding to higher strain rates. As a result, adaptation to a new strain rate takes longer at lower strain rates. The time needed for the sample to adjust to a new strain rate is thus higher at changes around low strain rates. This becomes clear by looking at the formulation of the transient function as shown in Equation 6.1.

$$m_t = \left(\frac{\rho_c}{\rho_\alpha} - 1\right) \cdot \left(\frac{\dot{\varepsilon}^{vp}}{\rho_r \cdot n}\right) + O(\dot{\varepsilon}) \qquad (6.1)$$

Where, in normally consolidated range, both the viscoplastic strain rate and total strain rate dominate the value of m_t. Consider again two cases;

A. $\dot{\varepsilon}_3 = 10^{-7}\ s^{-1}$ where, $m_t = 0.183\ h^{-1}$.
B. $\dot{\varepsilon}_4 = 10^{-8}\ s^{-1}$ where, $m_t = 0.018\ h^{-1}$.

Since it is assumed that $O(\dot{\varepsilon}) = \dot{\varepsilon}$, as per Equation 6.1, the added contingency term is larger when the total strain rate is high. In addition, the viscoplastic strain rate is higher in case A than in case B. As a result, the value of the transient coefficient m_t is higher in case A compared to case B. This ultimately results in case A adapting faster to a new strain rate than case B. This provides mathematical proof of the observed inverse proportionality in transient behaviour around a change in strain rate. It is of future interest to investigate the physical meaning of this transient coefficient and if this observed phenomena holds true for different types of peat as well.

6.4.5 Conclusion Y&W EVP Model

The Elasto-Viscoplastic model of Yuan and Whittle is able to simulate the compression behaviour of peat. As demonstrated, the model is able to accurately simulate the step changed CRS tests. When the rate sensitivity parameter is increased, a remarkable fit between the actual CRS data and the simulation is achieved. In addition, it has been shown that by increasing this rate sensitivity parameter the model is able to show the observed diverging isotachs corresponding to lower strain rates. As a result, the model is able to closely match the performed CRS tests.

Furthermore, it is concluded that the observed temporal behaviour in the performed CRS tests around a change in strain rate can mathematically be described using the Y&W EVP model formulation. The time needed for the sample to adjust to a new strain rate is thus dependent on both the total strain rate, as well as the viscoplastic strain rate. It is of future interest to investigate, from a physics point of view, why this appears to be true. No logic explanation is found for the observed temporal phenomena around a change in strain rate.

Depending on the transient coefficient and the rate sensitivity of the model, a close fit was achieved between the actual CRS data and the EVP model. The EVP model therefore provides an adequate mathematical description of the observed constitutive behaviour of the performed CRS tests. The EVP model is however, to the author's knowledge, not (yet) widely used (in the Netherlands) to model the compression behaviour of soft soils such as peat. The EVP model can be used to describe the constitutive behaviour of peat as shown in Section 6.4.1 and Section 6.4.2. The model has therefore been validated for describing the compression behaviour of peat. Increasing the rate sensitivity parameter beyond the limits stated by the paper improves the accuracy of the simulation. It is of future interest to investigate the physical meaning of this increased rate sensitivity.

6.5 Conclusions on Simulation Models

The following points are concluded from this chapter:

- The NEN-Bjerrum isotach model and the abc isotach model are both capable of simulating changes in strain rate. The models are less able of capturing the smooth transition around a change in strain rate observed in laboratory testing. The models are built on the assumed validity of the classical isotach framework. Consequently, the models are unable to simulate diverging isotachs.
- The abc-isotach model simulates changes in strain rate well. Transient behaviour around a change in strain rate is not captured well. The model is unable to simulate diverging isotachs.
- The NEN-Bjerrum isotach model provides an arguably better fit to the CRS laboratory data than the abc-isotach model. Nevertheless, it is advisable to use the abc-isoatch model to describe the compression behaviour of peat given in case of large strains above 40-50%.
- The soft soil creep model simulates the CRS laboratory data well. Both the changes in strain rate as well as the transient behaviour around a change in strain rate are captured with a high level of accuracy. In addition, the model is able to simulate an increased divergence of isotachs with a decreasing strain rate. As a result of this the SSC-model aligns well with the evaluated constitutive behaviour in the laboratory CRS tests.
- The MIT Y&W EVP is designed to model the compression behaviour of clay. It is demonstrated that the model is capable of simulating the compression behaviour of peat as well, thereby providing validation of this constitutive model.
- The MIT Y&W EVP model is able to describe different constitutive behaviour depending on the value of the rate sensitivity. In the model formulation the value of the rate sensitivity is capped. In this case the model simulates classical isotach behaviour consisting of parallel equidistant isotachs. Increasing the rate sensitivity allows for simulation of increased divergence of isotachs with a decrease in strain rate. This allows the model to accurately simulate the CRS laboratory tests. It is of future interest to further investigate the physical meaning of decoupling this rate sensitivity parameter.
- The MIT Y&W EVP model provides a mathematical explanation of the noted transient behaviour around a change in strain rate. This further solidifies the observations made in the analysis of the CRS laboratory results. It remains of future interest to investigate the physical meaning of this phenomena.

The four evaluated models are capable of simulating the step-changed CRS data. The MIT Y&W EVP describes the laboratory data with the highest level of accuracy. The model formulation is however considered more complicated than the other reviewed models. The results of Section 5.5 showed how the isotach trajectories corresponding to the lowest strain rate of $\dot{\varepsilon} = 10^{-8}$ s^{-1} are inconsistent with the classical isotach framework. This makes the NEN-Bjerrum isotach model and the abc-isotach model less suited in describing this behaviour since these models are unable to simulate diverging isotachs. Chapter 9 provides recommendations on what model is best used in different cases.

7. Conclusions

The objective of this thesis is to improve the understanding of the development of creep in peat. Identifying the difference in strain rates between field conditions and laboratory testing is aimed to give practical meaning to strain rate regime used in conventional CRS laboratory testing. Field strain rates are shown to be substantially lower than those applied in conventional CRS laboratory testing. Strain rate controlled CRS tests at low strain rates were performed on Zegveld peat to evaluate the practical consequences of the observed strain rate regime. The ultimate aim of performing these strain rate controlled CRS tests is to conclude on the validity of the classical isotach framework. The isotach behaviour around a change in strain rate is of particular interest since changing loading conditions in practice result in a different strain rate. The strain rate controlled CRS tests are simulated to conclude on the capability of commonly used constitutive models to simulate changes in strain rate. Regarding the objectives as formulated in Chapter 1, and as listed below;

1. Quantify the difference in estimated peat strain rates of field projects and strain rates used in conventional CRS laboratory testing on peat.
2. Conclude on the validity of the classical isotach framework based on parallel equidistant isotachs in describing the compression behaviour of peat.
3. Conclude on the practical consequences of the observed isotach behaviour in step-changed CRS testing and the identified difference between strain rates used in laboratory testing and those estimated in field conditions.
4. Analyse the isotach behaviour around a change in strain rate. By step-changed CRS testing, the time required for the soil to reach a new isotach is studied to give meaning to the classical isotach frameworks applicability in describing changing strain rates.
5. Evaluate the performance of different constitutive models used to make settlement predictions of soft soils and capture the extent to which these models are able to accurately simulate changes in strain rate.

The following is concluded:

1. Different strain rates in peat.
   i. The majority of performed studies on the constitutive behaviour of soft soils is based on clay instead of peat. The literature study conducted highlighted this knowledge gap. The well-established difference in strain rates in clay between laboratory testing and field conditions is shown to be even larger for peat. The difference in strain rate between conventional laboratory testing and field conditions can be as much as 10^6.

   ii. Analysis of the strain rates of an embankment built in a peat area indicate an estimated strain rate during construction of $\dot{\varepsilon} = 10^{-9}$ s^{-1} - 10^{-7} s^{-1}. The lower limit of conventional CRS testing corresponds to a strain rate of $\dot{\varepsilon} = 10^{-8}$ s^{-1} . Consequently, the strain rates of the analysed embankment and the lower limit of strain rates used in conventional CRS laboratory testing are (only) comparable during the first months of construction. The strain rate reduces as time progresses, making comparison of field strain rates to laboratory strain rates invalid.

   iii. The recorded settlement of subsidence plates placed below the groundwater table in the Zegveld polder is primarily caused by creep. The resulting strain rate of $\dot{\varepsilon} = 10^{-11}$ s^{-1} is approximately 10^3 times lower than the lowest possible strain rate in conventional CRS testing of $\dot{\varepsilon} = 10^{-8}$ s^{-1}. The estimated field strain rate of Zegveld serves as a lower limit since the Zegveld peat meadow is unaffected by construction. A similar strain rate of $\dot{\varepsilon} = 10^{-11}$ s^{-1} is estimated for part of the A2 embankment using InSAR, 20 years after construction is finished. From this it is concluded that the field strain rate of this embankment construction is comparable to a peat meadow unaffected by construction approximately 20 years after construction is finished.

2. The classical isotach framework, as implemented in the Netherlands, is built on three fundamental concepts as listed below. The following is concluded based on the performed CRS tests on Zegveld peat.

i. There exists a unique relationship between strain (ε), effective stress (σ'_v), and strain rate ($\dot{\varepsilon}$).
The performed CRS tests clearly show strain rate dependent constitutive behaviour. Changes in applied rate of displacement result in movement to a new isotach and thus visualisation of unique compression curves. The first fundamental concept of the classical isotach framework is therefore met.

ii. Lines of equal strain rate are parallel when plotted on strain vs. the logarithm of effective stress.
Within the evaluated strain rate regime, the divergence of different isotachs increases with decreasing strain rate. The trajectories of the isotachs corresponding to the lowest possible strain rate of $\dot{\varepsilon}_4 = 10^{-8}\ s^{-1}$ diverge compared to the other visualised isotachs. The second fundamental concept of the classical isotach framework for describing Zegveld peat is therefore <u>not</u> met below a strain rate of $\dot{\varepsilon} < 10^{-7}\ s^{-1}$.

iii. The mutual distance between different isotachs remains constant.
The five step-changed CRS tests showed an increase in mutual distance between different isotachs with decreasing strain rate. The CRS creep test underlined this observation. The third concept of the classical isotach is therefore <u>not</u> met below a strain rate of $\dot{\varepsilon} < 10^{-7}\ s^{-1}$.

The classical isotach framework is thus inadequate in capturing the compression behaviour of the tested Zegveld peat at low strain rates. This important since it was concluded that field strain rates are lower than those applied in conventional CRS testing.

3. Practical consequence of difference in strain rates and the classical isotach framework.

i. It is concluded that field strain rates are orders of magnitude lower than those applied in conventional CRS testing. As time progresses this difference can amount to a factor of 10^6. As a result of this conclusion and the observed increase of divergent isotachs with a decrease in strain rate, it is expected that isotachs corresponding to field conditions show even more divergence. This goes against the concepts of the classical isotach framework.

ii. The concepts of the classical isotach framework proved to be valid for strain rates in the range of $\dot{\varepsilon} = 10^{-7}\ s^{-1}$ - $10^{-6}\ s^{-1}$. This strain rate regime is however not comparable to field conditions. The validity of the classical isotach framework in describing the compression behaviour of peat is therefore questionable regarding field conditions for which it is demonstrated that strain rates are lower than $\dot{\varepsilon} = 10^{-7}\ s^{-1}$.

iii. Current existing implementation of the classical isotach framework assumes equidistant isotachs. If the mutual distance between different isotachs starts to increase, the rate at which creep takes place start to change over time. As a result the creep rate is not linear on logarithmic timescale, giving rise to tertiary creep due to an increasing mutual distance between different isotachs.

iv. The observed diverging isotachs with decreasing strain rate are observed in all five step-changed CRS tests. In practice this increased divergence with a decrease in strain rate results in stress dependency of creep corresponding to lower strain rates. As a result, as time progresses and the (creep) strain rate reduces, the stress-dependency of the soil could start to increase. No physical explanation is found for this observed divergence.

4. Transient behaviour around a change in strain rate.

i. The step-changed CRS test showed transient behaviour around a change in strain rate. Time is needed for the sample to adjust to the new applied rate of displacement. It is concluded that this transient behaviour is inversely proportional with strain rate. Stated differently, more time is needed for the sample to adjust to a lower strain rate compared to an increasing strain rate. This is especially evident around changes in strain rate corresponding to the lowest possible strain rate in CRS testing of $\dot{\varepsilon} = 10^{-8}\ s^{-1}$. Around this strain rate approximately 200 hours are already needed for the soil's state to fully move to a different isotach. This of no influence on conventional CRS tests in which the rate of displacement is kept constant.

ii. Different loading conditions in practice result in a different strain rates. Chapter 3 showed how field strain rates can be orders of magnitude lower than conventional CRS testing. If the observed inverse proportionality of transient behaviour with strain rate holds true for field conditions problems could arise with parameter determination since the soils state has not yet fully moved to a new isotach. No clear physical explanation is found for this observation. It is of future interest to further investigate and quantify this delayed response of the peat sample when subjected to a change in strain rate.

5. Evaluate the performance of different constitutive models.
   i. It is concluded that field strain rates are lower than strain rates applied during conventional CRS testing. The performed step-changed CRS tests showed an increased divergence wit decreasing strain rate. Moreover, the mutual distance between different isotachs was shown to increase with a decrease in strain rate. The NEN-Bjerrum isotach model and the abc-isotach model are based on the assumed validity of parallel equidistant isotachs. As a result, current implementation of the classical isotach framework builds on the assumption that creep takes place linearly on logarithmic time scale. Consequently, these models are unable to simulate diverging isotachs or an increased mutual distance between different isotachs. This shortcoming can result in the under-estimation of long-term settlement.

   ii. The MIT elasto-viscoplastic model of Yuan and Whittle and the soft soil creep model are able to simulate an increased divergence of isotachs with a decrease in strain rate. Consequently, these models are better able in describing the step changed CRS tests compared to the NEN-Bjerrum isotach model or the abc-isotach model.

   iii. The MIT elasto-viscoplastic model of Yuan and Whittle and the soft soil creep model excel at capturing the transient behaviour around a change in strain rate. This is of importance since it was concluded that not capturing this transient behaviour well could in practice result in invalid parameter determination. In addition, both models are able to simulate the observed transient behaviour of the five step-changed CRS tests by increasing the rate sensitivity. The physical meaning of this increased rate sensitivity resulting in diverging isotachs is of future interest to investigate.

   iv. The MIT elasto-viscoplastic model is designed to model the compression behaviour of clay. It has been demonstrated that this constitutive model can be used to accurately simulate the compression behaviour of peat as well. The model is therefore validated in describing the compression of peat. An accurate simulation of the step changed CRS tests is obtained when the rate sensitivity is increased beyond the limits stated in the paper. By decoupling the rate sensitivity parameter the model is able to simulate the observed increased divergence of isotachs corresponding to lower strain rates. The model is therefore validated for describing the compression behaviour of peat. It remains of future interest to investigate what the physical meaning of the increased rate sensitivity parameter means.

Comparison of the strain rates in field conditions underline the discrepancy between strain rates applied in conventional CRS testing and those encountered in field conditions. From the performed strain rate controlled CRS tests it is observed that the trajectories of different isotachs start to diverge with decreasing strain rate.

As the literature study demonstrated, recent studies on clay hypothesize creep eventually coming to an end. The observations made in this thesis on the mutual distance between different isotachs in peat contradict this and actually show an increased mutual distance between different isotachs. This is observed in each of the five long-term CRS tests. Similar results are noted in the CRS creep test as well. The classical isotach is therefore deemed invalid in describing the compression behaviour of Zegveld peat regarding field conditions.

In practice this increased mutual distance between different isotachs results in an increased creep rate with the logarithm of time. Tertiary creep, which is known to occur in peat, can help explain this observation. Current implementation of the classical isotach framework assumes parallel isotachs and thus a linear creep rate on logarithmic timescale. Existing settlement models such as the NEN-Bjerrum isotach model or the abc-isotach model are built on the assumed validity of the classical isotach framework. If the mutual distance between different isotachs starts to increase, the rate at which creep takes place starts to change over time. As a result, the creep rate is not linear on logarithmic timescale but increases with the logarithm of time. Current implementation of the classical isotach framework does not account for this. Consequently, it is concluded that this can result in the under-estimation of long-term settlement in peat.

8. Recommendations

Soft Soil Engineering continues to be a challenging domain within Civil Engineering. As demonstrated, the physical phenomena responsible for observed soil behaviour is in some cases still up for debate. It continues to be important to close the gap between theory and observed results, either in laboratory practice or in the field. Especially regarding a complex material such as peat. Validation of existing theories and conceptual frameworks therefore remains crucial in order to accurately predict settlement over time. The following is therefore recommended:

1. The CRS tests of this study are performed on Zegveld peat. It is recommended to repeat the tests on different types of peat extracted from locations different than Zegveld. Depending on the implications of the findings of this study it might be beneficial to compare the results of Zegveld peat with peat from other areas such as Canada, Japan, and Scandinavia. Ideally on peat having different main constituents such as sphagnum or reed than the wood and sedge dominated Zegveld peat. Comparison of results can help contextualize the results described in this thesis.
2. Analyse isotach behaviour at strain rates lower than the lower limit of the CRS apparatus of Deltares. If possible, by performing step-changed CRS tests at even lower strain rates it becomes possible to evaluate the hypothesis of increasing divergent isotachs with a decrease in strain rate.
3. The analysis of the CRS creep test showed an increasing mutual distance with a decrease in crossed isotachs. It is recommended to increase the total number of similar CRS creep tests with different durations of the creep phase. Not only would this increase the validity of the obtained results, it would improve understanding of the influence of the duration of the creep phase on isotach behaviour as well.
4. The CRS tests showed increasingly divergent isotachs with a decrease in strain rate. Consequently, the validity of the classical isotach framework is contested at lower strain rates. This is currently not (yet) implemented in common settlement prediction models such as the NEN-Bjerrum isotach model or the abc-isotach model. It is recommended to re-asses these models and allow for diverging isotachs at lower strain rates in peat, or otherwise;
5. Encourage the use of constitutive models that are able to simulate diverging isotachs such as the SSC-model or the MIT-EVP model. These models proved to be better at capturing changes in strain rate and isotach behaviour corresponding to lower strain rates. This is important since changing loading conditions in practice result in different strain rates.
6. The step-changed CRS test showed transient behaviour around a change in strain rate. It is concluded that this transient behaviour is inversely proportional with strain rate. A substantial amount of time (days) is needed for the soil to fully move to a different isotach due to a change in strain rate. It is recommended to improve understanding of this transient behaviour. Primarily since different loading conditions in practice result in a different strain rate. This might have practical consequences due to invalid parameter determination when the soils state has not yet fully moved to a new isotach. Consequently, it is recommended to use constitutive models able to accurately simulate this transient behaviour. The SSC-Model and the MIT-EVP Model are examples of models able to accurately simulate this transient behaviour. Usage of these models should therefore be encouraged in future projects to see if these models improve settlement prediction.
7. The MIT-EVP model is designed to simulate the compression behaviour of clay. This thesis showed its validity in describing the compression behaviour of peat. Improved accuracy between the simulation and the underlying laboratory data is achieved by increasing the rate sensitivity parameter beyond the limits stated in the model formulation. It is recommended to investigate, for example with the authors of the MIT-EVP model, why this parameter is capped and what decoupling of this parameter physically means.

In the future it is of interest to strive for a continued understanding of the constitutive behaviour corresponding to low strain rates. These low strain rates are difficult to evaluate in laboratory testing. Partly because of mechanical limitations, and partly because of the time needed to complete such tests. Further evaluation of recorded deformation rates of existing infrastructural project might therefore be beneficial. Especially for Rijkswaterstaat this continues to be important. The focus of Rijkswaterstaat will continue to be centred on maintaining and widening existing infrastructure. The difference in strain rates, and subsequently the development of creep, will therefore continue to stay relevant in the upcoming years.

References

Adams, A. L. (2011). *Laboratory Evaluation of the Constant Rate of Strain and Constant Head Techniques for Measurement of the Hydraulic Conductivity of Fine Grained Soils.* Master's thesis, Department of Civil and Environmental Engineering, Massachusetts Institute of Technology.

Augustesen, A. H., Liingaard, M., & Lade, P. V. (2004). Characterization of Models for Time-Dependent Behavior of Soils. International Journal of Geomechanics, 4(3), 137-156. https://doi.org/10.1061/(ASCE)1532-3641(2004)4:3(157)

Beuving, J., & van den Akker, J. J. H. (1996). Maaiveldsdaling van veengrasland bij twee slootpeilen in de polder Zegvelderbroek : vijfentwintig jaar zakkingsmetingen op het ROC Zegveld. (Rapport / DLO-Staring Centrum; No. 377). Staring Centrum. https://edepot.wur.nl/301596

Bishop, A. W., & Lovenbury, H. T. (1969). *Creep Characteristics of Two Undisturbed Clays.* International Society for Soil Mechanics and Geotechnical Engineering (ISSMGE). Retrieved from ISSMGE Online Library.

Brandl, H. (2018). *Creeping (Secondary/Tertiary Settlements) of Highly Compressible Soils and Sludge.* Building Materials and Structures, **61**(1), 27-36. https://doi.org/10.5937/GRMK1801027B

Brinkgreve, R.B.J. (2021). Soft Soil Creep model. Behaviour of Soils & Rocks (CIE4361) Lecture Notes. Delft University of Technology.

Brouwer, W. S., & Hanssen, R. F. (2023). *A Treatise on InSAR Geometry and 3-D Displacement Estimation.* IEEE Transactions on Geoscience and Remote Sensing, 61. https://doi.org/10.1109/TGRS.2023.3322595

Buisman, A. S. K. (1936). *Results of Long Duration Settlement Tests.* International Society for Soil Mechanics and Geotechnical Engineering (ISSMGE). Retrieved from ISSMGE Online Library.

Capes, R. and Passera, E., Copernicus (2023). *End-to-end implementation and operation of the European Ground Motion Service (EGMS): Product Description and Format Specification*. Version 2.0. EGMS SC1, ORIGINAL Consortium. Available at: https://land.copernicus.eu/pan-european/european-ground-motion-service

Casu, F., & Manconi, A. (2016). *Four-dimensional surface evolution of active rifting from spaceborne SAR data. Geosphere, 12*(3), 697–705. https://doi.org/10.1130/GES01225.1

Catalão, J., Nico, G., Hanssen, R. and Catita, C., (2011). *Merging GPS and Atmospherically Corrected InSAR Data to Map 3-D Terrain Displacement Velocity*. *IEEE Transactions on Geoscience and Remote Sensing*, 49, pp.2354-2360. Available at: https://doi.org/10.1109/TGRS.2010.2091963

Conroy, P., Lumban-Gaol, Y., van Diepen, S., van Leijen, F., & Hanssen, R. F. (2024). *First wide-area Dutch peatland subsidence estimates based on InSAR.* In *Proceedings of the IEEE International Geoscience and Remote Sensing Symposium (IGARSS 2024)*. IEEE. https://doi.org/10.1109/IGARSS53475.2024.10642504

Crosetto, M., Monserrat, O., Cuevas-González, M., Devanthéry, N., & Crippa, B. (2016). Persistent Scatterer Interferometry: A review. ISPRS Journal of Photogrammetry and Remote Sensing, 115, 78–89. https://doi.org/10.1016/j.isprsjprs.2015.10.011

Crosetto, M., Solari, L., Mróz, M., Balasis-Levinsen, J., Casagli, N., Frei, M., Oyen, A., Moldestad, D. A., Bateson, L., Guerrieri, L., Comerci, V., & Andersen, H. S. (2020). *The Evolution of Wide-Area DInSAR: From Regional and National Services to the European Ground Motion Service. Remote Sensing, 12*(12), 2043. https://doi.org/10.3390/rs12122043

Degago, S. A., Grimstad, G., Jostad, H. P., & Nordal, S. (2013). *Misconceptions about experimental substantiation of creep hypothesis A.* Proceedings of the 18th International Conference on Soil Mechanics and Geotechnical Engineering, Paris, France. International Society for Soil Mechanics and Geotechnical Engineering (ISSMGE). Retrieved from ISSMGE Online Library.

Degago, S. A., Grimstad, G., Jostad, H. P., Nordal, S., & Olsson, M. (2011). *Use and misuse of the isotache concept with respect to creep hypotheses A and B. Géotechnique, 61*(10), 897–908. https://doi.org/10.1680/geot.9.P.112

De Luca, C., Zinno, I., Manunta, M., Lanari, R., & Casu, F. (2017). Large areas surface deformation analysis through a cloud computing P-SBAS approach for massive processing of DInSAR time series. Remote Sensing of Environment, 202, 166–185. https://doi.org/10.1016/j.rse.2017.05.022

Den Haan, E. J. (1994). Vertical Compression of Soils. Ph.D. Thesis, Delft University of Technology, Delft, The Netherlands. ISBN 90-407-1062-7

Den Haan, E. J. (2003). *Het a, b, c-isotachenmodel: Hoeksteen van een nieuwe aanpak van zettingsberekeningen.* Geotechniek, 2003(4), 27-35.

Den Haan, E. J. (2007). *A History of the Development of Isotache Models.* Preprint. https://doi.org/10.13140/RG.2.2.32972.13441

Den Haan, E. J., & Sellmeijer, J. B. (2000). "Calculation of soft ground settlement with an isotache model." In *Soft Ground Technology* (pp. 194-206). ASCE.

Den Haan, E., Termaat, R., Den & Edil, T. B. (Eds.). (1994). Advances in Understanding and Modelling the Mechanical Behaviour of Peat. Proceedings of the International Workshop on Advances in Understanding and Modelling the Mechanical Behaviour of Peat, Delft, Netherlands, 16-18 June 1993. A.A. Balkema, Rotterdam.

Den Haan, E. J., van Essen, H. M., Visschedijk, M. A. T., & Maccabiani, J. (2004). *Isotachenmodellen: Help, hoe kom ik aan de parameters? Geotechniek, January 2004*, 62-69

Descartes Labs Team. (2020). SAR Technical Series Part 4: Sentinel-1 Global Velocity Layer Using Global InSAR at Scale. Medium. https://medium.com/descarteslabs-team/sar-technical-series-part-4-sentinel-1-global-velocity-layer-using-global-insar-at-scale-8ddee176ae01

Dhowian, A. W., & Edil, T. B. (1980). *Consolidation Behavior of Peats. Geotechnical Testing Journal, 3*(3), 105-114. https://doi.org/10.1520/GTJ10881J

Edil, T. B., & Dhowian, A. W. (1979). *Analysis of Long-Term Compression of Peats. Geotechnical Engineering, 10*.

Fialko, Y., Simons, M., & Agnew, D. (2001). The complete (3-D) surface displacement field in the epicentral area of the 1999 Mw7.1 Hector Mine earthquake, California, from space geodetic observations. Geophysical Research Letters, 28(16), 3063–3066. https://doi.org/10.1029/2001GL013174

Garthwaite, M. C., Nancarrow, S., Hislop, A., Thankappan, M., Dawson, J. H., & Lawrie, S. (2015). *The Design of Radar Corner Reflectors for the Australian Geophysical Observing System: A Single Design Suitable for InSAR Deformation Monitoring and SAR Calibration at Multiple Microwave Frequency Bands. Geoscience Australia, Record 2015/03.* https://doi.org/10.11636/Record.2015.003

Graham, J., Crooks, J. H. A., & Bell, A. L. (1983). *Time effects on stress-strain behavior of natural soft clays.* Géotechnique, **33**(3), 327-340. https://doi.org/10.1680/geot.1983.33.3.327

GroenRijk. (z.d.). Zegge (Carex oshimensis 'Evergold'). Geraadpleegd op 18 februari 2025, van https://www.groenrijk.nl/plantengids/plant/vaste-plant/carex-oshimensis-evergold

Heemstra, J. (2008). *De betekenis van klassieke matrassen in de wegenbouw voor de paalmatras van vandaag.* GEO-Kunst, **April 2008**.

Heemstra, J. (2012). *Wat wij nu nog van Keverling Buisman kunnen leren (2).* Geotechniek, January 2012.

Hoefsloot, F. J. M. (2022). *Simulatie en verbetering interpretatie CRS-proef.* Geotechniek, 32, June 2022, 32-37.

Hu, J., Li, Z. W., Ding, X. L., Zhu, J. J., Zhang, L., & Sun, Q. (2014). Resolving three-dimensional surface displacements from InSAR measurements: A review. Earth-Science Reviews, 133, 1–17. https://doi.org/10.1016/j.earscirev.2014.02.005

Imai, G., Tanaka, Y., & Saegusa, H. (2003). *One-dimensional consolidation modeling based on the isotach law for normally consolidated clays.* Soils and Foundations, **43**(4), 173-188. Japanese Geotechnical Society. https://doi.org/10.3208/sandf.43.4_173

Jia, R., Chai, J.-C., Hino, T., & Hong, Z.-S. (2010). *Strain-rate effect on consolidation behaviour of Ariake clay.* ICE Proceedings Geotechnical Engineering, 163 (5), 267-277. https://doi.org/10.1680/geng.2010.163.5.267

Jommi, C., Muraro, S., Trivellato, E., & Zwanenburg, C. (2019). Experimental results on the influence of gas on the mechanical response of peats. Géotechnique, 69(9), 753-766. https://doi.org/10.1680/jgeot.17.P.148

Kaczmarek, Ł., & Dobak, P. (2017). Contemporary overview of soil creep phenomenon. Contemporary Trends in Geoscience, 6(1), 28-40. https://doi.org/10.1515/ctg-2017-0003

Kasse, C. (2005). Late Weichselian and Holocene palaeogeography of the western Netherlands: Effects of relative sea-level rise, river avulsions, and coastal evolution. VU University Amsterdam. Retrieved from https://research.vu.nl/ws/portalfiles/portal/35617041/Kasse2005ICFSWest_NLopmaak.pdf

Kawabe, S., & Tatsuoka, F. (2013). *Creep characteristics of clay in one-dimensional compression with unloading/reloading cycles.* Proceedings of the 18th International Conference on Soil Mechanics and Geotechnical Engineering (ICSMGE), Paris, France, 235-238.

Kooi, H., Bakr, M., de Lange, G., den Haan, E., & Erkens, G. (2018). User guide to SUB-CR: A MODFLOW package for land subsidence and aquifer system compaction that includes creep. Deltares, Report 11202275-008.

Koster, K., Frumau, A., Stafleu, J., Dijkstra, J., Hensen, A., Velzeboer, I., Esteves Martins, J., & Zaadnoordijk, W. J. (2020). GreenhousePeat: a model linking CO_2 emissions from subsiding peatlands to changing groundwater levels. Proceedings of the International Association of Hydrological Sciences, 382, 609–614. https://doi.org/10.5194/piahs-382-609-2020

Kumara, A. N., Prakoso, W. A., & Ilyas, T. (2020). *Limitation in Conventional Oedometer Consolidation Test for Deep Layered Soil.* In *Proceedings of the 7th Engineering International Conference on Education, Concept and Application on Green Technology (EIC 2018)* (pp. 145-150). SCITEPRESS – Science and Technology Publications. https://doi.org/10.5220/0009007601450150

Leroueil, S. (2006). *The Isotache Approach: Where Are We 50 Years After Its Development by Professor Šuklje?* 2006 Prof. Šuklje's Memorial Lecture. Millpress.

Leroueil, S., & Hight, D. W. (1985). Behaviour and properties of natural soils and soft rocks. Characterisation and Engineering Properties of Natural Soils, 1, 29-48.

Leroueil, S., Samson, L., & Bozozuk, M. (1983). Laboratory and field determination of preconsolidation pressures at Gloucester. Canadian Geotechnical Journal, 20(3), 477-490. https://doi.org/10.1139/t83-057

Malinowska, E., Kaczmarek, Ł., & Dobak, P. (2016). Tertiary compression of peat. Przegląd Geologiczny, 64(4), 274-284.

Massop, H. T. L., Hessel, R., van den Akker, J. J. H., van Asselen, S., Erkens, G., Gerritsen, P. A., & Gerritsen, F. H. G. A. (2024). *Monitoring long-term peat subsidence with subsidence platens in Zegveld, The Netherlands.* Geoderma, **450**, 117039. https://doi.org/10.1016/j.geoderma.2024.117039

Mesri, G., Feng, T. W., & Shahien, M. (1995). Compressibility parameters during primary consolidation. In Proceedings of the International Symposium on Compression and Consolidation of Clayey Soils, Hiroshima, Japan, pp. 201-217.

Nash, D. F. T., & Brown, M. (2015). "Influence of Destructuration of Soft Clay on Time-Dependent Settlements: Comparison of Some Elastic Viscoplastic Models." *International Journal of Geomechanics*, 15(5), A4014004.

Nayak, S. (2020). Chapter five – Multivariable constrained nonlinear optimization. In Fundamentals of Optimization Techniques with Algorithms (pp. 135-170). Academic Press.

Normcommissie 351006 'Geotechniek'. (2024). *NEN 8992: Geotechnisch onderzoek en beproeving – Nederlandse aanvullingen bij internationale en Europese laboratoriumproeven.* Stichting Koninklijk Nederlands Normalisatie Instituut (NEN).

NWA-LOSS. (n.d.). Living on Soft Soils. https://nwa-loss.nl/

Olek, B. S. (2020). Experimental insights into consolidation rates during one-dimensional loading with special reference to excess pore water pressure. Acta Geotechnica, 15, 3495–3510. https://doi.org/10.1007/s11440-020-01042-3

Premchitt, J., Ho, K. S., & Evans, N. C. (1996). *Conventional and CRS Rowe Cell Consolidation Test on Some Hong Kong Clays (GEO Report No. 55).* Geotechnical Engineering Office, Civil Engineering Department, Hong Kong Government.

Rajapakse, R. (2016). Consolidation settlement of foundations. Retrieved from Elsevier.

Rijksoverheid Atlas Leefomgeving. (2024). Atlas Leefomgeving. https://www.atlasleefomgeving.nl/

Rijkswaterstaat, Provincie Utrecht. (2019, September 25). Bijlage 2: Brochure verbreding A2 traject Amsterdam–Utrecht [PDF]. Stateninformatie Provincie Utrecht. https://www.stateninformatie.provincie-utrecht.nl/Vergaderingen/Provinciale-Staten/2019/25-september/10:30/Bijlage-2-Brochure-verbreding-A2-traject-Amsterdam-Utrecht-tcm174-147251.pdf

Sentinel Hub. (n.d.). Sentinel-1 custom scripts. https://custom-scripts.sentinel-hub.com/custom-scripts/sentinel/sentinel-1/

Serrano-Juan, A., Pujades, E., Vázquez-Suñé, E., Crosetto, M., & Cuevas-González, M. (2017). *Leveling vs. InSAR in urban underground construction monitoring: Pros and cons. Case of La Sagrera railway station (Barcelona, Spain). Engineering Geology, 218*, 1–11. https://doi.org/10.1016/j.enggeo.2016.12.016

Sertçelik, F. (2019). InSAR study on July 21, 2017 Mw6.6 Bodrum earthquake. ResearchGate. https://www.researchgate.net/publication/336846723_INSAR_STUDY_ON_JULY_21_2017_Mw66_BODRUM_EARTHQUAKE

Suklje, L. (1957). *The analysis of the consolidation process by the isotaches method.* International Society for Soil Mechanics and Geotechnical Engineering (ISSMGE). Retrieved from ISSMGE Online Library.

Tanaka, H., Tsutsumi, A., & Ohashi, T. (2014). *Unloading behavior of clays measured by CRS test.* Soils and Foundations, 54(2), 81-93. https://doi.org/10.1016/j.sandf.2014.02.001

Tolunay, D., Kowalchuk, G. A., Erkens, G., & Hefting, M. M. (2024). *Aerobic and anaerobic decomposition rates in drained peatlands: Impact of botanical composition.* Science of the Total Environment, **930**, 172639. https://doi.org/10.1016/j.scitotenv.2024.172639

Tzouvaras, M., Danezis, C., & Hadjimitsis, D. G. (2020). Differential SAR interferometry using Sentinel-1 imagery—Limitations in monitoring fast moving landslides: The case study of Cyprus. Geosciences, 10(6), 236. https://doi.org/10.3390/geosciences10060236

Van Asselen, S., Hessel, R., Erkens, G., & van Essen, H. (2024). *NOBV Jaarrapportage 2024: Integratierapport Bodemdaling.* Nationaal Onderzoeksprogramma Broeikasgassen Veenweiden (NOBV), Deltares, Wageningen Environmental Research, Utrecht University.

Van Natijne, A. L. (2018). *Locating PS-InSAR derived deformation using LiDAR point clouds.* MSc Thesis, Delft University of Technology. Available at: http://repository.tudelft.nl/

Van Straaten, T., Beukema, H., & Bergsma, T. (2022). Maatgevende vorstindringing hoofdwegennet. Rijkswaterstaat, Versie 3

van Veen, J. (1962) Dredge, Drain, Reclaim: The Art of a Nation. The Hague: Martinus Nijhoff.

Vergote, T. A., Leung, C. F., & Chian, S. C. (2022). *Modelling creep and swelling after unloading under constant load and relaxation with Bayesian updating.* Géotechnique. https://doi.org/10.1680/jgeot.20.P.106

Vermeer, P. A., & Neher, H. P. (1999). A soft soil model that accounts for creep. Institute of Geotechnical Engineering, University of Stuttgart, Germany.

Wang, D., & Abriak, N. E. (2015). Compressibility behavior of Dunkirk structured and reconstituted marine soils. Marine Georesources & Geotechnology, 33(5), 419–428. https://doi.org/10.1080/1064119X.2014.950798

Watabe, Y., & Leroueil, S. (2012). Modeling and Implementation of the Isotache Concept for Long-Term Consolidation Behavior. International Journal of Geomechanics, 15(5), A4014006. https://doi.org/10.1061/(ASCE)GM.1943-5622.0000270

Watabe, Y., & Leroueil, S. (2013). Simplified prediction of long-term consolidation based on the isotache concept. ATC7 Workshop, 18th ICSMGE, Paris, France.

Watabe, Y., & Leroueil, S. (2015). Modeling and Implementation of the Isotache Concept for Long-Term Consolidation Behavior. International Journal of Geomechanics, 15(5), A4014006. https://doi.org/10.1061/(ASCE)GM.1943-5622.0000270

Watabe, Y., Udaka, K., Nakatani, Y., & Leroueil, S. (2012). *Long-term consolidation behavior interpreted with the isotache concept for worldwide clays.* Soils and Foundations, 52(3), 449–464. https://doi.org/10.1016/j.sandf.2012.05.005

Wright, T. J., Parsons, B. E., & Lu, Z. (2004). *Toward mapping surface deformation in three dimensions using InSAR. Geophysical Research Letters, 31*, L01607. https://doi.org/10.1029/2003GL018827

Yuan, Y., & Whittle, A. J. (2018). A novel elasto-viscoplastic formulation for compression behaviour of clays. Géotechnique, 68(3), 196-211. https://doi.org/10.1680/jgeot.16.P.276

Yuan, Y., & Whittle, A. J. (2020). Formulation of a new elastoviscoplastic model for time-dependent behavior of clay. International Journal for Numerical and Analytical Methods in Geomechanics. https://doi.org/10.1002/nag.3174

Zhu, G., Yin, J. H., & Graham, J. (2000). Finite element consolidation analysis of soils with vertical drains. International Journal for Numerical and Analytical Methods in Geomechanics, 24(4), 337-356. https://doi.org/10.1002/(SICI)1096-9853(20000410)24:4

Zwanenburg, C. (2021). *Settlement Prediction.* Report, Deltares, Netherlands.

Appendix 1 Sample Preparation and Initial CRS Test

All CRS tests described in this thesis are performed at the Geotechnical laboratory of Deltares in Delft. On Monday May 6th 2024 the peat samples were retrieved from storage at the Geotechnical laboratory of Deltares. The Zegveld peat samples were taken from the Zegveld polder and transported to the storage facility approximately three years ago. In the storage room at Deltares the samples are kept inside their steel tubes to prevent disturbance of the soil. The temperature is kept constant at 10 degrees centigrade. Inside the storage room the 0,5 meter tall steel tube is sealed off on both ends by means of a plastic lid.

The steel tube is connected to the automated lifting equipment by using straps and buckles. This not only allows for safe transportation of the steel tube, but also facilitates the retrieval of the peat from the inside of the tube. After the lid is removed from both ends of the tube, the steel casing is placed on a table. This table has a whole in it working surface that allows for the placement of a jack to extract the peat from the tube by slowly pushing it out. It is important to stress the speed at which the sample is pushed out. This is a delicate process where the speed at which the sample is pushed out is kept low. A low speed is important to prevent sample disturbance and to prevent the peat from already being consolidated by the forces of the jack exerted on the soil. In this stage, it is important to limit the forces exerted on the soil to only its own weight.

After approximately 15 cm of soil is pushed out of the steel tube, the disk shaped soil is extracted using a steel wire and moved to another working area. Already by visual inspection, it is evident that the Zegveld peat has a high organic content. The amount of wood, visible both as branches and roots, is clearly visible. As is shown in the Figure A1.1.

Figure A1.1: Extraction process of Zegveld peat used in CRS testing.
Upper left: Transportation of metal tube containing the undisturbed Zegveld peat.
Upper centre: Organic matter such as wood is visually identifiable.
Upper right: Large wooden branch present in the peat.
Lower left: Cross-section of peat disk in which wooden branches can clearly be identified.
Lower centre: Compared to the hand, large fibres, roots and branches are visible in the cut peat disks.
Lower right: Cut quarters of the peat disk from which the eventual samples are cut used in CRS testing.

The 15 cm disk is cut into four quarters. Each quarter is wrapped in plastic-wrap and aluminium cling foil and labelled with the correct depth. The wrapping of the soil samples is important since it prevents the peat from dehydrating. The labelling ensures knowing the top and bottom of the sample. The process where a disk of peat is carefully pushed out from the steel tube and cut into quarters is performed three times. This yields 12 segments of peat which after labelling and wrapping in are stored in the cooling facility until they are used to extract a sample with the correct dimensions for the CRS tests.

Table A1.1 shows the water content of the peat sample prior to testing. The dry bulk density of each sample is calculated which is ultimately used to determine the initial void ratio of the peat samples.

The sample preparation is performed by the laboratory technician of Deltares. All with accordance of the set safety guidelines and regulations as stipulated by Deltares. The samples are prepared in accordance with NEN0-EN 8992:2024. In order to use a pristine peat sample in CRS testing the laboratory technician ensures that no large pieces of organic matter such as wood or reeds are present in the sample. Using a metal ring, a sample with the exact dimensions is taken from the previously extracted peat blocks. A porous stone is paced on one side of the peat sample to allow for drainage of excess pore pressure during CRS testing. Figure A1.2 shows the sample preparation process.

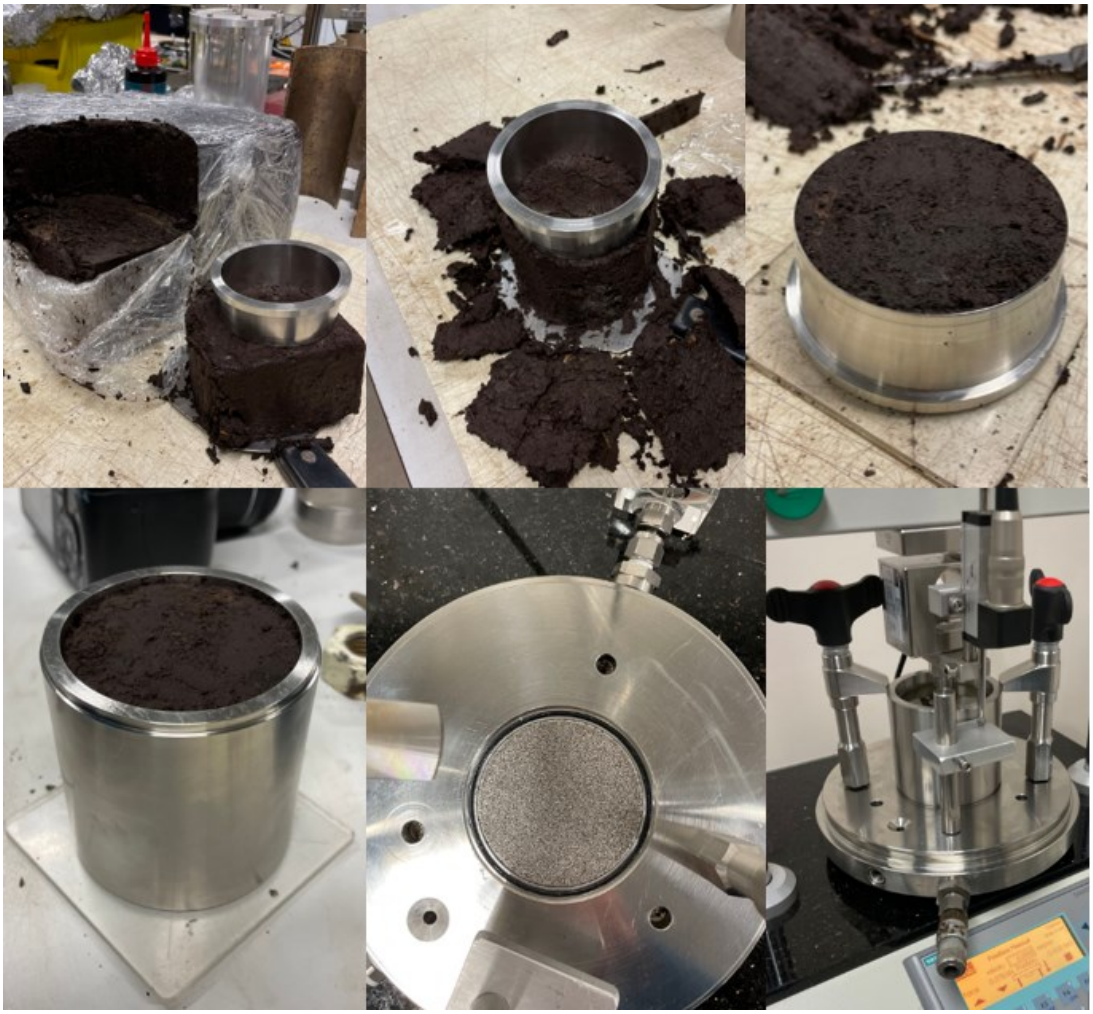

Figure A1.2: Sample preparation for CRS testing.
Upper left: part of the quartered peat disk is cut roughly matching the desired sample dimensions.
Upper centre: excess material is carefully trimmed-off to shape the sample.
Upper right: peat sample confined by the material ring with all excess material trimmed of.
Lower left: eventual peat sample with a height of 30.0 mm and a diameter of 62.5mm.
Lower centre: the porous stone used to allow drainage of the sample.
Lower right: peat sample placed in the CRS apparatus.

Table A1.1 shows the characteristics of the peat samples used in CRS testing.

Test	*Depth [m – MSL]*	*Initial watercontent [%]*	*Specific gravity [g cm^{-3}]*	*Initial void ratio [-]*	*Depth [m – MSL]*	*Initial unit weight [kN m^{-3}]*	*Sample height [mm]*
CRS 1	1.65 - 1.80	515.62	1.606	8.3	1.65 - 1.80	10.43	30.0
CRS 1.2	1.65 - 1.80	515.73	1.587	8.2	1.65 - 1.80	10.42	30.0
CRS 2	1.65 - 1.80	515.00	1.600	8.2	1.65 - 1.80	10.49	30.0
CRS 3	1.65 - 1.80	519.07	1.603	8.3	1.65 - 1.80	10.46	30.0
CRS 4	1.65 - 1.80	524.93	1.593	8.3	1.65 - 1.80	10.50	30.0
CRS 5	1.65 - 1.80	512.16	1.603	8.2	1.65 - 1.80	10.46	30.0
CRS 6	1.65 - 1.80	515.09	1.604	8.3	1.65 - 1.80	10.41	30.0
CRS 7	1.65 - 1.80	516.82	1.603	8.3	1.65 - 1.80	10.43	30.0
CRS Creep	1.65 - 1.80	501.65	1.622	8.1	1.65 - 1.80	10.52	30.0
CRS RT	1.65 - 1.80	505.92	1.629	8.2	1.65 - 1.80	10.53	30.0

Table A1.1: Peat characteristics.

The initial strain rate of CRS test 1 resulted in too much excess generated pore pressure being generated. This test was therefore stopped prematurely. CRS test 1.2 is used to determine the yield stress as shown in Annex 3. CRS test 2 failed due to technical difficulties during testing. CRS test 3, 4, 5, 6 and 7 are used to validate the classical isotach framework.

Figure A1.3 shows the resulting ratio of excess generated pore pressure u_b over total applied stress on the sample σ_v, in formula $\frac{u_b}{\sigma_v}$ [%]. From this it becomes clear that for this tested material, a strain rate of $\dot{\varepsilon} = 10^{-5}$ s^{-1} results in too much excess generated pore pressure. This becomes clear by looking at the first 4 hours of testing in Figure A1.3 . This step corresponds to a strain rate of $\dot{\varepsilon} = 10^{-5}$ s^{-1} which becomes clear by observing the change in displacement over time. In the Figure below it can then be observed that that during this first four hours of testing a sharp increase in excess generated pore pressure over total applied stress occurs.

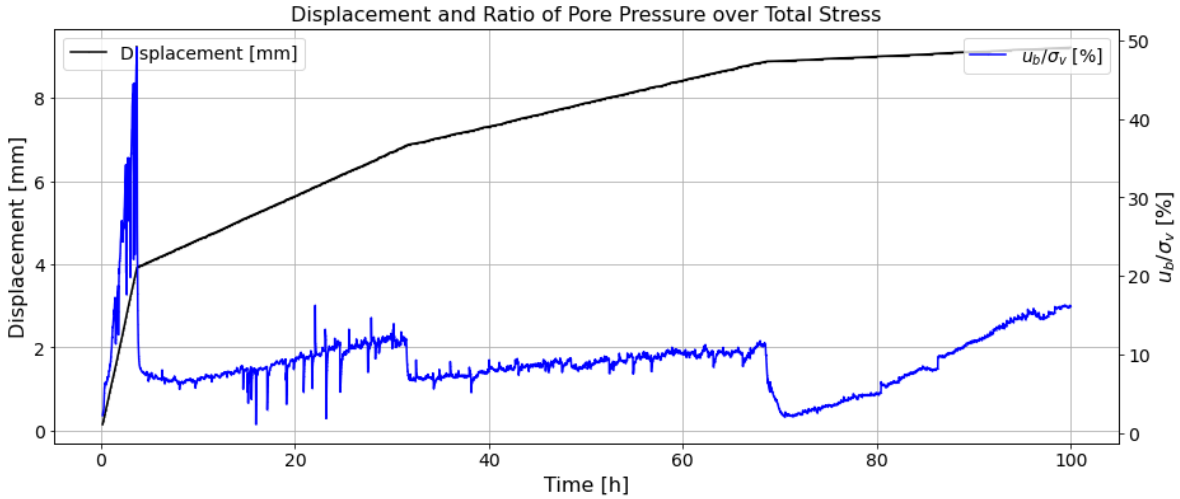

Figure A1.3: The initial strain rate of $\dot{\varepsilon} = 10^{-5}$ s^{-1} resulted in too much excess generated pore pressure as is visible by the sharp increase of pore pressure at t=5 hours.

As can be seen in Figure A1.4, the stress development throughout this CRS tests remains volatile. Even during stages corresponding to lower strain rates the amount of excess generated pore pressure remains relatively high. As a result of this, the difference between total stress and effective stress is substantial throughout the CRS test.

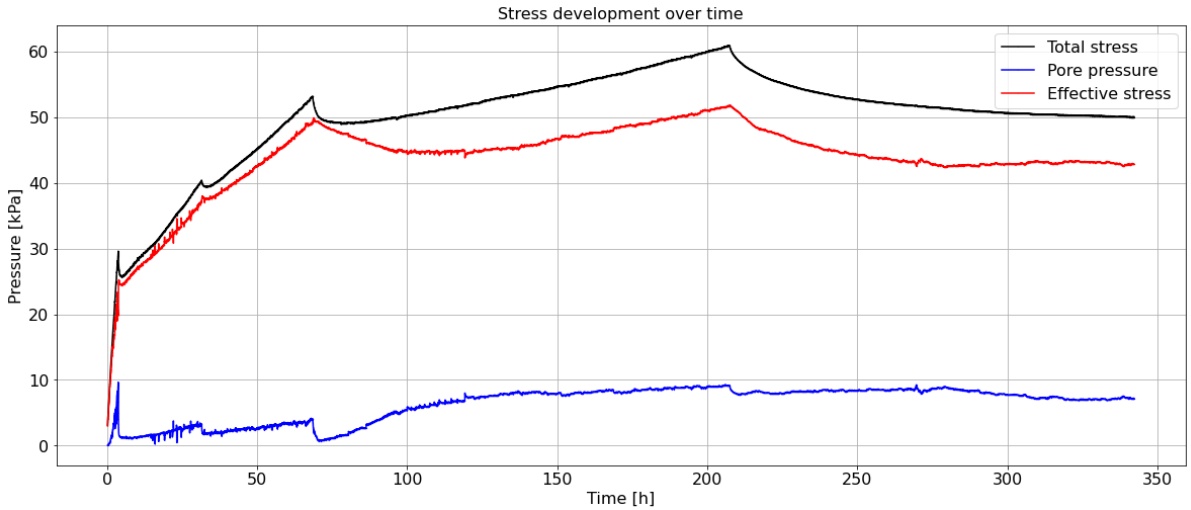

Figure A1.4: Stress development due to initial strain rate configuration shows volatile behaviour throughout the test due to the starting strain rate of $\dot{\varepsilon} = 10^{-5}\ s^{-1}$.

Figure A1.5 shows the logarithm of effective stress vs. natural strain of the CRS test with the setup as shown in the Table above. In here, the volatile behaviour can clearly be identified during the first stage of the CRS test. Because of this non-smooth behaviour the decision was made to no longer continue this test. Subsequently, the initially determined strain rate was decreased from $\dot{\varepsilon} = 10^{-5}\ s^{-1}$ to $\dot{\varepsilon} = 10^{-6}\ s^{-1}$ in the other performed CRS tests.

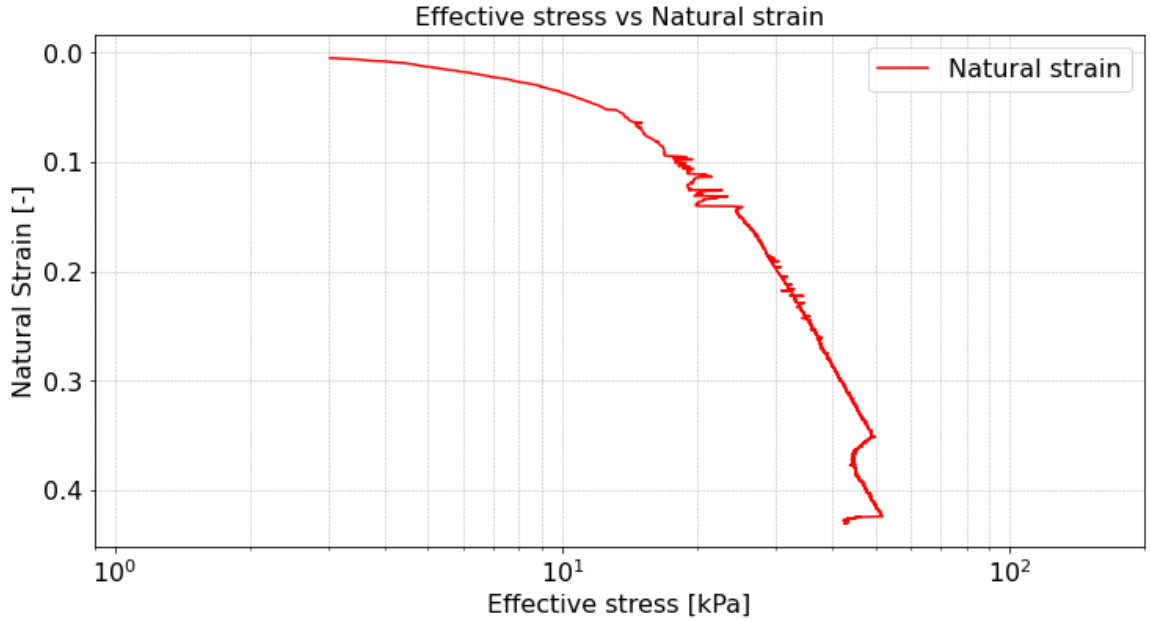

Figure A1.5: Due to the initial strain rate of ε ̇ = 10-5 s-1 being too high erratic behaviour in the transition from over-consolidated state to normally consolidated state is visible.

Appendix 2 Scans of Zegveld Peat

Computed Tomograph (CT) scans are made of the exact same peat as used in the performed CRS tests. These scans were made at the geotechnical laboratory at the TU-Delft. These scans were made in June and July of 2024. Because of this, the peat is transported from the cooled storage facility at Deltares to the TU-Delft using a container partly filled with ice in order to prevent dehydration of the peat.

As can be seen in the pictures in Figure A2.1, large chunks of wood, sedge and reed fibres and other organic material is present within the Zegveld peat.

Figure A2.1: Left: top view of peat sample clearly shows undecomposed wood and fibres.

Both medical CT scans are made of the Zegveld peat as well as industrial CT scans. Figure A2.2 shows the industrial C scanning process. The main difference is the size of the object of interest that can be scanned. In light of this, a large undisturbed peat block is scanned using the medical CT scan. A smaller cylinder is scanned using the industrial CT scanner. Figure A2.3 shows a 3-dimensional scan of the peat sample as shown in Figure A2.1. The organic matter is clearly visible in both images.

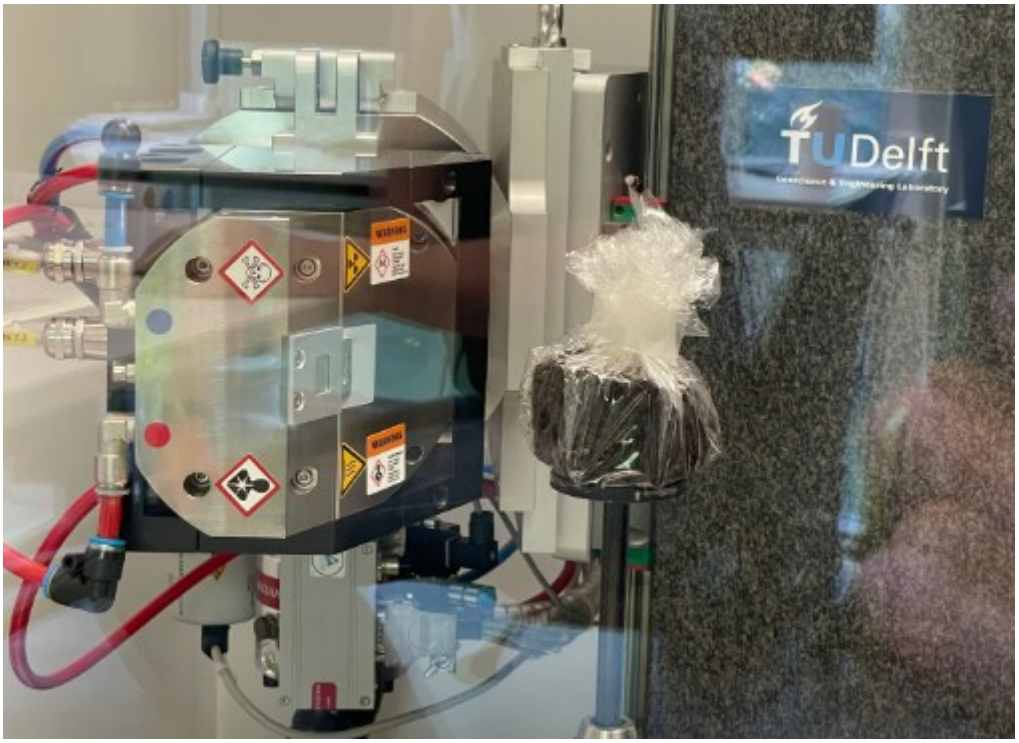

Figure A2.2: CT-scanning process of the peat disk at the TU-Delft laboratory.

After the 3-dimensional render is finished, cross-sections can be created which provide a clear view of the different peat constituents present within the sample. Figure A2.3 provides a three-dimensional render. A cross-sectional view of this peat cylinder is shown in Figure A2.4. Note that dark spots (black) indicate pore-volumes/voids. These can be filled with either air or water. White spots indicate granular material such as sand particles being present within the peat layer.

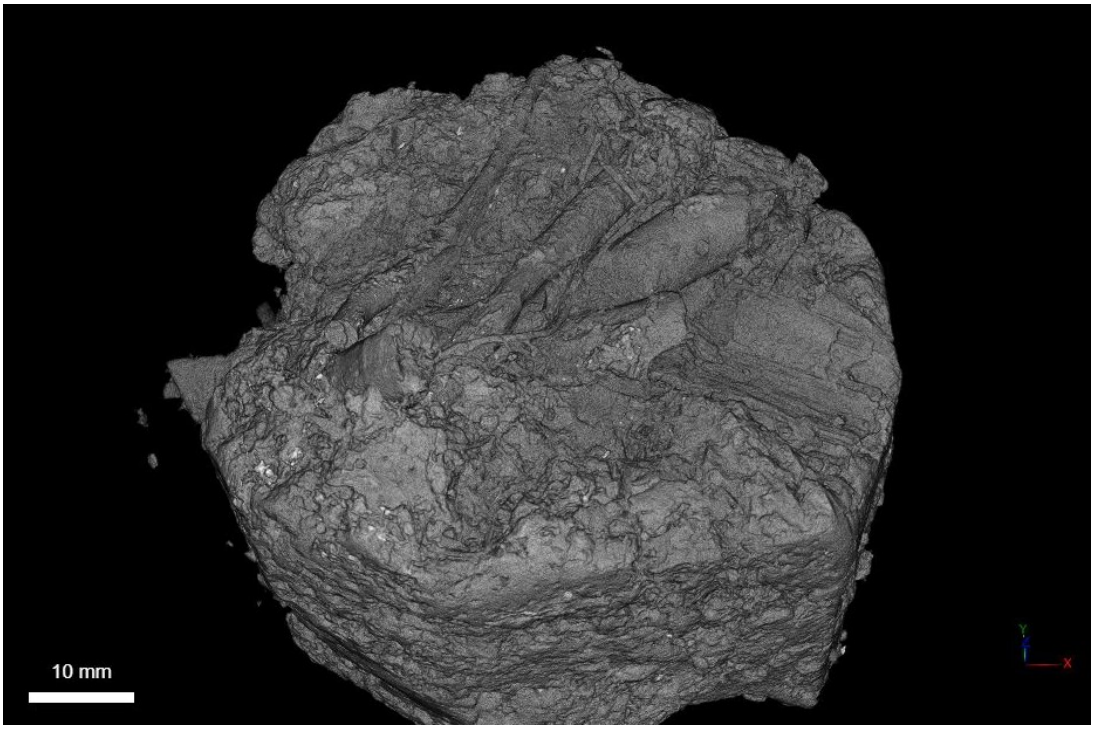

Figure A2.3: 3-dimensional rendering of the scanned peat sample. Note the clearly identifiable wooden branches at the top of the sample.

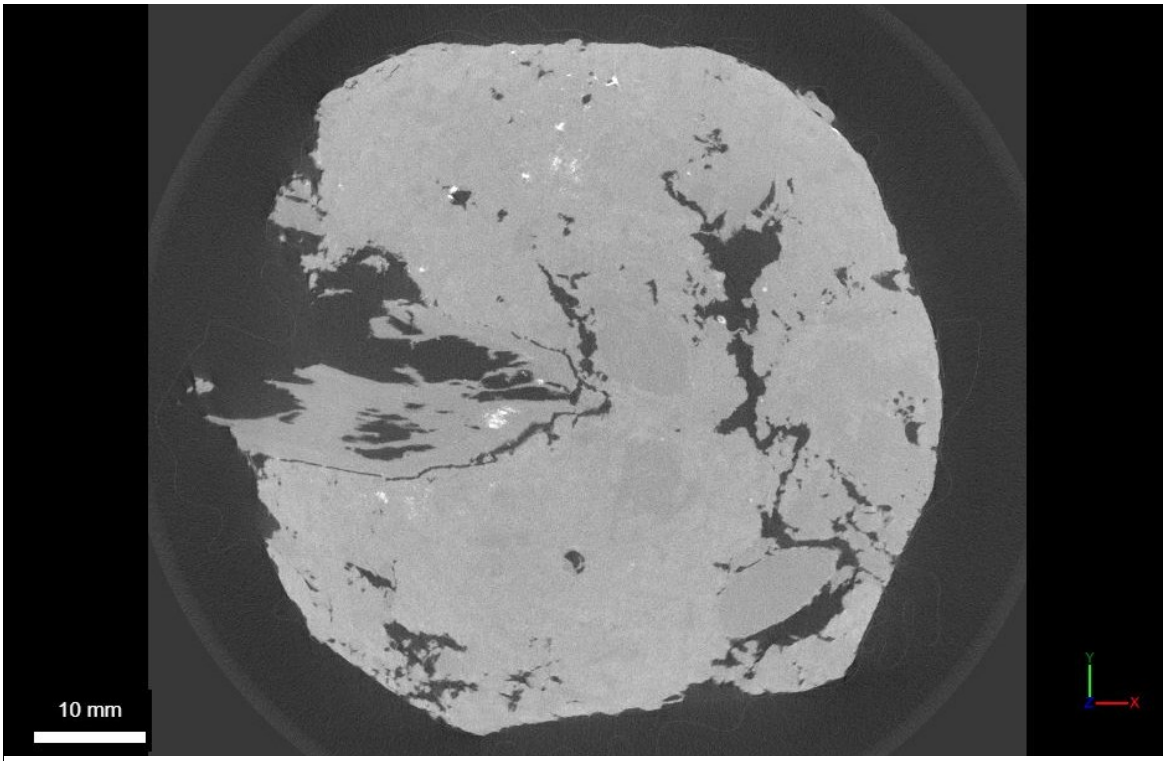

Figure A2.4: Top view of the CT scanned peat sample. Black areas indicate pore volumes which are distributed abundantly throughout the peat cylinder.

Figure A2.5 provides annotations of the clearly identifiable wooden branches present in the peat sample. These wooden branches can be identified in a cross-section of the sample as well. Figure A2.6 illustrates this where annotations are added to the cross sectional image of Figure A2.4.

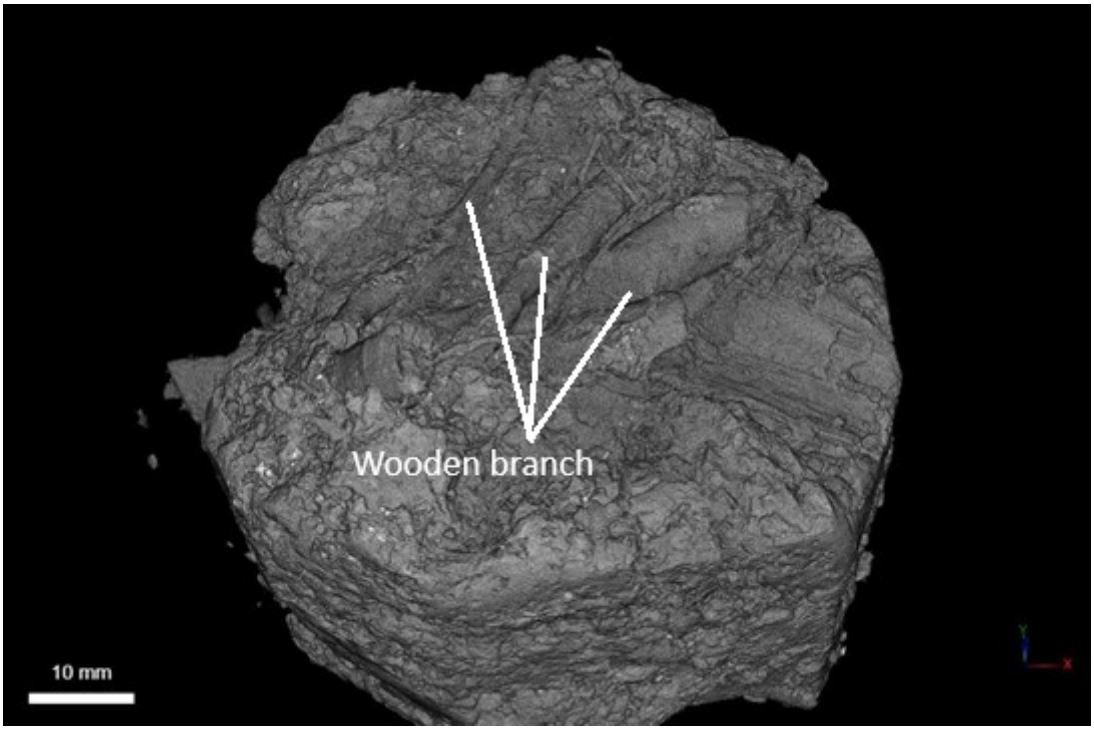

Figure A2.5: 3-dimensional rendering of the scanned peat sample with annotations of identifiable wooden branches.

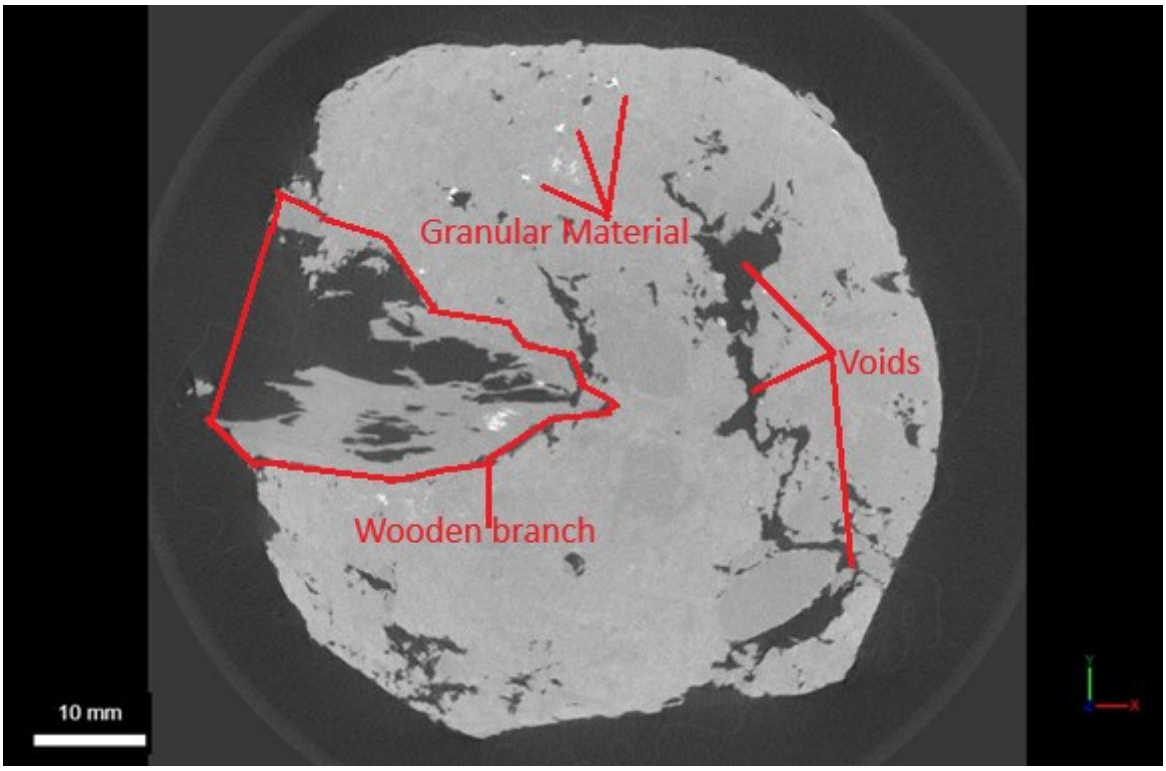

Figure A2.6: Top view of the CT scanned peat sample with annotations.

Figure A2.7 and Figure A2.8 provide a cross-sectional view of the scanned Zegveld peat.

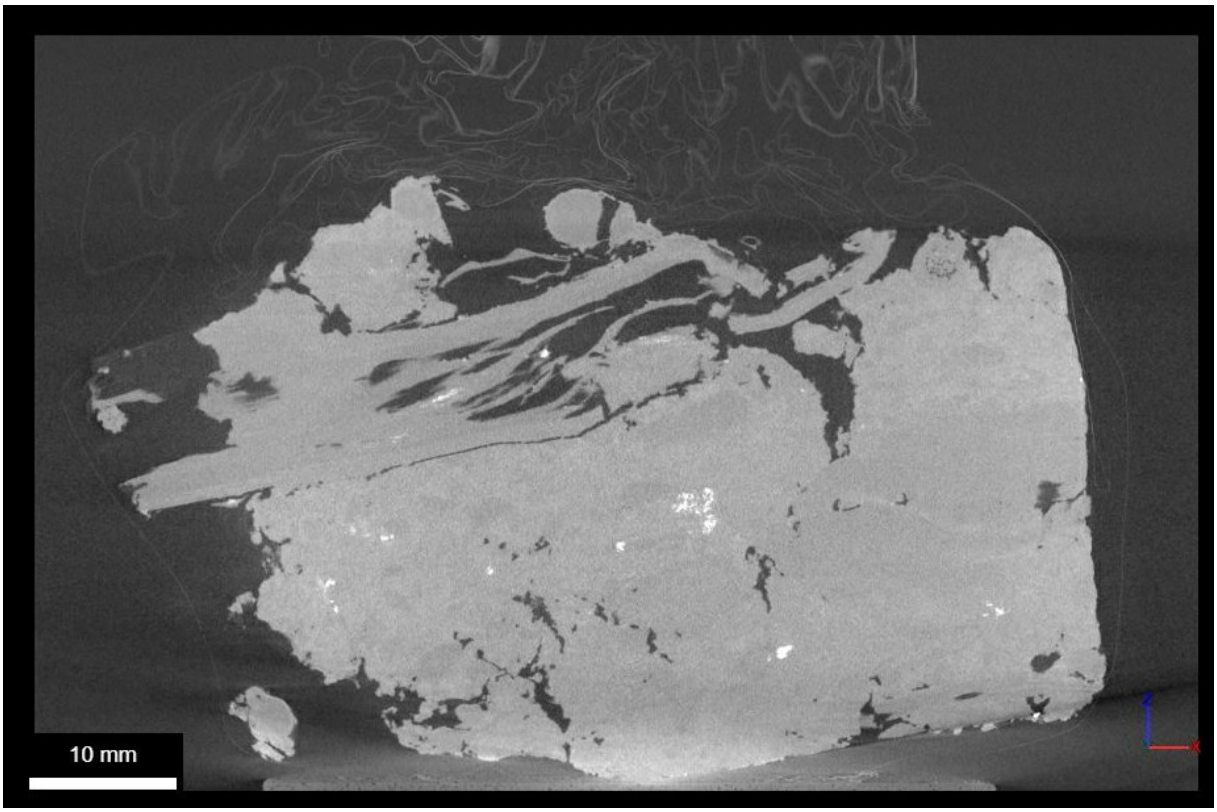

Figure A2.7: Cross-sectional view of the CT scanned peat. Note the large wooden branch at the upper left of the peat cylinder.

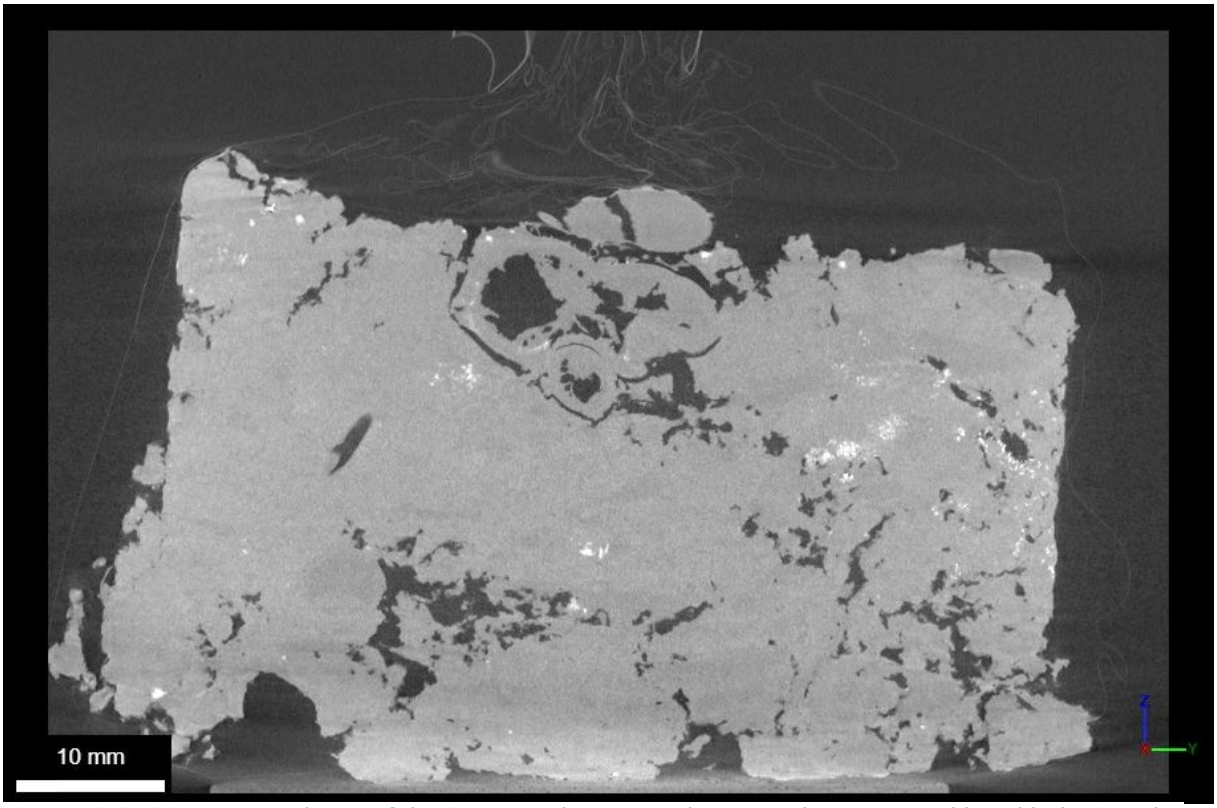

Figure A2.8: Cross-sectional view of the CT scanned peat sample. Pore volumes are visible in black. Granular material with a higher density than peat are visible by the white areas throughout the peat cylinder.

Figure A2.9 provides annotations to the cross-sectional image as shown in Figure A2.7. Note the large wooden branch at the top of the peat sample. Figure A2.10 provides annotations to the image in Figure A2.8. In here the wooden branch noted in Figure A2.7 and Figure A2.9 is again clearly visible.

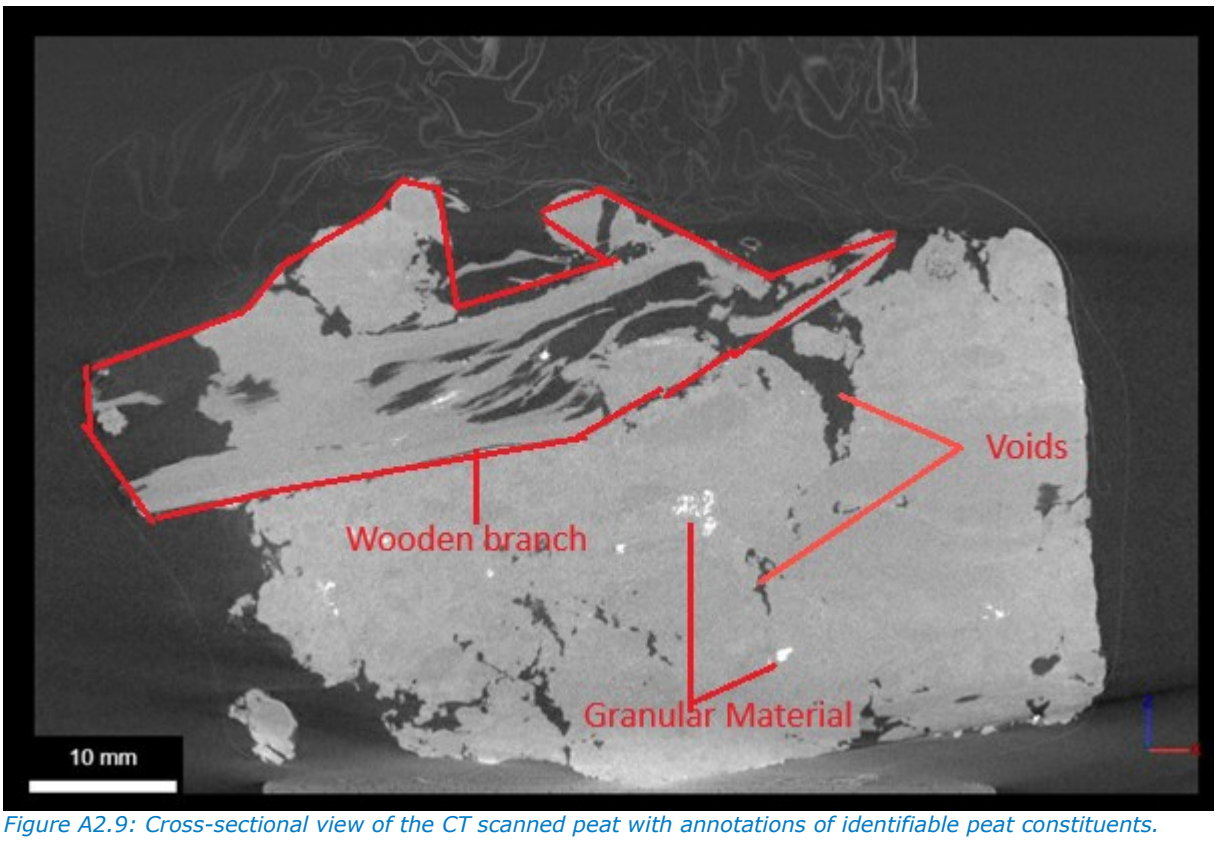

Figure A2.9: Cross-sectional view of the CT scanned peat with annotations of identifiable peat constituents.

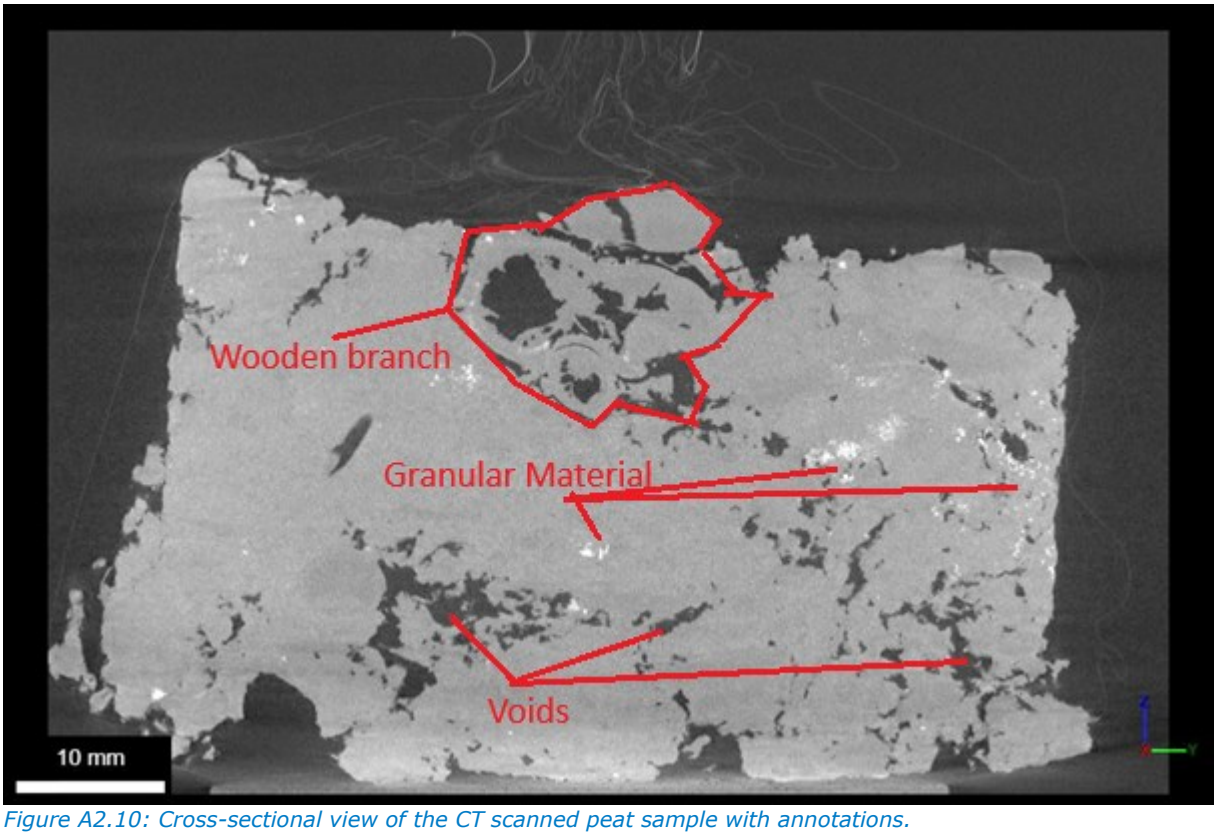

Figure A2.10: Cross-sectional view of the CT scanned peat sample with annotations.

A larger peat chunk is scanned using the medical CT-scanner of the TU-Delft as shown in Figure A2.12. As can be seen in Figure A2.11, this large peat chunk clearly shows a high degree of organic matter being present as well.

Figure A2.11: Cross-section of peat cylinder reveals the observations made in the CT scan where wooden branches are clearly visible.

Figure A2.12: Medical CT-scan of peat cylinder at the laboratory of the TU-Delft.

Figure A2.13 shows the mediacal CT-scan used. A real-time video of the peat sample can be monitored. This video can ultimately be paused in order to distinguis different cross-section as shown in Figure A2.14.

Figure A2.13: The medical CT-scan allows large part of the peat layer to be scanned.

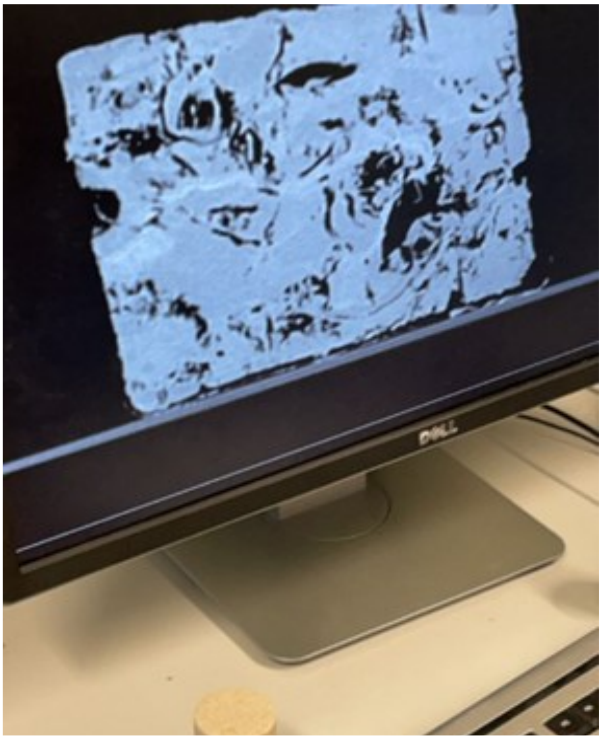

Figure A2.14: Real time video allows monitoring the peat during the scanning process.

Figure A2.15 provides a cross-section of the peat sample when scanned using the medical CT-scan. Again, note the large amount of black spots present in this cross-section. These spots indicate areas filled with either air or water. The marbling in this image underlines the heterogenic nature of the Zegveld peat. Figure A2.16 provides annotations to the image in Figure A2.15.

Figure A2.15: Cross-sectional view of the peat chunk scanned using the medical CT-scan of the TU-Delft. Note the large areas in black indicating pore volumes. This underlines the calculated void ratio of the Zegveld peat.

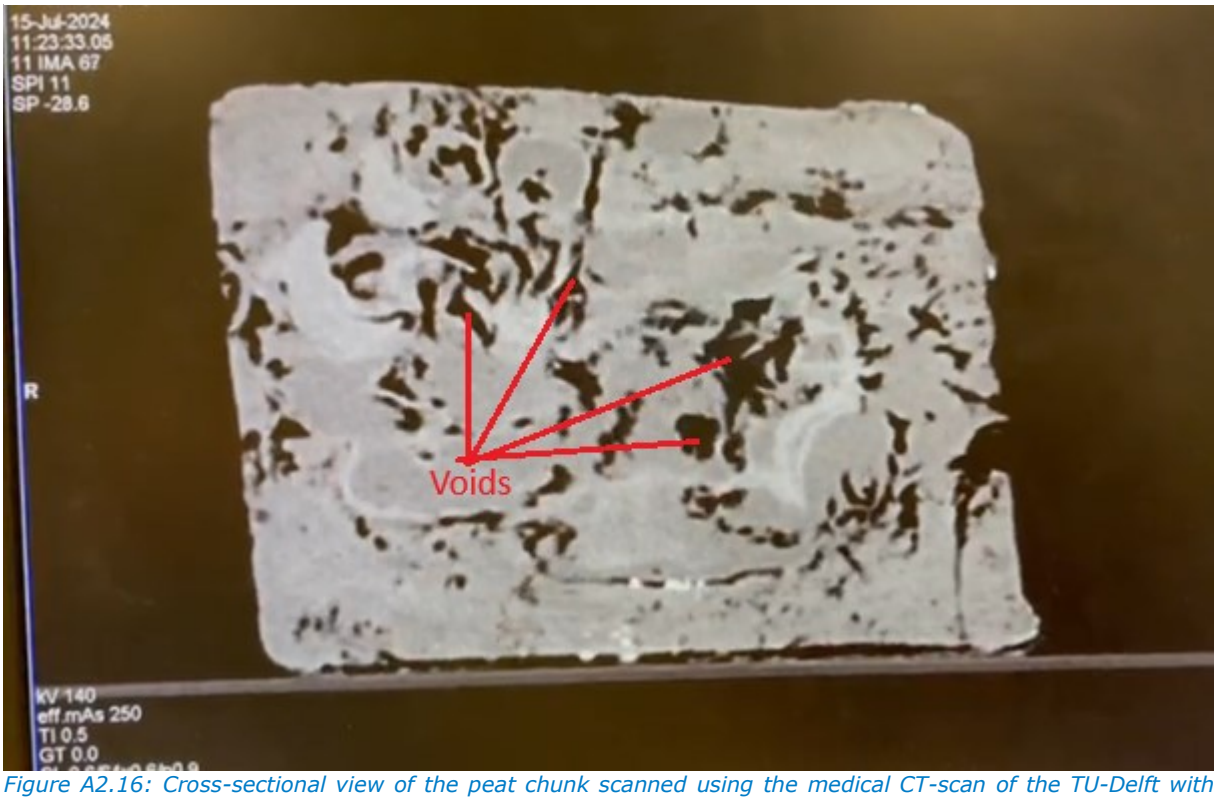

Figure A2.16: Cross-sectional view of the peat chunk scanned using the medical CT-scan of the TU-Delft with annotated voids.

Appendix 3 Yield Stress

A CRS test is performed to determine the yield stress of the Zegveld peat. This CRS test is performed with a strain rate of $\dot{\varepsilon} = 10^{-6}\ s^{-1}$. Since the strain rate is not changed throughout the test, the rate of displacement is constant over time. The yield stress is determined to be around 18 kPa as shown in Figure A3.1. Since the peat characteristics are similar for each of the used pat samples the value of this yield stress is deemed valid for all peat samples used in CRS testing. Note that determination of the yield stress is important in order to evaluate if the sample is fully in normally consolidated range.

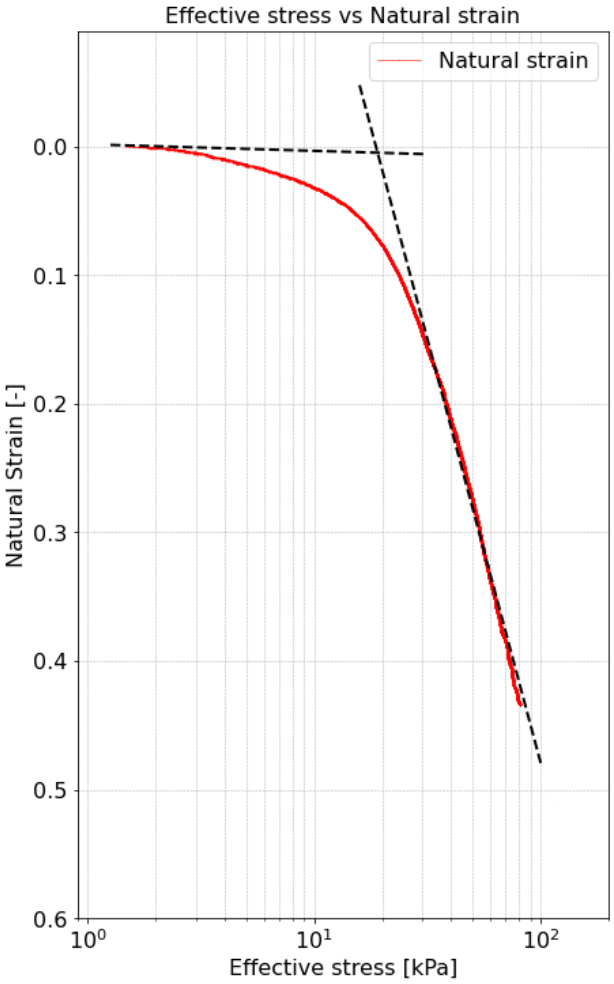

Figure A3.1: Yield stress determination of Zegveld peat.

Appendix 4 a, b, c - Parameter Derivation

The a,b,c, parameters are used to model/describe the settlement of a soil body in the abc-isotach model as described in (den Haan, 2004). NEN 8992 provides the derivation of the abc parameters as well. The formal definition as defined by den Haan (1994) are shown by Equation A4.1, Equation A4.2 and Equation A4.3.

Direct compression coefficient:

$a = \frac{\Delta \varepsilon_H^d}{\Delta \ln(\sigma_v')}$ where; (A4.1)

ε_H^d = direct elastic natural (Hencky) strain [-]
σ_v' = effective stress [kPa]

Secular compression coefficient:

$b = = \frac{\Delta \varepsilon_H}{\Delta \ln(\sigma_v')}$ where; (A4.2)

ε_H = elastic natural (Hencky) strain [-]
σ_v' = effective stress [kPa]

When a creep phase is performed the secular strain rate coefficient can calculated via Equation A4.3.

$c = \frac{\Delta \varepsilon_H}{\Delta \ln(t)}$ where; (A4.3)

ε_H = elastic natural (Hencky) strain [-]
t = time [s]

The secular strain rate coefficient can be determined by evaluating a relaxation phase or a change in applied rate of displacement when no creep phase is performed. This procedure is described in NEN-EN 8992:2024 and (Hoefsloot, 2022). This approach is used to determine the secular strain rate coefficient of CRS test 6 since no creep phase is performed in CRS test 6. By performing this method a value of the secular strain rate coefficient of 0.0167 is found as shown in Figure A4.1.

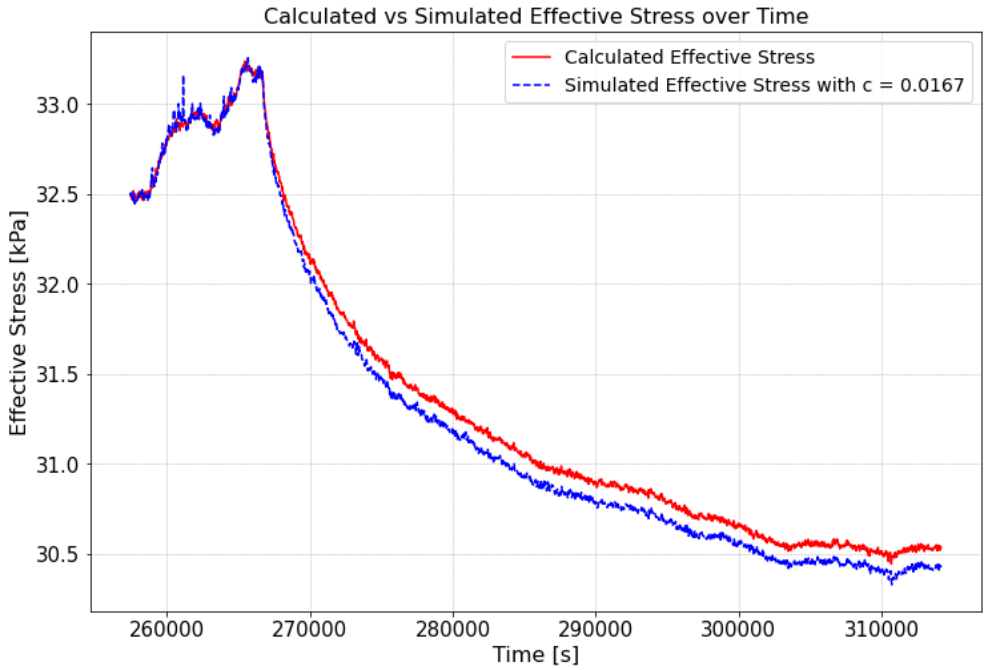

Figure A4.1: Estimation process of creep parameter based on change in strain rate as per NEN-EN 8992:2024.

Therefore, based on the results on CRS test 6 the calculated parameters are shown in Equation A4.4, Equation A4.5 and Equation A4.6

$a = \frac{\Delta \varepsilon_H^d}{\Delta \ln(\sigma_v')} = 0.014$ (A4.4)

$b = = \frac{\Delta \varepsilon_H}{\Delta \ln(\sigma_v')} = 0.263$ (A4.5)

$c = \frac{\Delta \varepsilon_H}{\Delta \ln(t)} = 0.0167$ (A4.6)

The direct compression coefficient and the secular compression coefficient are derived directly from the obtained compression curve of CRS test 6 as shown in Figure A4.2. Note that this serves as an initial parameter set which is optimised per simulation.

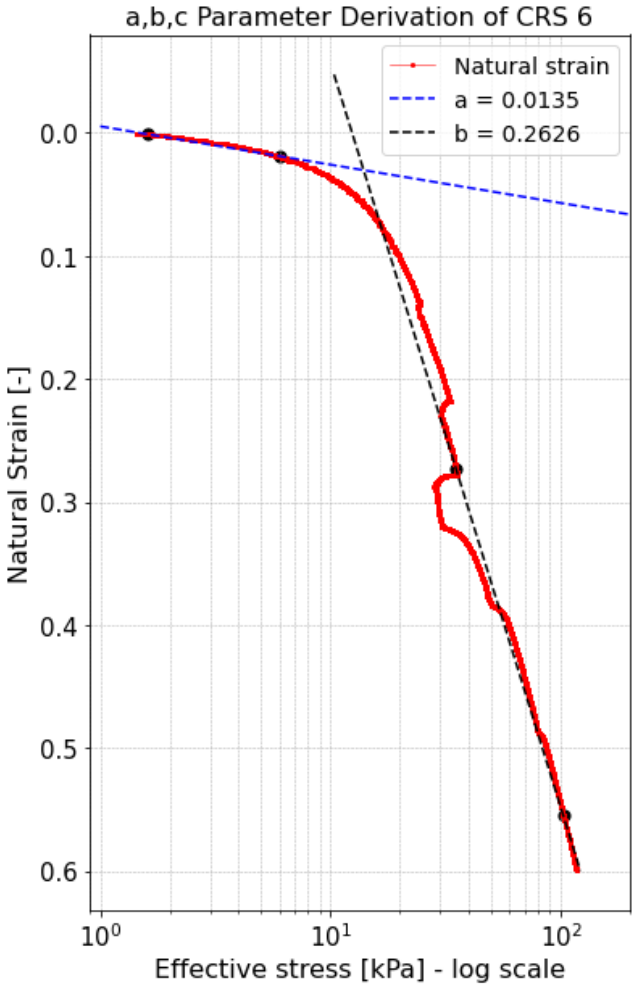

Figure A4.2: Determination of direct- and secular compression indices.

Note that the value of the secular compression coefficient is derived with respect to the reference isotach.

The reference strain rate is calculated by evaluating the previously calculated creep parameter of the a,b,c model. The amount of strain due to creep is calculated by Equation A4.7;

$$\Delta\varepsilon_H = c \ln\left(\frac{\tau}{\tau_0}\right) \quad \text{(A4.7)}$$

where;

$\Delta\varepsilon_H$ = accumulated creep strain
c = creep parameter
τ = reference isotach
τ_0 = 1 day isotach

With τ_0 = 1 day isotach and taking the derivative w.r.t. time;

$$\dot{\varepsilon}_{ref} = \frac{c}{\tau} \quad \text{(A4.8)}$$

With c = 0.0167 and the reference strain rate expressed in s^{-1};

$$\dot{\varepsilon}_{ref} = \frac{0.0167}{24 \cdot 3600} = 1.93287 \cdot 10^{-7}\ s^{-1}. \quad \text{(A4.9)}$$

Appendix 5 NEN-Bjerrum Parameter Derivation

The NEN-Bjerrum settlement parameters show a great level of similarity to the a,b,c settlement parameters. The main difference is in the strain notation. The NEN-Bjerrum parameters are derived by evaluating the change in linear strain. Note that the a,b,c parameters are derived by evaluation of the natural strain. The NEN-Bjerrum settlement parameters for the tested Zegveld peat read as per Equation A5.1, Equation A5.2 and Equation A5.3.

Recompression Ratio:

$$RR = \frac{\Delta\varepsilon_C^d}{\Delta\log(\sigma_v')} = \frac{C_R}{1+e_0} \quad \text{(A5.1)}$$

where;

ε_C^d = direct elastic linear (Cauchy) strain [-]
σ_v' = effective stress [kPa]

Compression Ratio:

$$CR = \frac{\Delta\varepsilon_C}{\Delta\log(\sigma_v')} = \frac{C_c}{1+e_0} \quad \text{(A5.2)}$$

where;

ε_C = elastic natural (Cauchy) strain [-]
σ_v' = effective stress [kPa]

Secular strain rate coefficient:

$$C_\alpha = \frac{\Delta\varepsilon_C}{\Delta\log(t)} = \frac{c\cdot\ln(10)}{1-\varepsilon} \quad \text{(A5.3)}$$

where;

ε_C = elastic natural (Cauchy) strain [-]
t = time [s]
c = secular strain rate coefficient from abc-isotach model
ε = average strain

In case of no creep phase in a CRS test the secular strain rate can be iteratively determined by performing a relaxation phase or a change in applied rate of displacement. The exact procedure of this approach is described in (NEN-EN 8992:2024) and (Hoefsloot, 2022). This procedure is similar to the method described in Annex 4 used to determine the secular strain coefficient of the abc-isotach model.

In addition, den Haan et al. (2004) show how the secular strain rate coefficient of the abc-isotach model can be converted to the secular strain rate coefficient of the NEN-Bjerrum isotach model via Equation A5.4.

$$C_\alpha = \frac{c\cdot\ln(10)}{1-\varepsilon} \quad \text{(A5.4)}$$

where;

c = secular strain rate coefficient from abc-isotach model
ε = average strain

The recompression ratio and the compression ratio are derived directly from the obtained compression curve of CRS test 6 as shown in Figure A5.1. Note that this serves as an initial parameter set which is optimised per simulation.

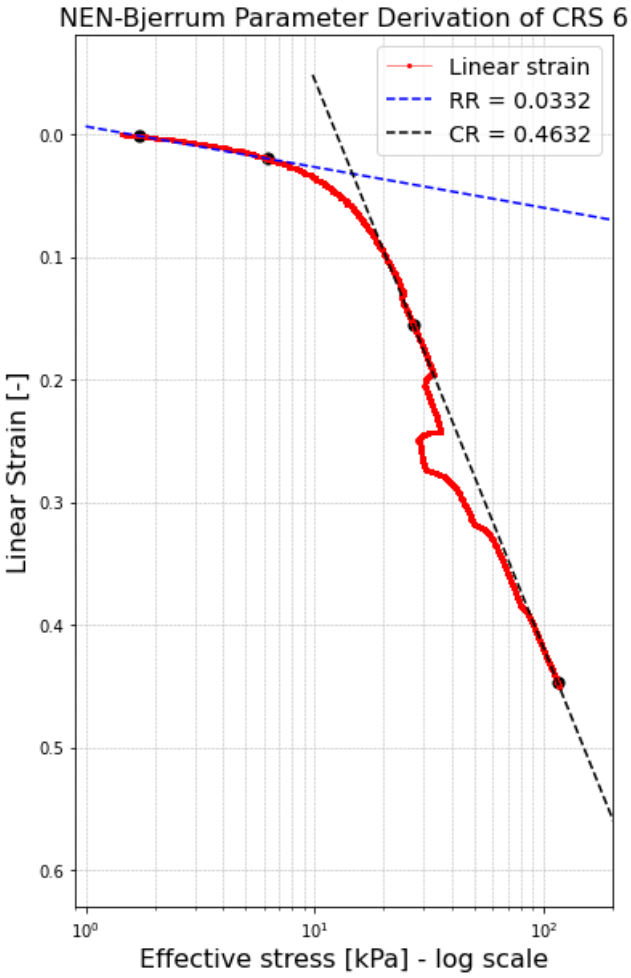

Figure A5.1:Determination of recompression- and compression ratios.

Therefore, based on the results on CRS test 6 the estimated parameters;

$$RR = \frac{\Delta\varepsilon_C^d}{\Delta\log(\sigma_v')} = 0.0332 \quad \text{(A5.5)}$$

$$CR = \frac{\Delta\varepsilon_C}{\Delta\log(\sigma_v')} = 0.4632 \quad \text{(A5.6)}$$

$$C_\alpha = = \frac{c \cdot \ln(10)}{1-\varepsilon} = 0.046 \quad \text{(A5.7)}$$

Appendix 6 Terzaghi 1D Parameter Derivation

Terzaghi's one-dimensional compression parameters can easily be calculated by plotting the change in void ratio vs. the logarithm of effective stress. This proves beneficial since these settlement parameters are widely used. The formal definition of the compression parameters are shown in Equation A6.1, Equation A6.2 and Equation A6.3.

Recompression index:

$$C_r = \frac{\Delta e^d}{\Delta \log(\sigma'_v)} \quad \text{where;} \quad (A6.1)$$

e^d = void ratio in reloading part of log *e* vs. log σ'_v graph [-]
σ'_v = effective stress [kPa]

Compression index:

$$C_c = \frac{\Delta e}{\Delta \log(\sigma'_v)} \quad \text{where;} \quad (A6.2)$$

e = void ratio in virgin part of log *e* vs. log σ'_v graph [-]
σ'_v = effective stress [kPa]

Secondary compression index:

$$C_{\alpha e} = \frac{\Delta e}{\Delta \log(t)} \quad \text{where;} \quad (A6.3)$$

e = void ratio [-]
t = time [s]

The Recompression index and the Compression index are determined by analysing the results of CRS test 6 as shown in Figure A6.1. In addition, the NEN-Bjerrum isotach parameters can be converted to 1D Terzaghi parameters as described in (Kooi et al., 2018). This approach is used to determine the secondary compression index since no creep phase is performed in CRS test 6. Note that this serves as an initial parameter set which is optimised per simulation.

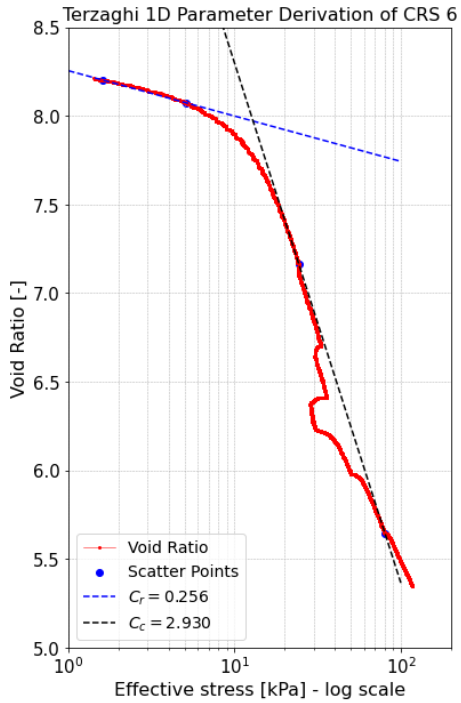

Figure A6.1: Determination of recompression and compression indices.

Regarding the results on CRS test 6 this the parameters as shown in A6.4, Equation A6.5 and Equation A6.6.

$$C_r = \frac{\Delta e^d}{\Delta \log(\sigma'_v)} = 0.256 \quad (A6.4)$$

$$C_c = \frac{\Delta e}{\Delta \log(\sigma'_v)} = 2.930 \quad (A6.5)$$

$$C_{\alpha e} = C_\alpha \cdot (1+e_0) = 0.4232 \quad (A6.6)$$

Appendix 7 Y&W EVP Model Parameter Derivation

The Elasto-Viscoplastic model of Yuan and Whittle can be used to model different strain rate effects in CRS testing (Yuan and Whittle, 2018). Note that the constitutive behaviour that describes the relationship between the reduction of pore volumes and effective stress is plotted as log *e* vs. log σ'_v in this EVP model. The formal definition of these parameters is shown in Equation A7.1, Equation A7.2 and Equation A7.3.

Elastic unloading/reloading parameter:

$$\rho_r = \frac{\Delta \log (e^d)}{\Delta \log (\sigma'_v)} = 0.434 \frac{C_r}{e} \quad \text{(A7.1)}$$

where;

C_r = Terzaghi 1D recompression index [-]
e^d = void ratio in reloading part of log *e* vs. log σ'_v graph [-]
σ'_v = effective stress [-]

Virgin compression parameter: (A7.2)

$$\rho_c = \frac{\Delta \log (e)}{\Delta \log (\sigma'_v)} = 0.434 \frac{C_c}{e}$$

where;

C_c = Terzaghi 1D compression index [-]
e = void ratio in virgin part of log *e* vs. log σ'_v graph [-]
σ'_v = effective stress [-]

Creep behaviour parameter

$$\rho_\alpha = \frac{\Delta \log (e)}{\Delta \log (t)} = 0.434 \frac{C_\alpha}{e} \quad \text{(A7.3)}$$

where;

C_α = Terzaghi 1D secondary compression index [-]
e = void ratio in virgin part of log *e* vs. log σ'_v graph [-]
t = time [s]

Note that the model parameters are derived w.r.t. the reference strain rate $\dot{\varepsilon}_{ref}$. The elastic unloading/reloading parameter and the virgin compression parameter are determined by analysing the results of CRS test 6 as shown in Figure A7.1. In addition, the creep parameter is approximated via Equation A7.3. Note that this serves as an initial parameter set which is optimised per simulation.

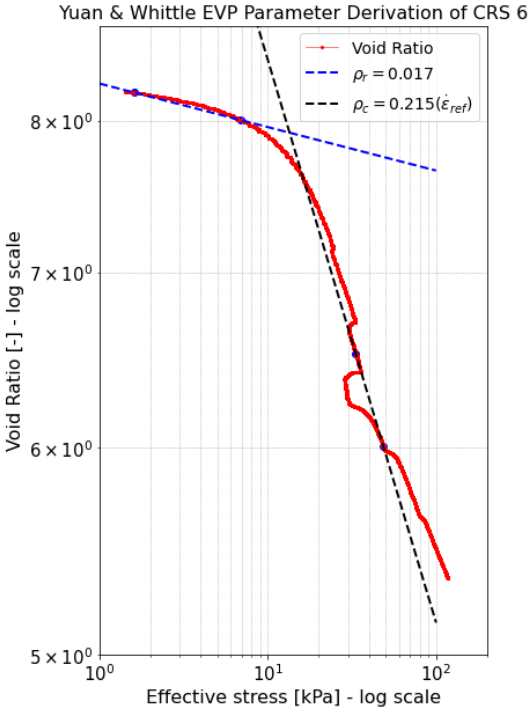

Figure A7.1: Determination of main compression parameters of MIT EVP model.

Regarding the results of CRS test 6 this yields the parameters as shown in Equation A7.4, A7.5 and A7.6.

$$\rho_r = \frac{\Delta \log (e^d)}{\Delta \log (\sigma'_v)} = 0.017 \quad \text{(A7.4)}$$

$$\rho_c = \frac{\Delta \log (e)}{\Delta \log (\sigma'_v)} = 0.215 \quad \text{(A7.5)}$$

$$\rho_\alpha = 0.434 \frac{C_\alpha}{e} = 0.022 \quad \text{(A7.6)}$$

Appendix 8 CRS Test Results

This appendix shows the effective stress vs. natural strain plots of the performed CRS tests. Of each performed test the following graphs are shown;

- Effective stress vs Natural strain.
- Polynomial fits through part of each different isotach.
- Tangent lines through part of each visualised isotach including the subsequent functions.
- Tangent lines through each unique strain rate.

Note that it has been concluded that the first strain rate of $\dot{\varepsilon} = 10^{-6}$ s^{-1} with a total displacement of 4.0 mm was not enough to fully load the peat sample past its yield stress. As a result, no isotach through this strain rate is drawn in the results shown in this annex.

The following order of results is shown in this appendix;

1. CRS 3
2. CRS 4
3. CRS 5
4. CRS 6
5. CRS 7
6. CRS Creep Test
7. CRS Rapid Transition Test

CRS test 1 resulted in too much excess generated pore pressure being generated as a result of a too high applied displacement rate. This test was therefore stopped prematurely. CRS test 1.2 is used to determine the yield stress as shown in Annex 3. Subsequently, this test is not shown in this annex since changes rate of displacement are applied. CRS test 2 failed due to technical difficulties during testing. The CRS Rapid Transition Test had to be repeated because of wood substantially larger than the peat fibres being present in the soil sample. Annex 12 describes this test.

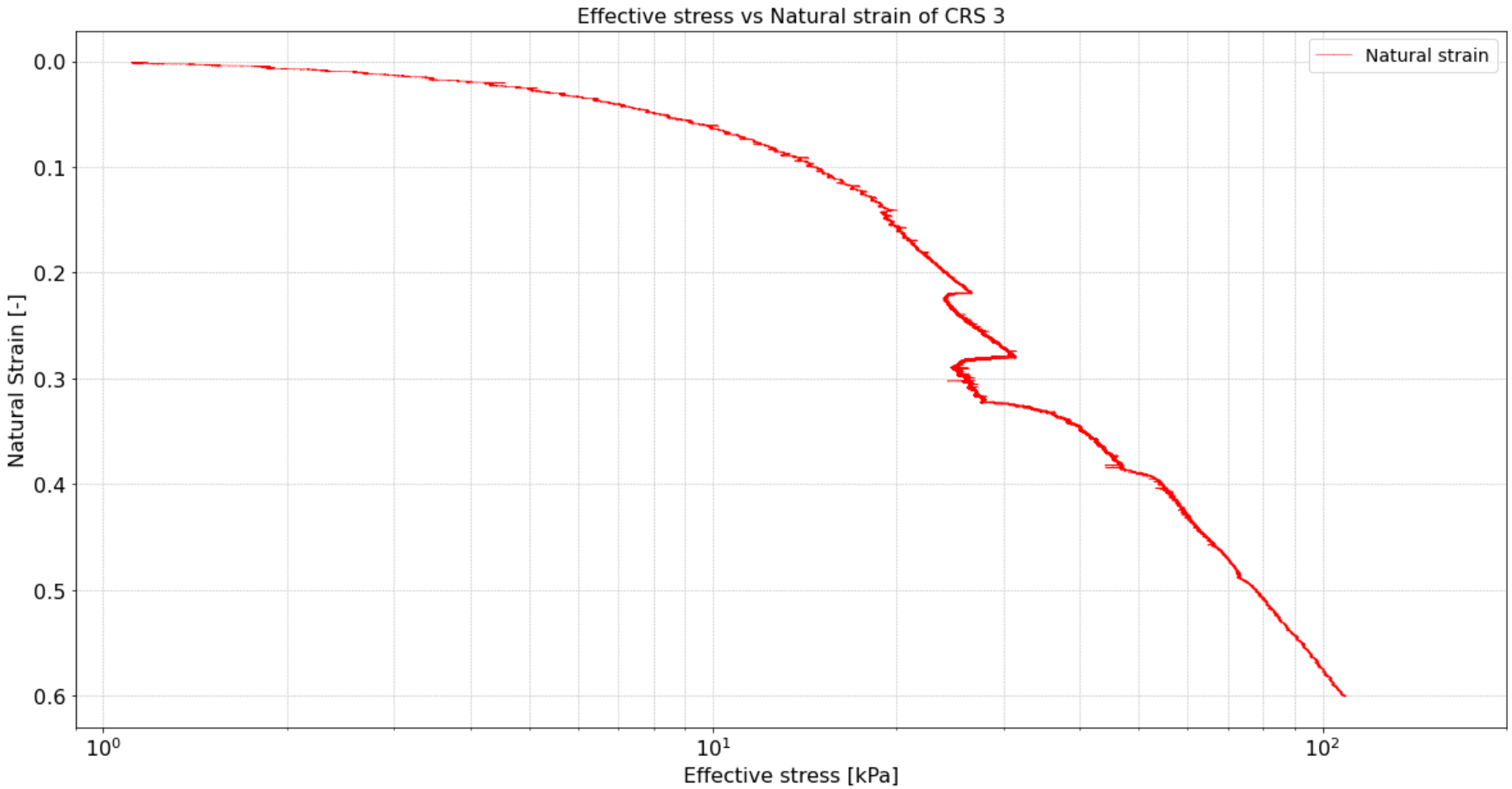

Figure A8.1:Effective stress vs natural strain of CRS 3. Effective stress is plotted on base-10 logarithmic scale.

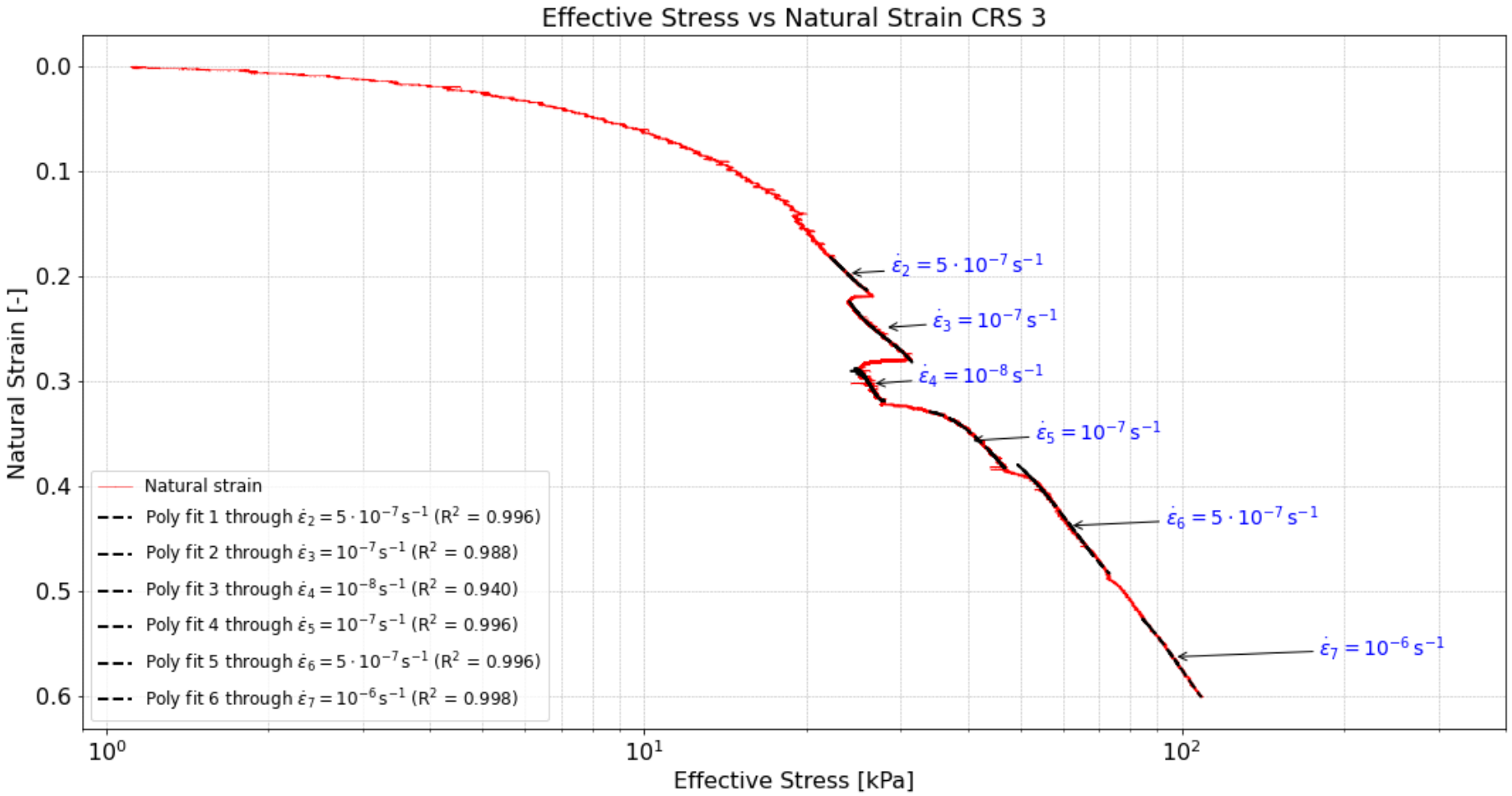

Figure A8.2: Effective stress vs natural strain of CRS 3 with polynomials fitted through different visualised isotachs. Effective stress is plotted on base-10 logarithmic scale.

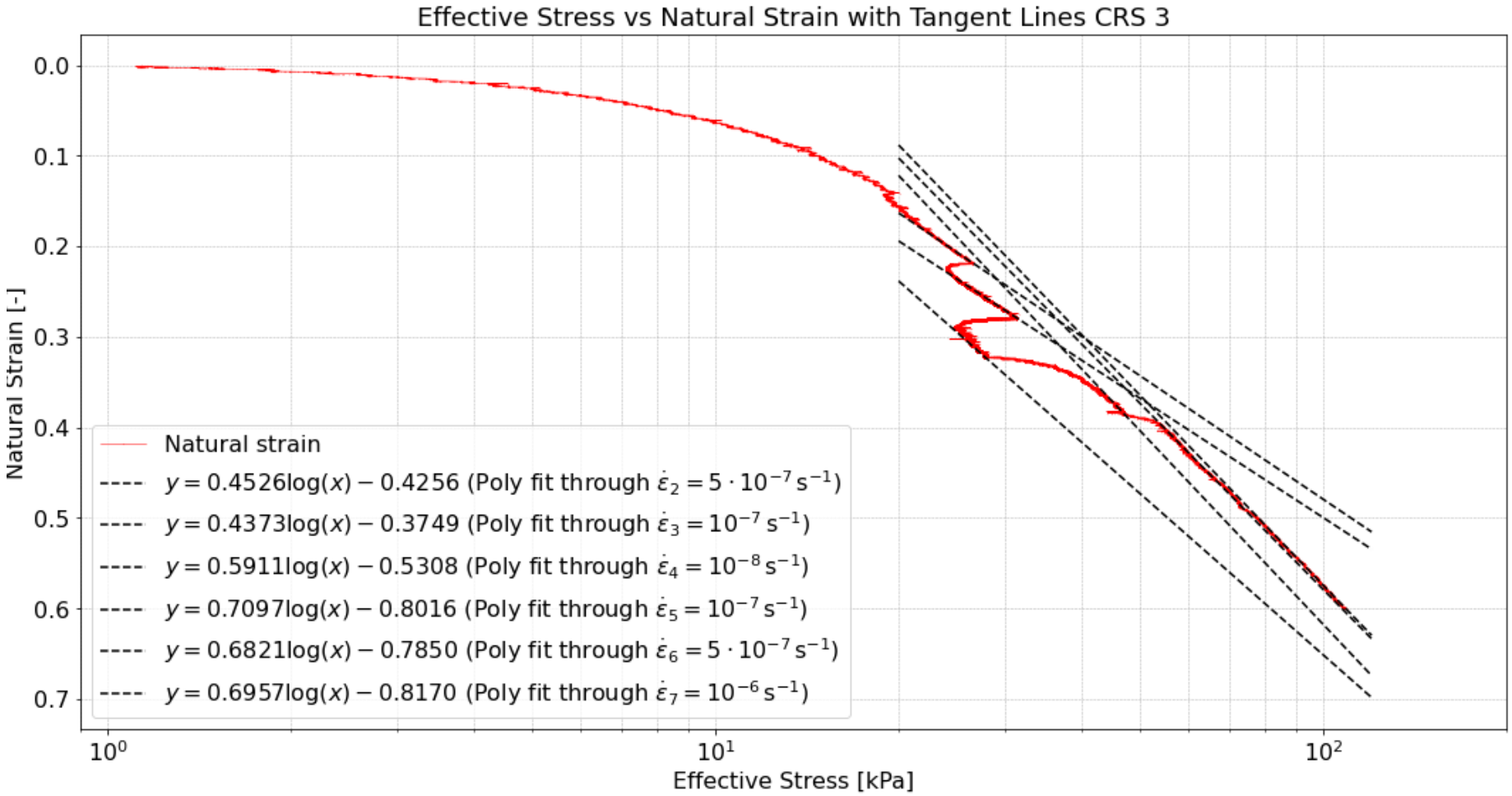

Figure A8.3: Effective stress vs natural strain of CRS 3 with tangent lines plotted through each different visualised isotach. Effective stress is plotted on base-10 logarithmic scale.

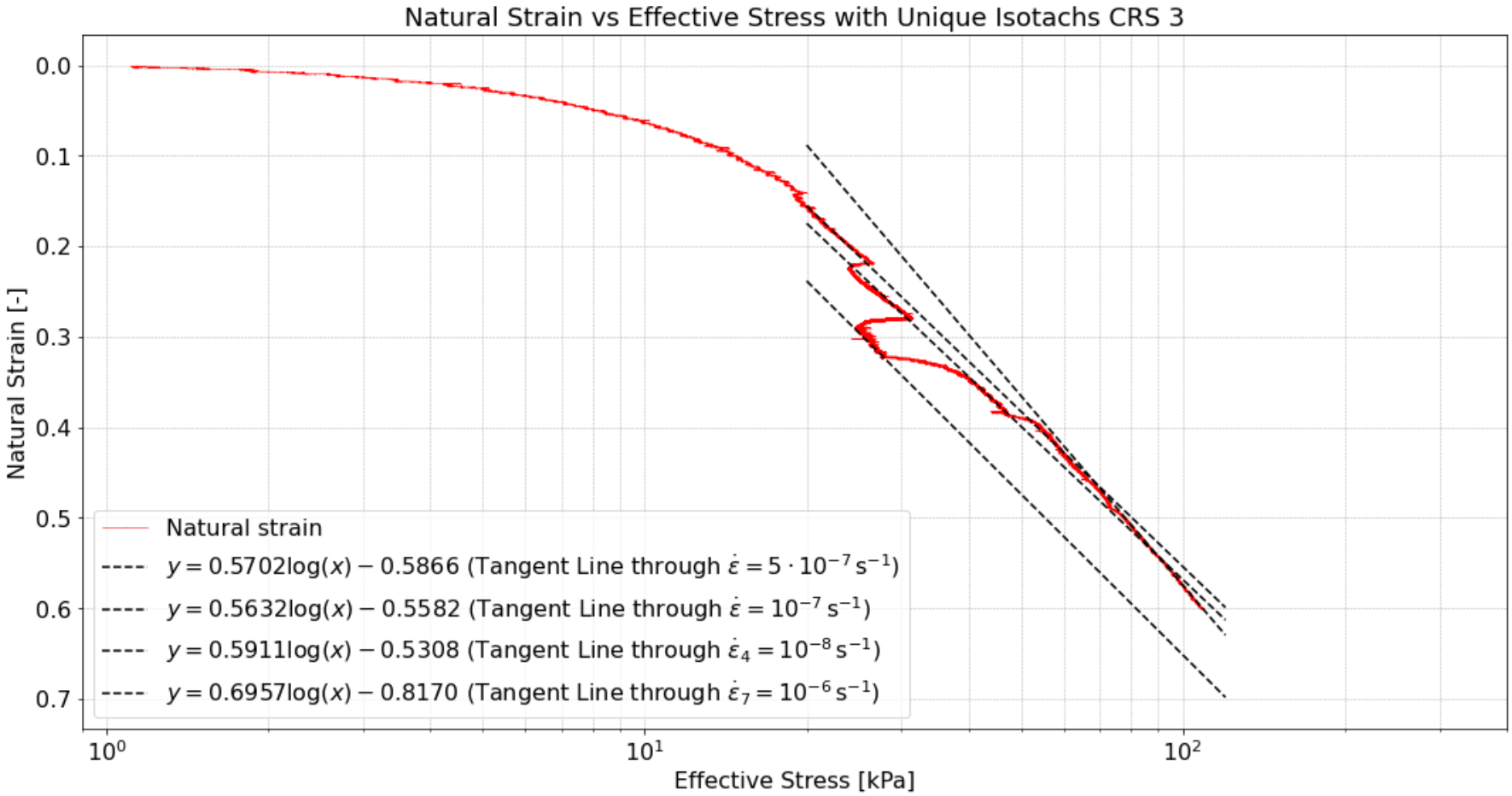

Figure A8.4: Effective stress vs natural strain of CRS 3 with tangent lines plotted through each unique strain rate. Effective stress is plotted on base-10 logarithmic scale.

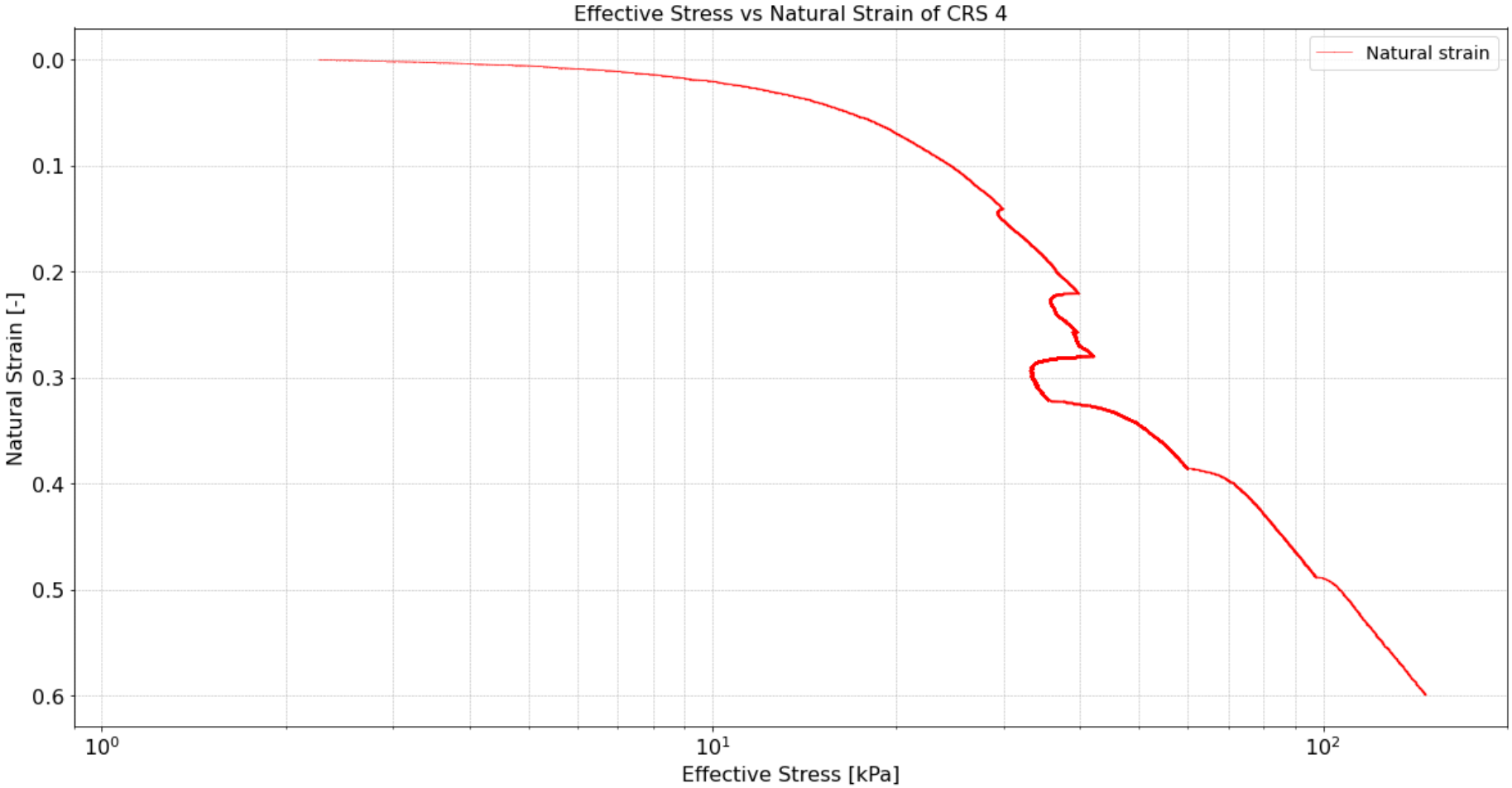

Figure A8.5: Effective stress vs natural strain of CRS 4. Effective stress is plotted on base-10 logarithmic scale.

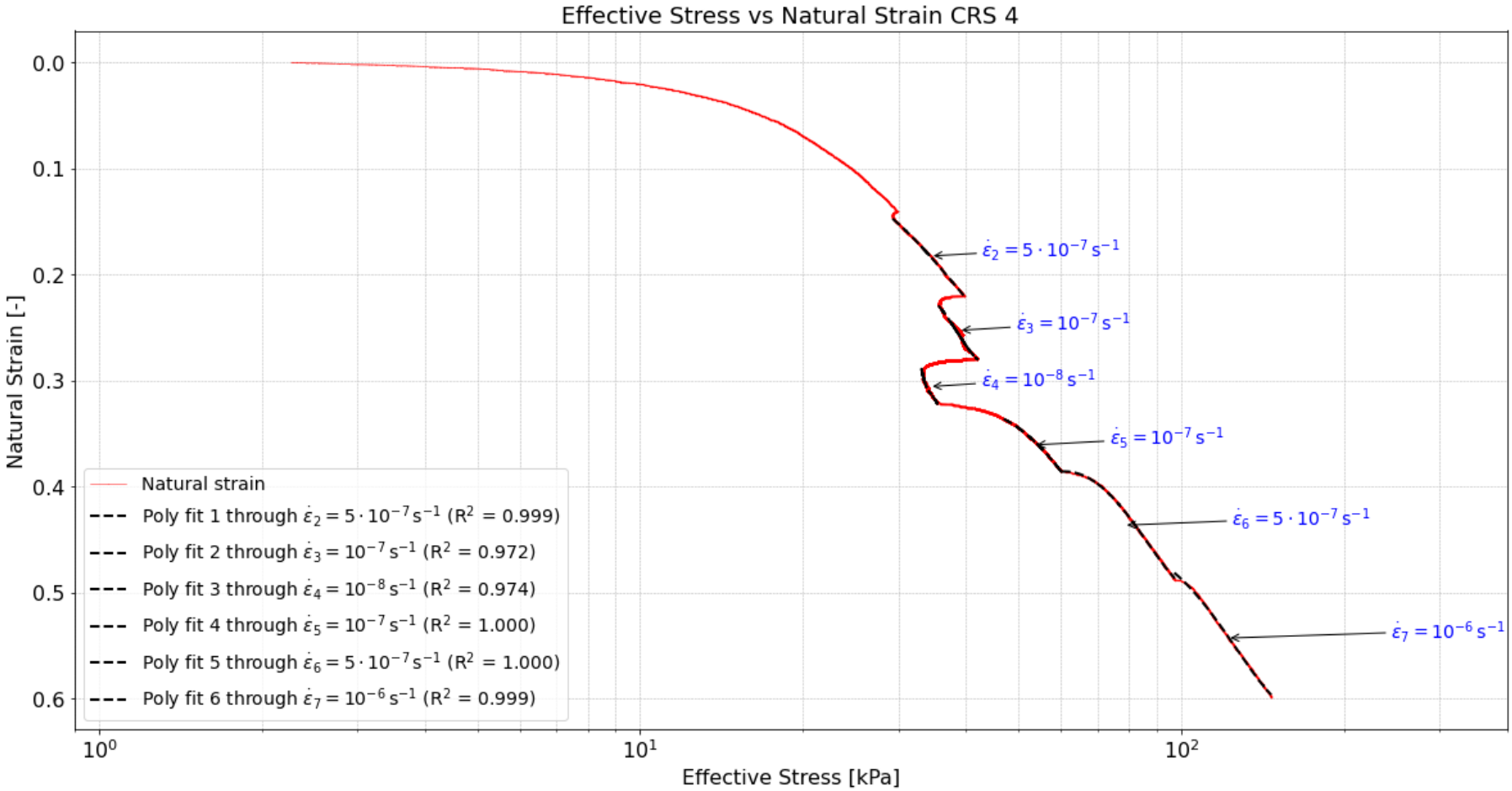

Figure A8 6: Effective stress vs natural strain of CRS 4 with polynomials fitted through different visualised isotachs. Effective stress is plotted on base-10 logarithmic scale.

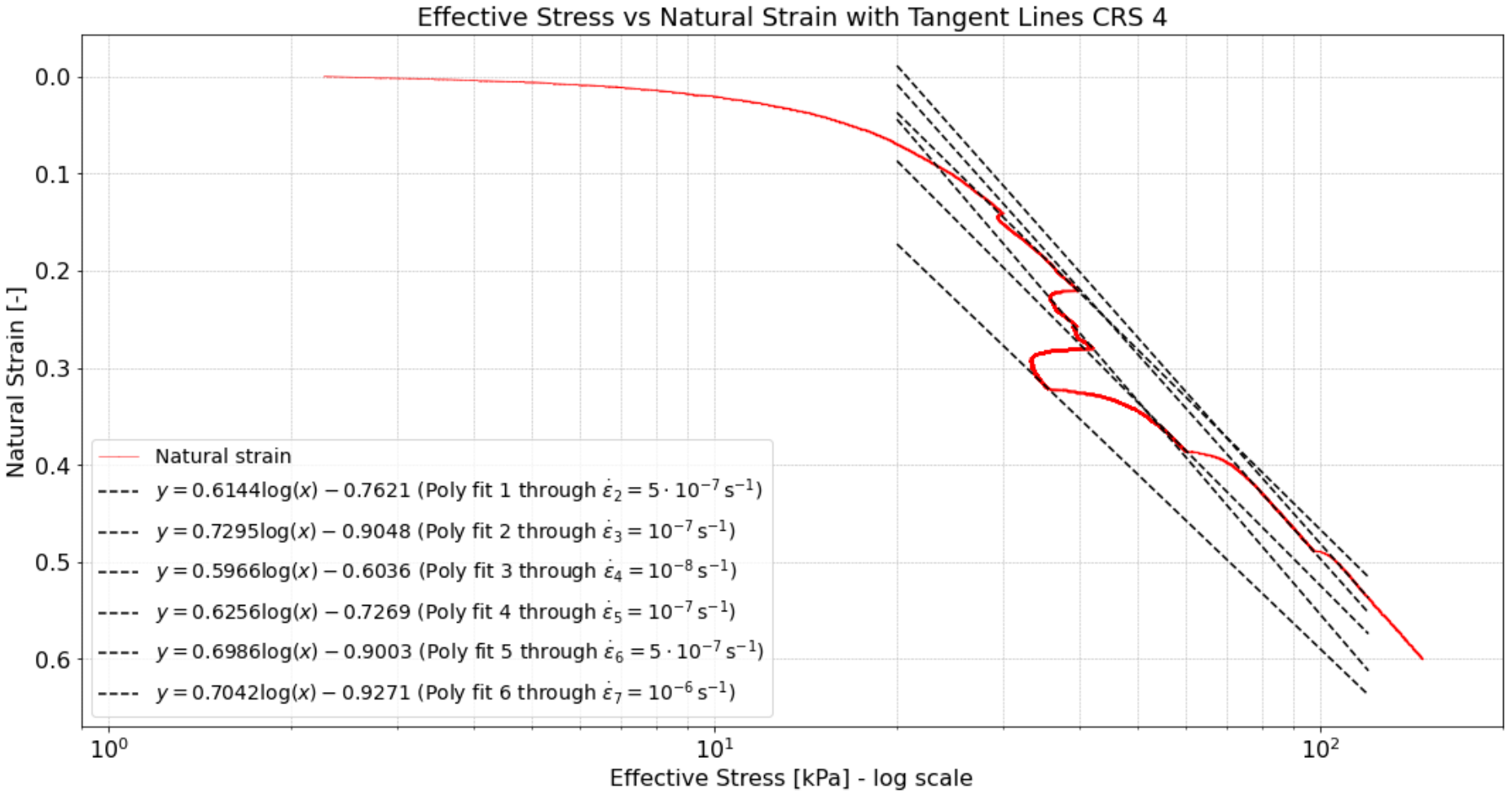

Figure A8.7: Effective stress vs natural strain of CRS 4 with tangent lines plotted through each different visualised isotach. Effective stress is plotted on base-10 logarithmic scale.

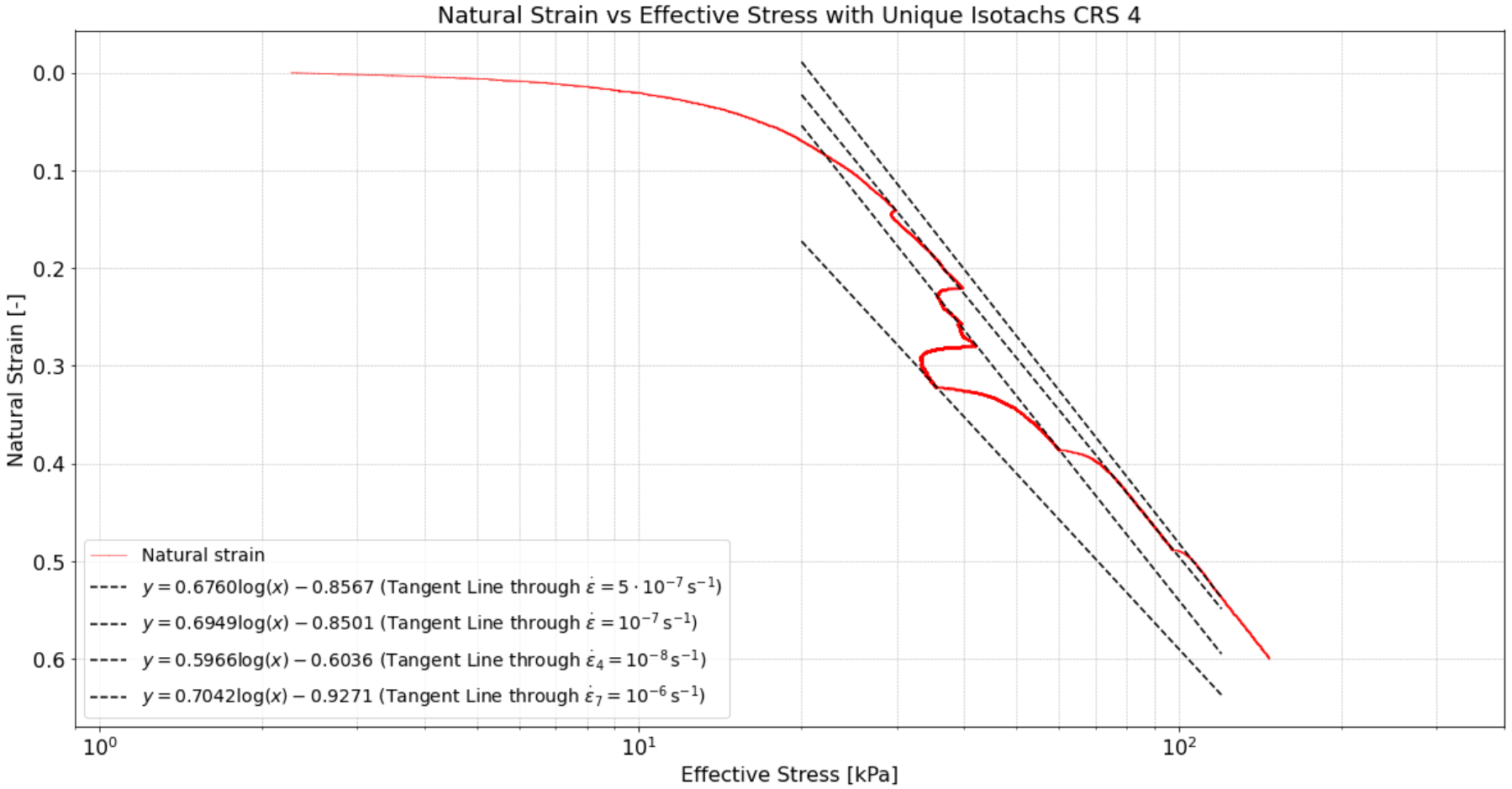

Figure A8.8: Effective stress vs natural strain of CRS 4 with tangent lines plotted through each unique strain rate. Effective stress is plotted on base-10 logarithmic scale.

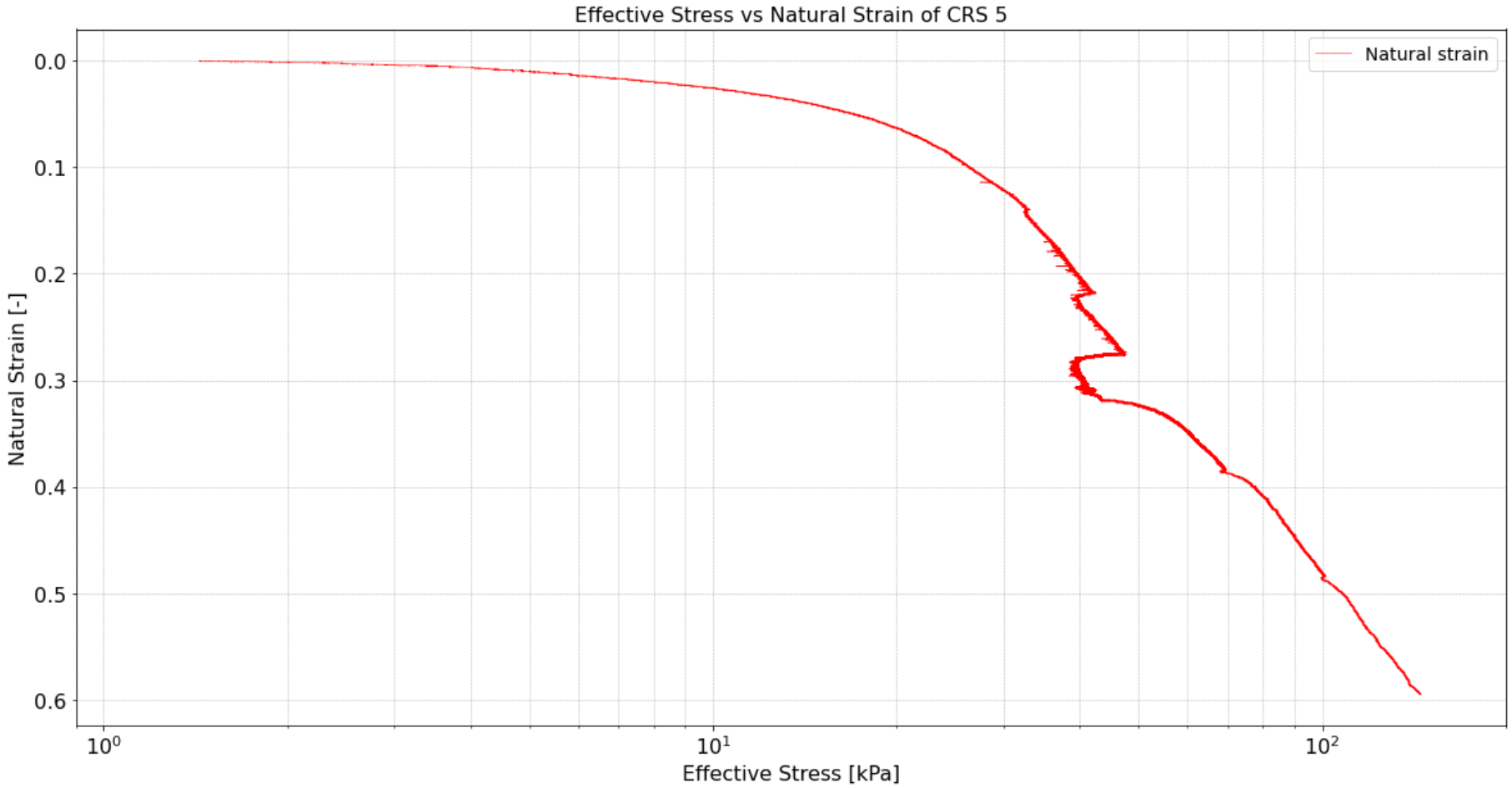

Figure A8.9: Effective stress vs natural strain of CRS 5. Effective stress is plotted on base-10 logarithmic scale.

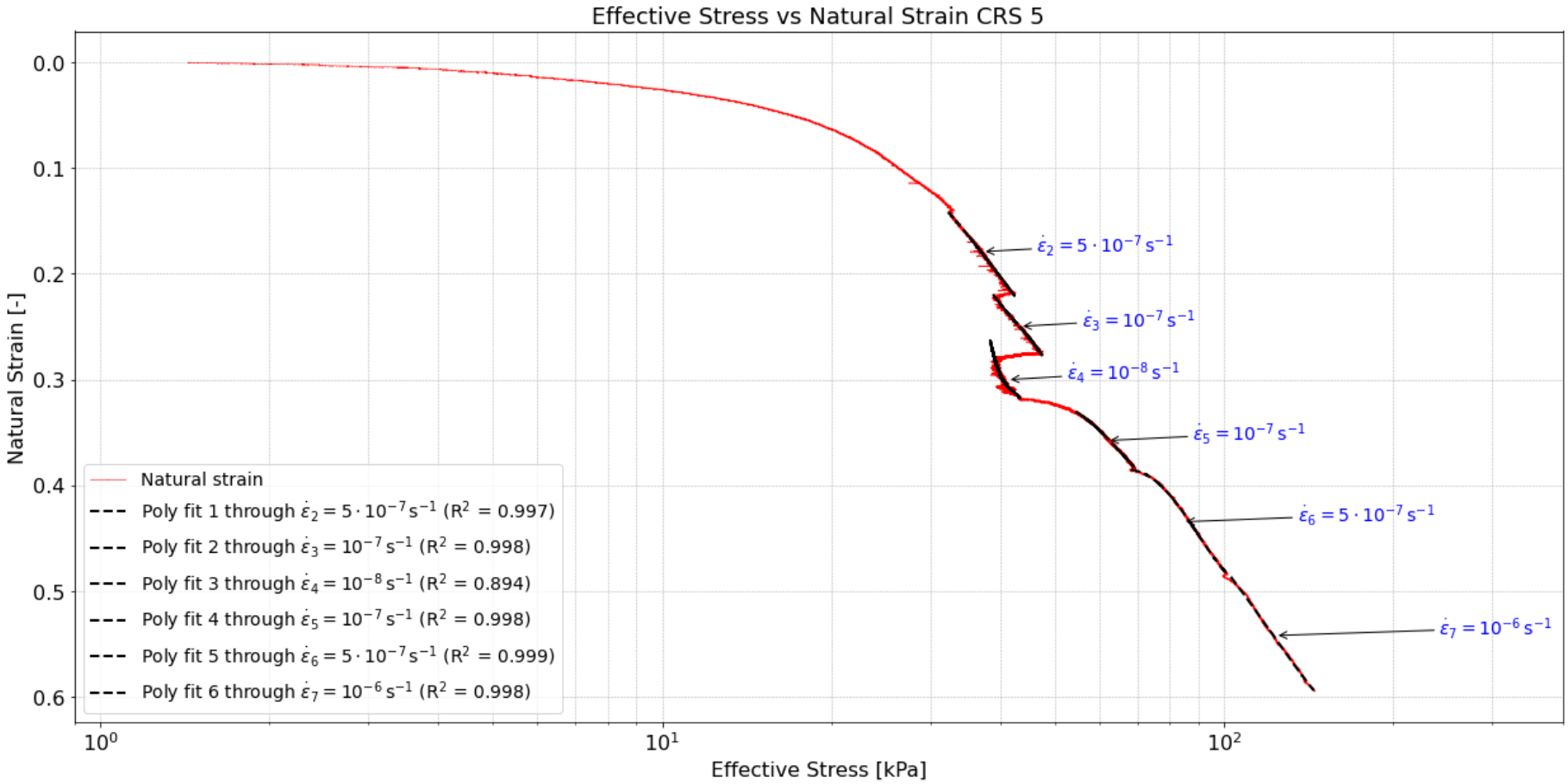

Figure A8.10: Effective stress vs natural strain of CRS 5 with polynomials fitted through different visualised isotachs. Effective stress is plotted on base-10 logarithmic scale.

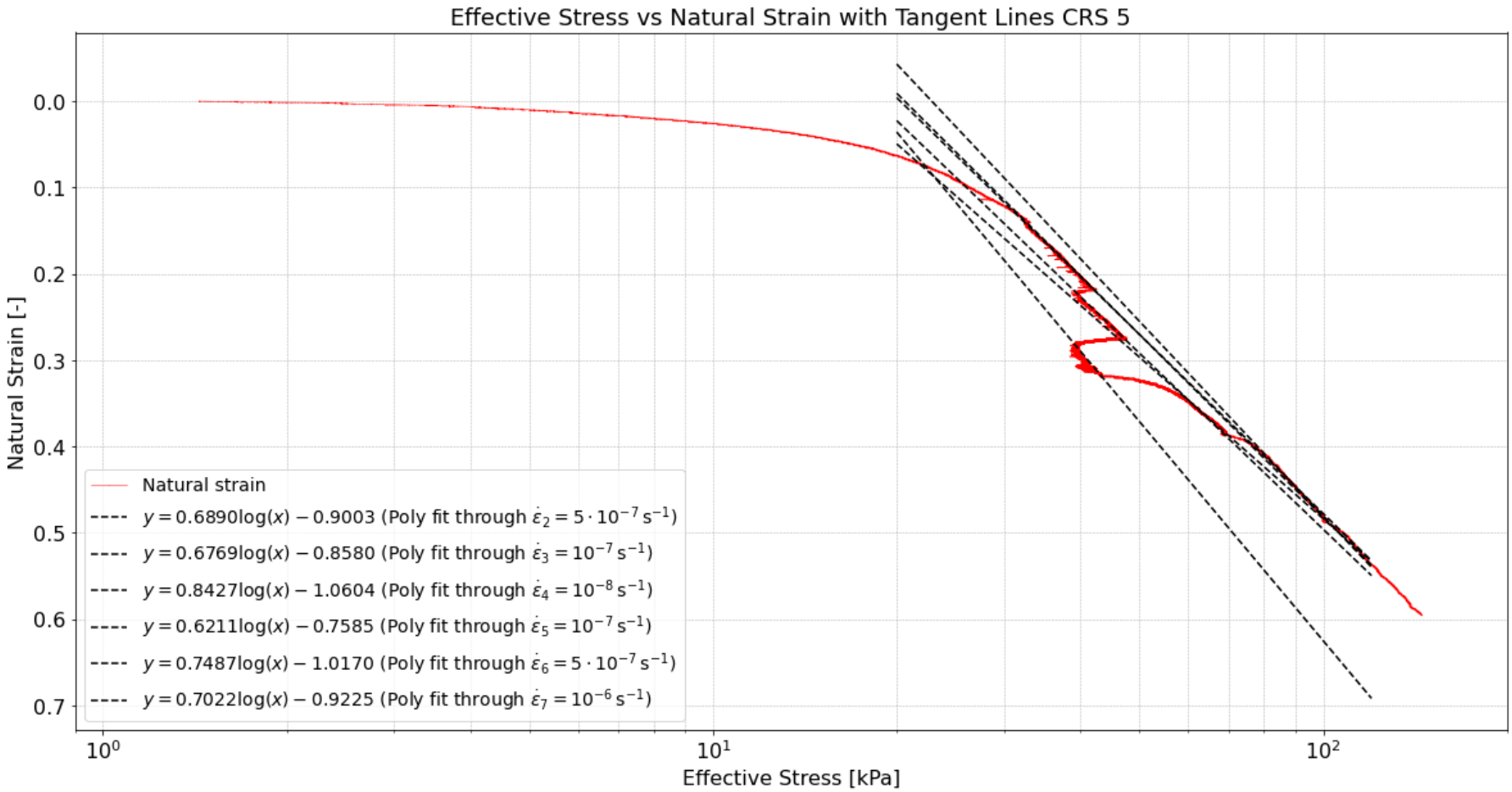

Figure A8.11: Effective stress vs natural strain of CRS 5 with tangent lines plotted through each different visualised isotach. Effective stress is plotted on base-10 logarithmic scale.

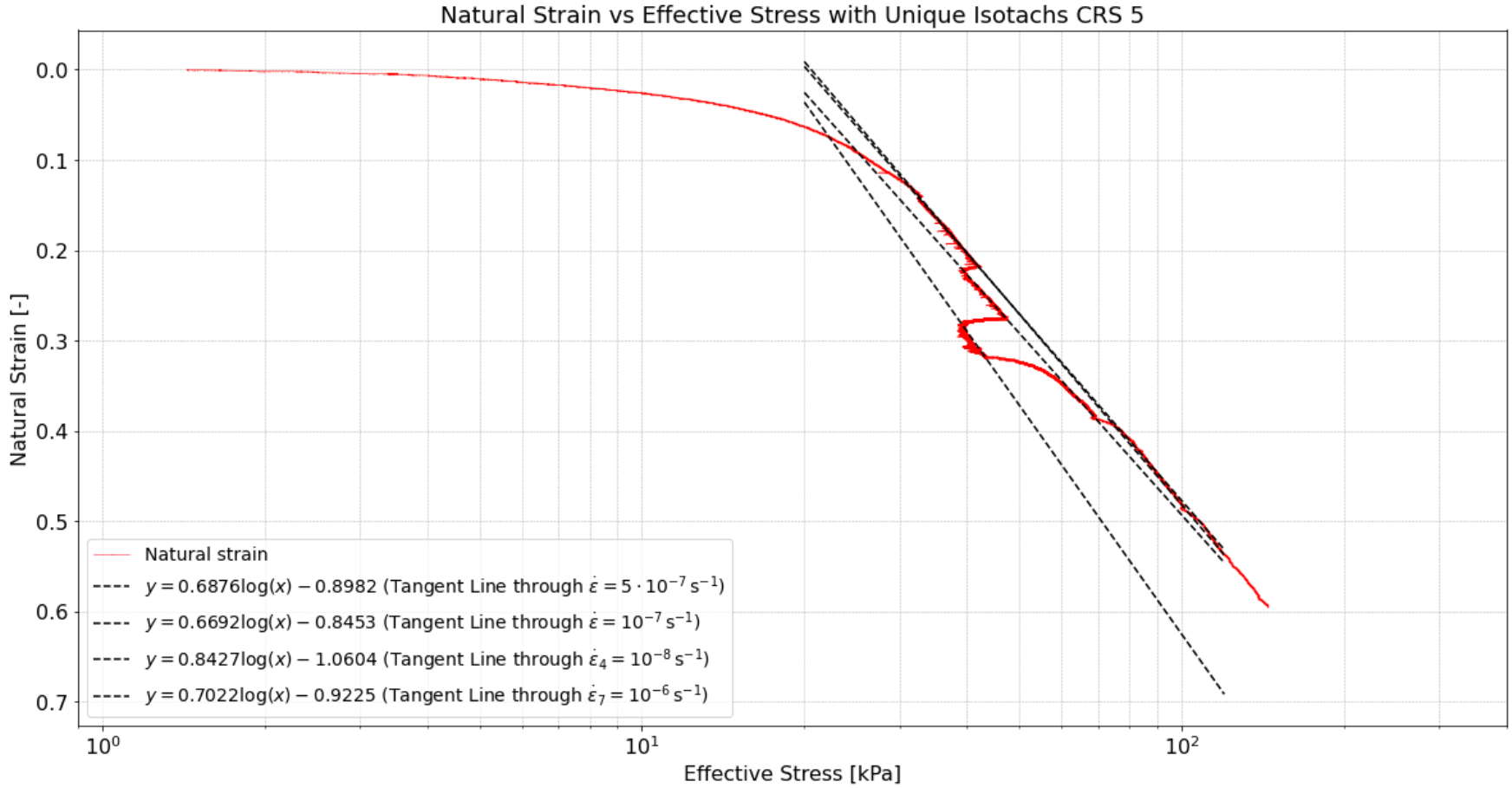

Figure A8.12: Effective stress vs natural strain of CRS 5 with tangent lines plotted through each unique strain rate. Effective stress is plotted on base-10 logarithmic scale.

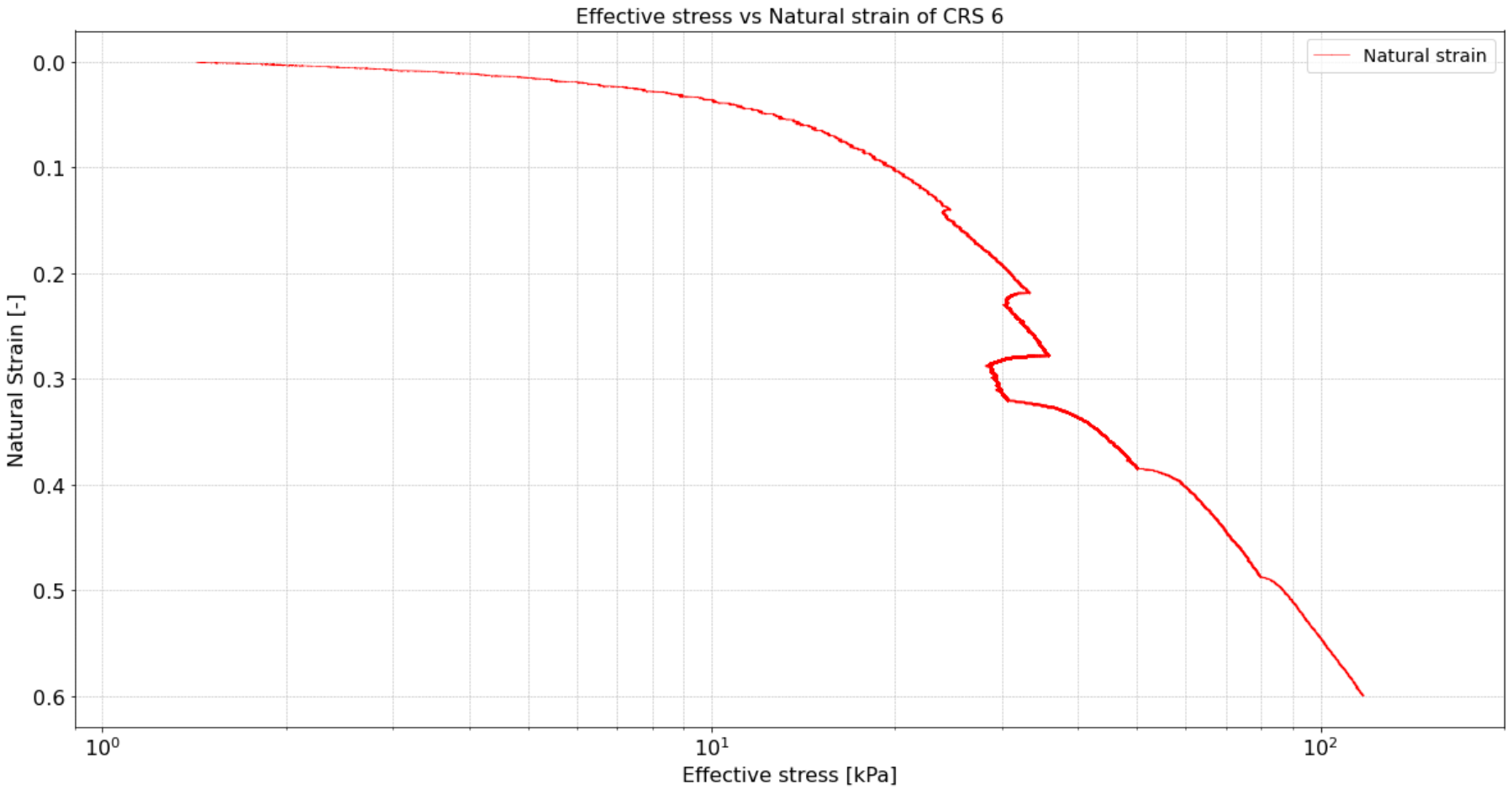

Figure A8.13: Effective stress vs natural strain of CRS 6. Effective stress is plotted on base-10 logarithmic scale.

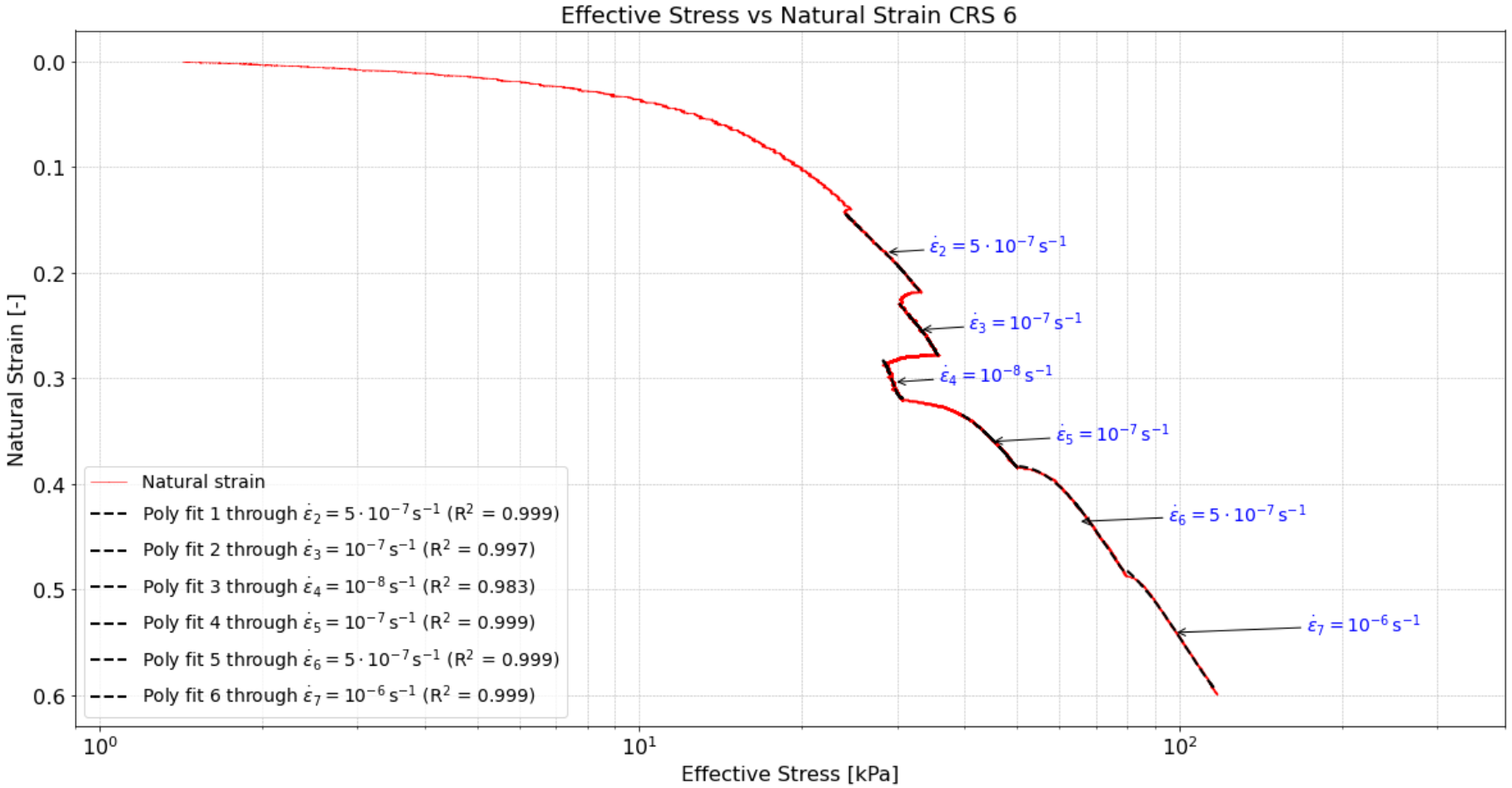

Figure A8.14: Effective stress vs natural strain of CRS 6 with polynomials fitted through different visualised isotachs. Effective stress is plotted on base-10 logarithmic scale.

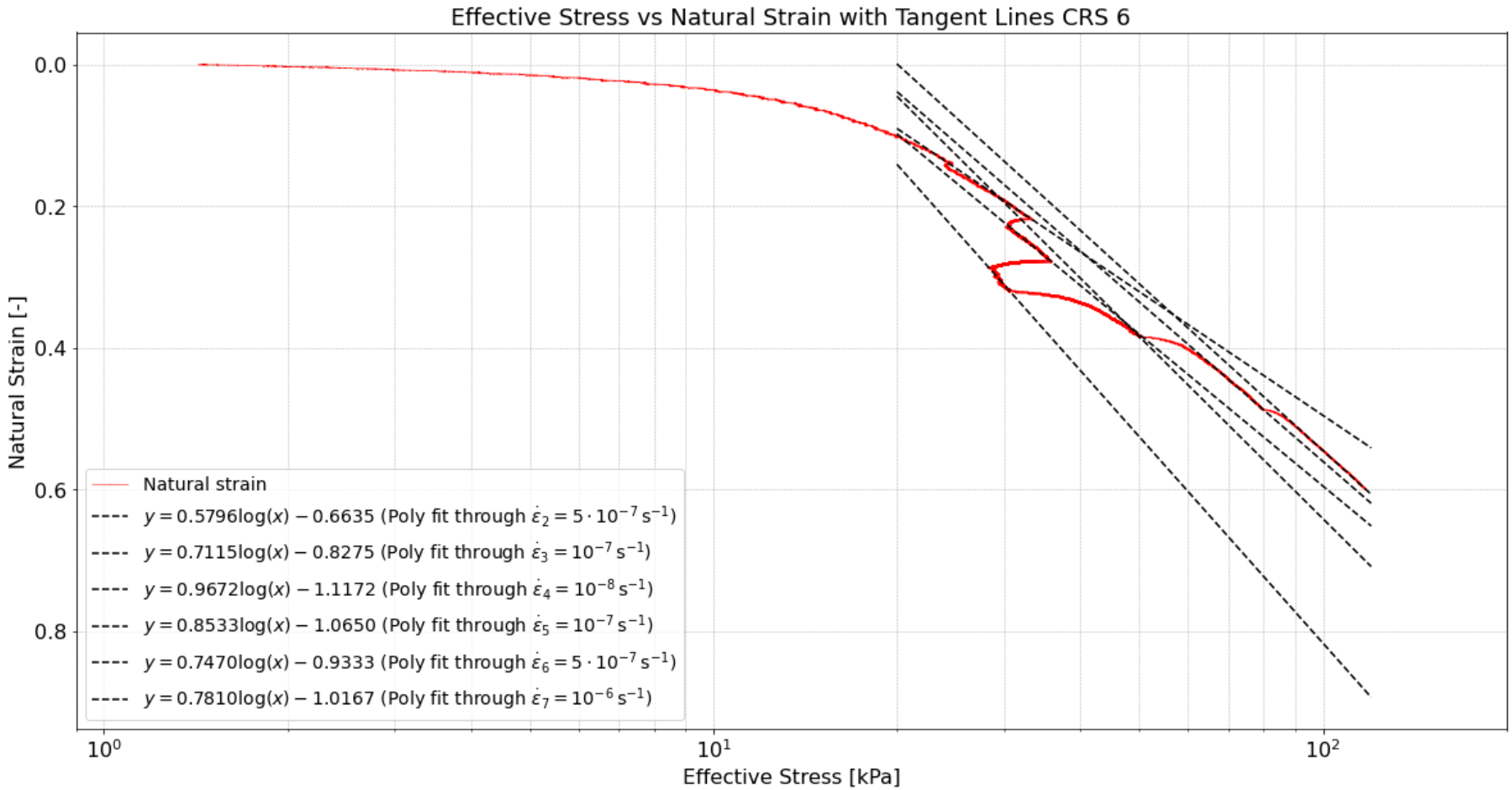

Figure A8.15: Effective stress vs natural strain of CRS 6 with tangent lines plotted through each different visualised isotach. Effective stress is plotted on base-10 logarithmic scale.

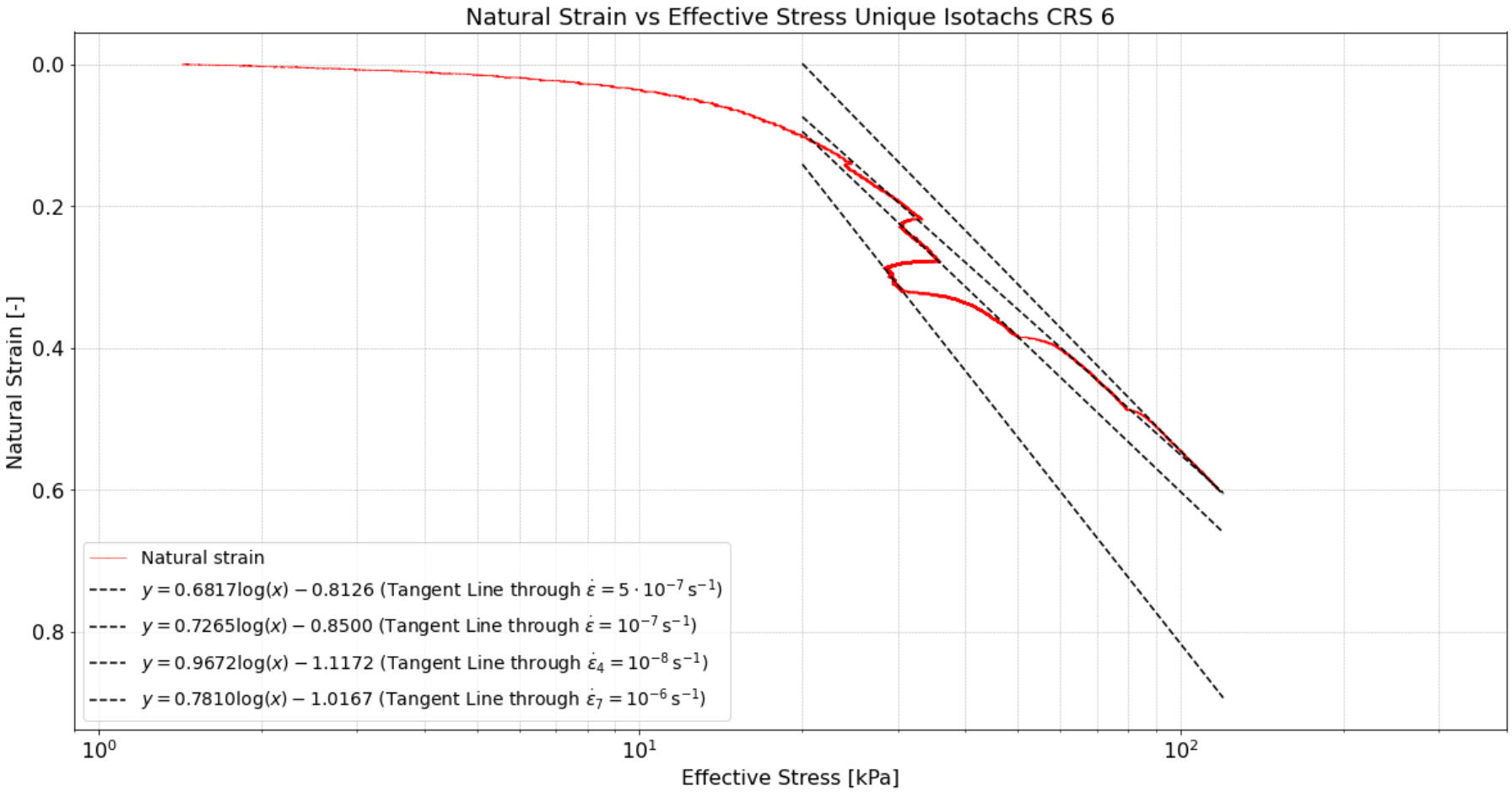

Figure A8.16: Effective stress vs natural strain of CRS 6 with tangent lines plotted through each unique strain rate. Effective stress is plotted on base-10 logarithmic scale.

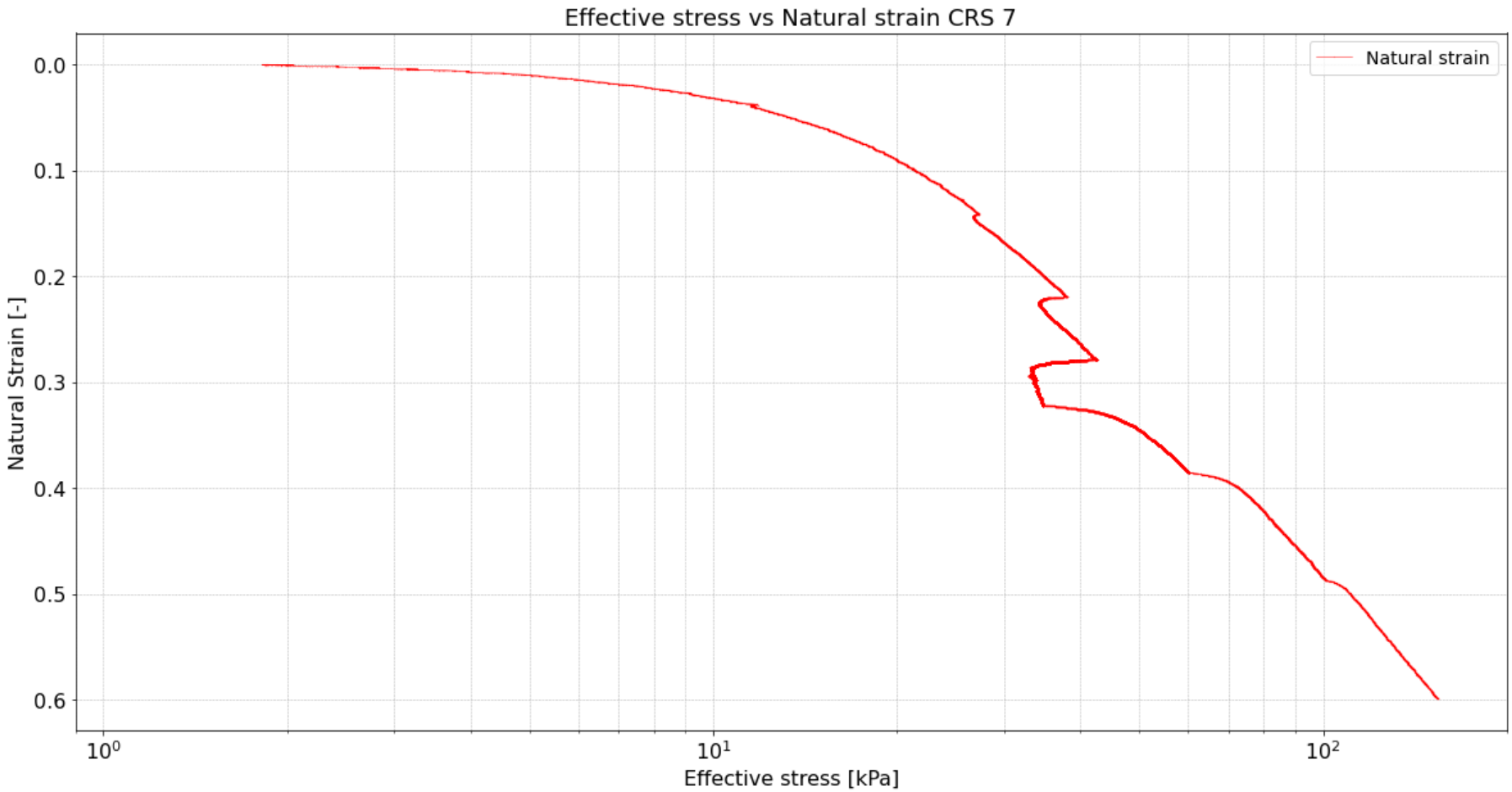

Figure A8.17: Effective stress vs natural strain of CRS 7. Effective stress is plotted on base-10 logarithmic scale.

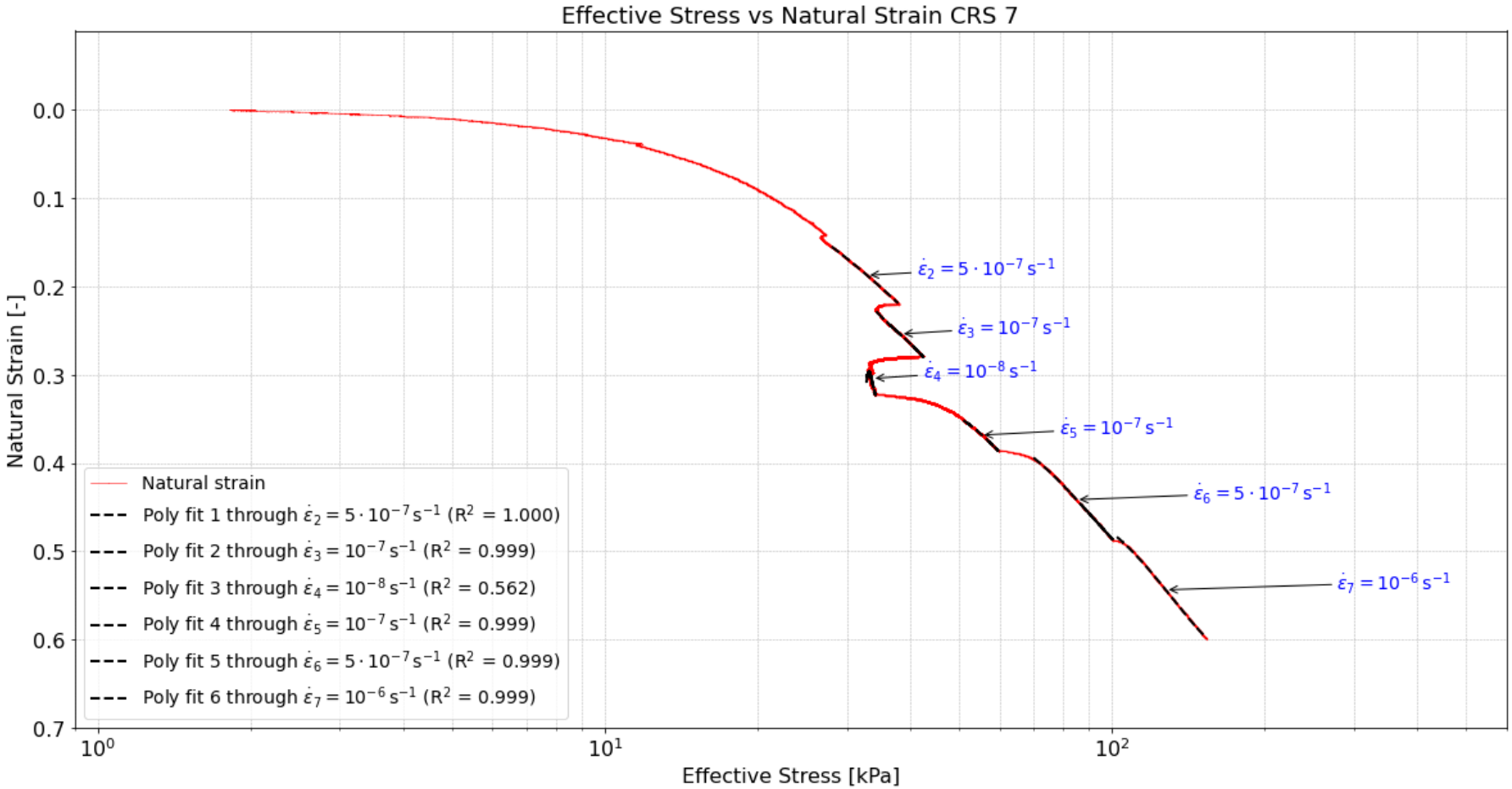

Figure A8.18: Effective stress vs natural strain of CRS 7 with polynomials fitted through different visualised isotachs. Effective stress is plotted on base-10 logarithmic scale.

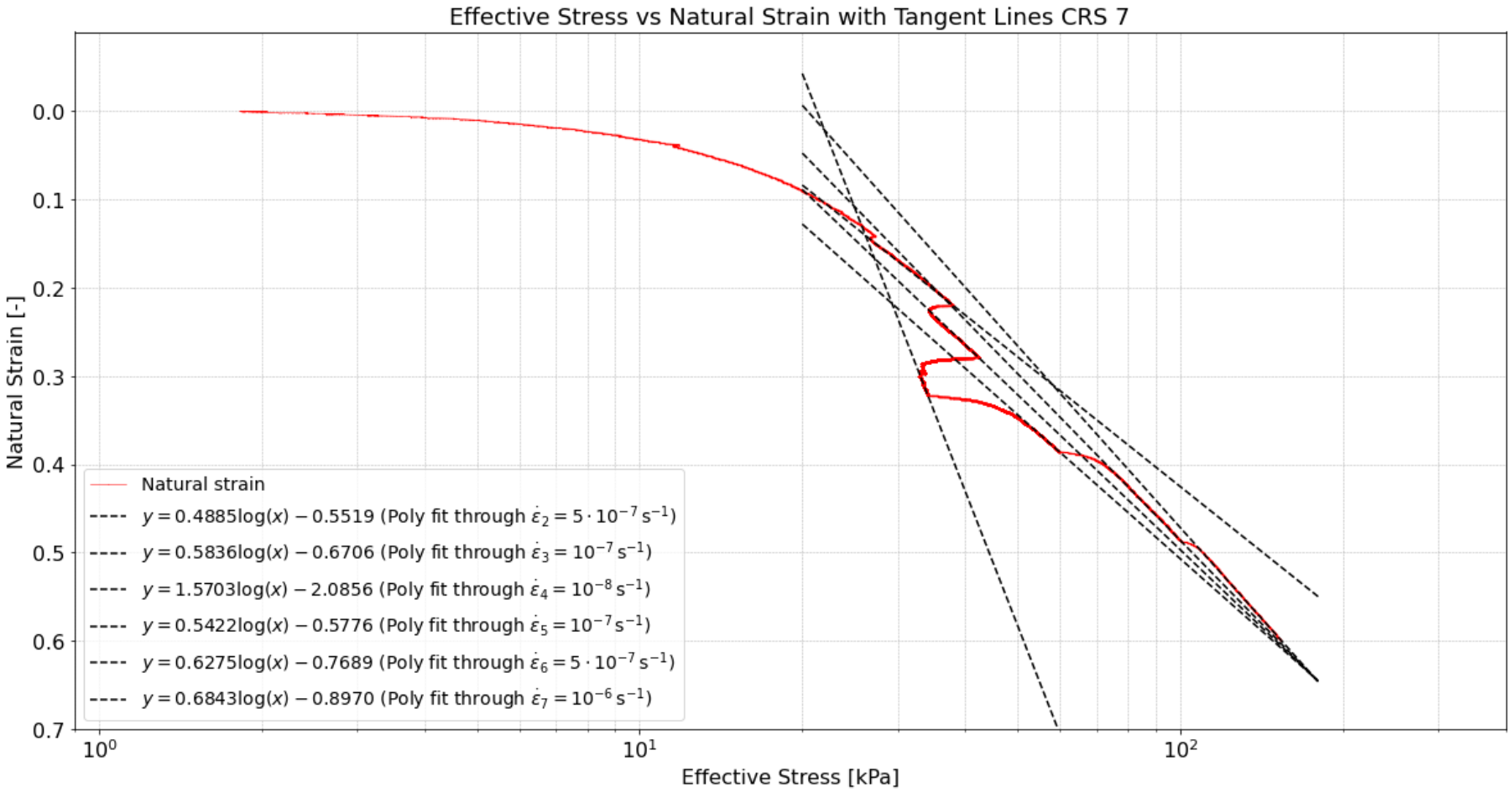

Figure A8.19: Effective stress vs natural strain of CRS 7 with tangent lines plotted through each different visualised isotach. Effective stress is plotted on base-10 logarithmic scale.

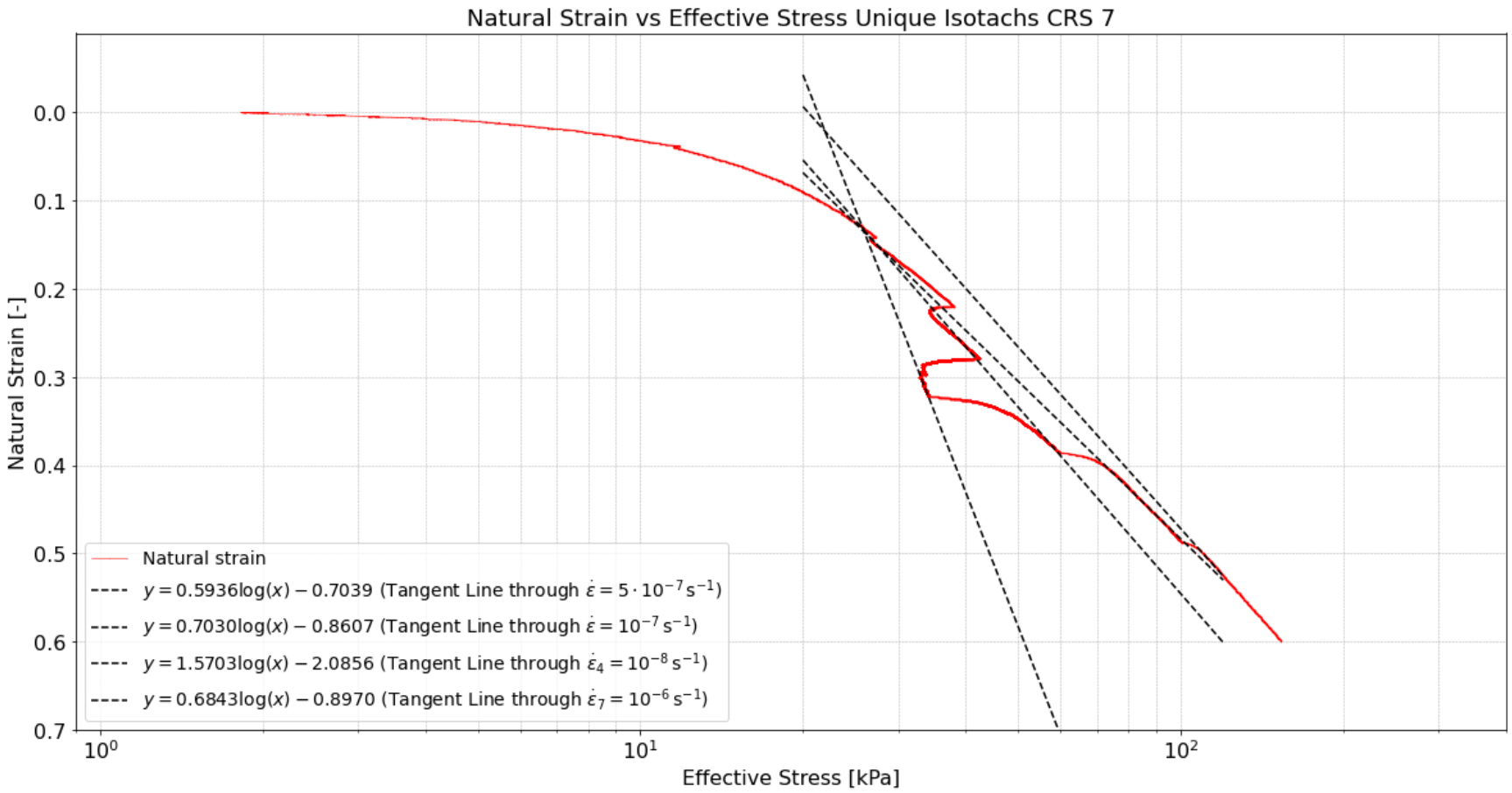

Figure A8.20: Effective stress vs natural strain of CRS 7 with tangent lines plotted through each unique strain rate. Effective stress is plotted on base-10 logarithmic scale.

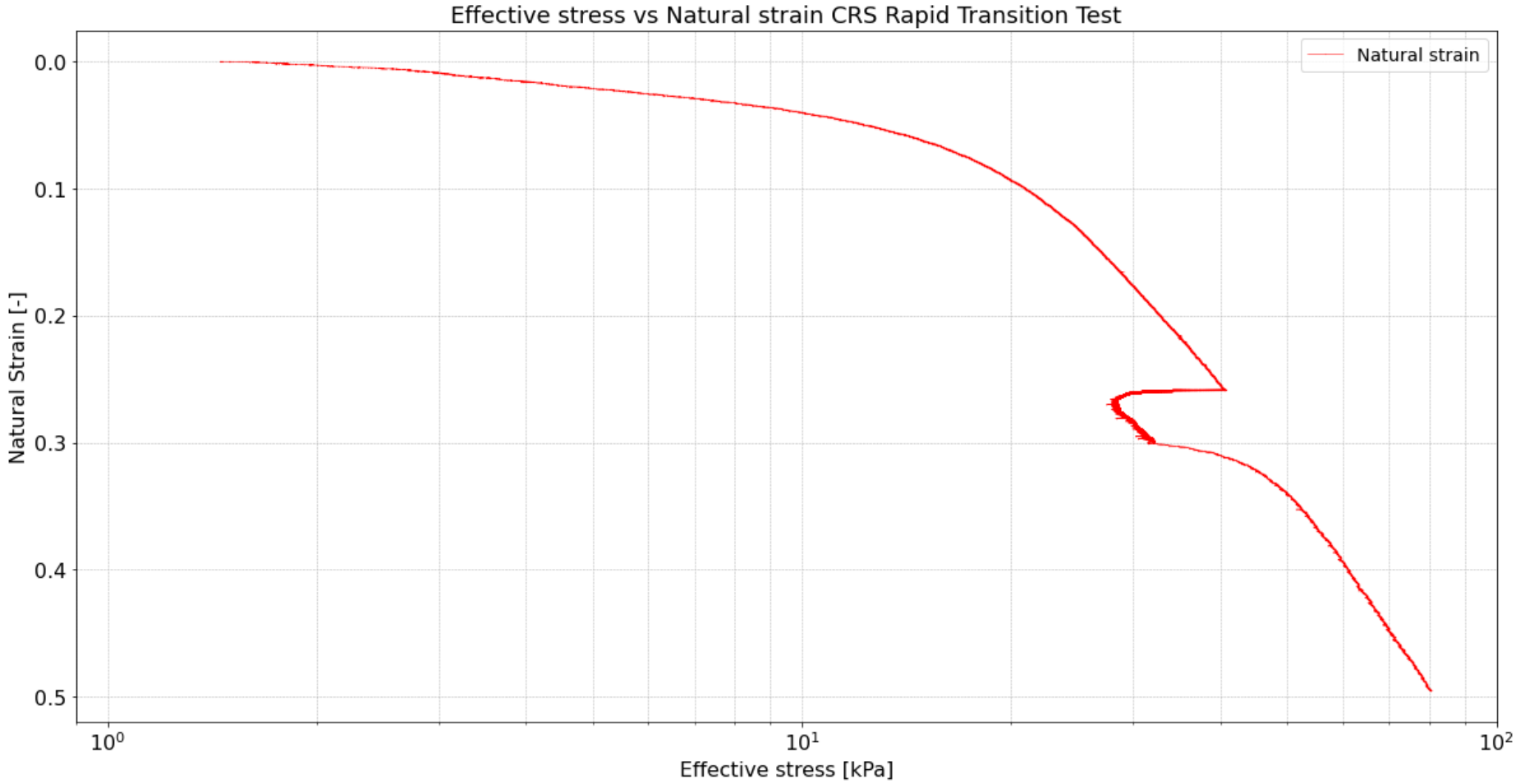

Figure A8.21: Effective stress vs natural strain of CRS Creep Test. Effective stress is plotted on base-10 logarithmic scale.

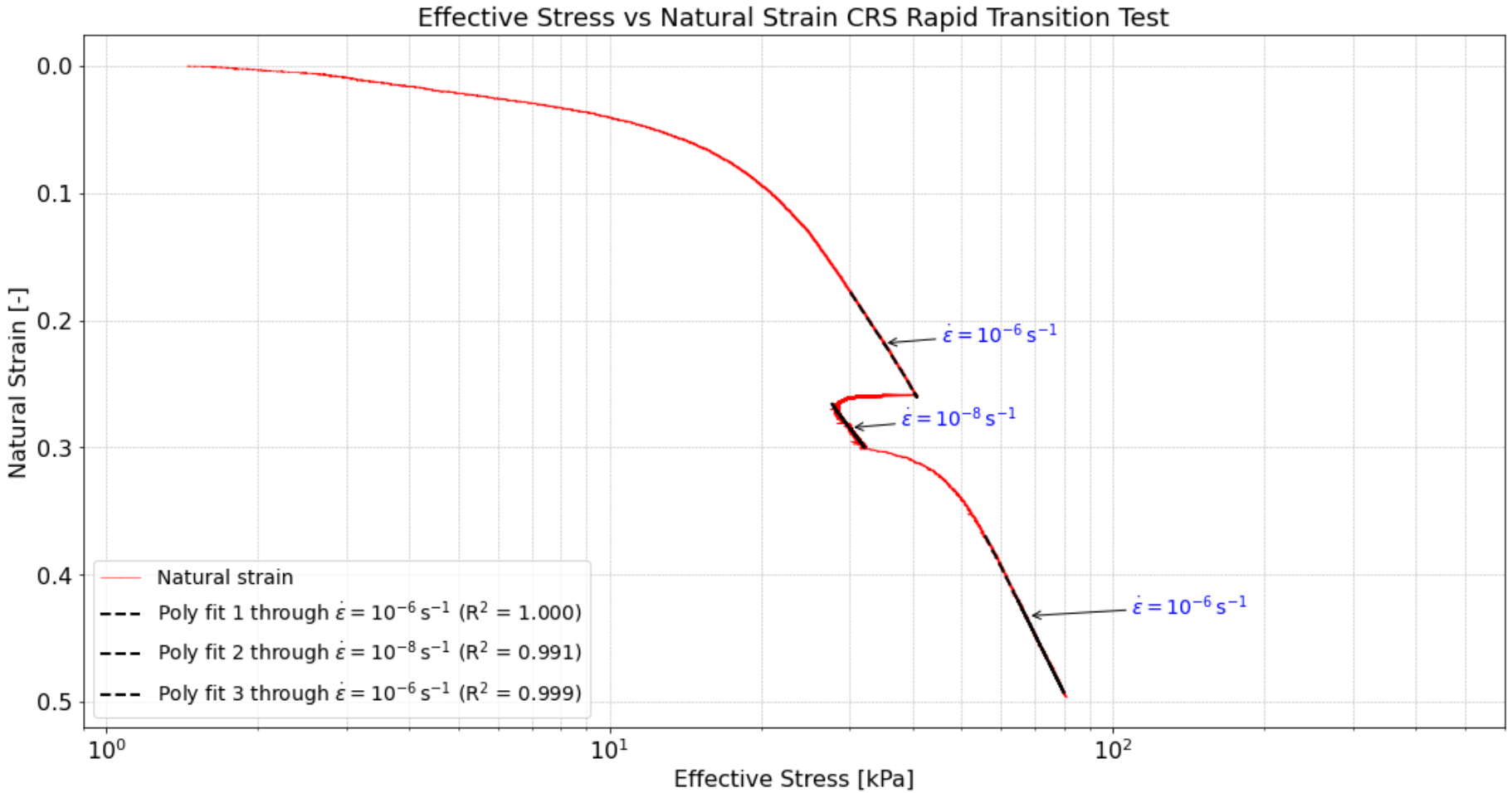

Figure A8.22: Effective stress vs natural strain of CRS Rapid Transition Test with polynomials fitted through different visualised isotachs. Effective stress is plotted on base-10 logarithmic scale.

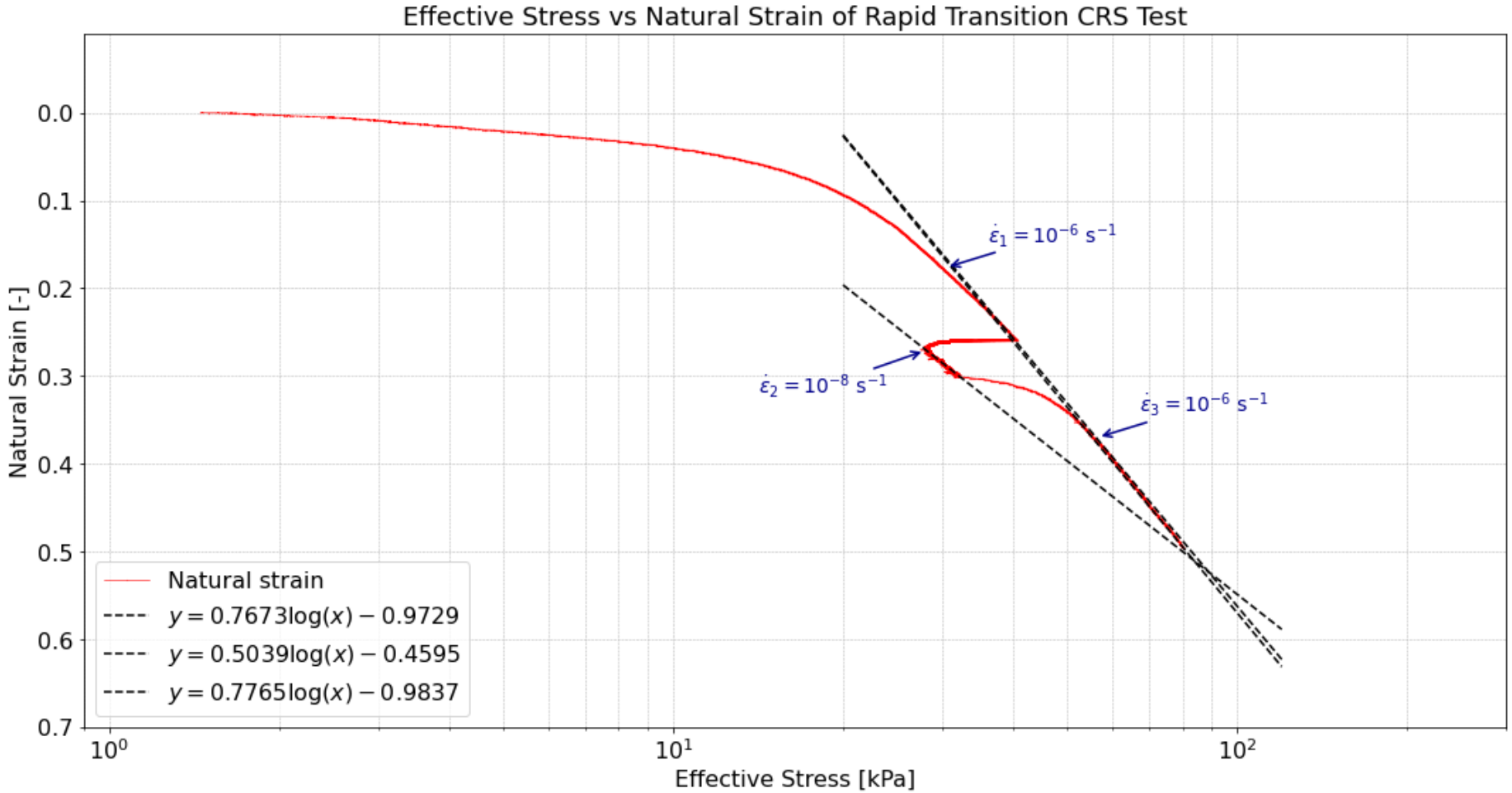

Figure A8.23: Effective stress vs natural strain of CRS Rapid Transition Test with tangent lines plotted through each different visualised isotach. Effective stress is plotted on base-10 logarithmic scale.

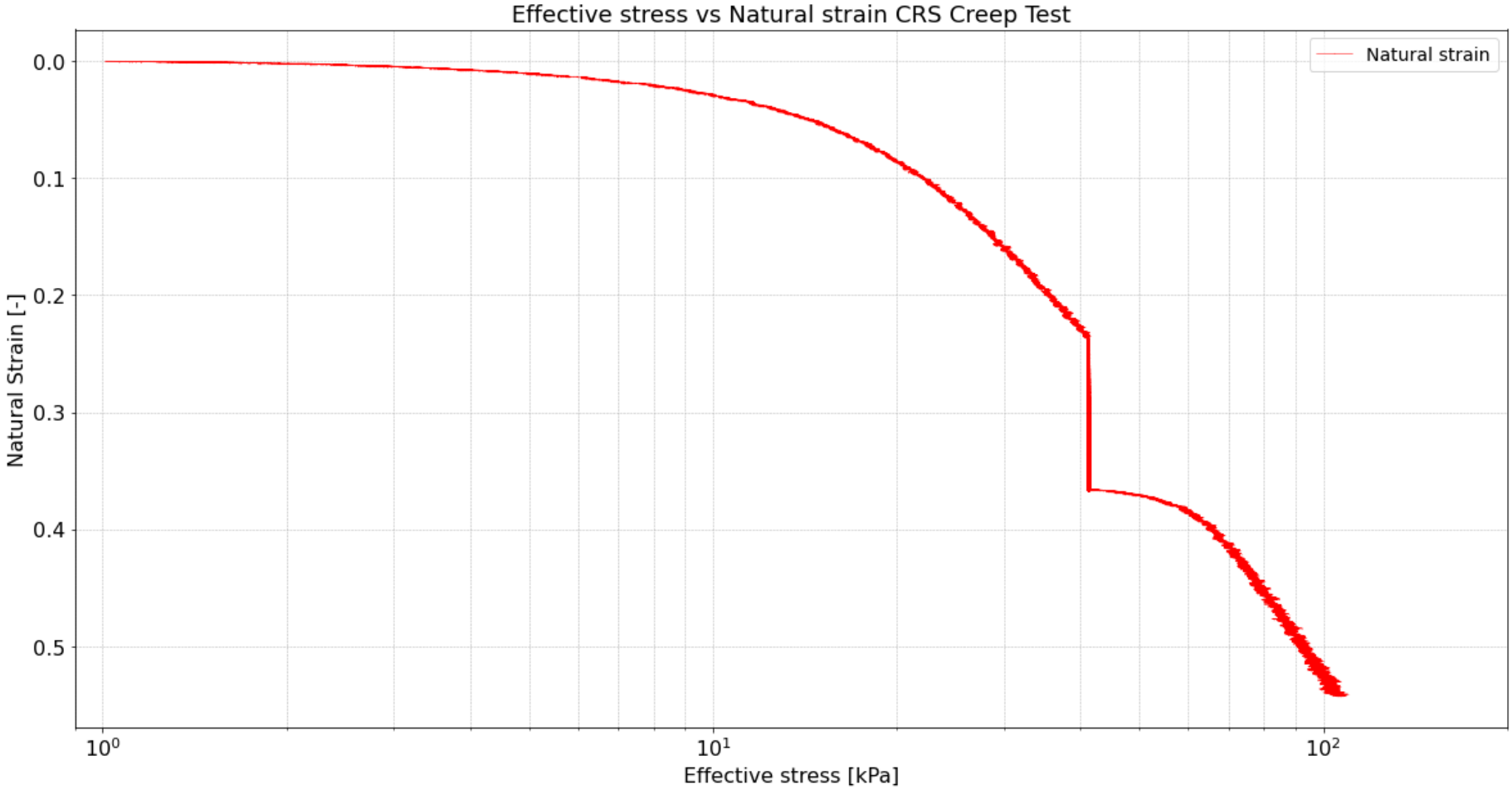

Figure A8.24: Effective stress vs natural strain of CRS Creep Test. Effective stress is plotted on base-10 logarithmic scale.

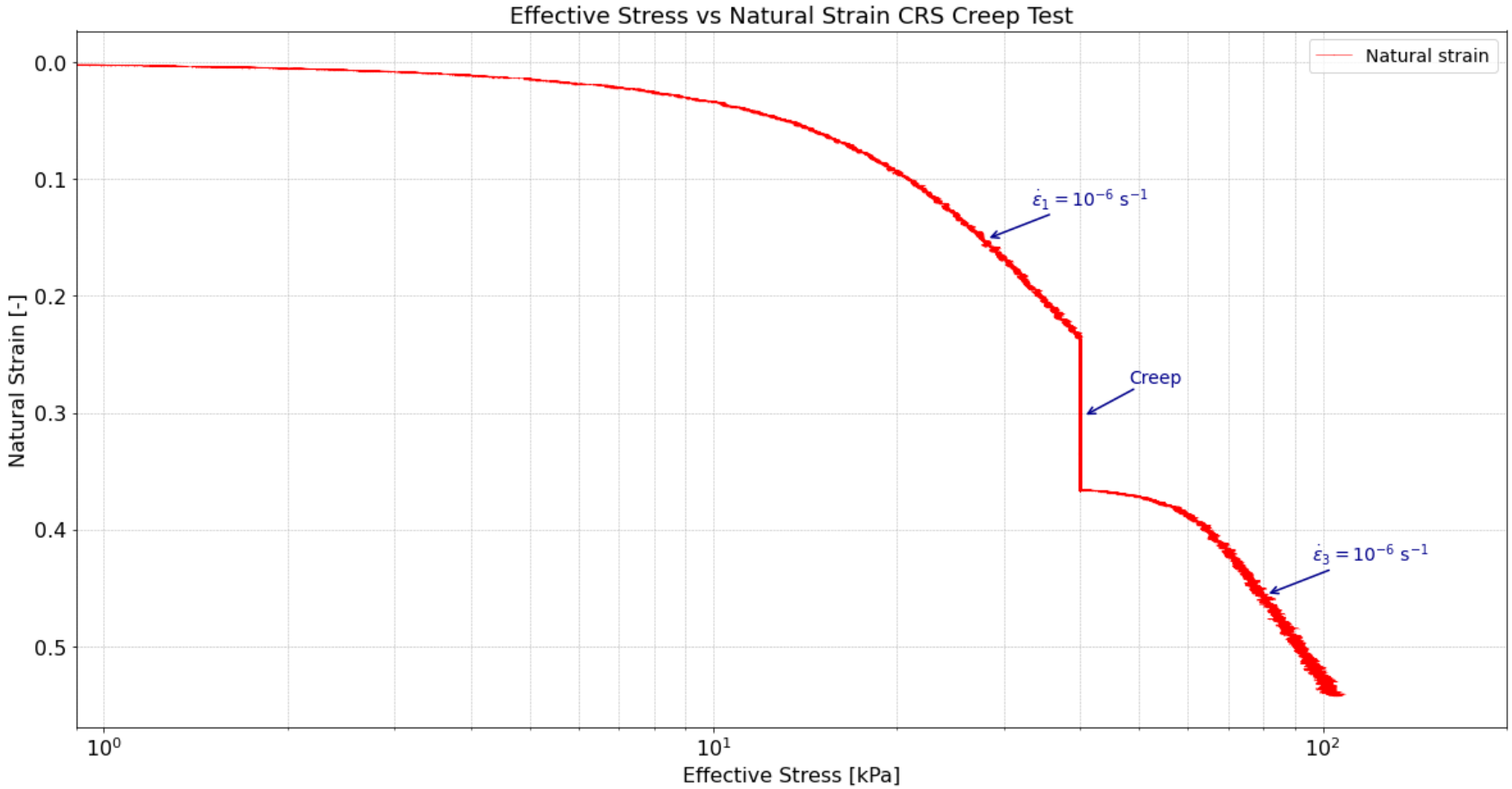

Figure A8.25: Effective stress vs natural strain of CRS Creep Test. Effective stress is plotted on base-10 logarithmic scale.

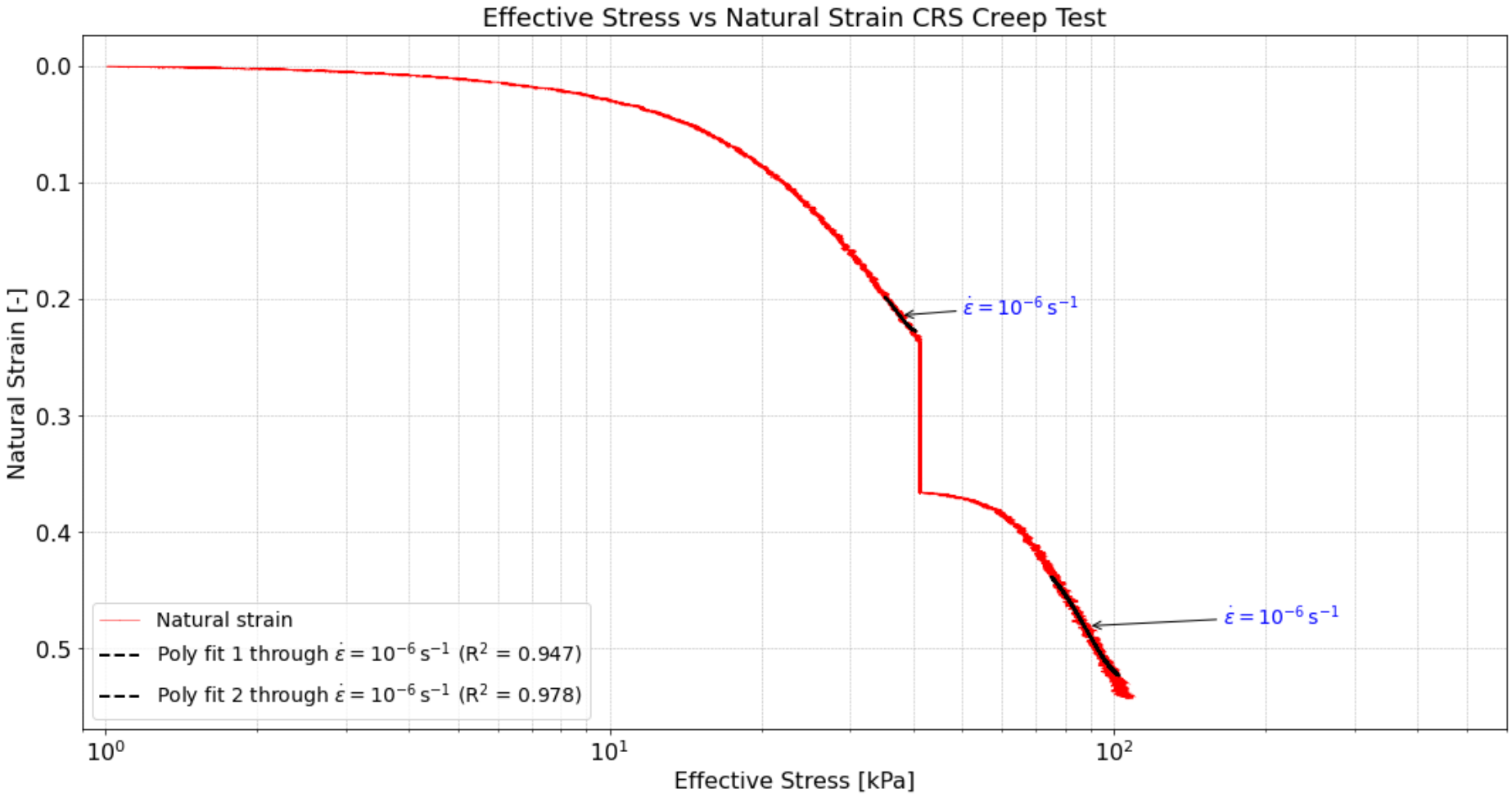

Figure A8.26: Effective stress vs natural strain of CRS Creep Test with polynomials fitted through different visualised isotachs. Effective stress is plotted on base-10 logarithmic scale.

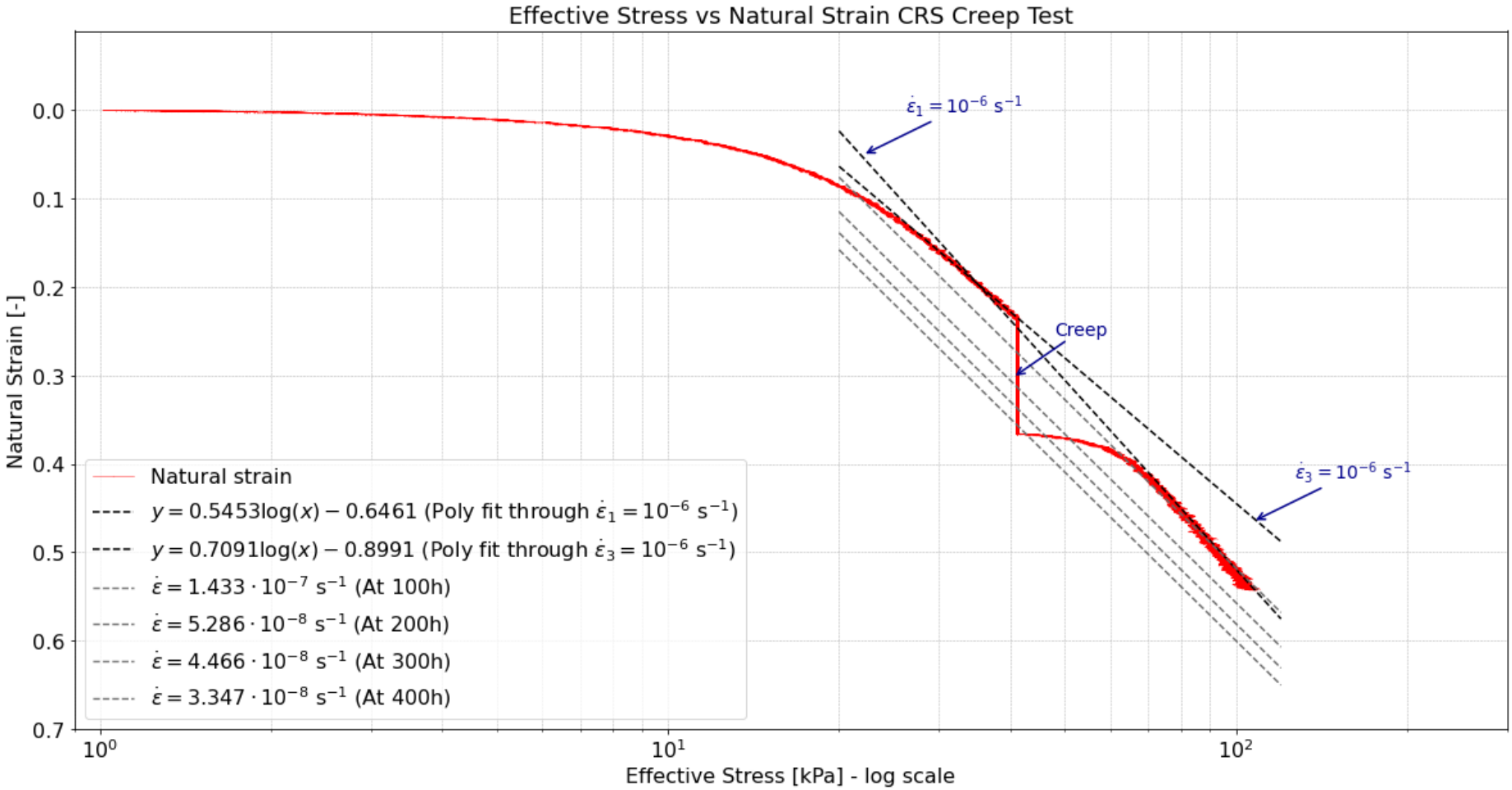

Figure A8.27: Effective stress vs natural strain of CRS Creep Test with tangent lines plotted through each different visualised isotach. Crossed isotachs during creep stage indicated in grey. Effective stress is plotted on base-10 logarithmic scale.

CRS 3	
Step	Slope
$\dot{\varepsilon}_2 = 5 \cdot 10^{-7}$	0.4526
$\dot{\varepsilon}_3 = 10^{-7}$	0.4373
$\dot{\varepsilon}_4 = 10^{-8}$	0.5911
$\dot{\varepsilon}_5 = 10^{-7}$	0.7097
$\dot{\varepsilon}_6 = 5 \cdot 10^{-7}$	0.6821
$\dot{\varepsilon}_7 = 10^{-6}$	0.6957

Table A8.1: slopes of tangent lines of CRS 3.

CRS 4	
Step	Slope
$\dot{\varepsilon}_2 = 5 \cdot 10^{-7}$	0.6144
$\dot{\varepsilon}_3 = 10^{-7}$	0.7295
$\dot{\varepsilon}_4 = 10^{-8}$	0.5966
$\dot{\varepsilon}_5 = 10^{-7}$	0.6265
$\dot{\varepsilon}_6 = 5 \cdot 10^{-7}$	0.6986
$\dot{\varepsilon}_7 = 10^{-6}$	0.7042

Table A8.2: slopes of tangent lines of CRS 4.

CRS 5	
Step	Slope
$\dot{\varepsilon}_2 = 5 \cdot 10^{-7}$	0.6890
$\dot{\varepsilon}_3 = 10^{-7}$	0.6769
$\dot{\varepsilon}_4 = 10^{-8}$	0.8427
$\dot{\varepsilon}_5 = 10^{-7}$	0.6211
$\dot{\varepsilon}_6 = 5 \cdot 10^{-7}$	0.7487
$\dot{\varepsilon}_7 = 10^{-6}$	0.7022

Table A8.3: slopes of tangent lines of CRS 5.

CRS RT	
Step	Slope
$\dot{\varepsilon}_1 = 10^{-6}$	0.7673
$\dot{\varepsilon}_2 = 10^{-8}$	05039
$\dot{\varepsilon}_3 = 10^{-7}$	0.7765

Table A8.4: slopes of tangent lines of CRS RT.

CRS 6	
Step	Slope
$\dot{\varepsilon}_2 = 5 \cdot 10^{-7}$	0.5796
$\dot{\varepsilon}_3 = 10^{-7}$	0.7115
$\dot{\varepsilon}_4 = 10^{-8}$	0.9672
$\dot{\varepsilon}_5 = 10^{-7}$	0.8533
$\dot{\varepsilon}_6 = 5 \cdot 10^{-7}$	0.7470
$\dot{\varepsilon}_7 = 10^{-6}$	0.7810

Table A8.5: slopes of tangent lines of CRS 6.

CRS 7	
Step	Slope
$\dot{\varepsilon}_2 = 5 \cdot 10^{-7}$	0.4885
$\dot{\varepsilon}_3 = 10^{-7}$	0.5836
$\dot{\varepsilon}_4 = 10^{-8}$	1.5703
$\dot{\varepsilon}_5 = 10^{-7}$	0.5422
$\dot{\varepsilon}_6 = 5 \cdot 10^{-7}$	0.6275
$\dot{\varepsilon}_7 = 10^{-6}$	0.6843

Table A8.6: slopes of tangent lines of CRS 7.

CRS Creep	
Step	Slope
$\dot{\varepsilon}_1 = 10^{-6}$	0.5507
$\dot{\varepsilon}_3 = 10^{-6}$	0.7147

Table A8.7: slopes of tangent lines of CRS Creep.

Appendix 9 Evaluation of Mutual Distance Isotachs

This appendix shows the effective stress vs. natural strain plots of the performed CRS tests from which the mutual distance between the visualised isotachs is analysed. For each test this is done at three different stress levels; σ_1 = 30 kPa, σ_2 = 35 kPa, σ_3 = 40 kPa.

Note that it has been concluded that the first strain rate of $\dot{\varepsilon} = 10^{-6}$ s^{-1} with a total displacement of 4.0 mm was not enough to fully load the peat sample past its yield stress. As a result, no isotach through this initial strain rate is drawn.

The following order of results is shown in this appendix;

1. CRS 3
2. CRS 4
3. CRS 5
4. CRS 6
5. CRS 7

CRS test 1 resulted in too much excess generated pore pressure being generated as a result of a too high applied displacement rate. This test was therefore stopped prematurely. CRS test 1.2 is used to determine the yield stress as shown in Annex 3. Subsequently, this test is not shown in this annex since changes rate of displacement are applied. CRS test 2 failed due to technical difficulties during testing. The CRS creep test and the rapid transition test have an insufficient amount of applied changes in displacement rate required to conclude on the mutual distance between different isotachs and are therefore not evaluated in this annex.

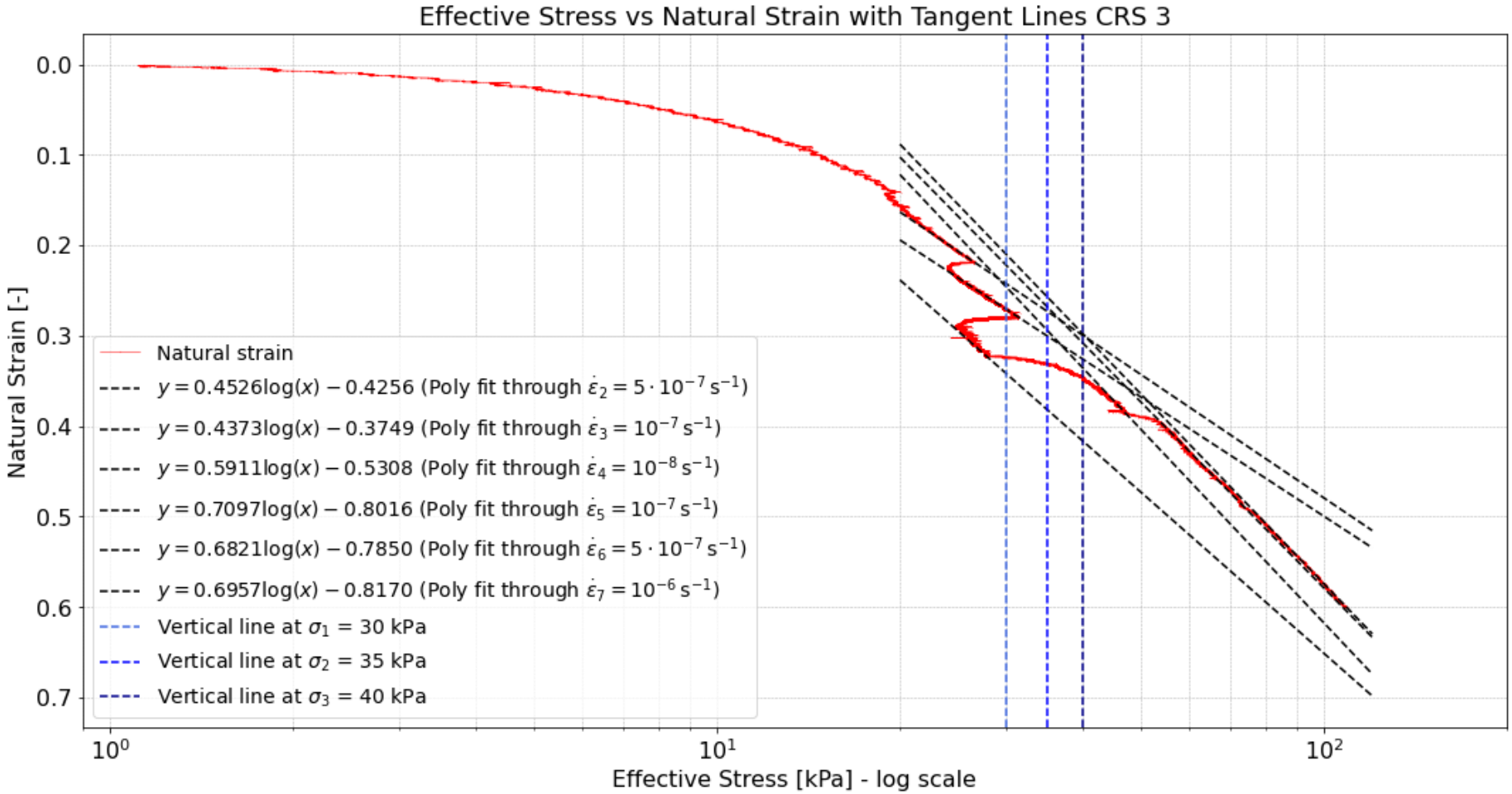

Figure A9.1: Effective stress vs natural strain of CRS 3 with tangent lines plotted through each different visualised isotach. Vertical lines plotted to determine mutual distance between different isotachs. Effective stress is plotted on base-10 logarithmic scale.

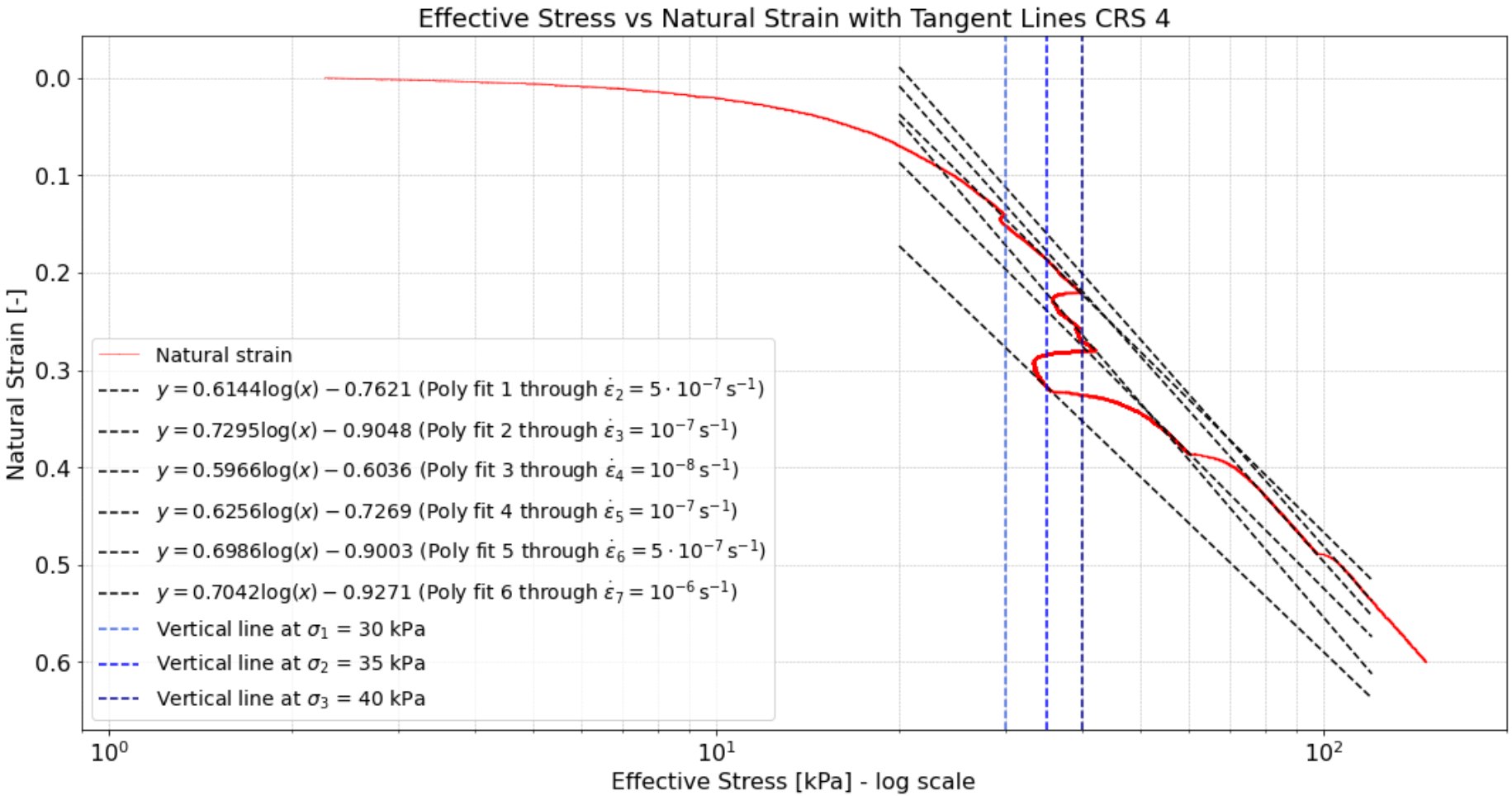

Figure A9.2: Effective stress vs natural strain of CRS 4 with tangent lines plotted through each different visualised isotach. Vertical lines plotted to determine mutual distance between different isotachs. Effective stress is plotted on base-10 logarithmic scale.

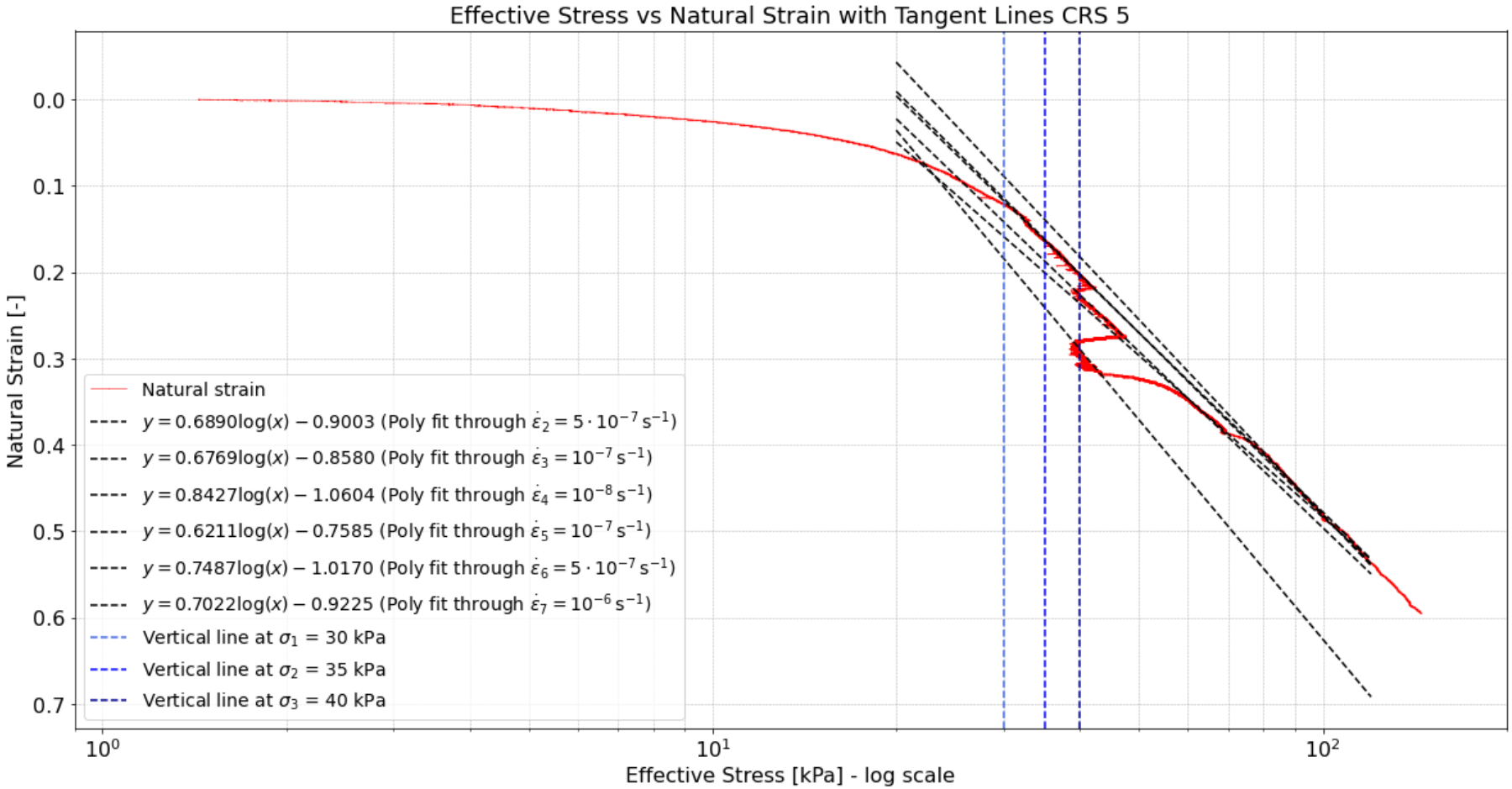

Figure A9.3: Effective stress vs natural strain of CRS 5 with tangent lines plotted through each different visualised isotach. Vertical lines plotted to determine mutual distance between different isotachs. Effective stress is plotted on base-10 logarithmic scale.

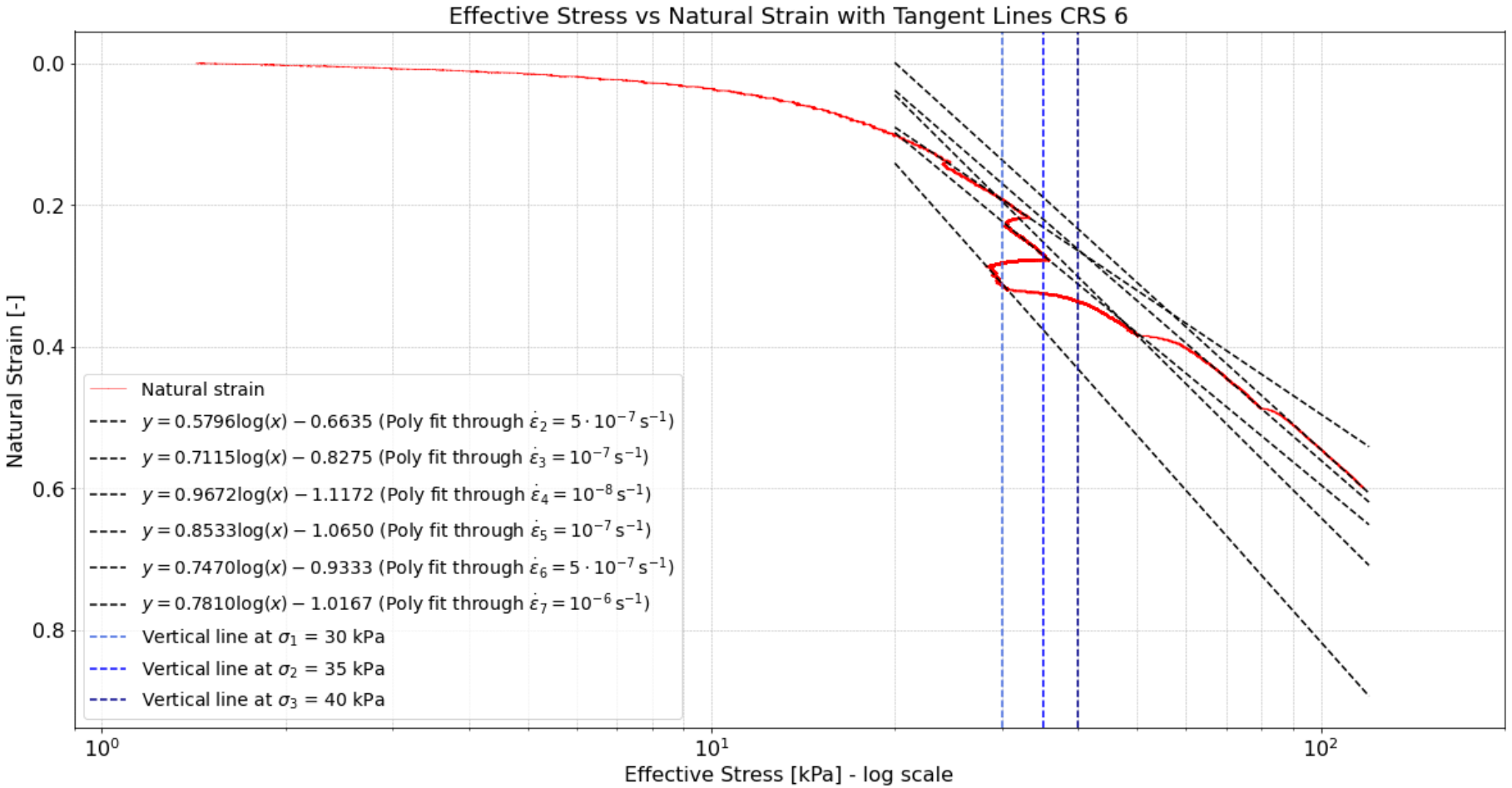

Figure A9.4: Effective stress vs natural strain of CRS 6 with tangent lines plotted through each different visualised isotach. Vertical lines plotted to determine mutual distance between different isotachs. Effective stress is plotted on base-10 logarithmic scale.

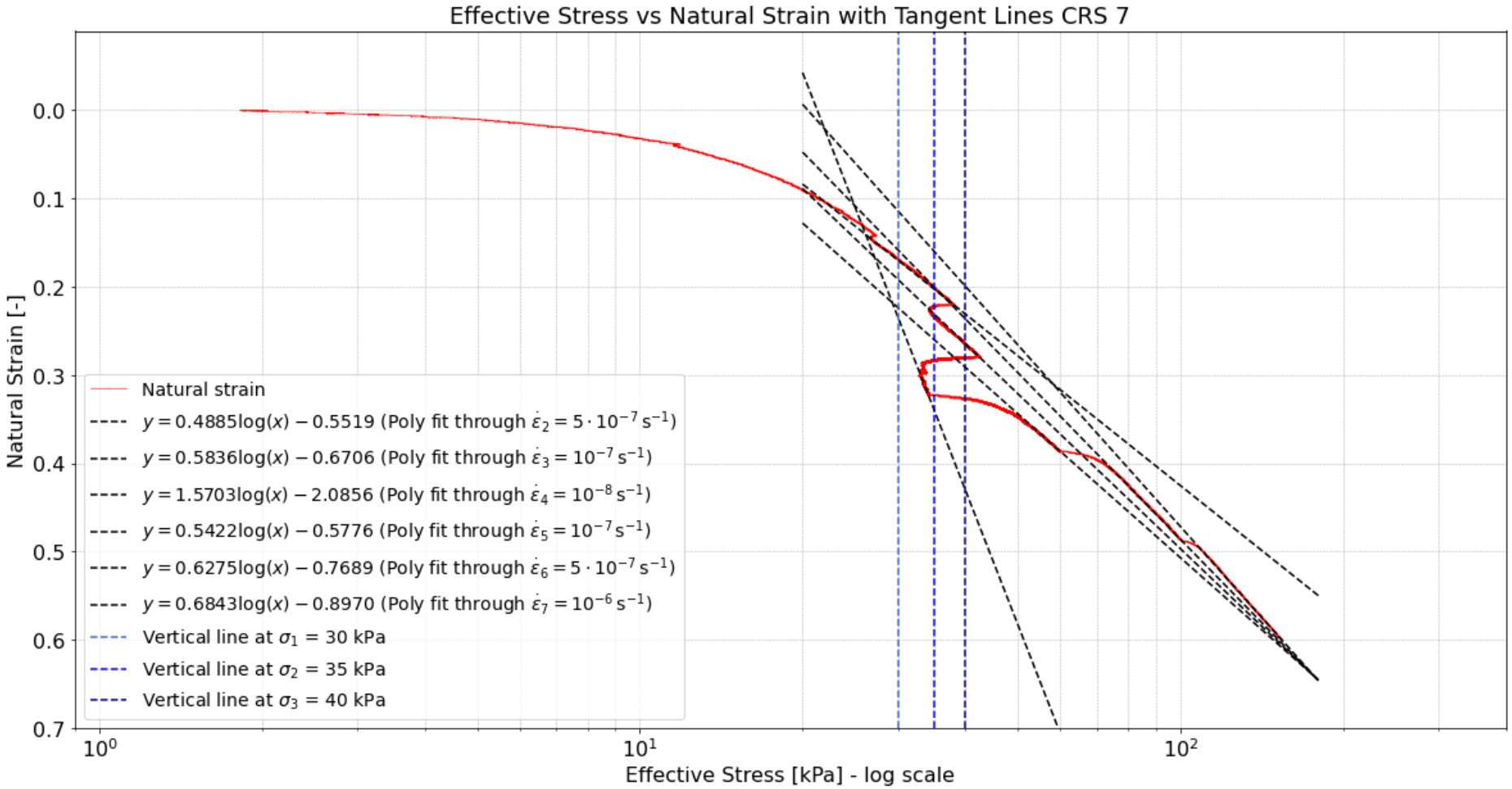

Figure A9.5: Effective stress vs natural strain of CRS 7 with tangent lines plotted through each different visualised isotach. Vertical lines plotted to determine mutual distance between different isotachs. Effective stress is plotted on base-10 logarithmic scale.

CRS Test 3				
Step	Strain rate [s^{-1}]	Distance at σ_1 = 30 kPa	Distance at σ_2 = 35 kPa	Distance at σ_3 = 40 kPa
2	$5 \cdot 10^{-7}$	0.028	0.027	0.026
3	10^{-7}			
3	10^{-7}	0.071	0.082	0.091
4	10^{-8}			
4	10^{-8}	0.096	0.088	0.081
5	10^{-7}			
5	10^{-7}	0.024	0.026	0.028
6	$5 \cdot 10^{-7}$			
6	$5 \cdot 10^{-7}$	0.012	0.011	0.010
7	10^{-6}			

Table A9.1: Calculated mutual distance between different isotachs of CRS 3.

CRS Test 4				
Step	Strain rate [s^{-1}]	Distance at σ_1 = 30 kPa	Distance at σ_2 = 35 kPa	Distance at σ_3 = 40 kPa
2	$5 \cdot 10^{-7}$	0.027	0.035	0.042
3	10^{-7}			
3	10^{-7}	0.105	0.096	0.088
4	10^{-8}			
4	10^{-8}	0.081	0.078	0.077
5	10^{-7}			
5	10^{-7}	0.066	0.061	0.057
6	$5 \cdot 10^{-7}$			
6	$5 \cdot 10^{-7}$	0.019	0.018	0.018
7	10^{-6}			

Table A9.2: Calculated mutual distance between different isotachs of CRS 4.

CRS Test 5				
Step	Strain rate [s^{-1}]	Distance at σ_1 = 30 kPa	Distance at σ_2 = 35 kPa	Distance at σ_3 = 40 kPa
2	$5 \cdot 10^{-7}$	0.025	0.024	0.023
3	10^{-7}			
3	10^{-7}	0.042	0.054	0.063
4	10^{-8}			
4	10^{-8}	0.025	0.040	0.053
5	10^{-7}			
5	10^{-7}	0.070	0.061	0.054
6	$5 \cdot 10^{-7}$			
6	$5 \cdot 10^{-7}$	0.026	0.023	0.019
7	10^{-6}			

Table A9.3: calculated mutual distance between different isotachs of CRS 5.

CRS Test 6				
Step	Strain rate [s^{-1}]	Distance at σ_1 = 30 kPa	Distance at σ_2 = 35 kPa	Distance at σ_3 = 40 kPa
2	$5 \cdot 10^{-7}$	0.031	0.039	0.047
3	10^{-7}			
3	10^{-7}	0.088	0.105	0.120
4	10^{-8}			
4	10^{-8}	0.116	0.124	0.130
5	10^{-7}			
5	10^{-7}	0.025	0.032	0.039
6	$5 \cdot 10^{-7}$			
6	$5 \cdot 10^{-7}$	0.033	0.031	0.029
7	10^{-6}			

Table A9.4: calculated mutual distance between different isotachs of CRS 6.

CRS Test 7				
Step	Strain rate [s^{-1}]	Distance at σ_1 = 30 kPa	Distance at σ_2 = 35 kPa	Distance at σ_3 = 40 kPa
2	$5 \cdot 10^{-7}$	0.022	0.028	0.034
3	10^{-7}			
3	10^{-7}	0.042	0.108	0.166
4	10^{-8}			
4	10^{-8}	0.011	0.079	0.139
5	10^{-7}			
5	10^{-7}	0.065	0.059	0.055
6	$5 \cdot 10^{-7}$			
6	$5 \cdot 10^{-7}$	0.044	0.040	0.037
7	10^{-6}			

Table A9.5: calculated mutual distance between different isotachs of CRS 7.

Appendix 10 CRS Test 7

CRS test 7 is corrected for a sudden unexpected increase in measured pore pressure during testing. As can be seen in the graph below, the displacement over time as shown in Figure A10.1 behaves exactly as expected given the used strain rate configuration as shown in Table 4.2.

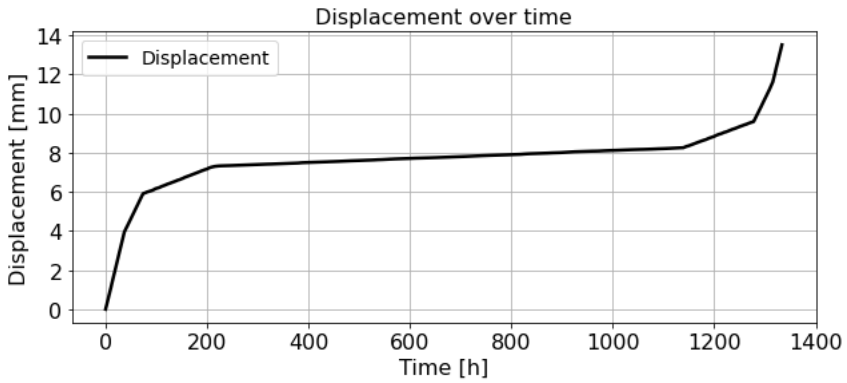

Figure A10.1: Displacement over time of CRS test 7.

However, when evaluating the measured pore pressure throughout the test, a sharp increase after approximately 605 hours of testing is clearly visible in Figure A10.2. Note that a similar increase is noticeable after 550 hours of testing. However the increase after 605 hours of testing is lasting and does not decrease after some time has passed, as is the case with the increase around 550 hours.

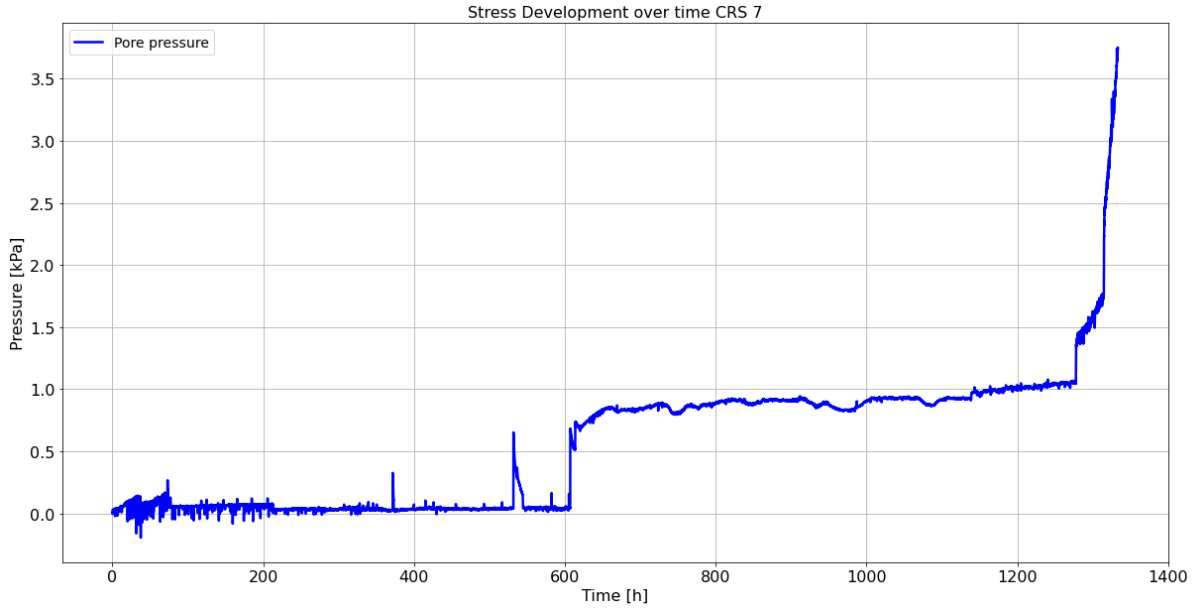

Figure A10.2: Excess generated pore pressure over time of CRS test 7.

No logical explanation is found for this sudden increase in pore water pressure. Especially since this behaviour is not noticed in the other performed CRS tests on the same material using the exact same strain rate configuration. One possibility is the access to the pore water pressure transducer getting blocked by some material from the sample. Afterall, the pore water pressure will increase if the same amount of excess generated pore water pressure needs to flow through a smaller area. This is however un-verifiable since the pore water pressure response is analysed after the test is completed. Furthermore, there is no possibility of preventing analysing the pore water transducer without dismantling the CRS test. Dismantling the CRS test inherently leads to a prematurely stopped test.

This sudden increase in pore water pressure after 605 hours of testing leads to a sudden reduction in effective stress as shown in Figure A10.3. This is visible in the effective stress vs. natural strain plot where a sudden decrease in effective stress is visible around a natural strain level of 0.29.

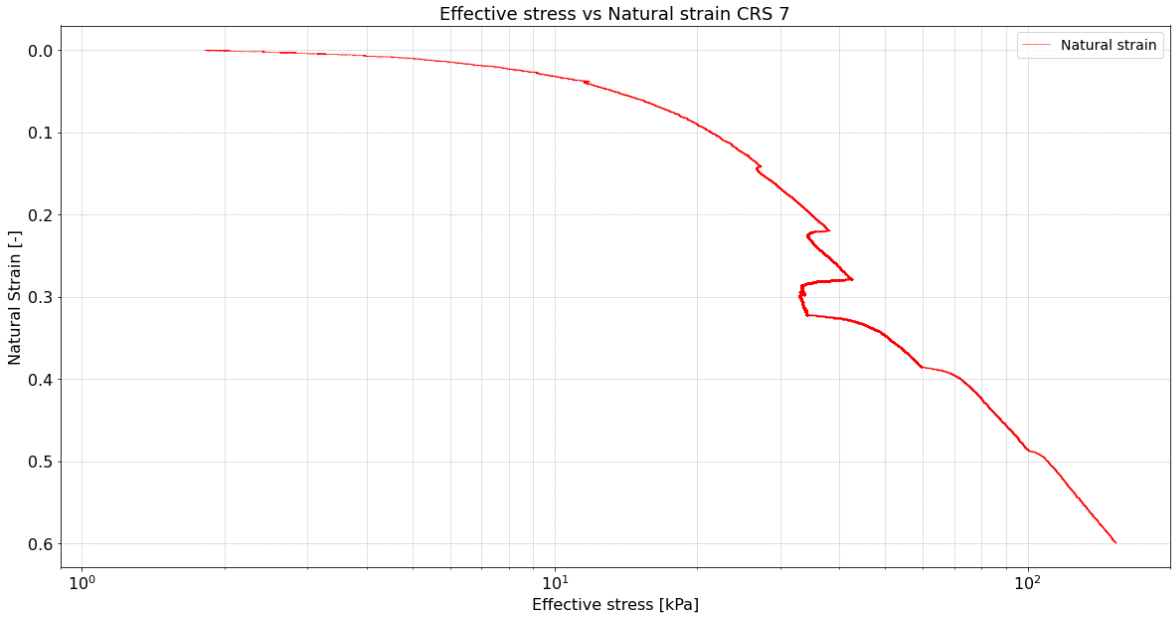

Figure A10.3: Effective stress vs natural strain of CRS 7. Effective stress is plotted on base-10 logarithmic scale.

Figure A10.4 shows an enlarged view of part of the natural strain vs. effective stress plot where the sudden reduction in effective stress occurs. Note that this coincides with the loading stage where the sample is compressed with a strain rate of $\dot{\varepsilon} = 10^{-8}\ s^{-1}$, the lowest possible strain rate of this test.

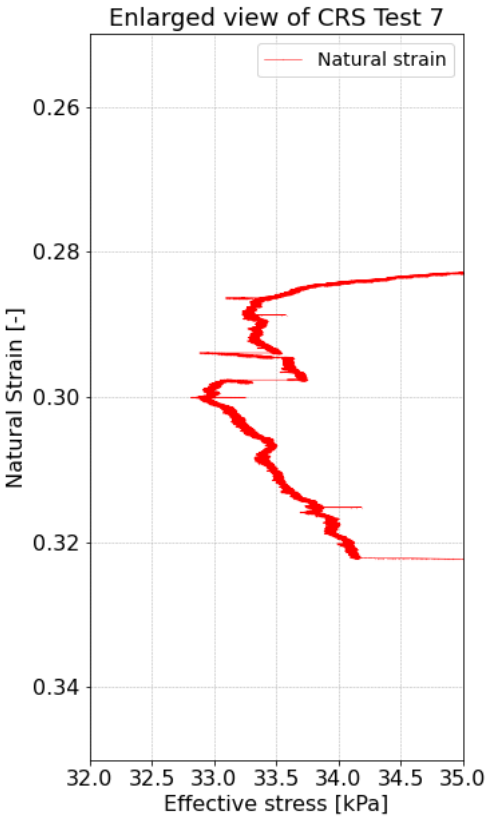

Figure A10.5: Effective stress development corresponding to the $\dot{\varepsilon} = 10^{-8}\ s^{-1}$ isotach.

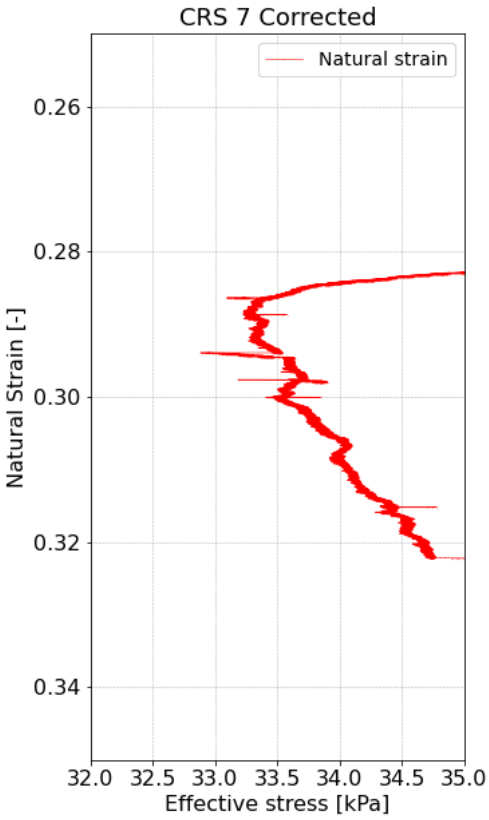

Figure A10.4: Corrected effective stress development corresponding to the $\dot{\varepsilon} = 10^{-8}\ s^{-1}$ isotach.

Because of this sudden unexpected reduction in effective stress the decision was made to correct the data. Figure A10.5 shows the corrected data. Note that after the data is corrected a smoother natural strain development is visible. This corrected response is in line what is to be expected based on the other performed CRS tests on the same material using the same strain rate configuration table. This correction ultimately results in the effective stress vs. natural strain as shown in Figure A10.6.

Figure A10. 6: Corrected effective stress vs natural strain of CRS 7. Effective stress is plotted on base-10 logarithmic scale.

The corrected data is in line with the other performed tests. The tangent line through this isotach is however not used in the analysis of the slope distribution. It is of further interest to investigate the physical reason for the observed phenomena. Since this is currently unclear, analysis of the slope through this isotach has been omitted. Similar phenomena were not found in any of the performed CRS tests.

Appendix 11 CRS Creep Test

Figure A11.1 shows the results of the CRS creep test. The start of the creep phase can clearly be identified corresponding to the approximate stress-strain coordinates of (40, 0.24). The start of the creep phase happens 64.8 hours after the start of loading. The creep phase ends when 384 hours have elapsed. This corresponds to the stress strain coordinate in Figure A11.1 of (40, 0.37).

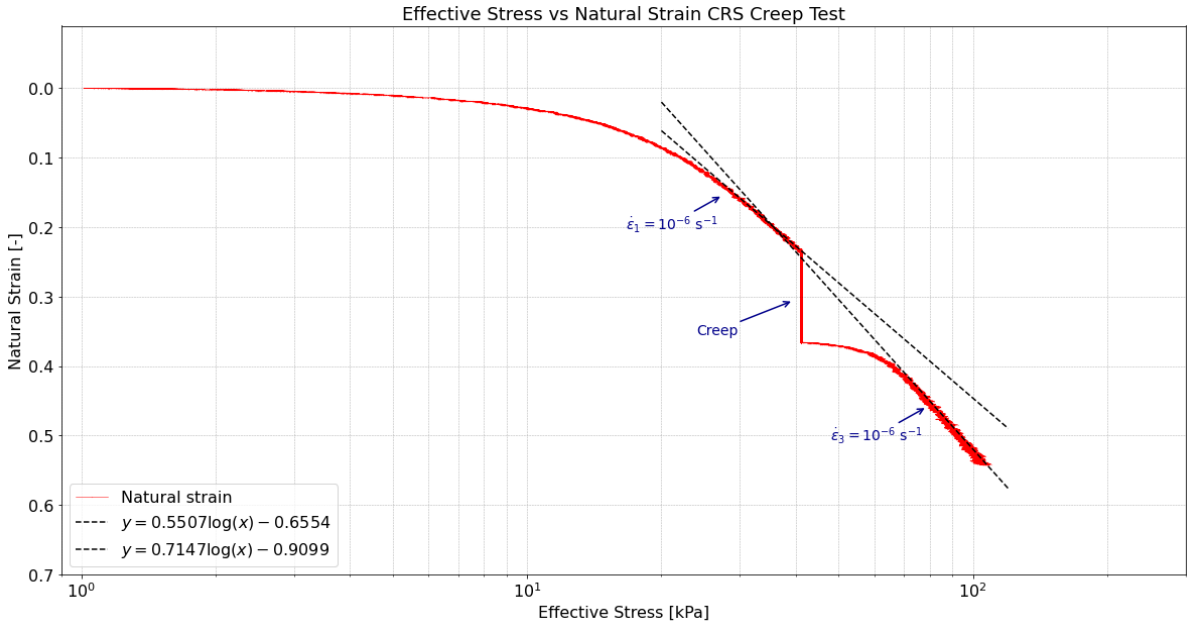

Figure A11.1: Effective stress vs natural strain of CRS Creep Test with tangent lines plotted through each different visualised isotach. Effective stress is plotted on base-10 logarithmic scale.

Figure A11.2 displays the axial strain during the creep phase over time. It is clearly visible that the amount of accumulated strain reduces as time progresses.

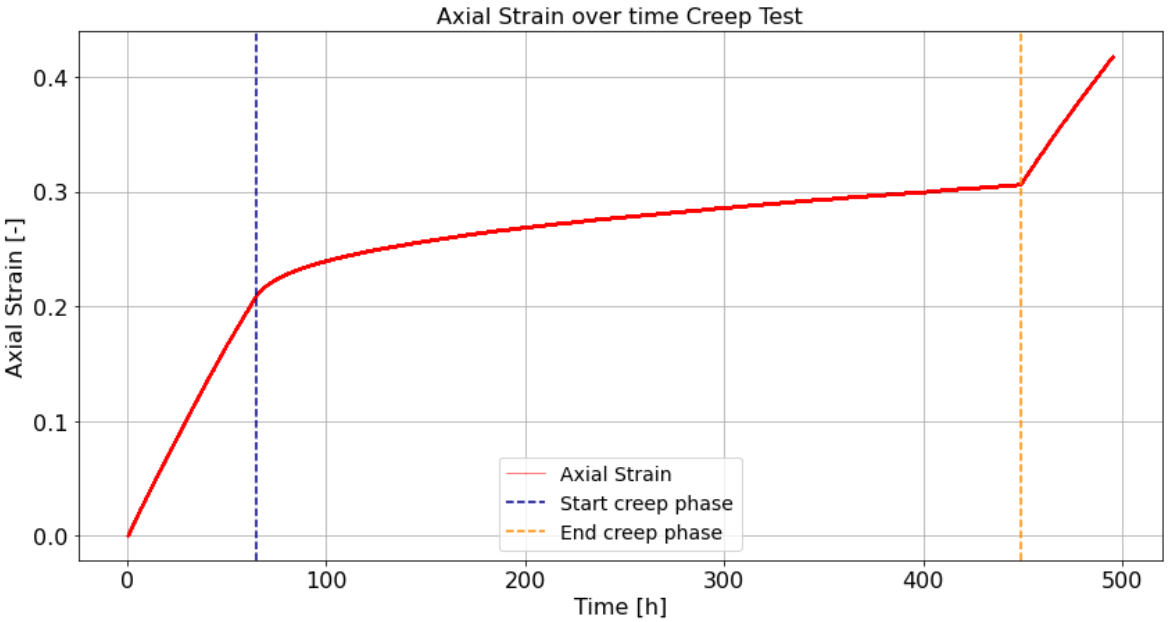

Figure A11.2: Axial strain development over time. The start of the creep phase is indicated by the purple vertical line. The end of the creep phase is indicated by the orange vertical line.

A fifth-order polynomial is fitted through the axial strain graph of Figure A11.2 corresponding to the creep phase. This results in Figure A11.3 where it is shown that the polynomial describes the data well over the testing period 64.8 hours until 448.8 hours.

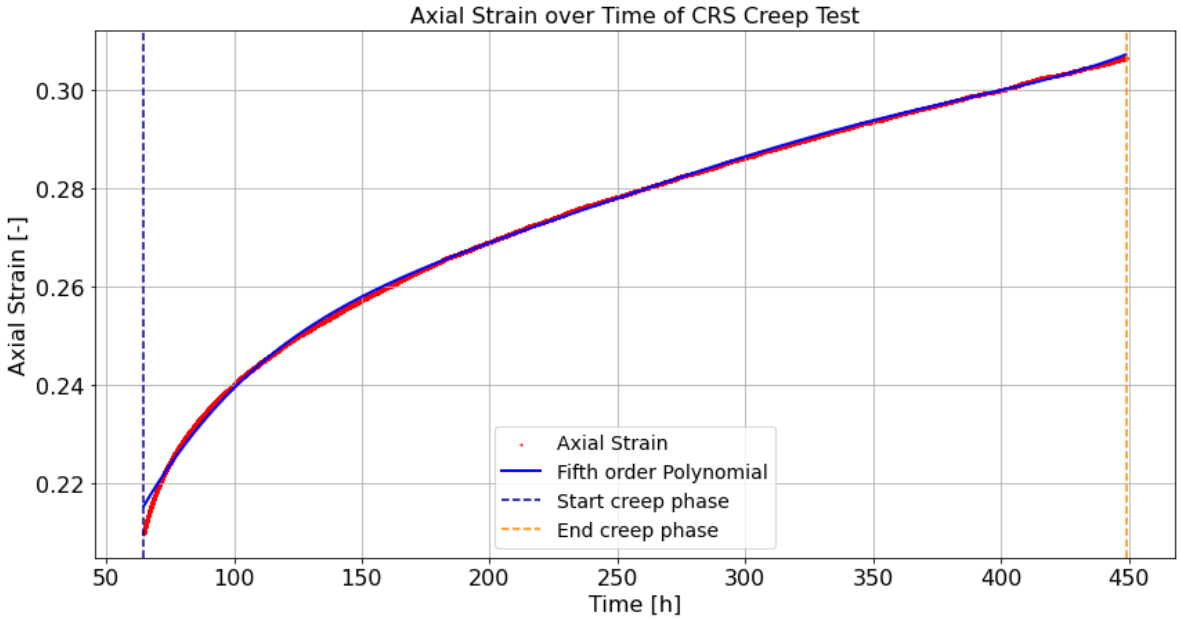

Figure A11.3: Enlarged view of axial strain development during creep phase with fifth order polynomial fitted through the recorded axial strain.

Taking the first derivative of this fitted polynomials allows for the estimation of the rate of change in strain over time. In other words, the strain rate can be approximated at each moment during the creep test. This results in the following estimated values as shown in Table A11.1.

Moment	*Strain rate*
t = 100h	$\dot{\varepsilon} = 1.433 \cdot 10^{-7}\ s^{-1}$
t = 200h	$\dot{\varepsilon} = 5.286 \cdot 10^{-8}\ s^{-1}$
t = 300h	$\dot{\varepsilon} = 4.466 \cdot 10^{-8}\ s^{-1}$
t = 400h	$\dot{\varepsilon} = 3.347 \cdot 10^{-8}\ s^{-1}$

Table A11.1: calculated strain rate at evaluated moments.

In here the function of the used polynomial is shown by Equation A11.1.

$$\varepsilon = 6.2241 \cdot 10^{-14}\, t^5 - 9.059 \cdot 10^{-11}\, t^4 + 5.1474 \cdot 10^{-8}\, t^3 - 1.4443 \cdot 10^{-5}\, t^2 + 2.1917 \cdot 10^{-3}\, t + 1.2154 \cdot 10^{-1}. \quad \text{(A11.1)}$$

The first derivative follows from Equation A11.1 and is shown by Equation A11.2.

$$\dot{\varepsilon} = 3.112 \cdot 10^{-13}\, t^4 - 3.6236 \cdot 10^{-10}\, t^3 + 1.5442 \cdot 10^{-7}\, t^2 - 2.8887 \cdot 10^{-5}\, t + 2.1917 \cdot 10^{-3}. \quad \text{(A11.2)}$$

Appendix 12 Failed CRS Test

The Rapid Transition CRS test initially failed due to the presence of wood in the sample much larger in size than the peat fibres. The CRS test was redone after the wood was detected. The strain rate configuration of this test is shown in Table A12.1.

Step	*Type*	*Strain rate [s^{-1}]*	*Displacement [mm]*	*Linear Strain [-]*	*Displacement rate [mm h^{-1}]*	*Time [h]*	*Time [days]*
1	Loading	10^{-6}	7.0	0.233	0.108	64.8	2.7
2	Loading	10^{-8}	1.0	0.033	0.00108	925.9	38.6
3	Loading	10^{-6}	4.0	0.133	0.108	37.0	1.5
Total			12.0	0.4		1027.7	42.8

Table A12.1: Test set-up of rapid transition CRS test that initially failed.

As can be seen in the stress development over time as shown in Figure A12.1, after 40 hours of testing a sudden unexpected sharp increase in vertical stress is noted.

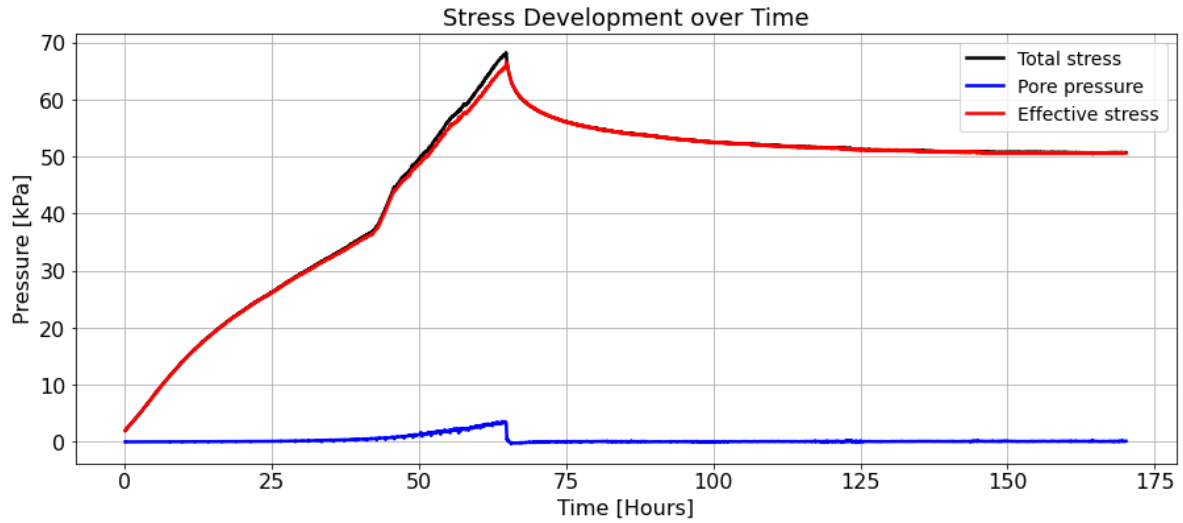

Figure A12.1: Stress development over time. Note the sudden unexpected increase in effective- and total stress after approximately 40 hours.

In the subsequent effective stress vs. natural strain of Figure A12.2 this sudden increase in effective stress is clearly visible as well. Note that this sudden increase occurs around a natural strain level of 0.17.

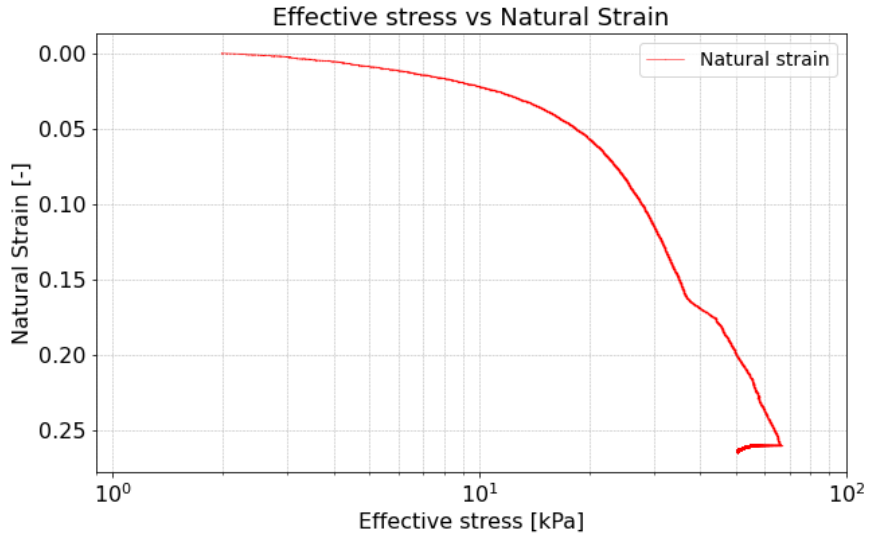

Figure A12.2: Effective stress vs. natural strain. The sudden increase in effective stress around a natural strain level of 0.17 is the result of wood being present in the sample.

Based on these intermediate results the decision was made to no longer continue this particular CRS test. The test was stopped by the laboratory technician after which the sample was decomposed. The images of Figure A12.3 show the decomposed peat sample. As can be seen in these images, a large wood/reed fibre is present within the sample. This organic material resulted in a failed test and underlines the sensitivity of performing CRS tests on a heterogenous material like peat. After the dismantling of the CRS apparatus the test was redone with a new pristine peat sample.

Figure A12. 3: After stopping the CRS test and dismantling the soil sample the presence of wood was confirmed. Note that wood much larger than the peat fibres is clearly visible in the soil sample.

Appendix 13 Parameter Influence abc-Isotach Model

Figures A13.1 shows the influence of parameter variation on the isotach trajectory of the abc-Isotach model. By definition, parameter variation results in equidistant parallel isotachs when using the abc-Isotach Model. The default parameters used in the simulation of Figure A13.1 are; a=0.0135, b=0.2626, c=0.0167.

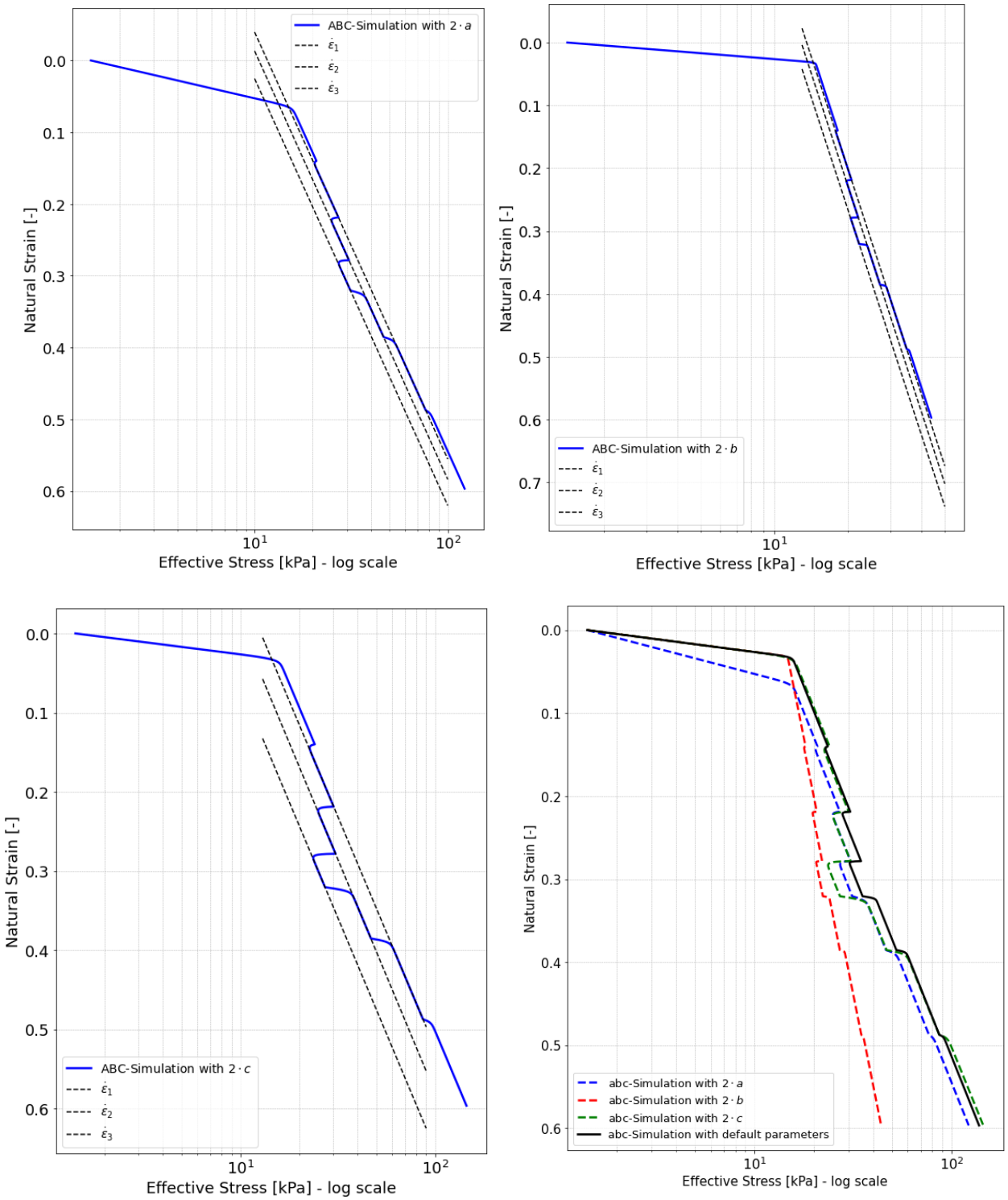

Figure A13.1: Upper left: abc-simulation with increased direct compression index.
Upper right: abc-simulation with increased direct compression index.
Lower left: abc-simulation with increased direct compression index.
Lower right: combined view of abc-simulation including simulation using default parameters.

Appendix 14 Simulation of CRS tests

This appendix shows the results of simulations of the five step-changed CRS tests. The order of constitutive models used in the simulation is NEN-Bjerrum isotach-model, abc-isotach model, SSC-model and MIT-EVP model to match the order followed in Section 2.7. Regarding model formulation the reader is referred to Section 2.7. Note that this appendix shows the results using optimised parameters sets based on the initial parameter set as derived in Appendix 4 to Appendix 7. This approach is deemed valid since Section 4.1.2 showed that the different peat samples showed a high degree of uniformity in initial characteristics. The usage of this initial parameter set is therefore deemed acceptable.

CRS NEN-Bjerrum

Figure A14.1 shows the combined simulation results of the five step-changed CRS tests using the NEN-Bjerrum model.

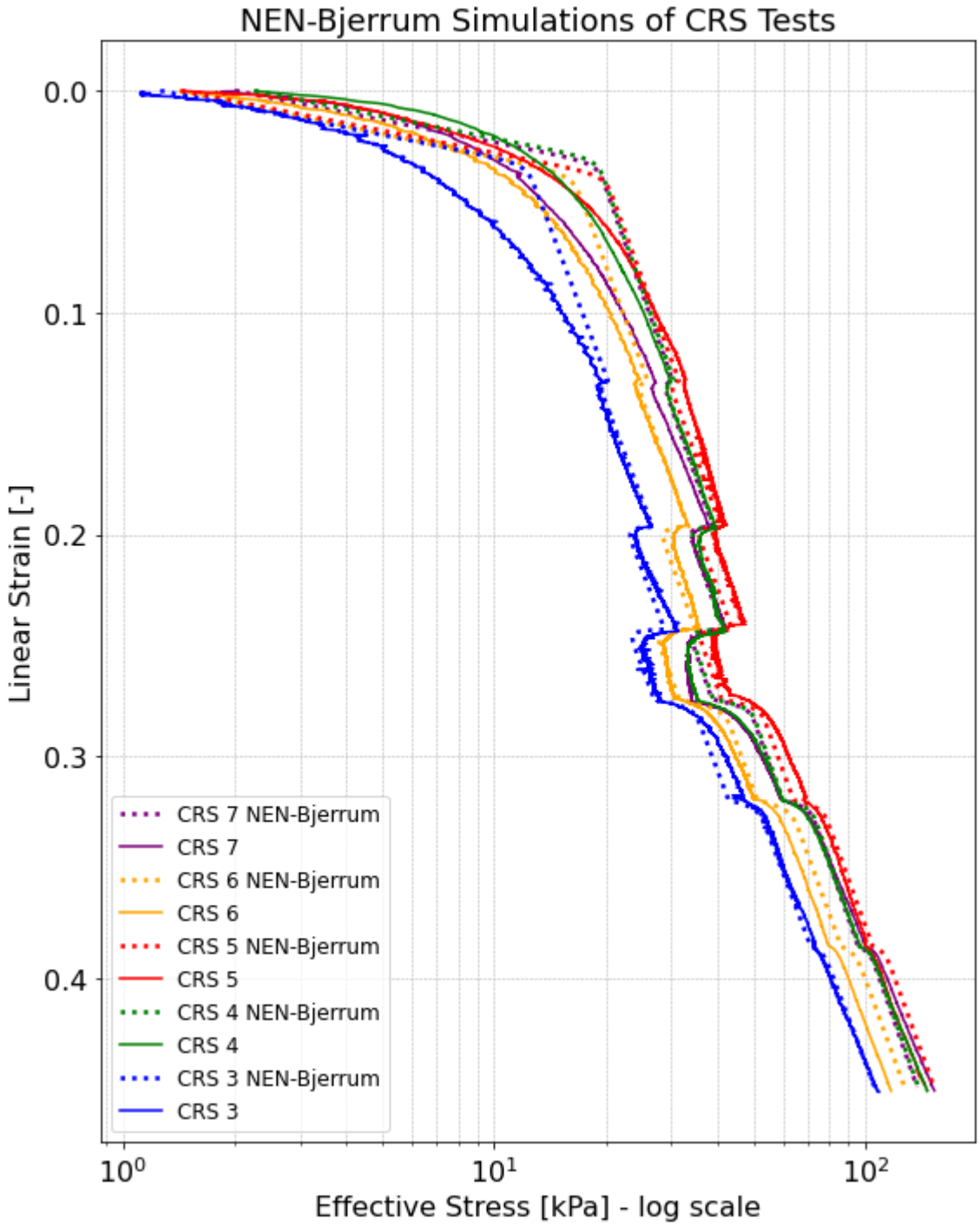

Figure A14.1: Combined NEN-Bjerrum isotach model simulation results of CRS Tests.

CRS abc-Isotach Model

Figure A14.2 shows the combined simulation results of the five step-changed CRS tests using the abc-isotach model.

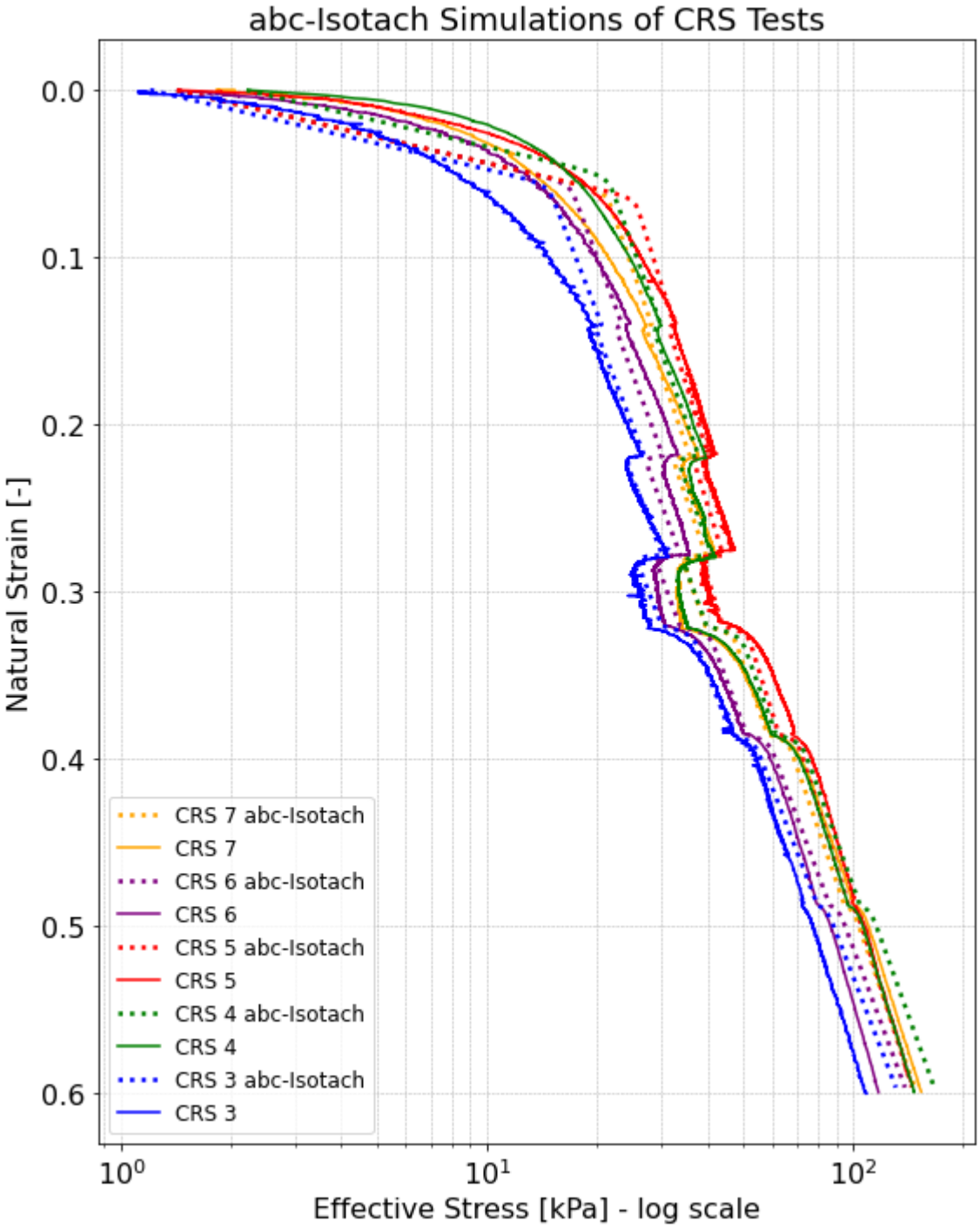

Figure A14.2: Combined abc-isotach model simulation results of CRS Tests.

CRS SSC-Model

Figure A14.3 shows the combined simulation results of the five step-changed CRS tests using the SSC-Model.

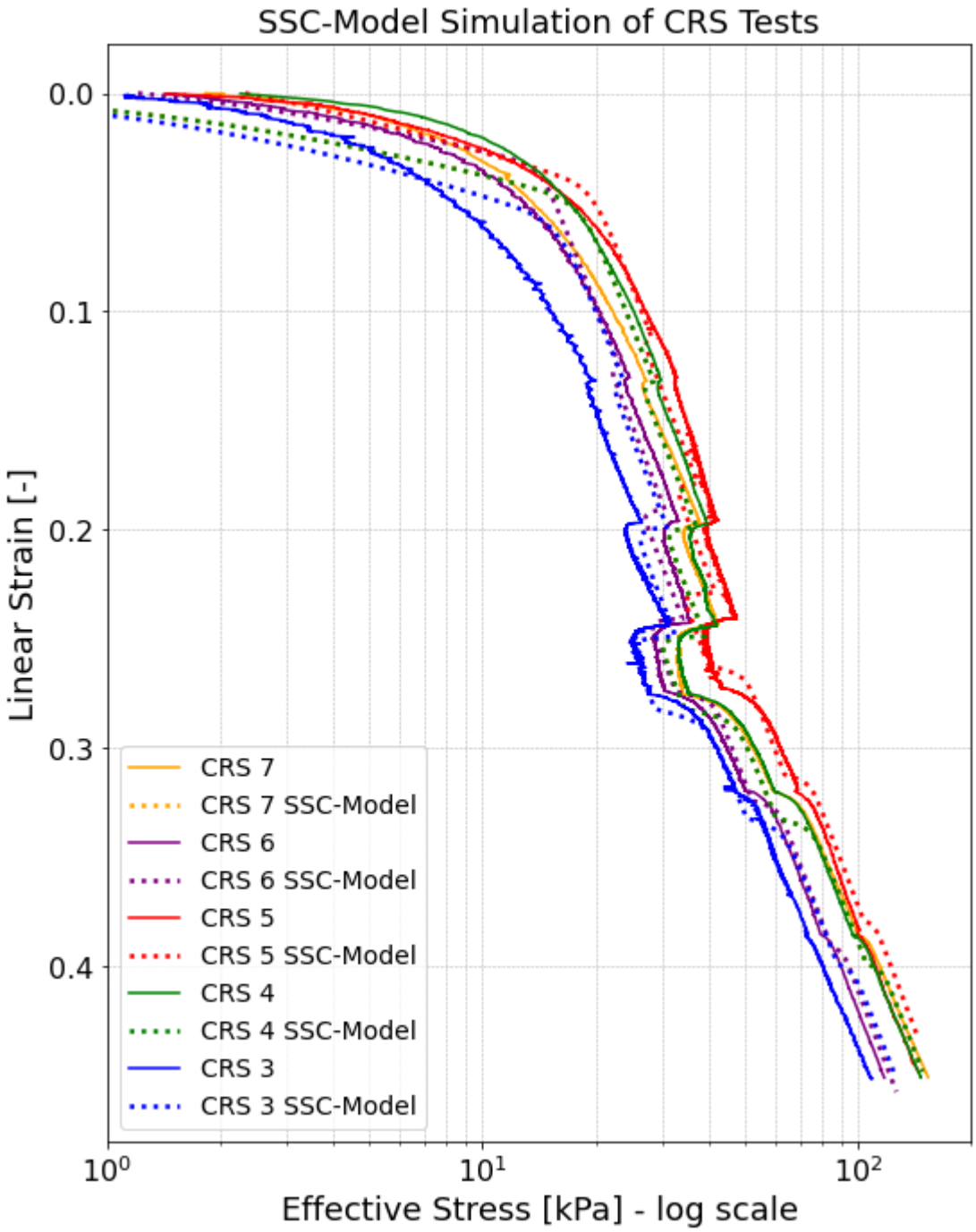

Figure A14.3: Combined soft soil creep model simulation results of CRS Tests.

CRS Y&W MIT EVP-Model

Figure A14.4 shows the combined simulation results of the five step-changed CRS tests using the MIT Y&W EVP-Model.

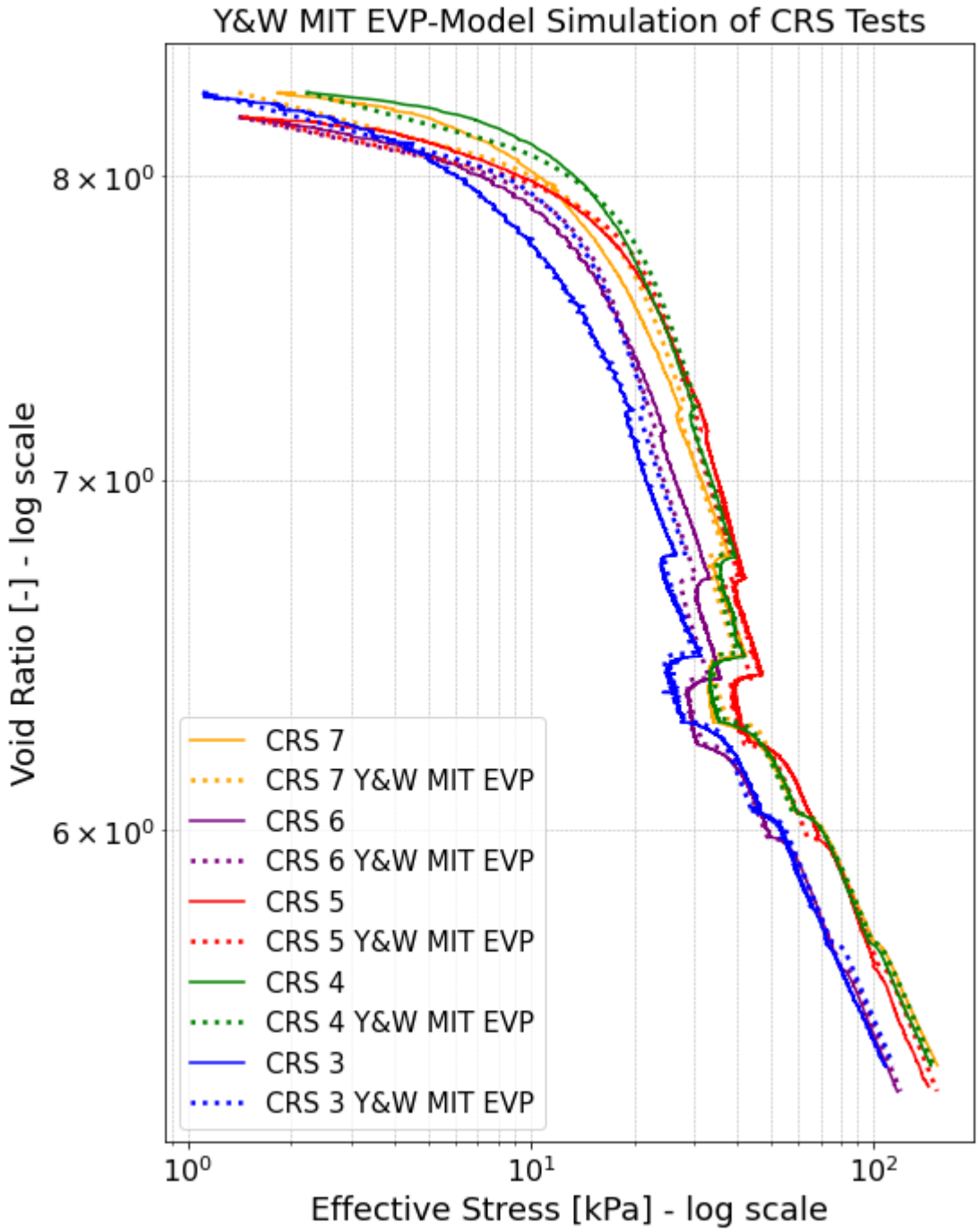

Figure A14.4: Combined Yuan and Whittle MIT EVP model simulation results of CRS Tests.

CRS 3 NEN-Bjerrum

The results of the step-changed CRS 3 test are simulated using the NEN-Bjerrum isotach-model and shown in Figure A14.5. Table A14.1 shows the parameters used.

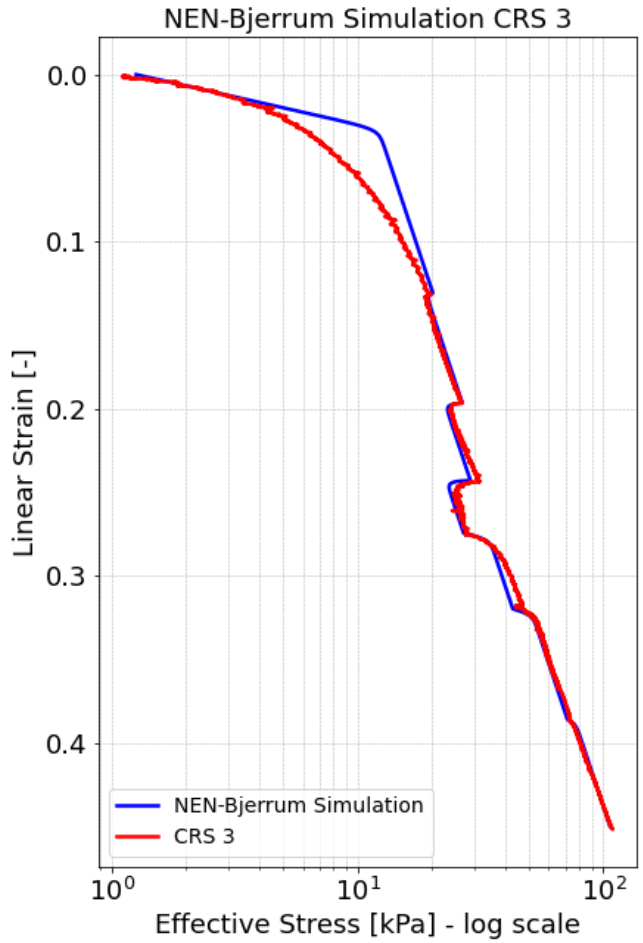

Figure A14.5: Simulation of CRS test 3 using the NEN-Bjerrum isotach model.

Parameter	*Symbol*	*Value*
Recompression Ratio	RR	0.033
Compression Ratio	CR	0.483
Secular strain rate coefficient	C_α	0.046
Reference time	τ_0	24 h

Table A14.1: Parameters used in NEN-Bjerrum isotach simulation of CRS test 3.

CRS 3 abc-Isotach Simulation

The results of the step-changed CRS 3 test are simulated using the abc-isotach-model and shown in Figure A14.6. Table A14.2 shows the parameters used.

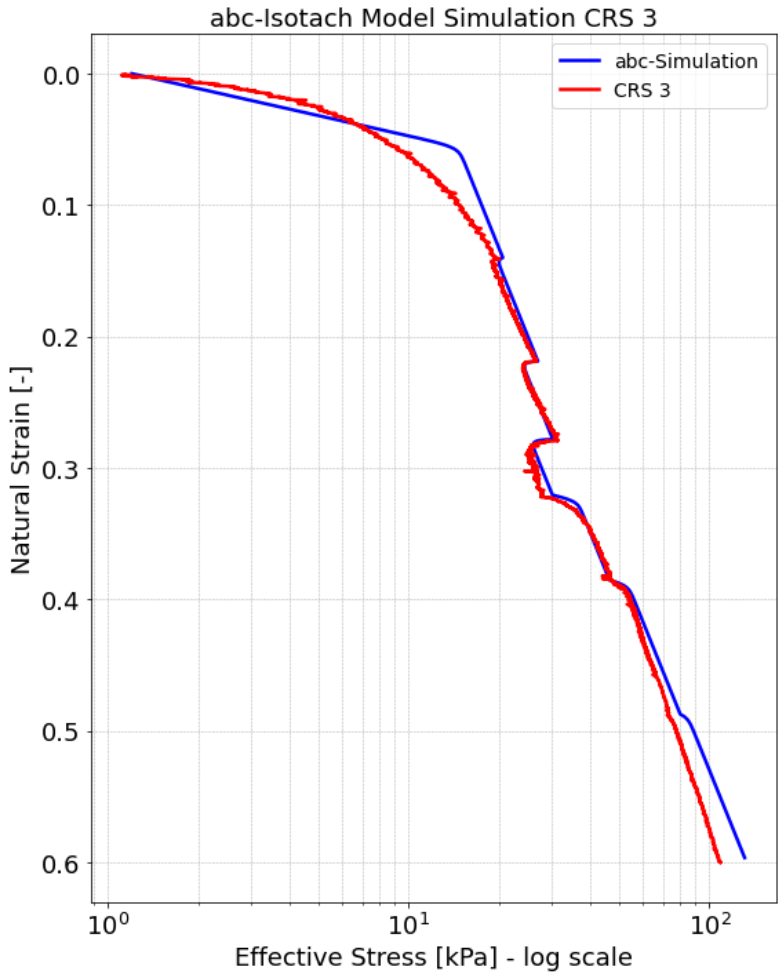

Figure A14.6: Simulation of CRS test 3 using the abc-isotach model.

Parameter	*Symbol*	*Value*
Direct compression coefficient	a	0.022
Secular compression coefficient	b	0.251
Secular strain rate coefficient	c	0.019
Reference time	τ_0	24 h

Table A14.2: Parameters used in abc-isotach simulation of CRS test 3.

CRS 3 SSC-Model Simulation

The results of the step-changed CRS 3 test are simulated using the Soft Soil Creep (SSC)-model and shown in Figure A14.7. Table A14.3 shows the parameters used.

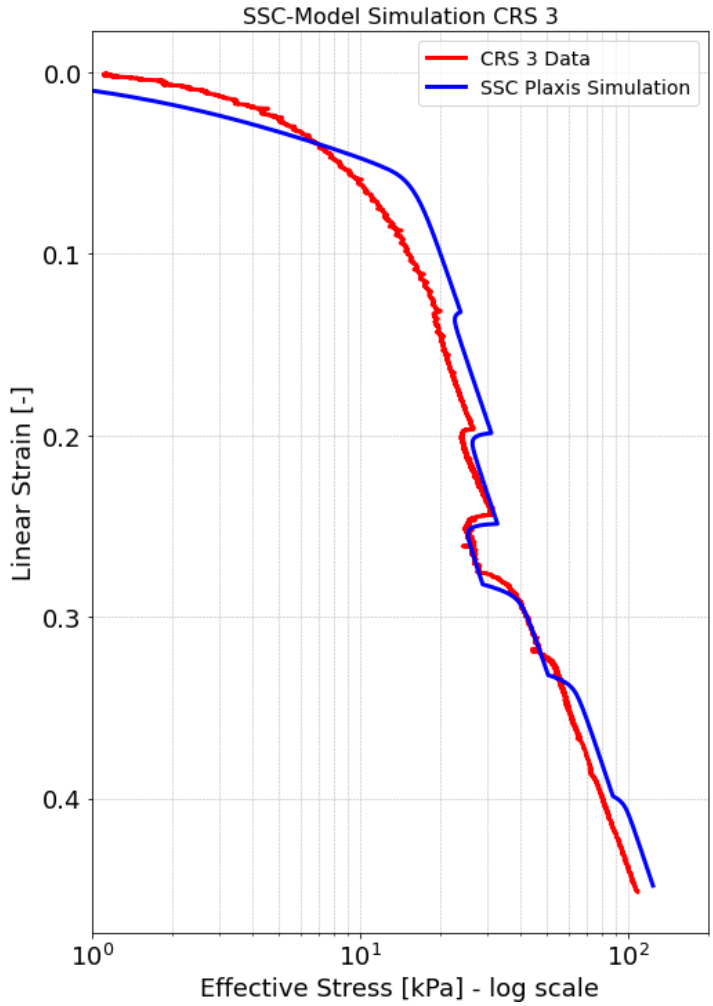

Figure A14.7: Simulation of CRS test 3 using the SSC model.

Parameter	*Symbol*	*Value*
Modified swelling index	κ^*	0.022
Modified compression index	λ^*	0.205
Modified creep index	μ^*	0.019
Poisson ratio	υ	0.15
Cohesion	c	0 kPa
Effective friction angle	φ'	40°
Dilatancy angle	ψ	5°

Table A14.3: Parameters used in SSC simulation of CRS test 3.

CRS 3 MIT EVP-Model Simulation

The results of the step-changed CRS 3 test are simulated using the MIT-EVP-model and shown in Figure A14.8. Table A14.4 shows the parameters used.

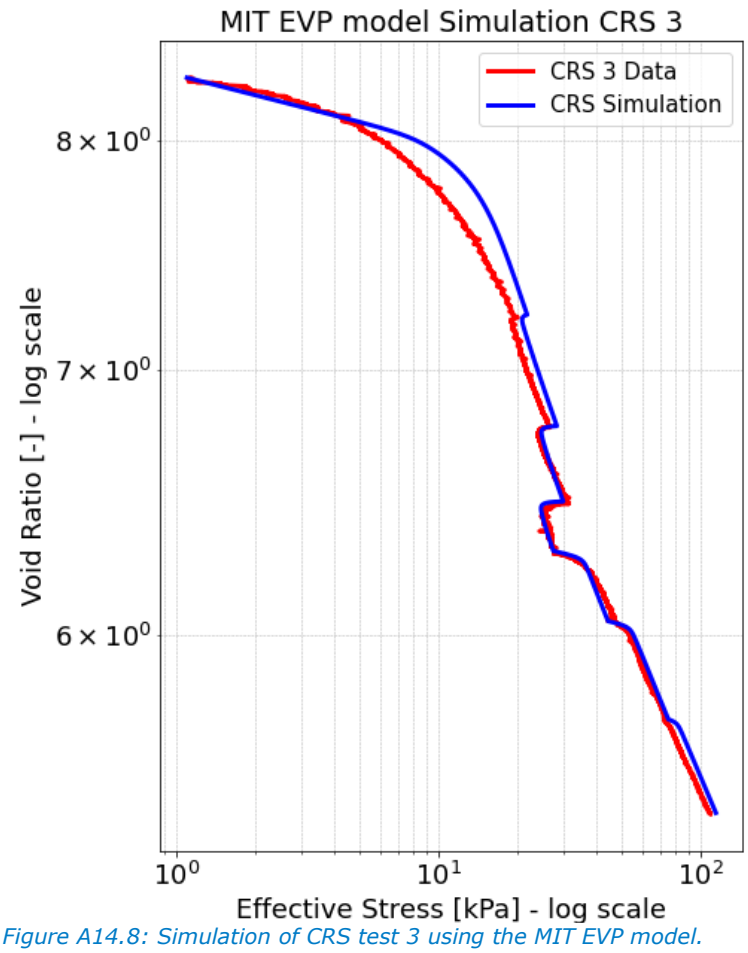

Figure A14.8: Simulation of CRS test 3 using the MIT EVP model.

Parameter	*Symbol*	*Value*
Slope of linearised elastic unloading/reloading curve	ρ_r	0.017
Slope of linearised virgin compression curve	ρ_c	0.225
Material constant characterising creep behaviour	ρ_α	0.020
Total strain rate as applied by the CRS apparatus	$\dot{\varepsilon}_t$	~
Reference strain rate	$\dot{\varepsilon}_{ref}$	$1.93 \cdot 10^{-7}\ s^{-1}$
Initial void ratio	e_0	8.3
Initial effective stress	σ'_{v0}	1.1 kPa.
Rate sensitivity	β	0.11 ($> \frac{\rho_\alpha}{\rho_c} = \frac{0.020}{0.225} = 0.088$)

Table A14.4: Parameters used in MIT EVP simulation of CRS test 3.

CRS 4 NEN-Bjerrum

The results of the step-changed CRS 4 test are simulated using the NEN-Bjerrum isotach-model and shown in Figure A14.9. Table A14.5 shows the parameters used.

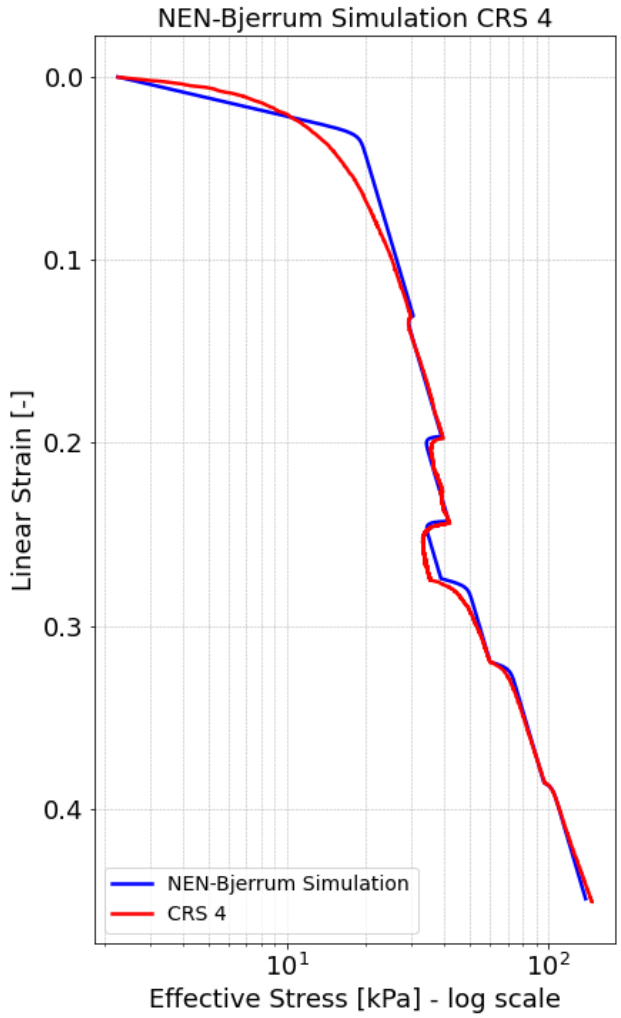

Figure A14.9: Simulation of CRS test 4 using the NEN-Bjerrum isotach model.

Parameter	*Symbol*	*Value*
Recompression Ratio	RR	0.033
Compression Ratio	CR	0.483
Secular strain rate coefficient	C_α	0.046
Reference time	τ_0	24 h

Table A14.5: Parameters used in NEN-Bjerrum isotach simulation of CRS test 4.

CRS 4 abc-Isotach Simulation

The results of the step-changed CRS 4 test are simulated using the abc-isotach-model and shown in Figure A14.10. Table A14.6 shows the parameters used.

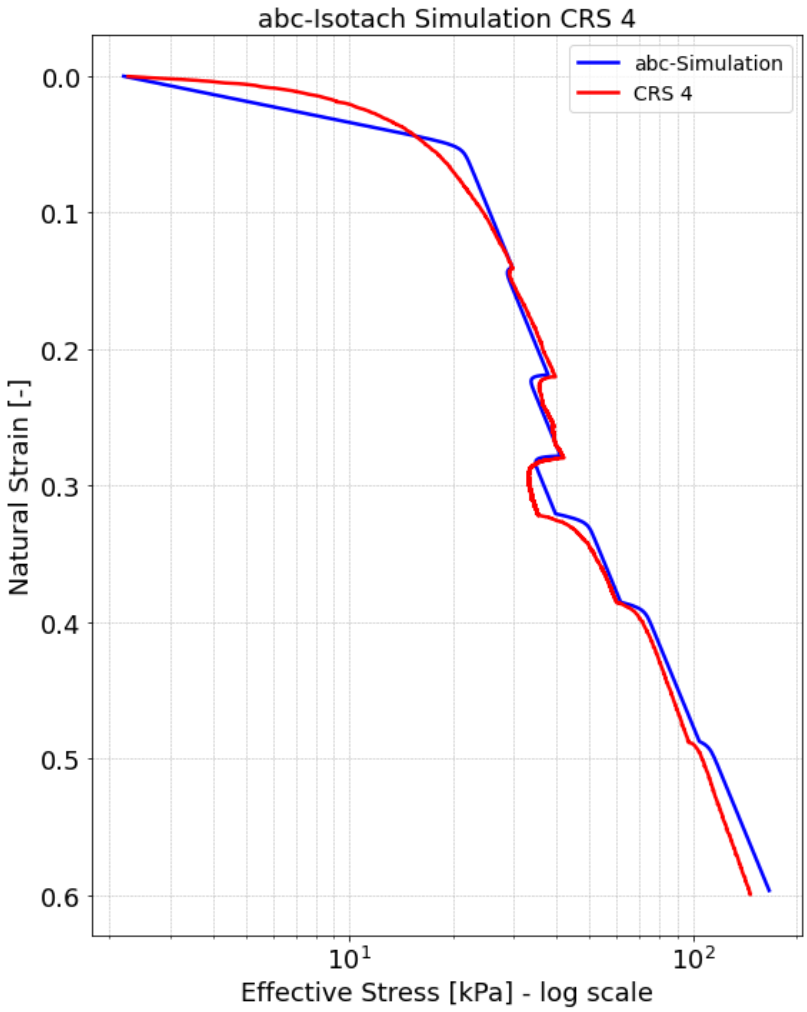

Figure A14.10: Simulation of CRS test 4 using the abc-Isotach model.

Parameter	*Symbol*	*Value*
Direct compression coefficient	a	0.022
Secular compression coefficient	b	0.271
Secular strain rate coefficient	c	0.023
Reference time	τ_0	24 h

Table A14.6: Parameters used in abc-isotach simulation of CRS test 4.

CRS 4 SSC-Model Simulation

The results of the step-changed CRS 4 test are simulated using the Soft Soil Creep (SSC)-model and shown in Figure A14.11. Table A14.7 shows the parameters used.

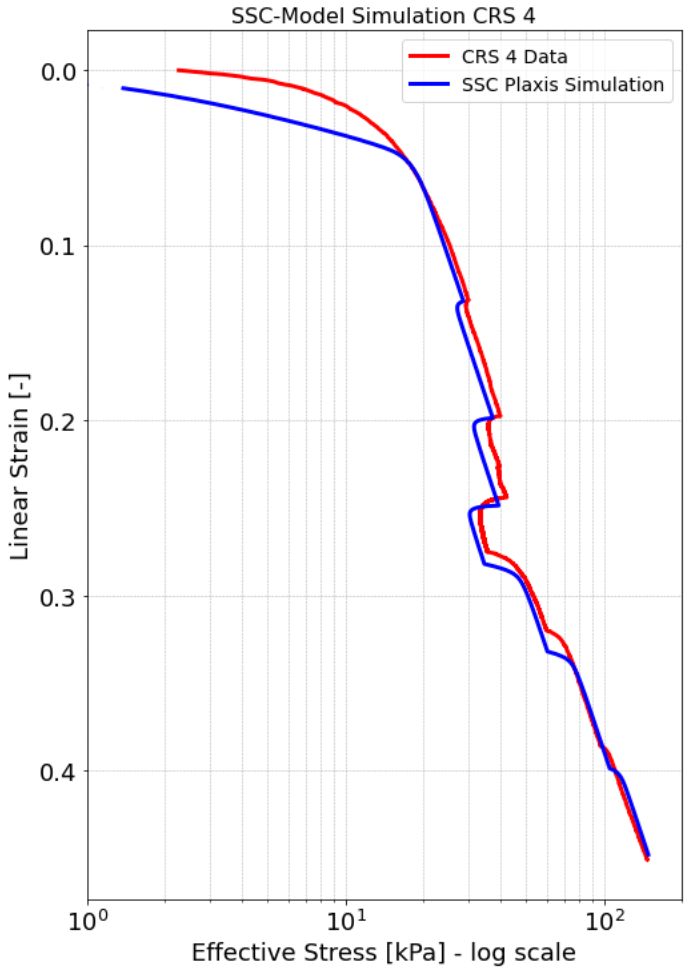

Figure A14.11: Simulation of CRS test 4 using the SSC model.

Parameter	*Symbol*	*Value*
Modified swelling index	κ^*	0.021
Modified compression index	λ^*	0.21
Modified creep index	μ^*	0.018
Poisson ratio	υ	0.15
Cohesion	c	0 kPa
Effective friction angle	φ'	40°
Dilatancy angle	ψ	5°

Table A14.7: Parameters used in SSC simulation of CRS test 4.

CRS 4 MIT EVP-Model Simulation

The results of the step-changed CRS 4 test are simulated using the MIT-EVP-model and shown in Figure A14.12. Table A14.8 shows the parameters used.

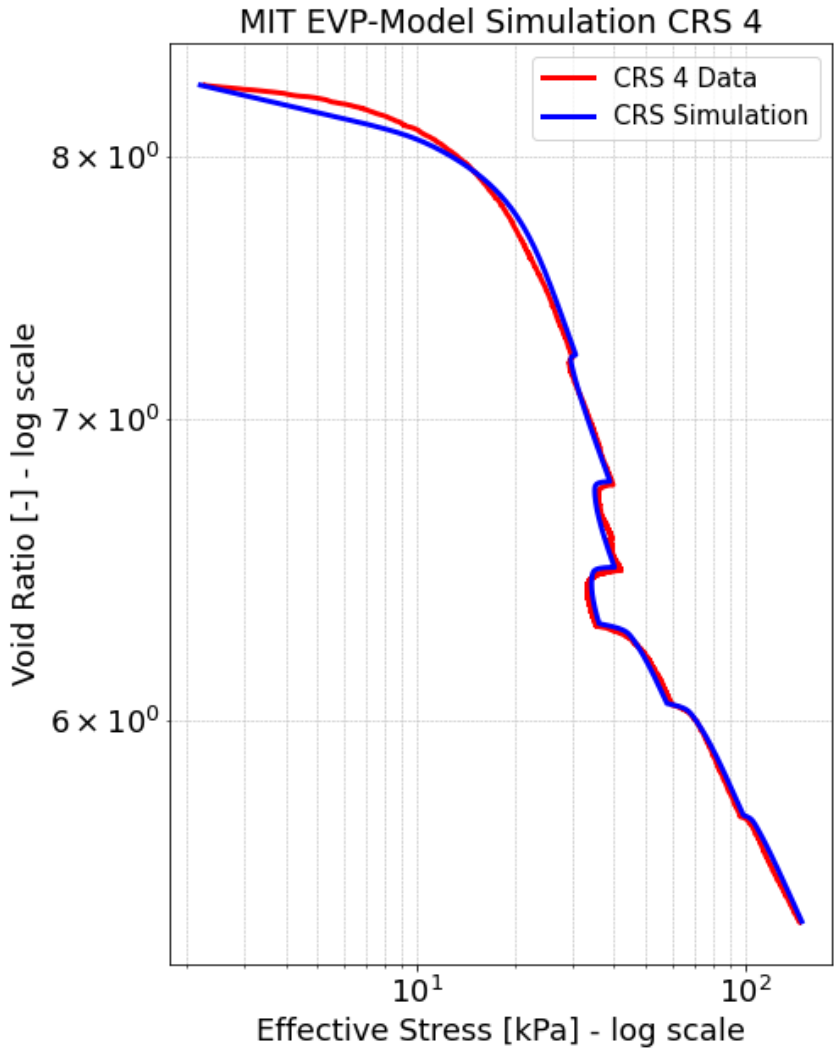

Figure A14.12: Simulation of CRS test 4 using the MIT EVP model.

Parameter	*Symbol*	*Value*
Slope of linearised elastic unloading/reloading curve	ρ_r	0.017
Slope of linearised virgin compression curve	ρ_c	0.235
Material constant characterising creep behaviour	ρ_α	0.015
Total strain rate as applied by the CRS apparatus	$\dot{\varepsilon}_t$	~
Reference strain rate	$\dot{\varepsilon}_{ref}$	$1.93 \cdot 10^{-7}\ s^{-1}$
Initial void ratio	e_0	8.3
Initial effective stress	σ'_{v0}	1.1 kPa.
Rate sensitivity	β	0.12 ($> \frac{\rho_\alpha}{\rho_c} = \frac{0.015}{0.235} = 0.068$)

Table A14.8: Parameters used in MIT EVP simulation of CRS test 4.

CRS 5 NEN-Bjerrum

The results of the step-changed CRS 5 test are simulated using the NEN-Bjerrum isotach-model and shown in Figure A14.13. Table A14.9 shows the parameters used.

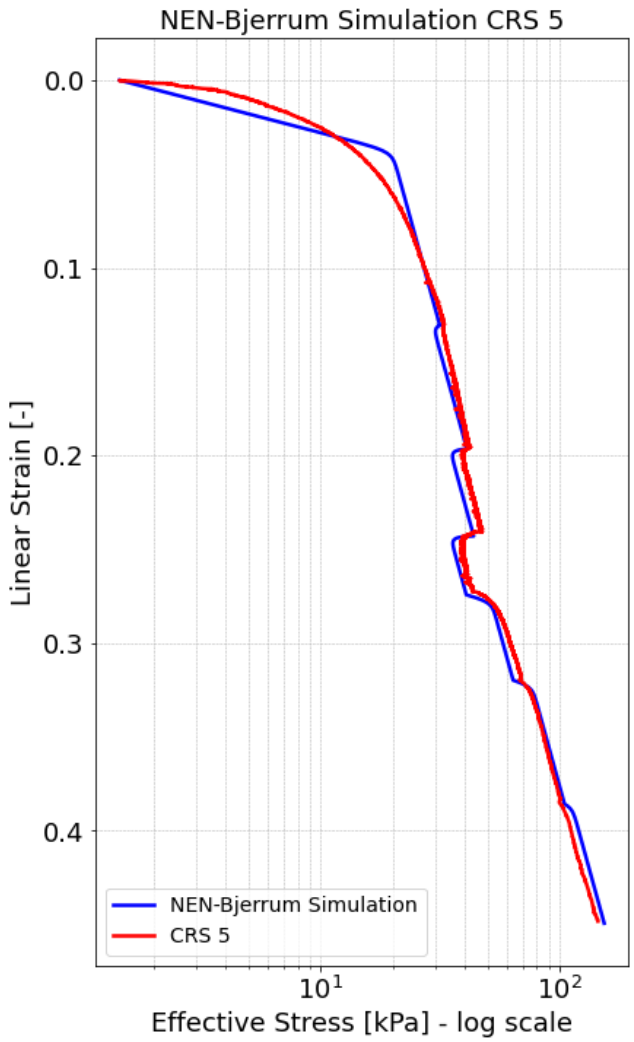

Figure A14.13: Simulation of CRS test 5 using the NEN-Bjerrum isotach model.

Parameter	*Symbol*	*Value*
Recompression Ratio	RR	0.033
Compression Ratio	CR	0.465
Secular strain rate coefficient	C_α	0.044
Reference time	τ_0	24 h

Table A14.9: Parameters used in NEN-Bjerrum isotach simulation of CRS test 5.

CRS 5 abc-Isotach Simulation

The results of the step-changed CRS 5 test are simulated using the abc-isotach-model and shown in Figure A14.14. Table A14.10 shows the parameters used.

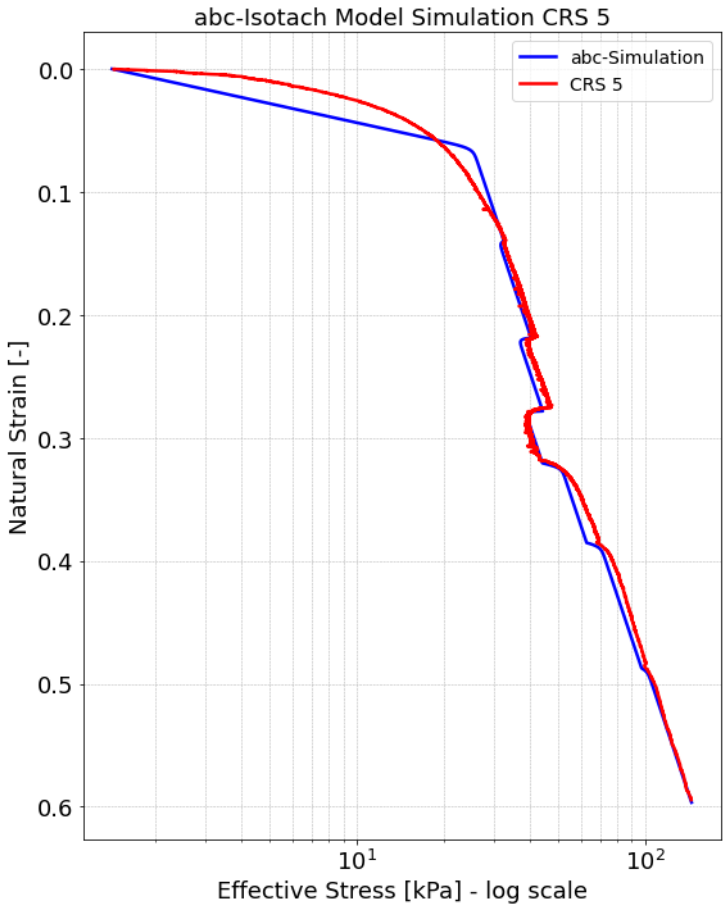

Figure A14.14: Simulation of CRS test 5 using the abc-Isotach model.

Parameter	*Symbol*	*Value*
Direct compression coefficient	a	0.021
Secular compression coefficient	b	0.311
Secular strain rate coefficient	c	0.019
Reference time	τ_0	24 h

Table A14.10: Parameters used in abc-isotach simulation of CRS test 5.

CRS 5 SSC-Model Simulation

The results of the step-changed CRS 5 test are simulated using the Soft Soil Creep (SSC)-model and shown in Figure A14.15. Table A14.11 shows the parameters used.

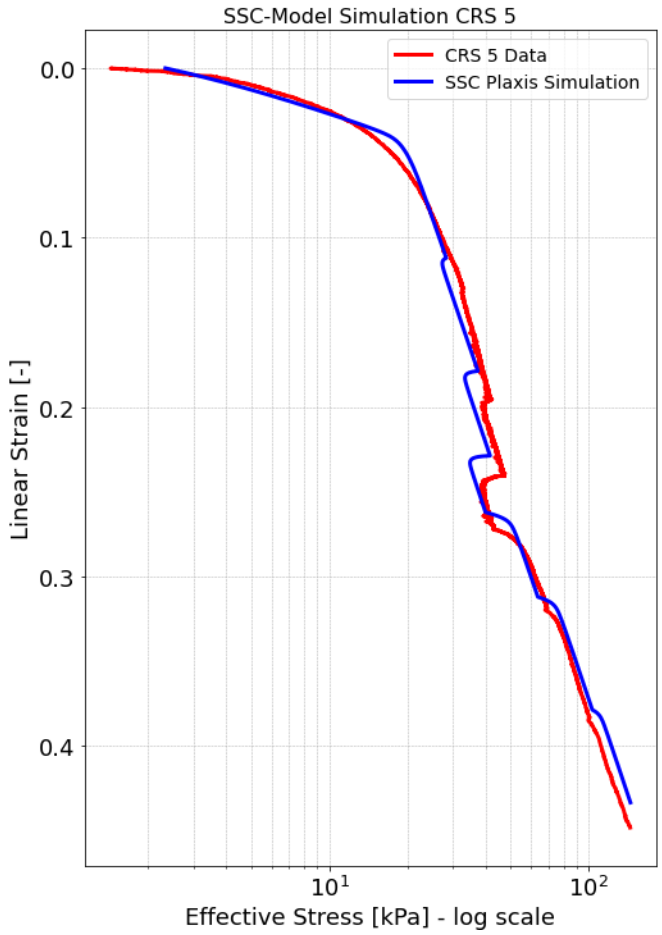

Figure A14.15: Simulation of CRS test 5 using the SSC model.

Parameter	*Symbol*	*Value*
Modified swelling index	κ^*	0.024
Modified compression index	λ^*	0.215
Modified creep index	μ^*	0.018
Poisson ratio	υ	0.15
Cohesion	c	0 kPa
Effective friction angle	φ'	40°
Dilatancy angle	ψ	5°

Table A14.11: Parameters used in SSC simulation of CRS test 5.

CRS 5 MIT EVP-Model Simulation

The results of the step-changed CRS 5 test are simulated using the MIT-EVP-model and shown in Figure A14.16. Table A14.12 shows the parameters used.

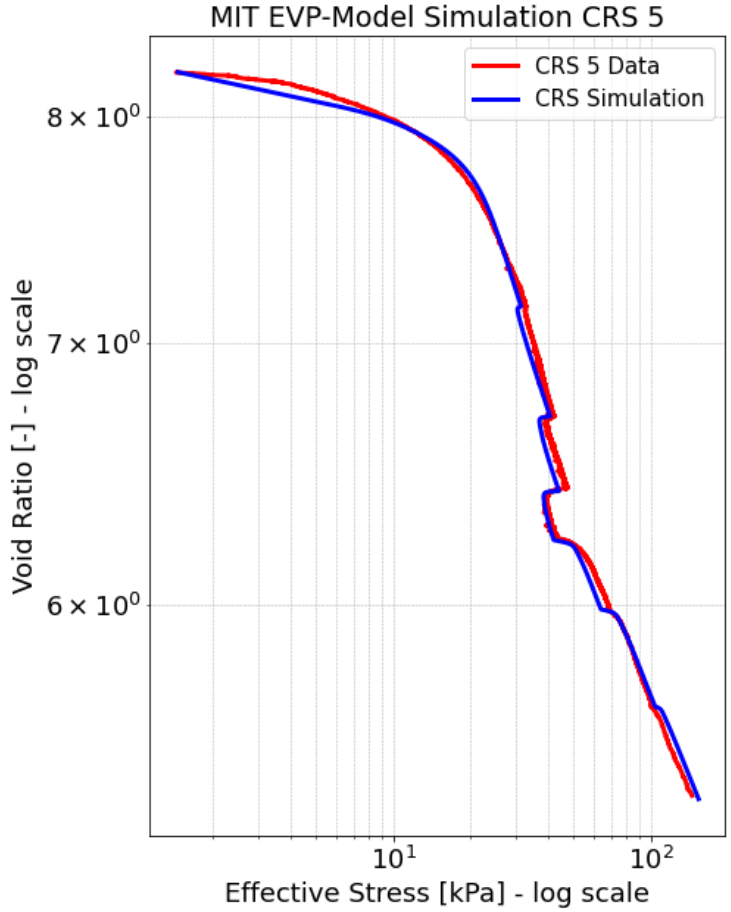

Figure A14.16: Simulation of CRS test 5 using the MIT EVP model.

Parameter	*Symbol*	*Value*
Slope of linearised elastic unloading/reloading curve	ρ_r	0.014
Slope of linearised virgin compression curve	ρ_c	0.235
Material constant characterising creep behaviour	ρ_α	0.014
Total strain rate as applied by the CRS apparatus	$\dot{\varepsilon}_t$	~
Reference strain rate	$\dot{\varepsilon}_{ref}$	$1.93 \cdot 10^{-7}\ s^{-1}$
Initial void ratio	e_0	8.2
Initial effective stress	σ'_{v0}	1.5 kPa.
Rate sensitivity	β	0.09 ($> \frac{\rho_\alpha}{\rho_c} = \frac{0.014}{0.235} = 0.059$)

Table A14.12: Parameters used in MIT EVP simulation of CRS test 5.

CRS 6 NEN-Bjerrum

The results of the step-changed CRS 6 test are simulated using the NEN-Bjerrum isotach-model and shown in Figure A14.17. Table A14.13 shows the parameters used.

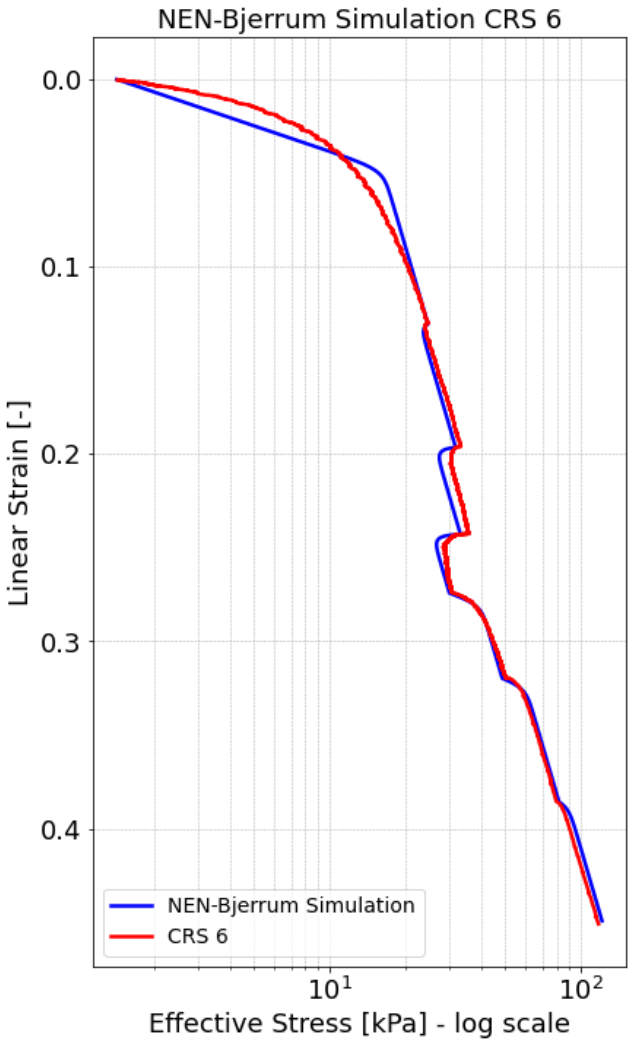

Figure A14.17: Simulation of CRS test 6 using the NEN-Bjerrum isotach model.

Parameter	*Symbol*	*Value*
Recompression Ratio	RR	0.045
Compression Ratio	CR	0.460
Secular strain rate coefficient	C_α	0.052
Reference time	τ_0	24 h

Table A14.13: Parameters used in NEN-Bjerrum isotach simulation of CRS test 6.

CRS 6 abc-Isotach Simulation

The results of the step-changed CRS 6 test are simulated using the abc-isotach-model and shown in Figure A14.18. Table A14.14 shows the parameters used.

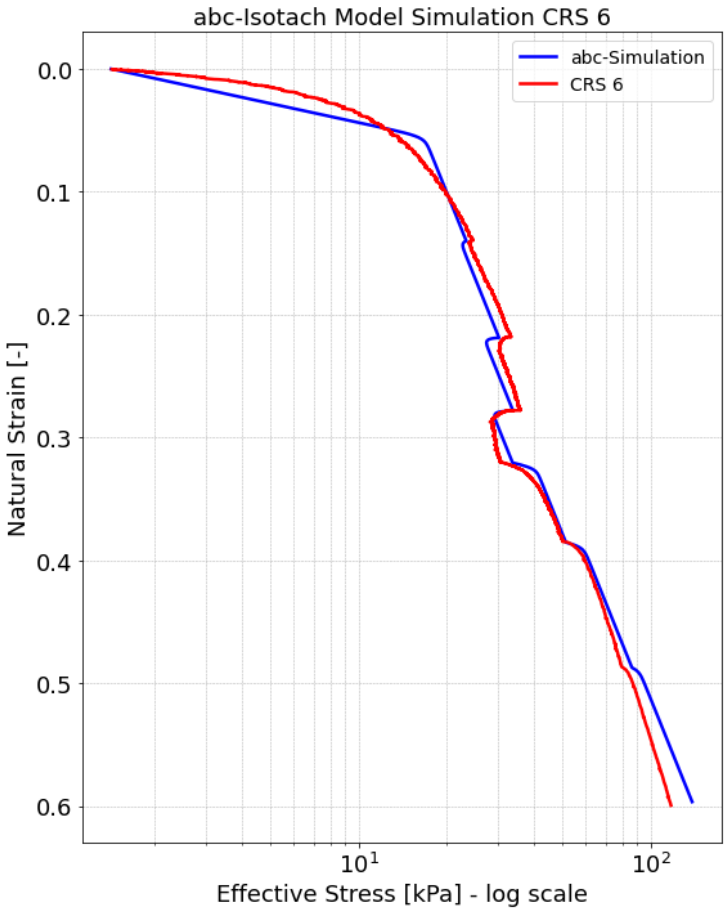

Figure A14.18: Simulation of CRS test 6 using the abc-Isotach model.

Parameter	*Symbol*	*Value*
Direct compression coefficient	a	0.023
Secular compression coefficient	b	0.261
Secular strain rate coefficient	c	0.019
Reference time	τ_0	24 h

Table A14.14: Parameters used in abc-isotach simulation of CRS test 6.

CRS 6 SSC-Model Simulation

The results of the step-changed CRS 6 test are simulated using the Soft Soil Creep (SSC)-model and shown in Figure A14.19. Table A14.15 shows the parameters used.

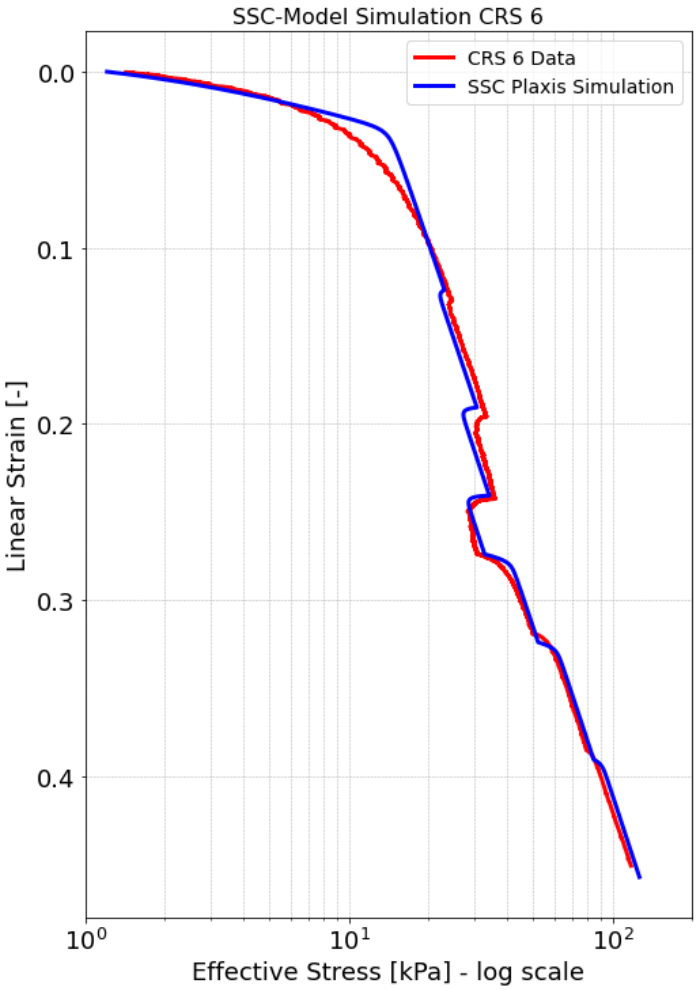

Figure A14.19: Simulation of CRS test 6 using the SSC model.

Parameter	*Symbol*	*Value*
Modified swelling index	κ^*	0.020
Modified compression index	λ^*	0.200
Modified creep index	μ^*	0.018
Poisson ratio	υ	0.15
Cohesion	c	0 kPa
Effective friction angle	φ'	40°
Dilatancy angle	ψ	5°

Table A14.15: Parameters used in SSC simulation of CRS test 6.

CRS 6 MIT EVP-Model Simulation

The results of the step-changed CRS 6 test are simulated using the MIT-EVP-model and shown in Figure A14.20. Table A14.16 shows the parameters used.

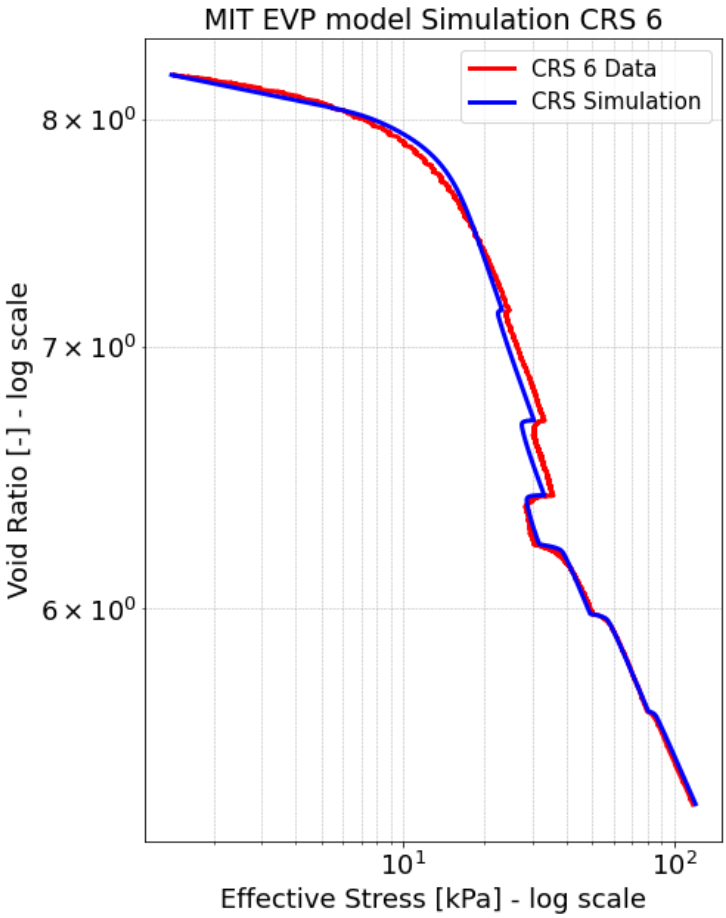

Figure A14.20: Simulation of CRS test 6 using the MIT EVP model.

Parameter	*Symbol*	*Value*
Slope of linearised elastic unloading/reloading curve	ρ_r	0.014
Slope of linearised virgin compression curve	ρ_c	0.227
Material constant characterising creep behaviour	ρ_α	0.015
Total strain rate as applied by the CRS apparatus	$\dot{\varepsilon}_t$	~
Reference strain rate	$\dot{\varepsilon}_{ref}$	$1.93 \cdot 10^{-7}\ s^{-1}$
Initial void ratio	e_0	8.2
Initial effective stress	σ'_{v0}	1.5 kPa.
Rate sensitivity	β	0.09 ($> \frac{\rho_\alpha}{\rho_c} = \frac{0.015}{0.227} = 0.066$)

Table A14.16: Parameters used in MIT EVP simulation of CRS test 6.

CRS 7 NEN-Bjerrum

The results of the step-changed CRS 7 test are simulated using the NEN-Bjerrum isotach-model and shown in Figure A14.21. Table A14.17 shows the parameters used.

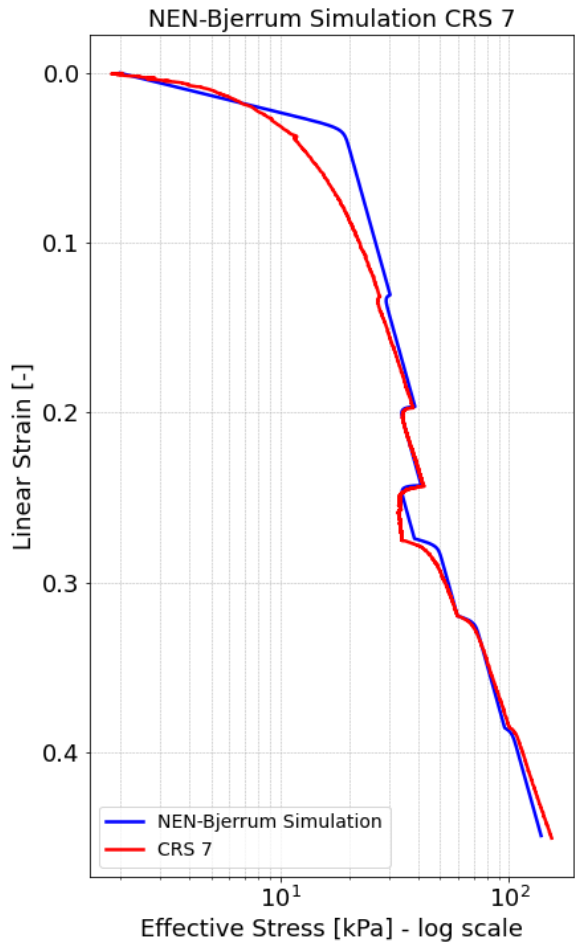

Figure A14.21: Simulation of CRS test 7 using the NEN-Bjerrum isotach model.

Parameter	*Symbol*	*Value*
Recompression Ratio	RR	0.033
Compression Ratio	CR	0.465
Secular strain rate coefficient	C_α	0.044
Reference time	τ_0	24 h

Table A14.17: Parameters used in NEN-Bjerrum isotach simulation of CRS test 7.

CRS 7 abc-Isotach Simulation

The results of the step-changed CRS 4 test are simulated using the abc-isotach-model and shown in Figure A14.22. Table A14.18 shows the parameters used.

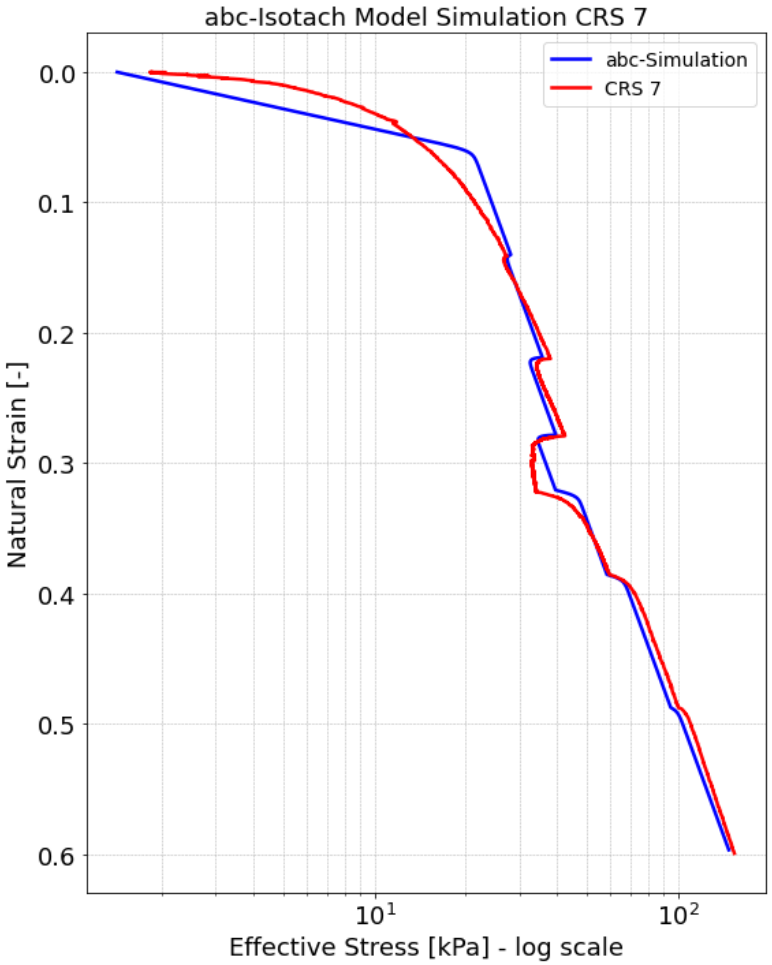

Figure A14.22: Simulation of CRS test 7 using the abc-Isotach model.

Parameter	*Symbol*	*Value*
Direct compression coefficient	a	0.022
Secular compression coefficient	b	0.281
Secular strain rate coefficient	c	0.019
Reference time	τ_0	24 h

Table A14.18: Parameters used in abc-isotach simulation of CRS test 7.

CRS 7 SSC-Model Simulation

The results of the step-changed CRS 7 test are simulated using the Soft Soil Creep (SSC)-model and shown in Figure A14.23. Table A14.19 shows the parameters used.

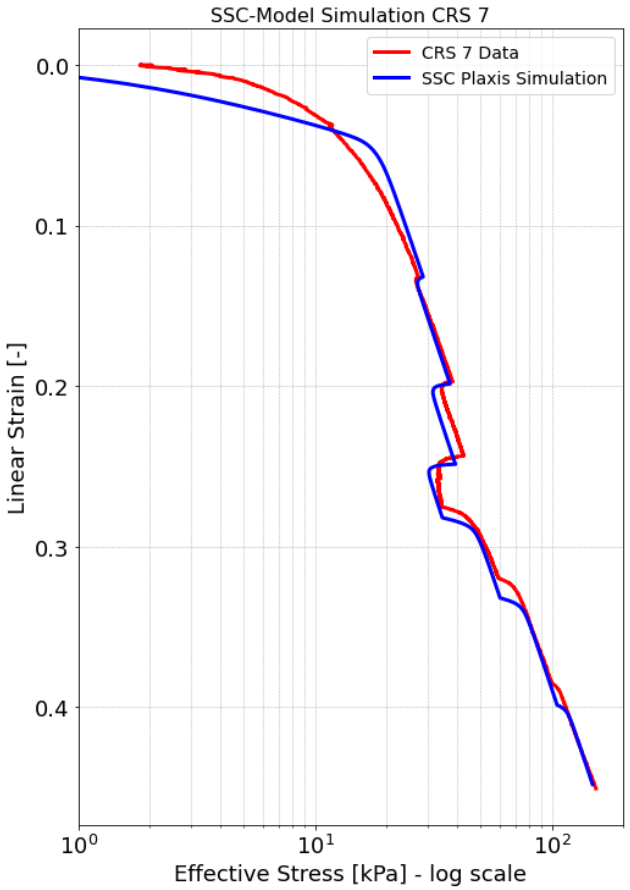

Figure A14.23: Simulation of CRS test 5 using the SSC model.

Parameter	*Symbol*	*Value*
Modified swelling index	κ^*	0.022
Modified compression index	λ^*	0.213
Modified creep index	μ^*	0.017
Poisson ratio	υ	0.15
Cohesion	c	0 kPa
Effective friction angle	φ'	40°
Dilatancy angle	ψ	5°

Table A14.19: Parameters used in SSC simulation of CRS test 7.

CRS 7 MIT EVP-Model Simulation

The results of the step-changed CRS 7 test are simulated using the MIT-EVP-model and shown in Figure A14.24. Table A14.20 shows the parameters used.

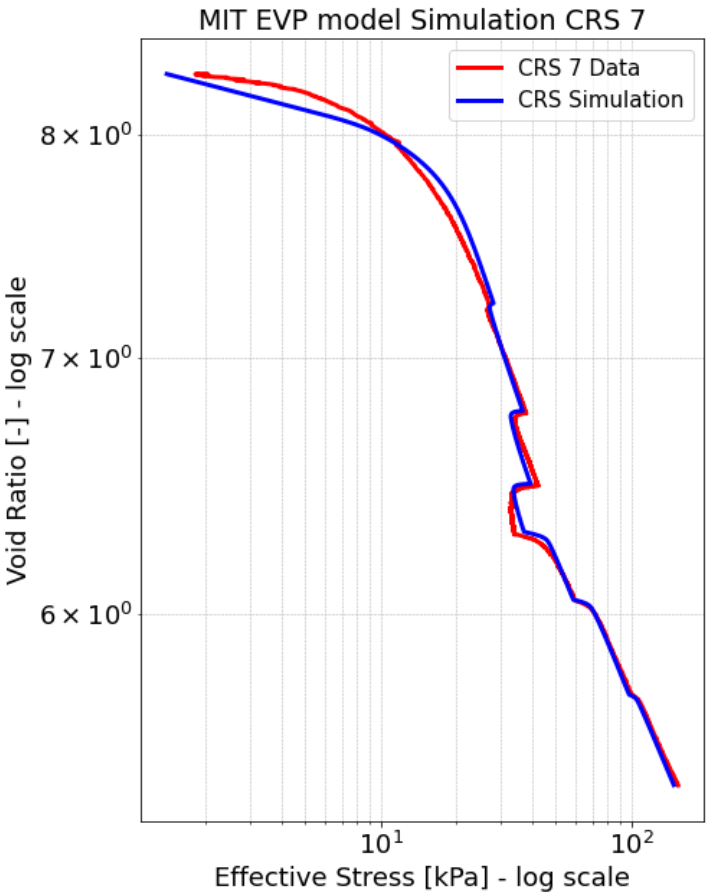

Figure A14.24: Simulation of CRS test 7 using the MIT EVP model.

Parameter	*Symbol*	*Value*
Slope of linearised elastic unloading/reloading curve	ρ_r	0.017
Slope of linearised virgin compression curve	ρ_c	0.225
Material constant characterising creep behaviour	ρ_α	0.016
Total strain rate as applied by the CRS apparatus	$\dot{\varepsilon}_t$	~
Reference strain rate	$\dot{\varepsilon}_{ref}$	$1.93 \cdot 10^{-7}\ s^{-1}$
Initial void ratio	e_0	8.3
Initial effective stress	σ'_{v0}	1.1 kPa.
Rate sensitivity	β	0.10 ($> \frac{\rho_\alpha}{\rho_c} = \frac{0.016}{0.225} = 0.071$)

Table A14.20: Parameters used in MIT EVP simulation of CRS test 7.

CRS Rapid Transition Test NEN-Bjerrum isotach Model Simulation

The results of the rapid transition CRS test are simulated using the NEN-Bjerrum isotach model and shown in Figure A14.25. Table A14.21 shows the parameters used.

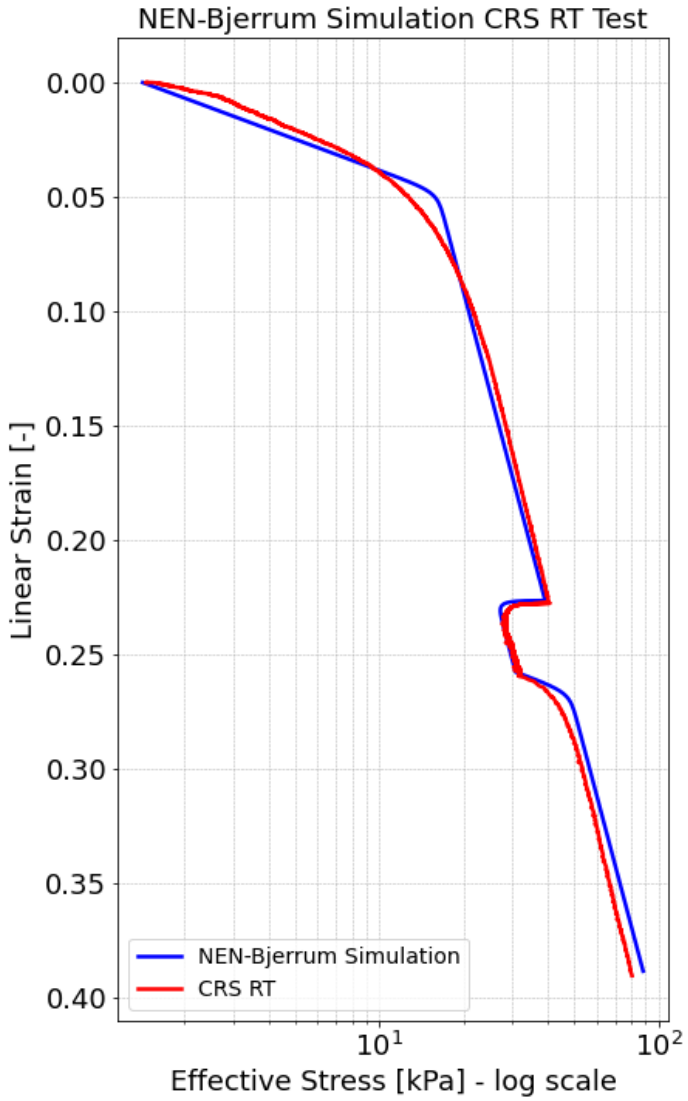

Figure A14.25: Simulation of CRS RT test using the NEN-Bjerrum isotach model.

Parameter	*Symbol*	*Value*
Recompression Ratio	RR	0.045
Compression Ratio	CR	0.462
Secular strain rate coefficient	C_α	0.040
Reference time	τ_0	24 h

Table A14.21: Parameters used in CRS RT test NEN-Bjerrum isotach model simulation.

CRS Rapid Transition Test abc-isotach Model Simulation

The results of the rapid transition CRS test are simulated using the abc-isotach model and shown in Figure A14.26. Table A14.22 shows the parameters used.

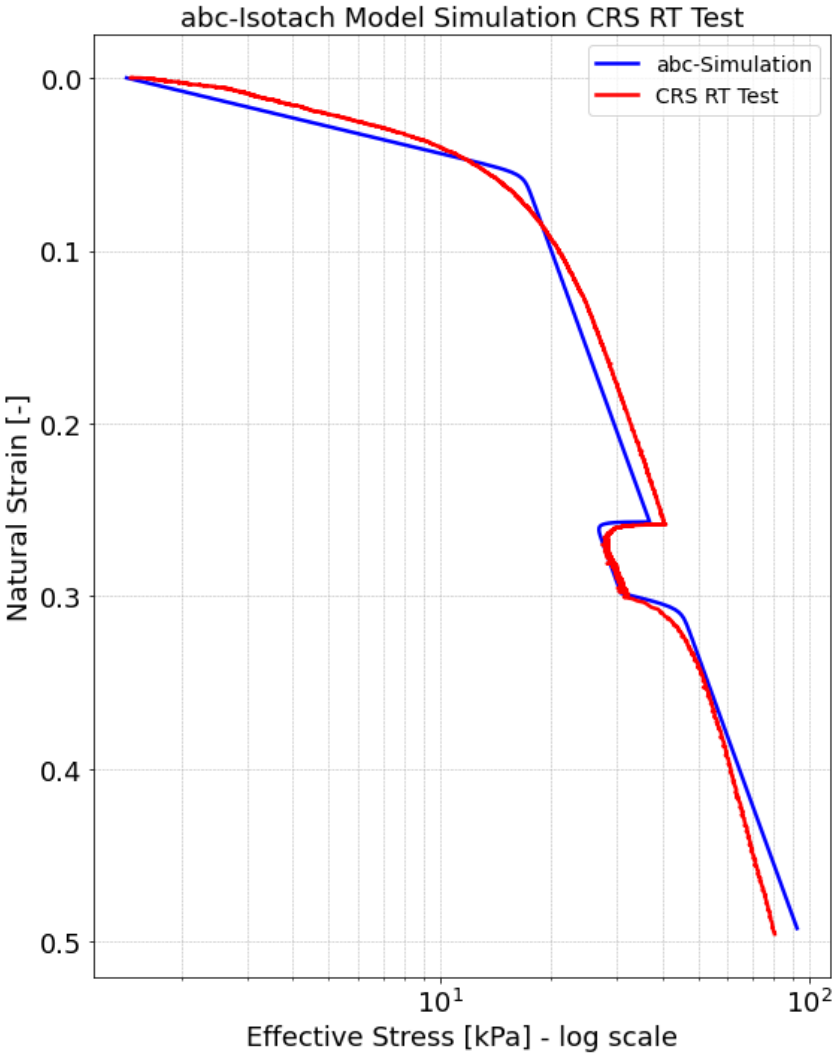

Figure A14.26: Simulation of CRS rapid transition test using the abc-isotach model.

Parameter	*Symbol*	*Value*
Direct compression coefficient	a	0.022
Secular compression coefficient	b	0.261
Secular strain rate coefficient	c	0.019
Reference time	τ_0	24 h

Table A14.22: Parameters used in CRS RT test abc-isotach model simulation.

CRS Rapid Transition Test Soft Soil Creep Model Simulation

The results of the rapid transition CRS test are simulated using the SSC-model and shown in Figure A14.27. Table A14.23 shows the parameters used.

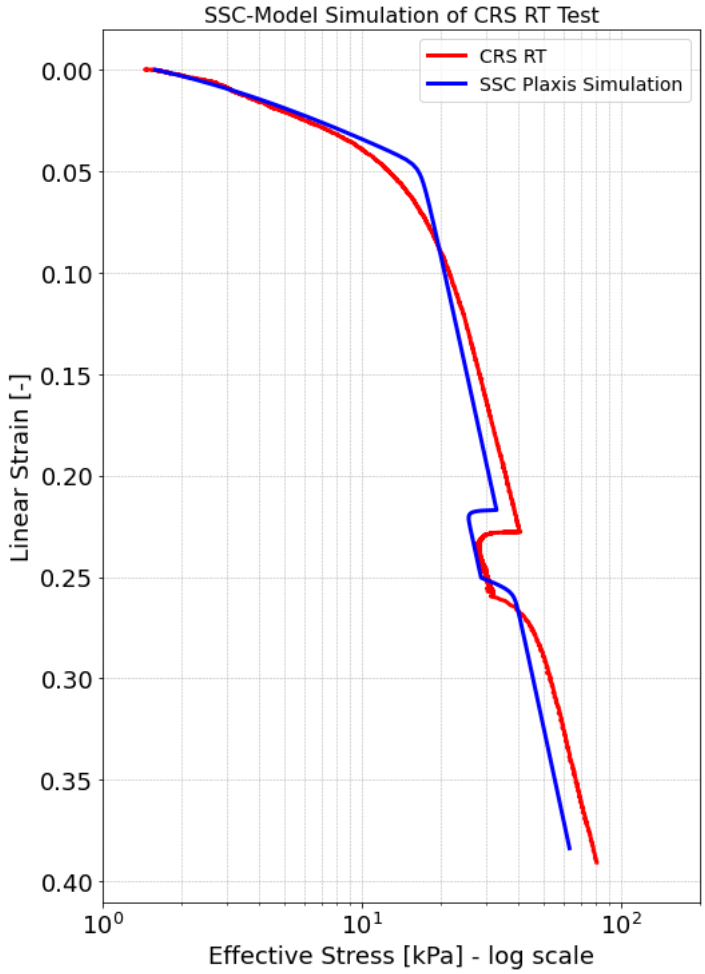

Figure A14.27: Simulation of CRS rapid transition test using the soft soil creep model.

Parameter	*Symbol*	*Value*
Modified swelling index	κ^*	0.021
Modified compression index	λ^*	0.204
Modified creep index	μ^*	0.017
Poisson ratio	υ	0.15
Cohesion	c	0 kPa
Effective friction angle	φ'	40°
Dilatancy angle	ψ	5°

Table A14.23: Parameters used in CRS RT test SSC model simulation.

CRS Rapid Transition Test MIT-Y&W EVP Model Simulation

The results of the rapid transition CRS test are simulated using the Y&W MIT-EVP-model and shown in Figure A14.25. Table A14.21 shows the parameters used.

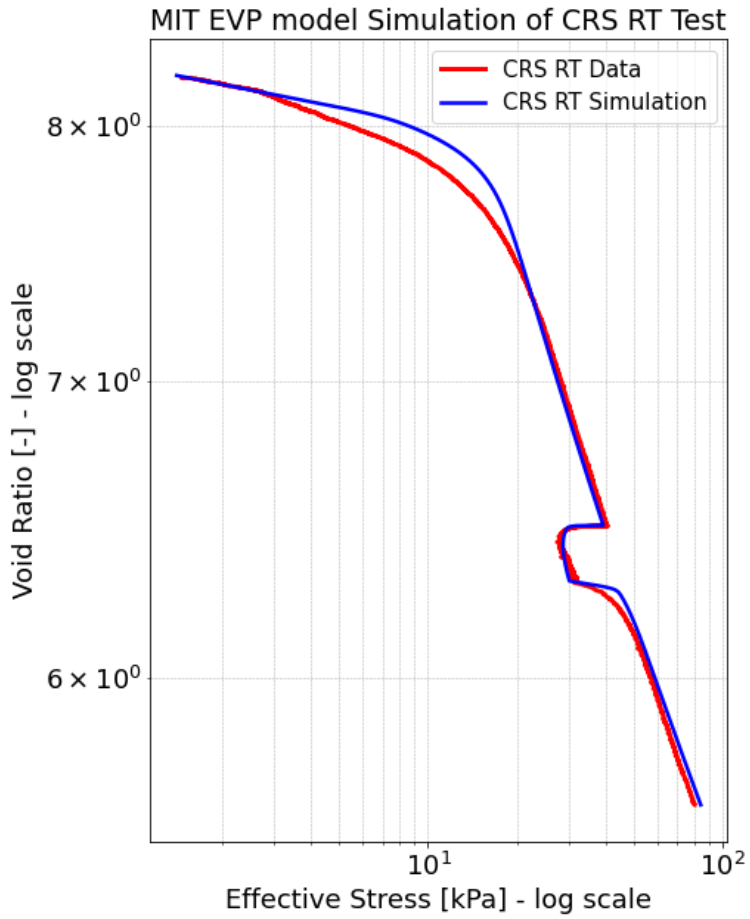

Figure A14.28: Simulation of CRS rapid transition test using the MIT Yuan and Whittle EVP model.

Parameter	*Symbol*	*Value*
Slope of linearised elastic unloading/reloading curve	ρ_r	0.013
Slope of linearised virgin compression curve	ρ_c	0.250
Material constant characterising creep behaviour	ρ_α	0.015
Total strain rate as applied by the CRS apparatus	$\dot{\varepsilon}_t$	~
Reference strain rate	$\dot{\varepsilon}_{ref}$	$1.93 \cdot 10^{-7}\ s^{-1}$
Initial void ratio	e_0	8.3
Initial effective stress	σ'_{v0}	1.1 kPa.
Rate sensitivity	β	0.09 ($> \frac{\rho_\alpha}{\rho_c} = \frac{0.015}{0.250} = 0.06$)

Appendix 15 InSAR Data

This appendix shows the calculated annual deformation rate of different parts of the embankment connecting Vinkeveen to the A2. For each location the approximate location of the RUM is indicated in the lower left corner. This estimated annual deformation rate is ultimately used to approximate the strain rate of the embankment connecting Vinkeveen to the A2.

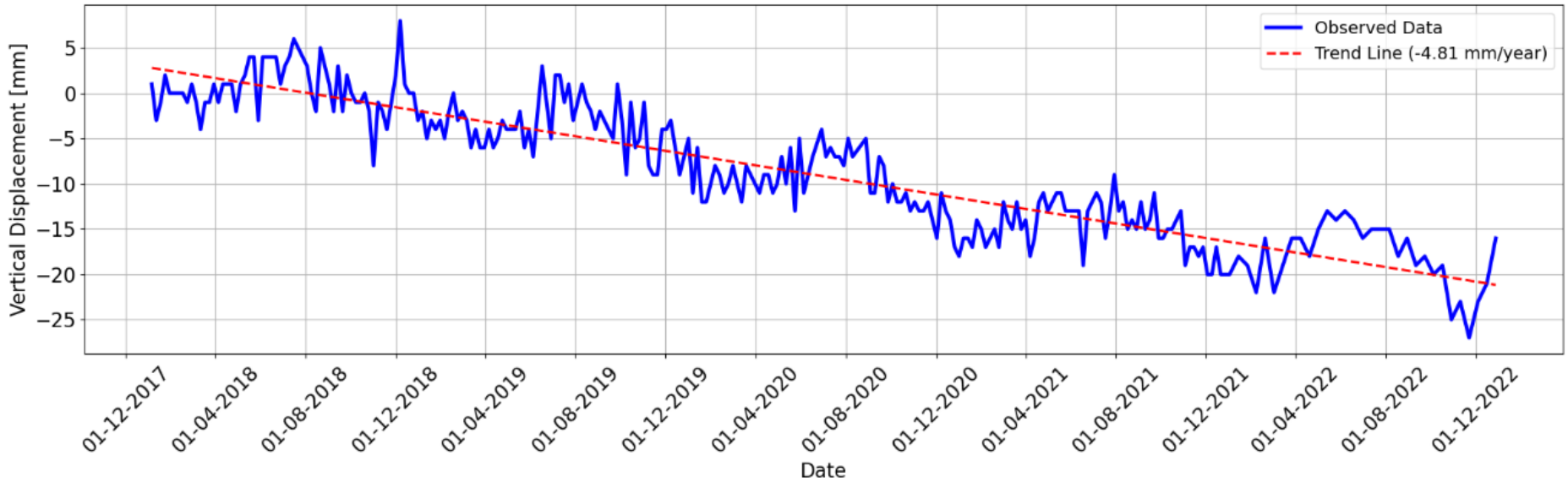

Figure A15.1: Estimated deformation timeseries of single datapoint by projection on vertical displacement vector. The estimated timeseries shows clear seasonality. A fitted linear trendline provides an estimated annual deformation rate.

Figure A15.2: Location of datapoint used in the timeseries estimate. Note that the location of the datapoint is on the embankment constructed during the period 2003-2006.

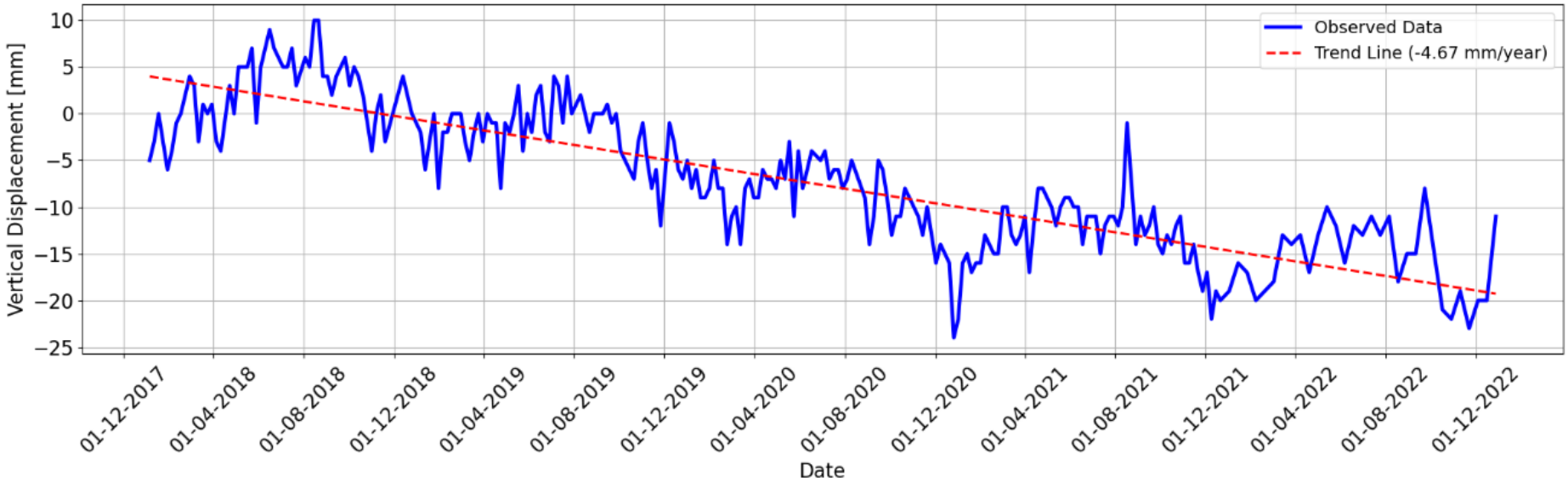

Figure A15.3: Estimated deformation timeseries of single datapoint by projection on vertical displacement vector. The estimated timeseries shows clear seasonality. A fitted linear trendline provides an estimated annual deformation rate.

Figure A15.4: Location of datapoint used in the timeseries estimate. Note that the location of the datapoint is on the embankment constructed during the period 2003-2006.

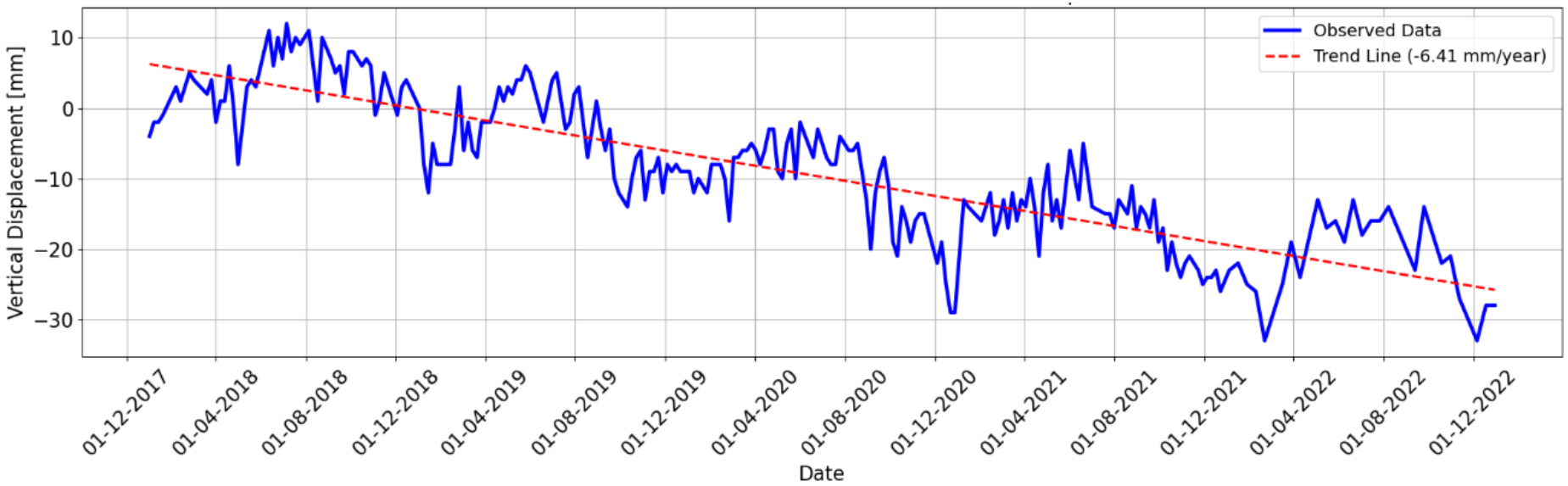

Figure A15.5: Estimated deformation timeseries of single datapoint by projection on vertical displacement vector. The estimated timeseries shows clear seasonality. A fitted linear trendline provides an estimated annual deformation rate.

Figure A15.6: Location of datapoint used in the timeseries estimate. Note that the location of the datapoint is on the embankment constructed during the period 2003-2006.

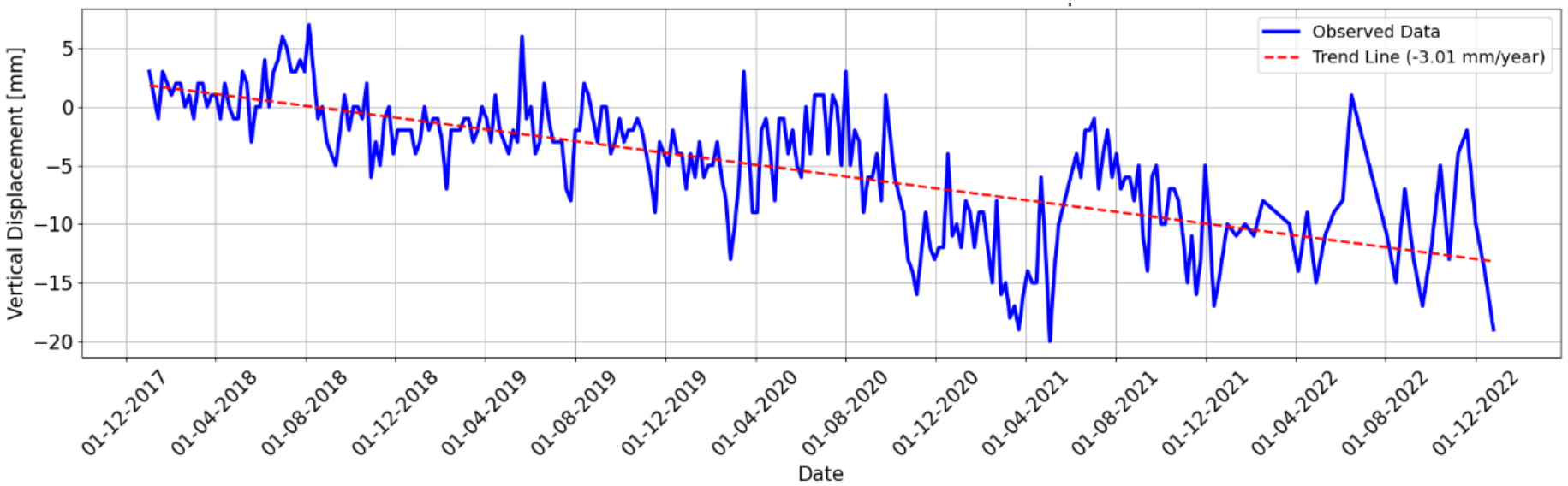

Figure A15.7: Estimated deformation timeseries of single datapoint by projection on vertical displacement vector. The estimated timeseries shows clear seasonality. A fitted linear trendline provides an estimated annual deformation rate. Note that the location of this datapoint is along the already existing part of the A2 which results in a lower estimated annual deformation rate.

Figure A15.8: Location of datapoint used in the timeseries estimate. Note that the location of the datapoint is next to the embankment constructed during the period 2003-2006 resulting in a lower estimated annual deformation rate.

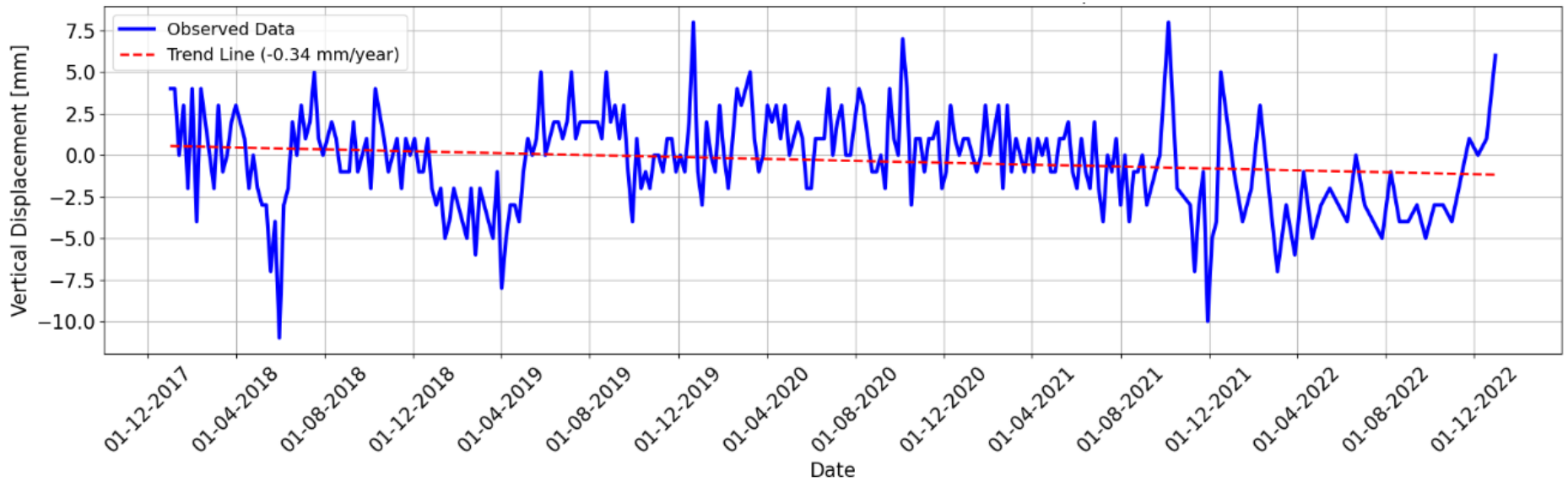

Figure A15.9: Estimated deformation timeseries of single datapoint by projection on vertical displacement vector. The estimated timeseries shows clear seasonality. A fitted linear trendline provides an estimated annual deformation rate. Note that the location of this datapoint is on the bridge crossing the Oukoop waterway. As a result, the estimated annual deformation rate is close to zero. This makes sense because the foundations of the bridge are most likely founded on the Pleistocene sand layer resulting in minimal estimated deformation over time.

Figure A15.10: Location of the datapoint used in the timeseries estimate. Note that the location of the datapoint is on the bridge crossing the Oukoop waterway.

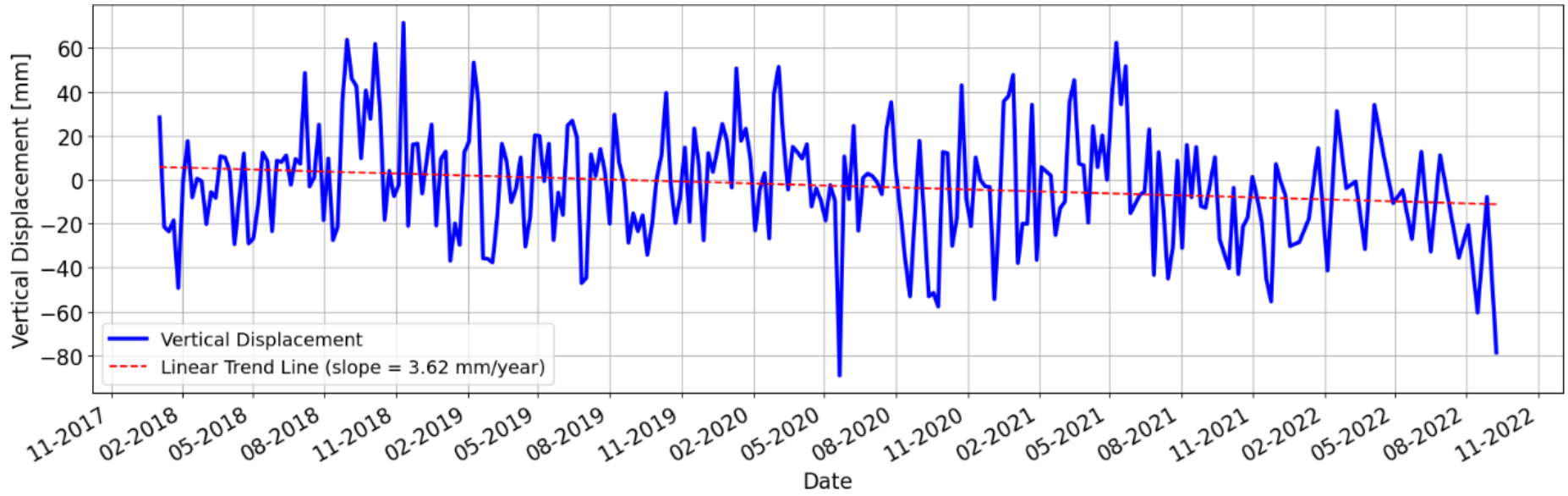

Figure A15.11: Estimated deformation timeseries of multiple, in this case 6, datapoints by solving for the full three-dimensional displacement vector by applying a least-squares estimate solution. The estimated timeseries shows clear seasonality. A fitted linear trendline provides an estimated annual deformation rate.

Figure A15.12: Location of datapoints used in the timeseries estimate. In this case it is assumed that the 6 datapoints in the RUM undergo the same deformation pattern.

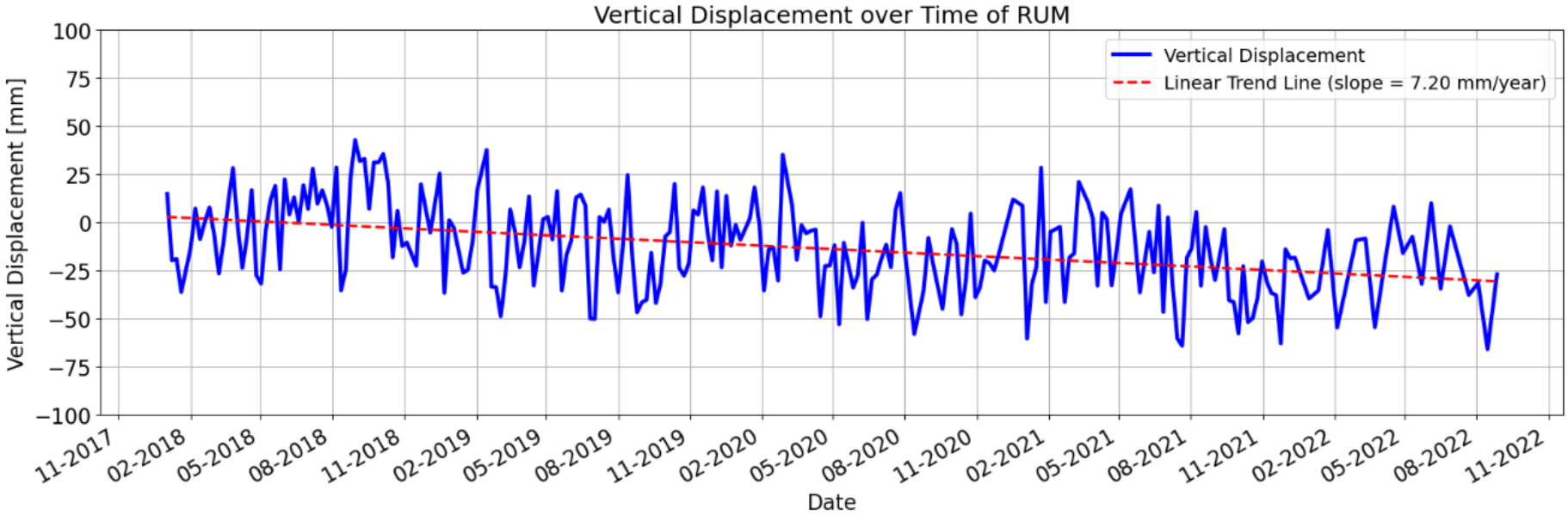

Figure A15.13: Estimated deformation timeseries of multiple, in this case 6, datapoints by solving for the full three-dimensional displacement vector by applying a least-squares estimate solution. The estimated timeseries shows clear seasonality. A fitted linear trendline provides an estimated annual deformation rate.

Figure A15.14: Location of datapoints used in the timeseries estimate. In this case it is assumed that the 6 datapoints in the RUM undergo the same deformation pattern.

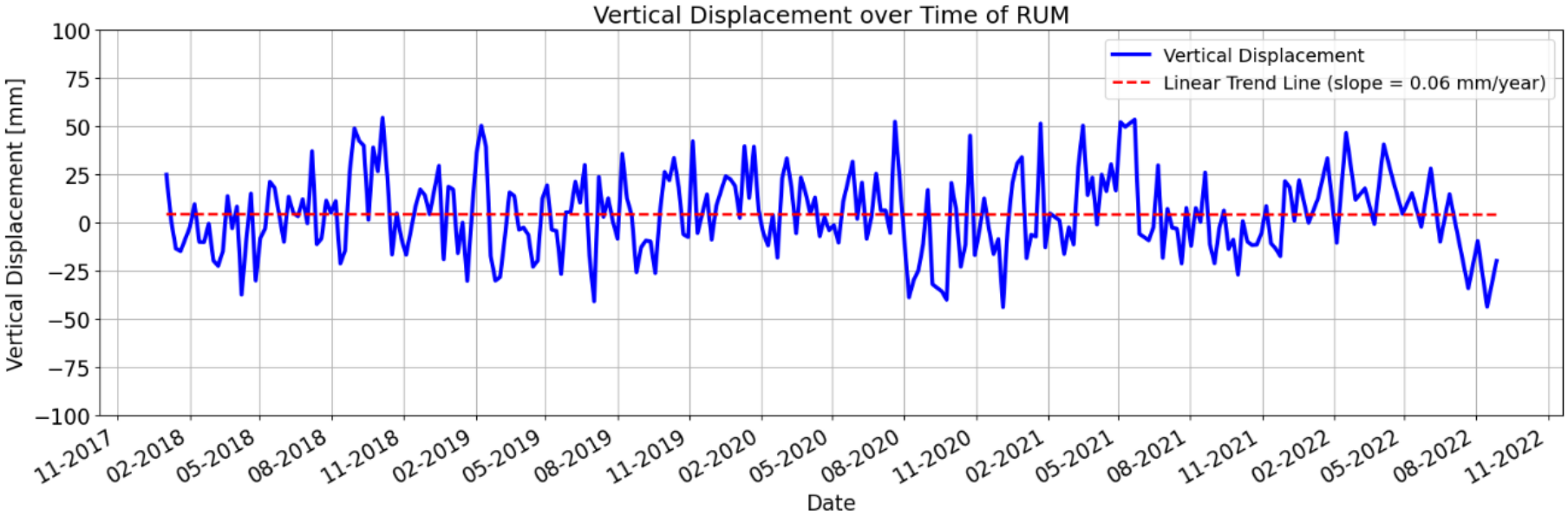

Figure A15.15: Estimated deformation timeseries of multiple, in this case 6, datapoints by solving for the full three-dimensional displacement vector by applying a least-squares estimate solution A fitted linear trendline provides an estimated annual deformation rate. Note that the location of this RUM is on the bridge crossing the Oukoop waterway. As a result, the estimated annual deformation rate is close to zero. This makes sense because the foundations of the bridge are most likely founded on the Pleistocene sand layer resulting in minimal estimated deformation over time.

Figure A15.16: Location of the RUM used in the timeseries estimate. Note that the location of the RUM is on the bridge crossing the Oukoop waterway.

Appendix 16 A2 Vinkeveen Data

This appendix shows the recorded settlement of the embankment connecting Vinkeveen to the A2. This data is owned and archived by Rijkswaterstaat. Figure A16.1 shows the recorded height of the embankment connecting Vinkeveen to the A2 over time. In here the gradual increase of embankment height to not cause an excess in pore water pressure is clearly visible. Figure A16.2 shows the recorded settlement over time of the embankment recorded by subsidence plates. Figure A16.3 shows the recorded settlement using subsidence plates plotted on logarithmic time scale. Figure A16.4 shows the estimated displacement rate in millimetres per week based on the recorded settlement over time of Figure A16.1.

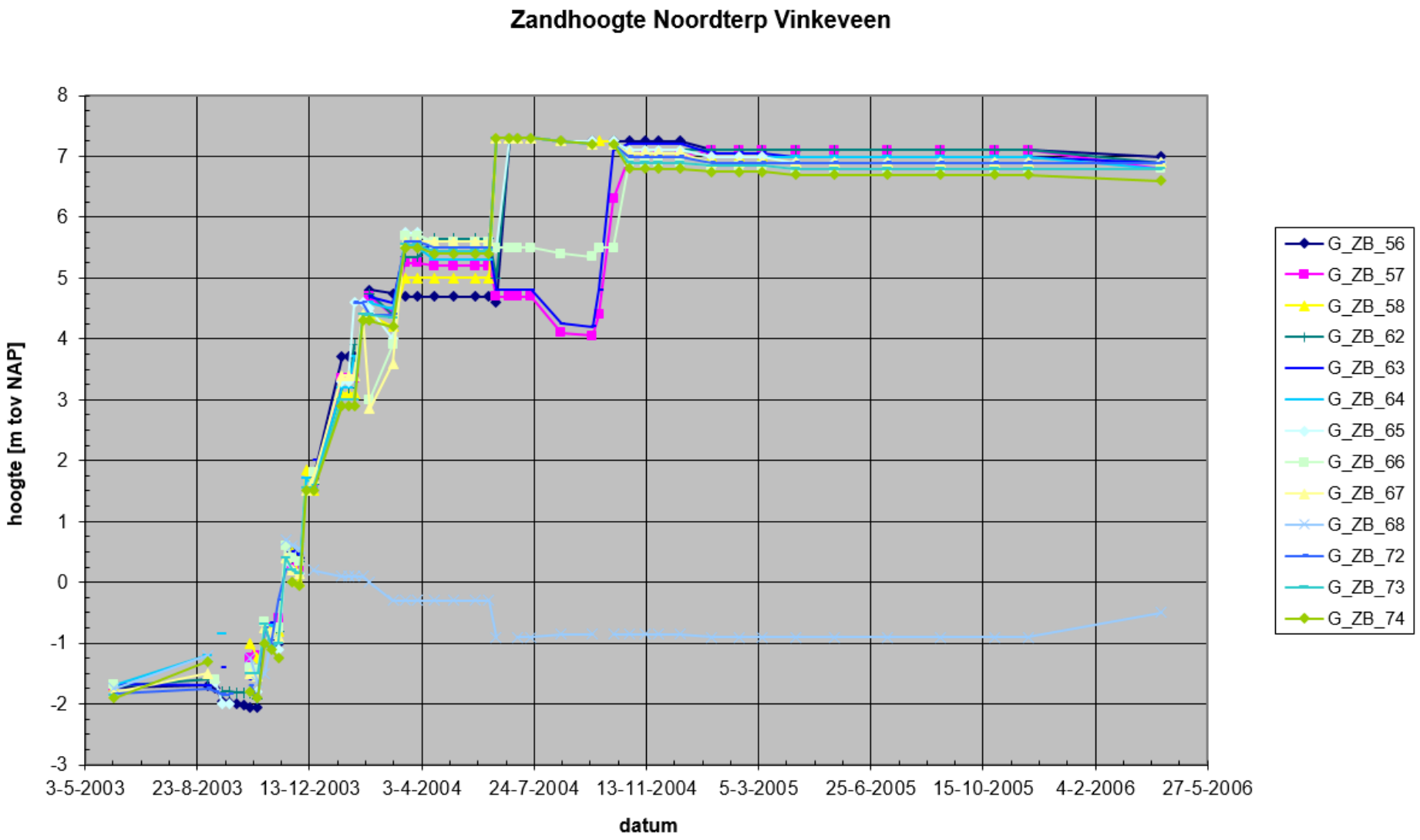

Figure A16.1: Height of the embankment connecting Vinkeveen to the A2 during construction. The gradual adding of sand, resulting in an increased height over time, is clearly visible.

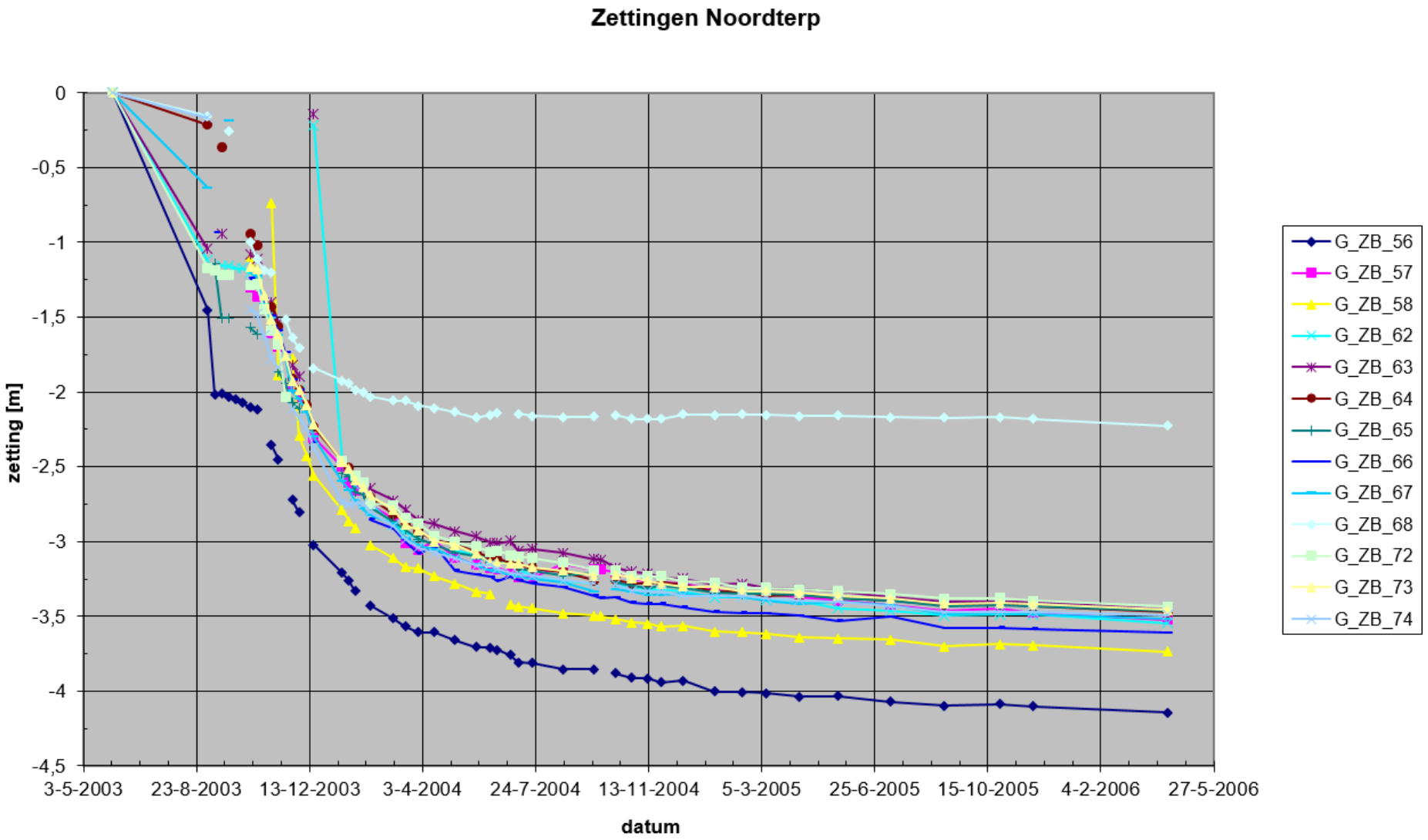

Figure A16.2: Recorded settlement of the embankment connecting Vinkeveen to the A2 using subsidence plates. The recorded settlement over time. Note how the recorded settlement becomes close to constant around October 2005 indicating the primary consolidation phase coming to an end.

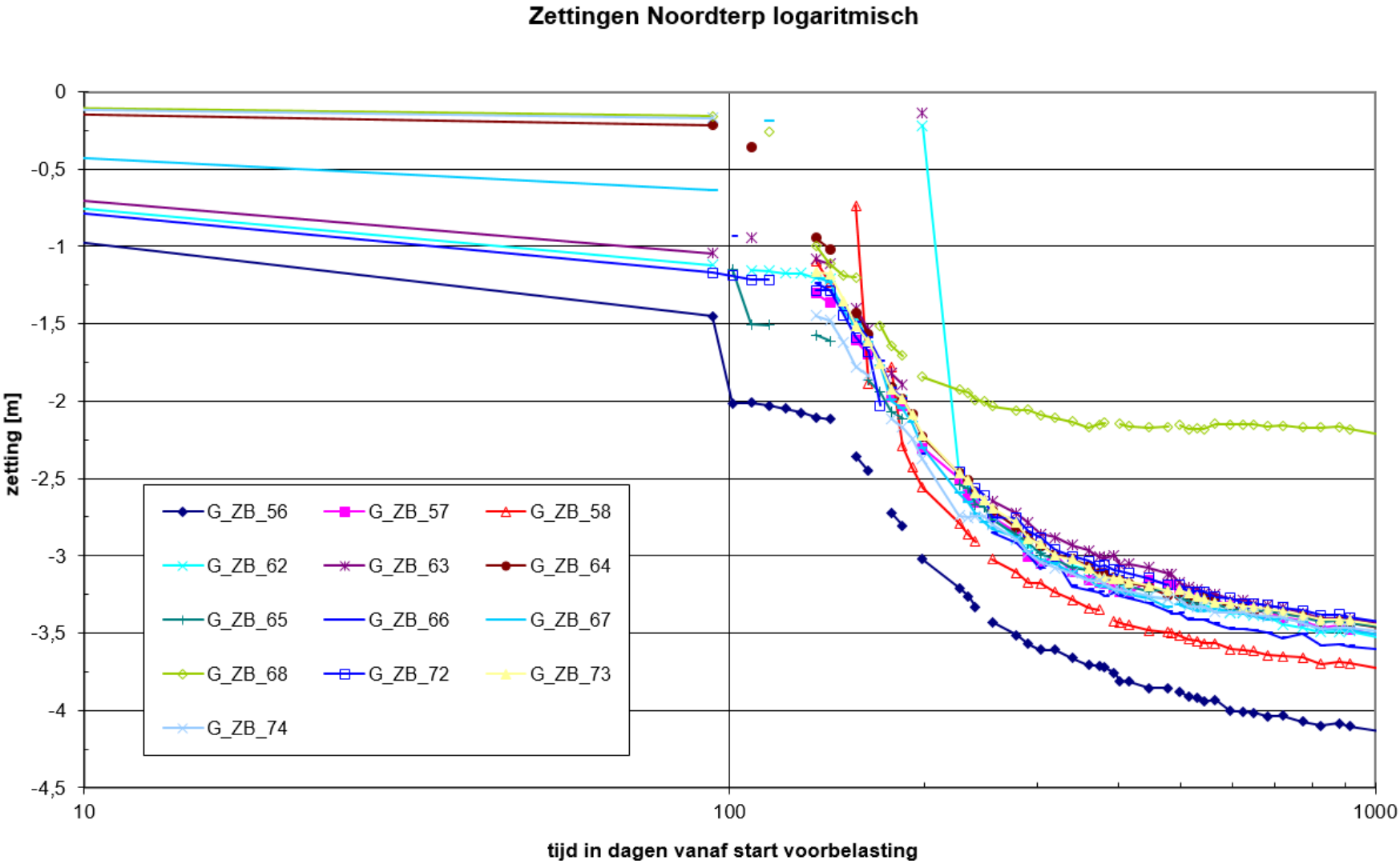

Figure A16.3: Recorded settlement of embankment construction connecting Vinkeveen to the A2 using subsidence plates plotted on logarithmic time scale in days after start of construction.

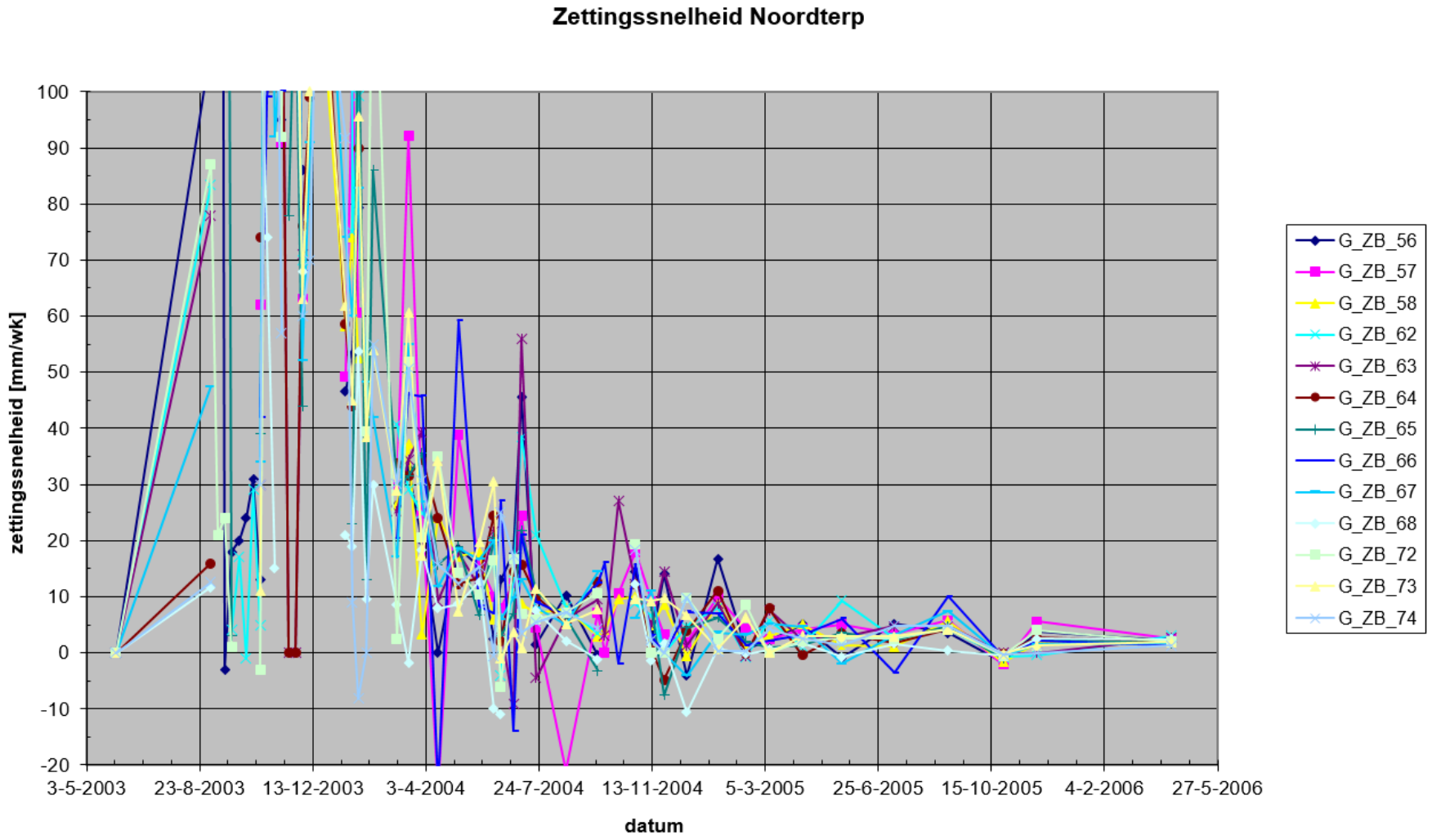

Figure A16.4: Estimated settlement rate, expressed in millimetres per week, of embankment construction connecting Vinkeveen to the A2.

Appendix 17 InSAR Methodology

A17.1.1 Deformation Measurement Technique

This annex covers the main principles of using Interferometric Synthetic Aperture Radar (InSAR) techniques to estimate deformation timeseries. Using InSAR to measure surface deformation poses multiple advantages over more common techniques such as settlement plates or levelling. Not only are settlement plates sensitive to mishaps on a project site, such as hitting the settlement plates with heavy equipment, they require continuous manual monitoring too. However, measuring techniques such as levelling generally have a higher precision compared to InSAR deformation estimation (Serrano-Juan et al., 2017). Depending of the required level of accuracy this can be an important consideration.

Depending on the satellite orbit, InSAR allows for a continuous gathering of surface deformation information. A location of interest can be measured every 12 days in case of a single orbit of the Sentinel-1 mission for example. In order to accurately estimate the surface deformation from this, understanding the working principles and current state of the art is required. This is especially important since a possible disadvantage of using InSAR is the complexity of decomposing the InSAR data into useable deformation data.

A17.1.2 Orbital Flight Path

Two flight trajectories can be distinguished. A near-polar flight trajectory moving from south to north is called ascending. The opposite direction, form north to south, is called descending (ESA, 2024). In general, satellites are right-side looking. This means the radar wave of the satellite is emitted on the right side of the satellites flight direction, as illustrated in Figure A17.1. Complex geometry can therefore be evaluated when combining the data of an ascending and descending satellite orbit as shown in Figure A17.1.

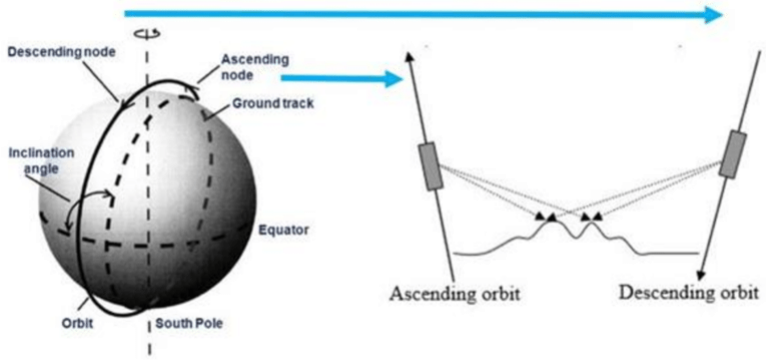

Figure A17.1: Definition of ascending and descending flight tracks [After Sertçelik, 2019].

A17.2 Method of Operation

Using InSAR as a method to evaluate deformation behaviour of a location of interest over time inherently requires geometric transformations of the available observations (Brouwer et al., 2023). This section therefore describes the steps needed to obtain deformation data which can be used as an estimated deformation timeseries of the location of interest.

A17.2.1 Phase Comparison

Each Synthetic Aperture Radar (SAR) image acquired by the radar device consists of multiple pixels, which form a two-dimensional (2D) matrix structure composed of rows and columns. This matrix constitutes the SAR image. Each pixel carries both phase and amplitude as a complex number, holding information about the signal's backscatter (Crosetto et al., 2016).

In general, objects in urban areas, such as rooftops, provide better backscatter compared to areas such as forests. After all, regarding vegetation, the majority of the radio pulse is absorbed instead of reflected back (Crosetto et al., 2016). The phase of a single SAR image is of little interest. A second image of the same area of interest taken at a different time is needed for analysis, as is shown in Figure A17.2. By applying double differencing and analysing the phase changes over time, valuable information—such as ground deformation—can be extracted from the SAR signal. Pixels that provide continuous backscatter with each satellite orbit are called persistent scatterers (PS) (Crosetto et al., 2020). These pixels can be used to deduce the deformation behaviour of the same scatter over time. Distributed scatters (DS) on the other hand are composed of multiple weaker scatterers. These are not used in this thesis.

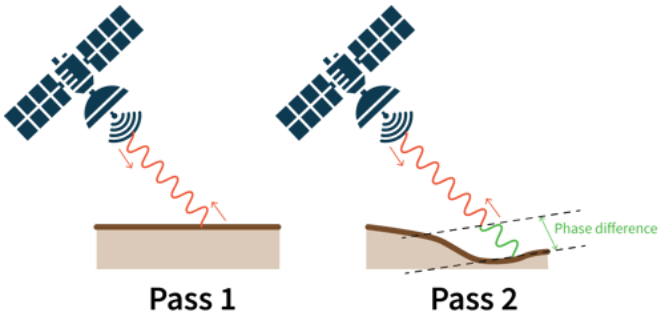

Figure A17.2: Phase comparison between different satellite passings [After DescartesLab].

A17.2.2 Terminology

To fully understand InSAR and its applications, it is essential to understand key terms that define its working principles. The following section describes some of the main concepts that are used in the deformation analysis of (part of) the A2 highway in the Netherlands, as described in Chapter 3 of this thesis.

Temporal coherence

For each measuring point (mp) the temporal coherence serves as a measure of radar signal consistency of a certain location of interest over time (Copernicus, 2024). This factor can be thought of as an indication of the stability of a mp between different SAR images. In here, a value close to 1 indicates good coherence over time. For example, the radar signal remains relatively unchanged over time. This factor is computed by comparing the phase values of different SAR images with respect to the displacement model used.

Amplitude dispersion

The amplitude dispersion between SAR images is calculated as the standard deviation of the amplitude of a SAR image divided by the mean amplitude over different SAR images (Copernicus, 2024). Due to the fact that vegetation often results in improper backscatter of the radar pulse, areas covered with canopy often have high amplitude dispersion. Areas that provide good backscatter such as steel barriers provide low amplitude dispersion. High amplitude dispersion suggests a weak and/or inconsistent scatter. When constructing a deformation time series, it therefore proves beneficial to analyse points with low amplitude dispersion. Buildings and line-infrastructure often have low amplitude dispersion which makes them suitable for estimating a deformation time series since they remain stable over time. This is generally not true for vegetation for example.

LOS
The satellite radar emits a radar beam towards the area of interest under an angle. Depending on this angle and surface roughness, the radar beam is scattered back toward the satellite. The direction in which the radar pulse is emitted is defined as the line of sight (LOS) of the satellite. This LOS direction is dependent on the viewing geometry towards the satellite (Brouwer et al., 2023).

Zero Doppler Plane
Most satellites follow a near polar-orbit. The Zero Doppler Plane (ZDP) is defined as the plane perpendicular to the flight direction of the satellite. Consequently, the LOS vector is positioned in the ZDP (Brouwer et al., 2023). Figure A17.3 illustrates the Zero Doppler Plane in blue where it is clearly demonstrated that the LOS direction is situated in this plane perpendicular to the flight direction.

Track angle
The track angle is defined as the clock-wise angle between the orbital direction of the satellite and the true North of Earth. The track angle can be used to distinguish ascending flight paths from descending ones. The orbital heading of the satellite changes ever so slightly over time due to the convergence of the Earths meridians.

Incidence angle
The incidence angle is defined as the angle between the emitted radar beam and a vertical reference line that is perpendicular to the Earth's surface (Copernicus, 2024). The incidence angle is thus used to describe the angle of the satellite beam.

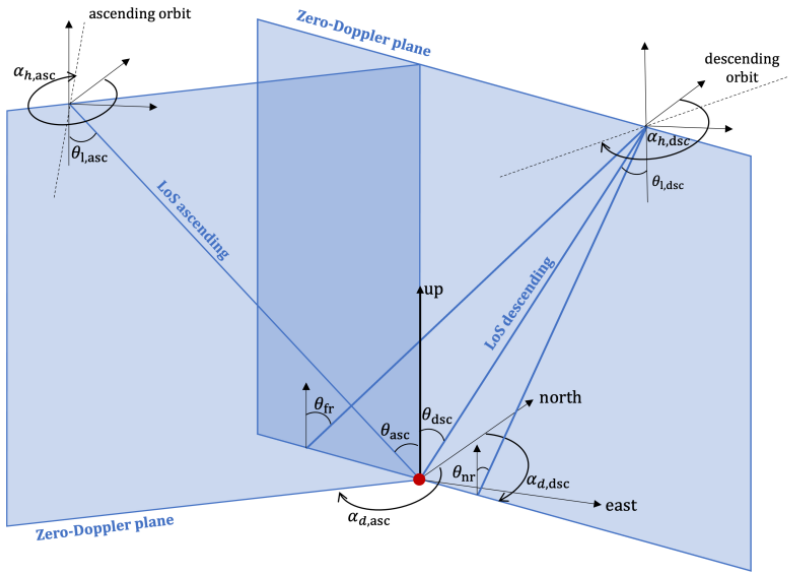

Figure A17.3: Schematic illustration of common terminology used to describe the viewing geometry of the satellite radar device [After Brouwer et al., 2023].

A17.3.1 Displacement Decomposition
From the estimated InSAR data retrieved from multiple satellite orbits, it becomes possible to decompose the terrain deformation behaviour of an area of interest. Distinction must be made between the deformation data obtained in line of sight of the satellite look-angle and the eventual direction of interest. In order to decompose the LOS terrain deformation into the directions of interest, information about the track angle and incidence angles is required. LOS displacements obtained from multiple satellite orbits allow for the decomposition into the full 3-dimsional displacement field (De Luca et al., 2017), (Casu et al., 2016), (Brouwer et al., 2023).

A17.3.2 RUM
It is crucial to include only those datapoints for which the assumption holds that they belong to a Region of Uniform Motion (RUM) (Brouwer et al., 2023). This assumption implies that the deformation behaviour of the selected datapoints is governed by the same underlying physical phenomena. Consequently, these datapoints can be grouped to form a set used for decomposing the full displacement vector. The final size of the resulting matrix , specifically the total number of rows, depends on the number of line-of-sight (LOS) datapoints used to construct the full Cartesian three-dimensional displacement vector. The selection of these datapoints is determined by the location of interest. Incorporating more datapoints theoretically enhances the robustness of the solution by mitigating the influence of noise and errors in individual LOS values.

The size of each set may vary, as the number of available coherent scatterers within a RUM differs. Therefore, an optimal balance must be achieved. A RUM containing a large number of datapoints risks incorporating points that do not follow the same deformation behaviour, leading to inaccuracies. A RUM too small risks there not being enough available datapoints from different viewing directions. Generally, the size of a RUM is influenced by the location of interest and the number of usable datapoints that maintain temporal coherence above a predefined threshold throughout the measurement period.

A17.3.3 LOS projection
To use InSAR as a method of estimating deformations over time of a location of interest it is important that the observations in the LOS direction are Spatio-Temporally Coinciding and Independent (STCI) (Brouwer et al., 2023). For example, it is important that a the deformation pattern of the analysed observations is caused by the same physical phenomena. If this is not the case, it is difficult to construct a decisive deformation time series of that particular RUM. Using LOS observations of different viewing directions improves the stability of the matrix. In addition, it is important to underline the importance of realising that InSAR analysis is a 3-dimenional method. On a 2-dimensional map for example, two points can be close together after which one could assume that these points automatically undergo the same deformation pattern. In practice however this is not automatically the case since each point can be of a different object with a different height which can show different deformation patterns. An example of this is a light post and a road barrier. Even though from above measuring points can be close together, they do not necessary undergo the same deformation pattern. Ensuring spatial coinciding datapoints is therefore important in obtaining a deformation estimate representing the location of interest.

A17.3.4 Time series
The Sentinel-1 satellite has a revisiting time of 6-12 days (Sentinelhub, 2025). This means that after 6 days the same area of interest is measured by the radar beam emitted from Sentinel-1. The displacement after every passing of 6 days is measured in the line-of-sight (LOS) direction of the radar looking direction and the Earth's surface. If only the displacement in the LOS is available, this can still provide useful information about the deformation pattern of the location of interest. Therefore, transformations of the observed LOS displacement vectors are required in order to estimate deformation rates in the directions of interest. The LOS displacement vector should therefore be projected on the conventional Cartesian reference system to ultimately distinguish the deformation rates in East-West, North-South and Up-Down (ENU) direction. Different approaches exist, all with different assumptions and biases, that will be described in the following section.

A17.3.5 Vertical Decomposition

A common misconception when working with InSAR data is the assumption that the LOS displacement in fact equals the vertical deformation without discussing the horizontal contribution to the original measurements (Brouwer et al., 2023). This procedure neglects the horizontal components of motion that would also be mapped into the full three-dimensional displacement vector (Hu et al., 2014).

In some situations however it proves possible to (only) focus on the vertical displacement field, thereby omitting terrain deformations in the horizontal directions. Under the assumption that horizontal deformations are negligible compared to vertical displacements, it is possible to project the LOS displacement on the Cartesian vertical directions by dividing the LOS displacement value by the cosine of the incidence angle, as is depicted in Figure A17.4 (Fialko et al., 2001), (Catalao et al., 2011).

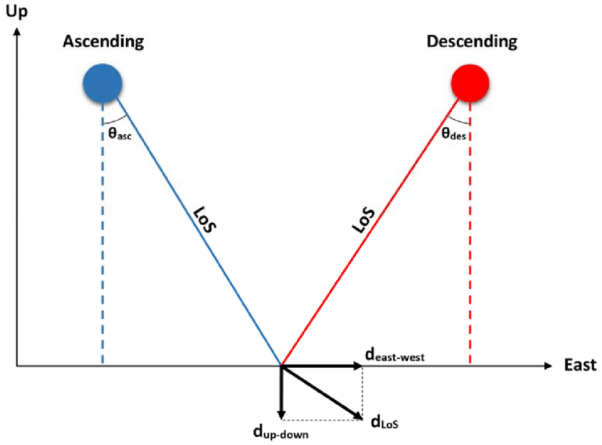

Figure A17.4: Line of site direction vector decomposed into vertical and horizontal deformation [After Tzouvaras et al].

However, depending on the deformation phenomenon causing the surface displacements this can result in errors at some pixels (Wright, et al., 2004). Depending on the location of interest, decomposition of the LOS displacement vector into the vertical direction can serve as a first estimate of the vertical deformation field. One should be aware however of the influence of neglecting horizontal deformations. The assumption of only vertical motion can hold true in some particular cases such as level areas like meadows and agricultural fields.

A17.3.6 System of Equations

By combining the LOS displacement vectors of both ascending and descending satellite orbits it becomes possible to estimate the deformation patterns in the ENU directions. By definition, to get an estimation of the full 3D- displacement vector in ENU direction, the information of at least three independent viewing directions, obtained by at least three satellite orbits, are required. This allows for a full-rank matrix with three unknowns. Under the assumption that the three ENU directions are independent, the constructed matrix containing the 3D displacement decomposition generally has a rank of 3 leading to three independent displacement directions estimates. The three unknown displacement values can be solved by solving this inverse problem (Brouwer et al., 2023).

One of the major difficulties of estimating the 3-D displacement vector arises from the track angles of different satellite orbits. The difference in track angle between ascending and descending is evident and is in the order of 180 degrees. The difference in track angles between adjacent flight orbits however is limited and only varies by a few degrees since all satellite orbits are near polar (Brouwer et al., 2024). As a consequence, the matrix describing the deformation in the three Cartesian directions can become unbalanced leading to an ill-conditioned matrix. This makes estimation of the 3D displacement vector sensitive to small perturbations in the LOS displacement signal vector over time resulting in inadequate deformation estimates. The possible ill-conditioning of a matrix is easily evaluated by calculating the conditioning number. The conditioning number is checked by evaluating the norm of the matrix or by evaluating the ratio of highest singular value over smallest singular value in a matrix.

A17.3.7 Inverse Problem

In order to produce 3D Cartesian displacement estimates, the 1-dimensional LOS deformation values of at least three independent satellite orbits are required. These displacements in LOS direction can then be decomposed into the three Cartesian directions, namely; vertical displacement (v_U), East-west displacement (v_E) and North-South displacement (v_N).

The SAR acquisition in LOS direction is in principle defined by the track angle (α) and the incidence angle (θ). As is described in Section A17.2, in todays practice most satellites follow a near polar orbit. This means a track angle of around 350° for ascending satellites and around 190° for descending satellite orbits. In here, variation of the track angle proves beneficial since it allows for independent viewing angles which inherently reduces the possibility of the system of equations becoming ill-conditioned (Brouwer et al., 2023). The 1-dimensional LOS displacement is decomposed in the Cartesian directions as per Equation A15.1

$$v_{\mathrm{LOS}} = \begin{pmatrix} \cos(\theta) & -\sin(\theta)\cos(\alpha) & \sin(\theta)\sin(\alpha) \end{pmatrix} \begin{pmatrix} v_U \\ v_E \\ v_N \end{pmatrix} \quad . \tag{A15.1}$$

In here, v_U, v_E and v_N are the deformation values in vertical, East and North direction respectively. By looking at Equation A15.2 it becomes evident that the LOS deformation values of at least three independent satellite orbits are required to solve for the unknown Cartesian displacements. This creates the following inverse problem;

$$\begin{pmatrix} V_{\mathrm{LOS1}} \\ V_{\mathrm{LOS2}} \\ V_{\mathrm{LOS3}} \end{pmatrix} = \begin{bmatrix} \cos(\theta_1) & -\sin(\theta_1)\cos(\alpha_1) & \sin(\theta_1)\sin(\alpha_1) \\ \cos(\theta_2) & -\sin(\theta_2)\cos(\alpha_2) & \sin(\theta_2)\sin(\alpha_2) \\ \cos(\theta_3) & -\sin(\theta_3)\cos(\alpha_3) & \sin(\theta_3)\sin(\alpha_3) \end{bmatrix} \begin{pmatrix} v_U \\ v_E \\ v_N \end{pmatrix} \quad . \tag{A15.2}$$

Evidently, the system of Equations in A15.2 can be extended to incorporate the LOS displacement of other satellite orbits. This ultimately leads to an overdetermined inverse problem as per Equation A15.3

$$\begin{pmatrix} V_{\mathrm{LOS1}} \\ V_{\mathrm{LOS2}} \\ V_{\mathrm{LOS3}} \\ \vdots \\ V_{\mathrm{LOS}n} \end{pmatrix} = \begin{bmatrix} \cos(\theta_1) & -\sin(\theta_1)\cos(\alpha_1) & \sin(\theta_1)\sin(\alpha_1) \\ \cos(\theta_2) & -\sin(\theta_2)\cos(\alpha_2) & \sin(\theta_2)\sin(\alpha_2) \\ \cos(\theta_3) & -\sin(\theta_3)\cos(\alpha_3) & \sin(\theta_3)\sin(\alpha_3) \\ \vdots & \vdots & \vdots \\ \cos(\theta_n) & -\sin(\theta_n)\cos(\alpha_n) & \sin(\theta_n)\sin(\alpha_n) \end{bmatrix} \begin{pmatrix} v_U \\ v_E \\ v_N \end{pmatrix} + \epsilon \quad . \tag{A15.3}$$

Where;

$$\begin{pmatrix} \hat{v}_U \\ \hat{v}_E \\ \hat{v}_N \end{pmatrix} = \begin{cases} A^{-1}y, & \text{for } n = 3, \text{ and} \\ \left(A^T A\right)^{-1} A^T y, & \text{for } n > 3 \end{cases} \quad \text{with} \quad y = \begin{pmatrix} V_{\mathrm{LOS1}} \\ V_{\mathrm{LOS2}} \\ V_{\mathrm{LOS3}} \end{pmatrix} \quad . \tag{A15.4}$$

In this case the overdetermined inverse problem can be found by finding the least squares solution to the problem. In this case there is no exact solution to the problem. This method thus aims to find the solution that minimises the residuals between the observed values and the model predictions.

Appendix 18 A2 Soil Profiles

This appendix shows the soil profiles of Vinkeveen and Gaasp. These soil profiles are used to estimate the strain rates of the embankment connecting Vinkeveen to the A2 and the peat meadow near Gaasp. Both cpt's aswell as bore profile indicate a compare soil stratigraphy where approximately 6 meters of peat are found below mean surface level.

Figure A18.1 shows the bore profile next to the A2 connecting Vinkeveen to the A2. This profile shows a peat layer of approximately 6 meters. Combined with the cpt profile of Figure A18.4 this gives an indication of the peat layer thickness directly below surface level.

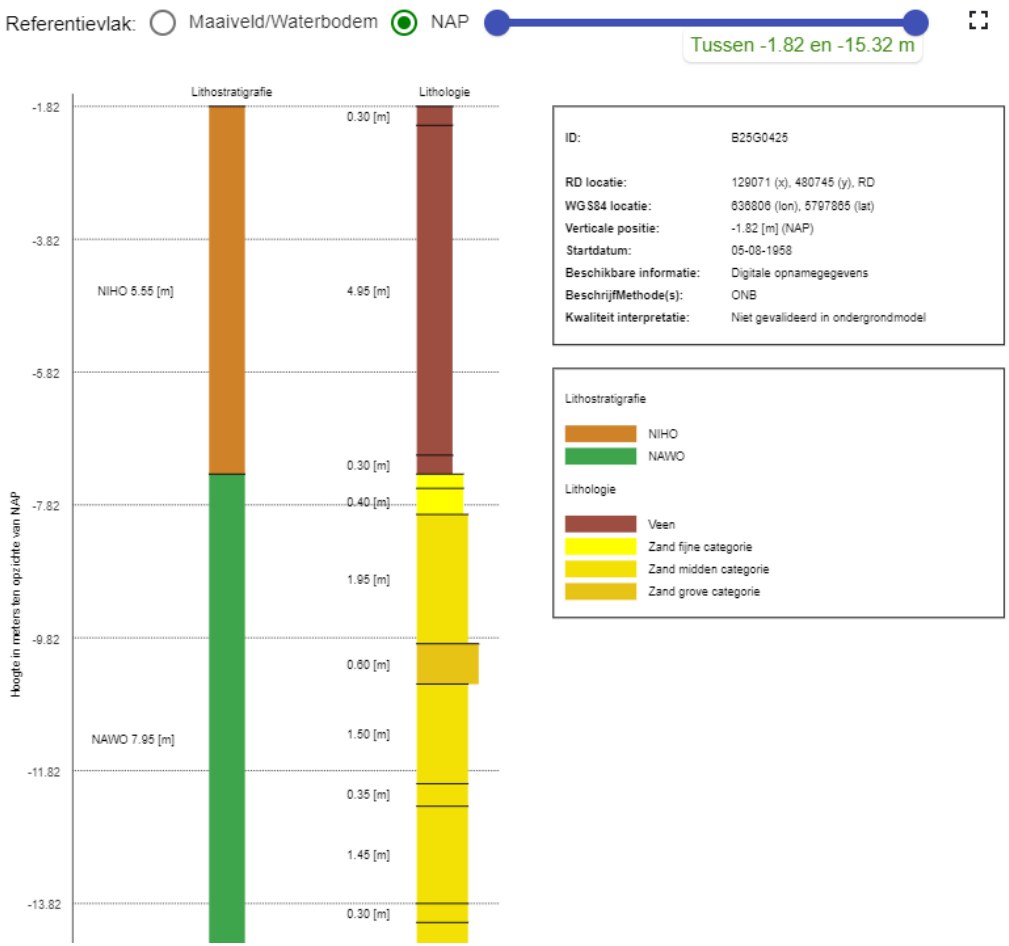

Figure A18.1: Bore profile next to the embankment connecting Vinkeveen to the A2. Measurement depts are with respect to Nap. Observe the 6 meter thick peat later directly below surface level.

Figure A18.2 shows a bore profile near the corner reflector placed in a meadow near Gaasp. A 5-6 meter thick peat layer can clearly be identified.

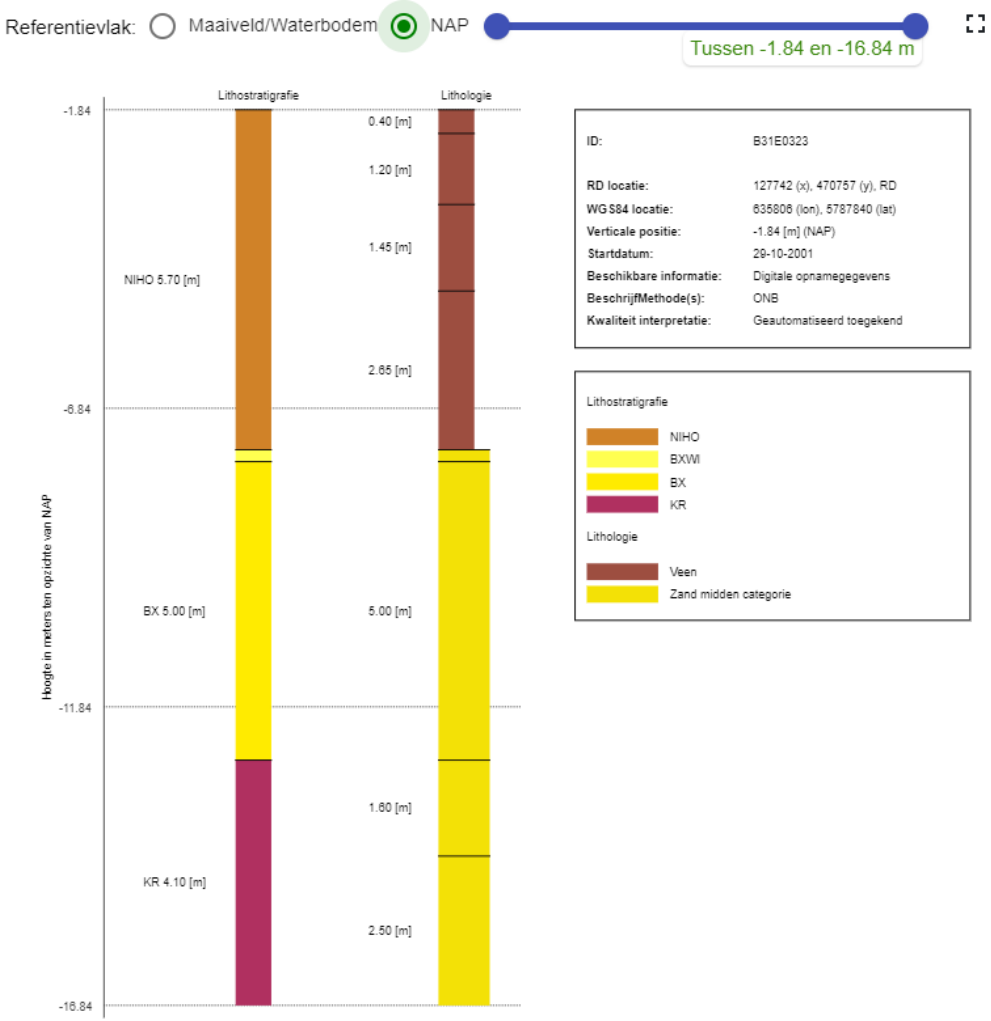

Figure A18.2: Bore profile next to the corner reflector in Gaasp. Measurement depths are with respect to NAP.

Figure A18.3 shows a bore profile near the Zegveld polder. A 6 meter thick peat layer can clearly be identified.

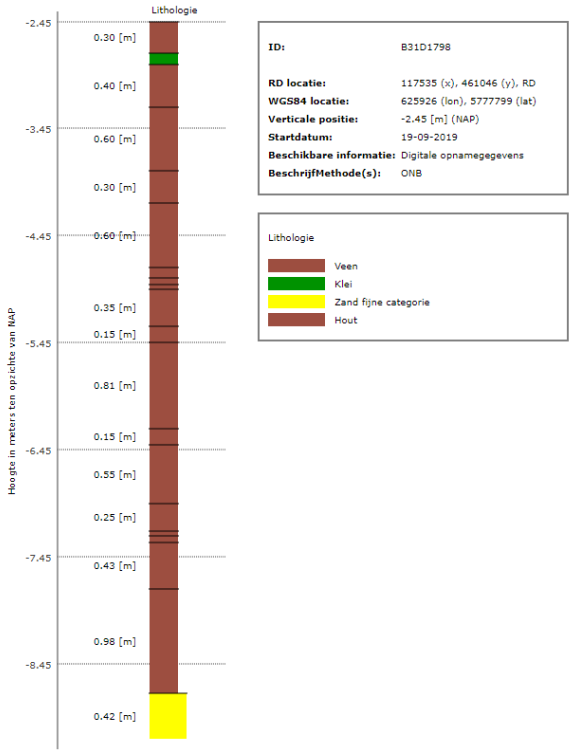

Figure A18.3: Bore profile of Zegveld polder shows a 6 meter thick peat deposit.

The CPT profile of Figure A18.4 taken directly adjacent to the A2 near Vinkeveen clearly shows Holocene layers within the first 6-7 meters of the profile. The relatively high friction angle combined with a low cone resistance indicates peat. This is to be expected for this part of the A2, as indicated in the bore profile in Figure A18.1.

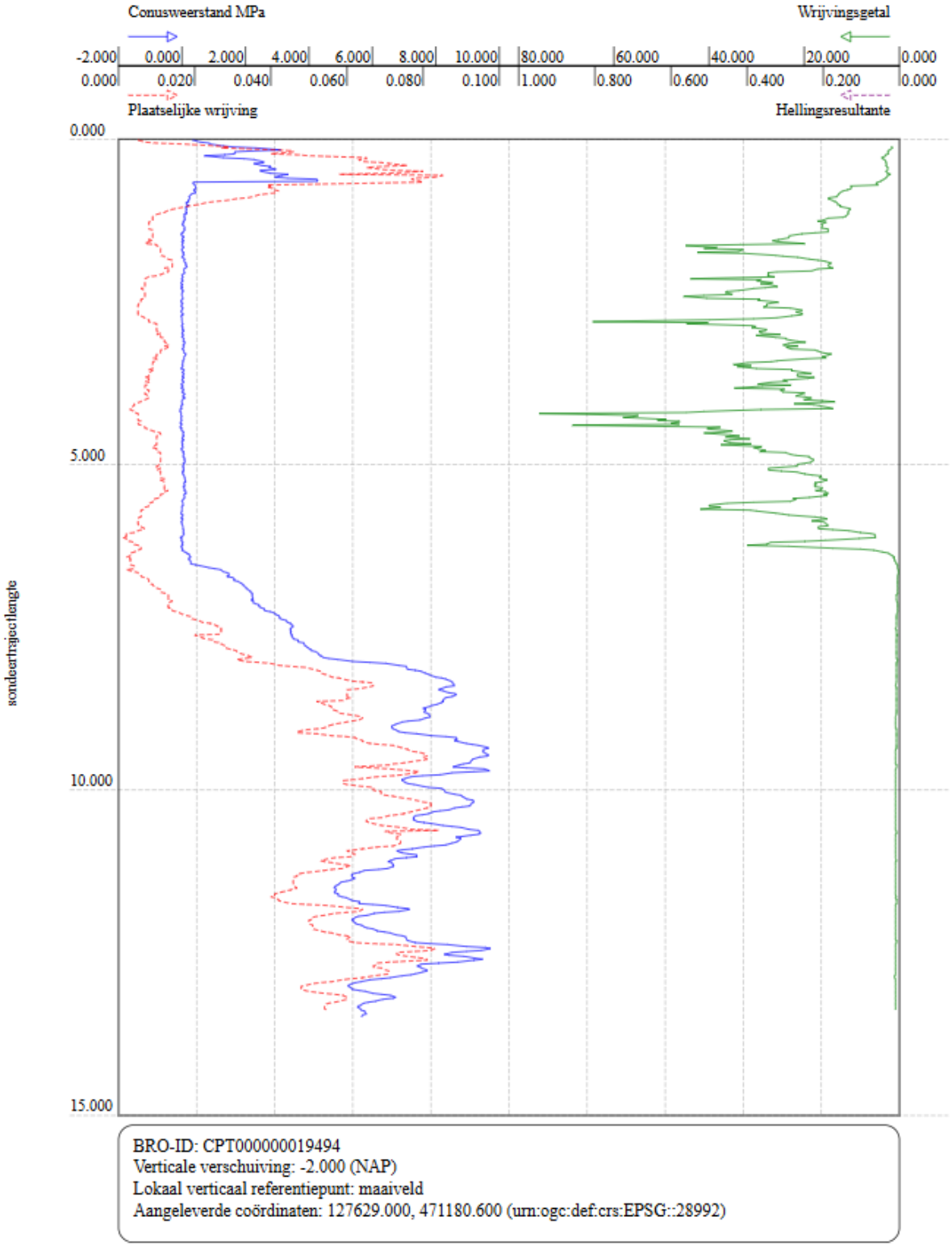

Figure A18.4: CPT-profile next to the embankment connecting Vinkeveen to the A2 clearly shows a 6 meter thick peat deposit.

The CPT profile of Figure A18.5 is near the location of the corner reflector near Gaasp. The low cone resistance and high friction angle indicate a peat layer of approximately 5-6 meters directly below surface level. This observation is in line with the bore profile of Figure A18.2. Furthermore the base peat layer approximately 10 meters below surface level can clearly be identified.

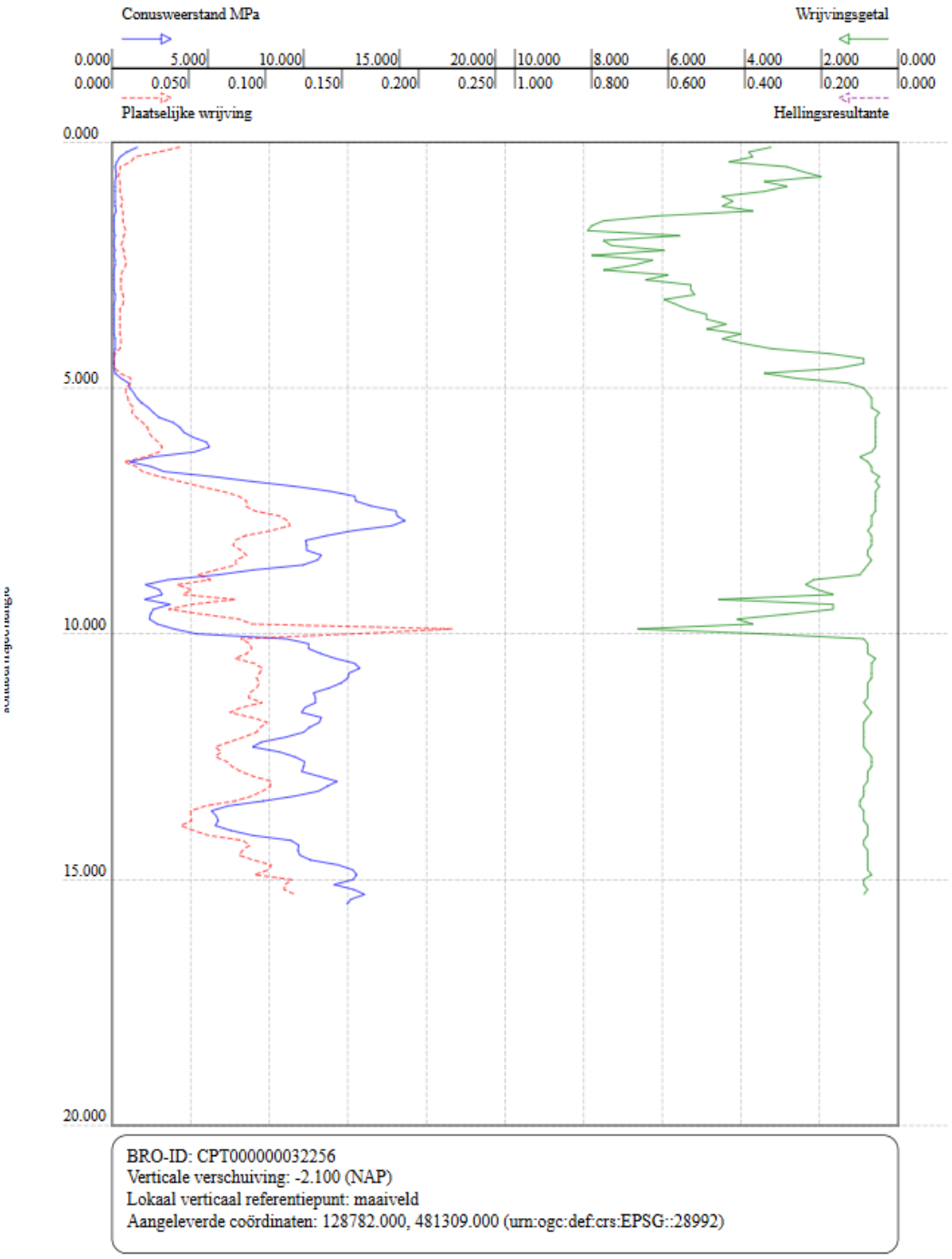

Figure A18.5: CPT-profile next to the corner reflector near Gaasp.